January 2015

AN INNOVATIVE WORKING CONCEPT FOR VARIABLE DELIVERY FLOW EXTERNAL GEAR MACHINE

Ram Sudarsan Devendran
Purdue University

PURDUE UNIVERSITY
GRADUATE SCHOOL
Thesis/Dissertation Acceptance

This is to certify that the thesis/dissertation prepared

By Ram Sudarsan Devendran

Entitled

An Innovative Working Concept for Variable Delivery Flow External Gear Machine

For the degree of Doctor of Philosophy

Is approved by the final examining committee:

Andrea Vacca
Chair

Monika Ivantysynova

John Lumkes Jr.

John M. Starkey

To the best of my knowledge and as understood by the student in the Thesis/Dissertation Agreement, Publication Delay, and Certification Disclaimer (Graduate School Form 32), this thesis/dissertation adheres to the provisions of Purdue University's "Policy of Integrity in Research" and the use of copyright material.

Approved by Major Professor(s): Andrea Vacca

Approved by: Ganesh Subbarayan 7/8/2015

Head of the Departmental Graduate Program Date

AN INNOVATIVE WORKING CONCEPT FOR VARIABLE DELIVERY FLOW EXTERNAL GEAR MACHINE

A Dissertation

Submitted to the Faculty

of

Purdue University

by

Ram Sudarsan Devendran

In Partial Fulfillment of the

Requirements for the Degree

of

Doctor of Philosophy

August 2015

Purdue University

West Lafayette, Indiana

To my parents, my sister and my advisor.

ACKNOWLEDGEMENTS

First of all, I would like to thank my advisor, Prof. Andrea Vacca for giving me an opportunity to work towards my PhD degree at Maha Fluid Power Research Center of Purdue University. He has played a major role in my development as a researcher and a professional. His continuous support and constant motivation has always been vital in making even the most stressful times manageable. I am very grateful to him for making me the person who I am now! I would also like to thank Prof. Monika Ivantysynova for inspiring me and provide guidance throughout the course of my study at Maha. I extend my gratitude to: Prof. John Lumkes and Prof. John Starkey for graciously agreeing to be a part of my advisory committee and their guidance.

I would like to express my gratitude to my parents and my sister for their immense love, support and trusting me in whatever I wanted to pursue. I am deeply indebted for all the sacrifices they have made for me so that I could live a successful and happy life. I would also like to thank my friends and previous members of the lab, especially Sujan, Davide, Marco for their support and motivation which drove me to pursue a PhD degree. I would also like to thank my close friends in the lab, Sidhant and Pulkit for all the fun and enjoyable times which we partook together.

I would like to thank Anthony Franklin for always being friendly and positive whenever approached for questions related to the test rig. Thanks are due to Susan Gauger for being a mother away from home and always being gracious with a beautiful smile. Finally, I would like to thank all the other members of the lab for making this journey a great experience.

TABLE OF CONTENTS

Page

Page

LIST OF TABLES

Table Page

LIST OF FIGURES

Figure Page

Figure Page

Figure Page

Figure Page

Figure Page

Figure Page

NOMENCLATURE

Symbol	Description	Units
D	Vertical distance of the delivery groove from the line joining the inter-axis of the two gears	mm
H	Horizontal dimension of the delivery and suction grooves	mm
M	Torque	Nm
N	Number of fundamental frequencies of interest	-
P	Pressure in the TSV	bar
$P(f)$	Fourier transform of the pressure ripple signal	bar
$P_{D,avg}$	Average pressure at the delivery	bar
P_{out}	Outlet/Delivery Pressure	bar
P_{sat}	Saturation pressure of the operating fluid	bar
$P_{TSV,peak}$	Pressure in the tooth space volume	bar
Q_{avg}	Average delivery flow rate	lpm
Q_i	Instantaneous delivery flow rate	lpm
Q_m	Mean delivery flow rate	lpm
S	Vertical distance of the suction groove from the line joining the inter-axis of the two gears	mm
V	Displacement of the pump	m^3
k	Index for the fundamental frequency of the FFT	-
l	Line of action	-
m	Normal module	mm
$\dot{m}$	Mass flow rate	kg/s

Symbol	Description	Units
r_a	Addendum radius	mm
r_0	Pitch radius	mm
r_b	Base circle radius	mm
r_r	Root circle radius	mm
r_{bd}	Drive side base circle radius	mm
r_{bc}	Coast side base circle radius	mm
t	Tooth thickness of the gear cutter	mm
Z	Number of teeth	-
α_{DL}	Angular position of the left wing of the delivery groove	°
α_{DR}	Angular position of the right wing of the delivery groove	°
α_{SL}	Angular position of the left wing of the suction groove	°
α_{SR}	Angular position of the right wing of the suction groove	°
α_0	Pressure angle	°
α_a	Pressure angle at the addendum circle	°
α_{0d}	Drive pressure angle	°
α_{0c}	Coast pressure angle	°
β	Level of displacment	-
δ_Q	Non-uniformity in flow rate	lpm
δ_M	Non-uniformity in input torque	Nm
θ_D	Angular position at which the TSV begins to be trapped between the points of contact of the teeth.	°
θ_S	Angular position at which the TSV ends to be trapped between the points of contact of the teeth.	°
η_v	Volumetric efficiency	-
ρ	Density of the operating fluid	kg/m^3
ρ_r	Root fillet radius of the rack cutter	mm
θ, ϑ	Involute co-ordinate parameter	°
ν, ξ	Trochoid co-ordinate parameter	°

Symbol	Description	Units
Ω	Orifice area of the connections between the two TSVs	mm^2

ABBREVIATIONS

Symbol	Description
EGM	External Gear Machine
FD	Fixed displacement
FSI	Fluid Structure Interaction
HP	High Pressure
LP	Low Pressure
TSV	Tooth Space Volume
VD	Variable Displacement
avg	Average
max	Maximum value
min	Minimum value

ABSTRACT

Devendran, Ram Sudarsan. Ph.D., Purdue University, August 2015. An Innovative Working Concept for Variable Delivery Flow External Gear Machine. Major Professor: Andrea Vacca, School of Mechanical Engineering.

An innovative and unique working concept for variable delivery external gear machines (VD-EGMs) is presented in this study. The proposed design not only encompasses all the well-known and important advantages of traditional external gear machines but also introduces a feature for varying the displacement (flow delivered per unit revolution). The novel principle of achieving variable displacement in EGMs is based on the variable timing of the connections of the displacement chambers/tooth space volumes (TSVs) with the inlet/outlet ports. The timing variation is obtained by the addition of a simple element (called a "slider") within the lateral bushings. The position of the slider determines the amount of flow displaced per unit revolution. Starting from the geometry of the design and the proposed concept, analytical expressions for predicting displacement variation, flow rate and input shaft torque were derived. With this working principle, the range of variation of the displacement can be significantly increased by modifying the gear profiles. Therefore, in this work, novel gears with asymmetric teeth profile are designed with the help of a novel tool developed particularly for this process. However, due to the inherent nature of the displacing action of the EGM due to the meshing of the gears, it is not possible to achieve a full flow variation from 0%-100%. Therefore, to maximize the range of flow variation while considering all the other important performance features of the machine to be maintained at an optimum, a multi-objective genetic algorithm based optimization method is used to identify the optimal design of gears and grooves in the lateral bushings. The performance of the design

configurations were analyzed in detail by using HYGESIM (HYdraulic GEar machines SIMulator) Simulation tool. An optimal design of the machine was identified which was capable of maximizing the reduction (100% - 68%) in flow variation, thereby providing lower delivery flow at the expense of reduced torque (hence reduced input power). The validity of the proposed novel VD-EGM was demonstrated using a proof of concept test performed using the prototypes of the optimal design. The simulated results provided by HYGESim were validated with those obtained from the measured data thereby accomplishing a very good agreement between the experimental data and the model predictions. The successful proof of concept test results, lead to the design of two flow control actuation systems which represent a manual system and an automatic pressure compensated system. The performances of the prototypes were analyzed using a steady state test rig. Experimental results show that the flow rate and input shaft torque reduces proportionally with displacement in the case of the manual flow control system. The measured volumetric efficiencies at lower levels of displacement were found to be lesser than those at maximum displacement, which are in line with the performance of typical other VD units in the market. The flow control actuation system based on pressure compensator principle was designed to reduce the flow automatically depending on the pressure at the outlet. Experimental performance of the VD-EGM with pressure compensated actuation system show that the delivered flow reduces automatically after the preset pressure is reached. The input shaft torque was also seen to reduce proportionally with the corresponding displacement. The experimental results show positive potentials in the working concept of the VD-EGM, which would lead to a new direction in designing cost effective VD units that can be used in place of fixed displacement units to provide the additional flow on demand functionality; thereby significantly increasing the overall energy efficiency of the hydraulic system in which the VD-EGM is used.

1. INTRODUCTION

In this chapter, an introduction to the problem that is addressed by the research is provided. Firstly, the motivation behind the study is described to highlight the specific reasons that led to the study. Secondly, a short description of the design and working of the external gear machines (EGMs) is provided, followed by the objectives of the research that are being addressed. Lastly, a summary of an extensive review of the previous literature in the considered field has been provided.

1.1. Research Motivation

In a typical hydraulic circuit, the pump generates the flow that is used by the other components (actuators – cylinders, motors etc.) thus converting mechanical energy into hydraulic energy. Broadly, the same operation can be obtained by using fixed or variable displacement pumps, which consume different levels of energy. A fixed displacement (FD) pump transfers a fixed amount of fluid from the inlet to the outlet for a particular operating speed. However, a variable displacement (VD) unit is capable of changing the amount of fluid delivered to the outlet for the same operating speed. The VD units offer flow on demand capabilities, which are utilized in modern systems such as load sensing systems and displacement controlled systems. However, with FD units, there is an inevitable wastage of energy when the actuator requires lesser flow. The difference between the operations of the circuits with fixed and variable displacement units can be explained as follows.

Firstly, Figure 1(A), shows a circuit with a FD unit (very often an EGM), represented by ‘P’, and connected parallel with a pressure relief valve ‘R1’. During operation, the pump

provides a constant flow rate which depends on the displacement of the pump and the speed of rotation of the pump. The constant flow is delivered up to the maximum pressure value (p*) reached in the system, which is controlled by the setting of the relief valve. If the pressure at the delivery of the pump reaches the value p*, the relief valve starts to open, thereby directing more flow to the tank and less flow (Q_u) to the user. Assuming all the components are ideal, the efficiency of the system can be expressed by Eq. (1.1) as the ratio of useful power, P_u over the input power, P_{in} provided by the electric motor, EM.

$$\eta = \frac{P_u}{P_{in}} = \frac{Q_u \cdot p_u}{T \cdot \omega} = \frac{(Q_0 - Q_{valve}) \cdot p_u}{V_d \cdot p_u \cdot \omega} = 1 - \frac{Q_{valve}}{Q_0}. \quad (1.1)$$

As can be seen from Figure 1(B), as long as the pressure at the delivery of the pump is less than p*, the efficiency of the system is one as depicted by the blue striped box. When the pressure rises above p*, the displaced flow is lower (Q_u) and energy is dissipated through the relief valve (represented by the red box). Therefore, the efficiency of the system reduces and eventually falls to zero when the entire pump flow goes through the relief valve back to the tank. It can be clearly understood that the control of delivered flow and hence the power using a FD unit is always energy dissipative.

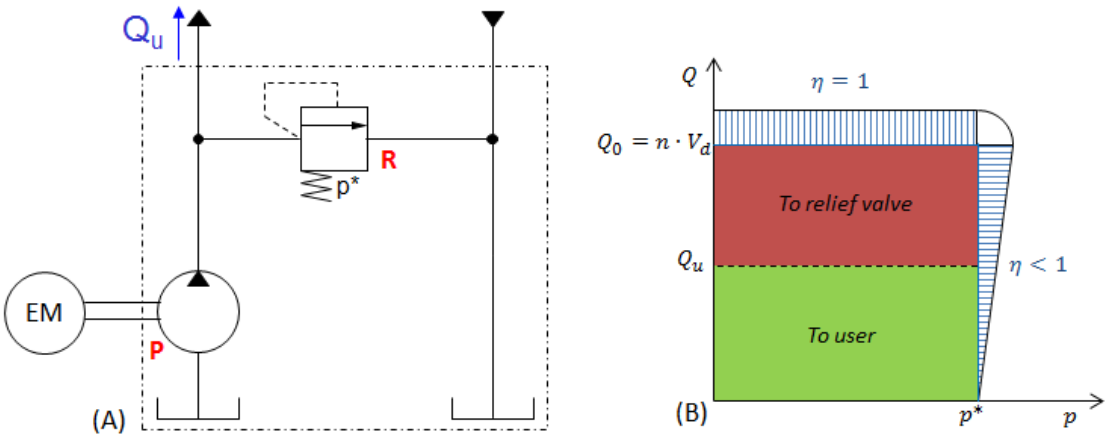

Figure 1: (A) Hydraulic circuit with a FD unit as the flow source; (B) Characteristic curve and efficiency for the system using a FD unit.

Differently from controlling the delivered flow using FD units, VD units are used for the same purpose by being capable of changing their displacement. A simple example is

shown in Figure 2(A), where a VD unit is used with a pressure compensator/regulator without the use of a pressure relief valve.

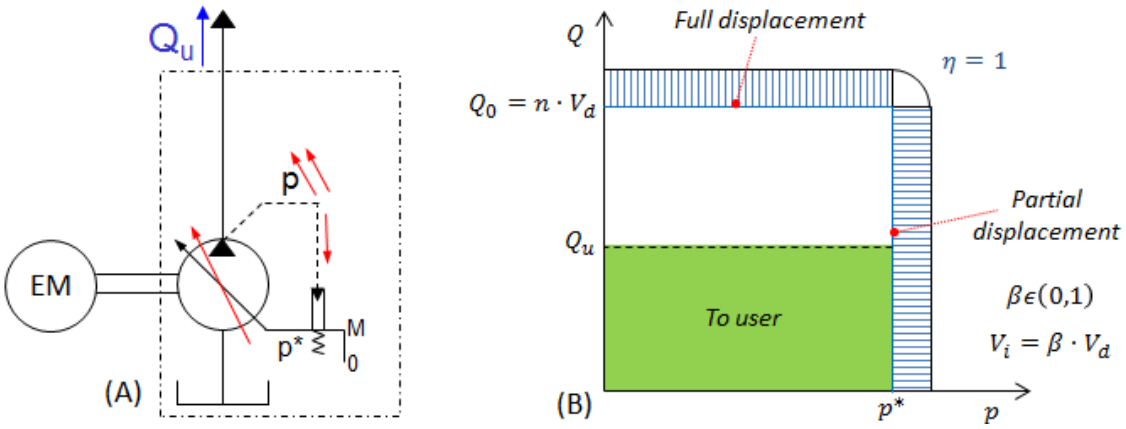

Figure 2: (A) Hydraulic circuit with VD unit as the flow source; (B) Characteristic curve and efficiency of a system using VD unit.

During the operation of the system, the pump is set to maximum displacement by a spring which is adjustable. When the pressure at the delivery of the pump reaches the pre-set value (p*) of the spring, the displacement control system (pressure compensator) of the pump automatically varies the displacement of the pump, providing lower flow while still maintaining the pressure at p*. This setup of changing the displacement using a spring as a compensator is popularly known as actuation using pressure compensation. When the displacement of the pump is changed, the unit is operating at a lower or partial capacity thereby adapting to the lower flow requirements of the user. As can be seen from Figure 2(B), the efficiency of the system always remains at one even while operating at partial capacity, because the whole pump flow rate serves the user directly. The expression for efficiency can be written as,

$$\eta = \frac{P_u}{P_{in}} = \frac{Q_u \cdot p_u}{T \cdot \omega} = \frac{\beta \cdot V_d . \omega \cdot p_u}{\beta \cdot V_d \cdot p_u \cdot \omega} = 1 \qquad (1.2)$$

Even though, traditional EGMs possess several advantages (as described in Section 1.2), they are inherently FD type units hence they call for a procedure for controlling the delivered flow which is usually severe in energy dissipation, hence are unsuitable for applications in energy efficient system layout configurations [1], [2]. In contrast, the VD units (using electrohydraulic controls) are more efficient (advantageous in terms of

energy consumption and also offer better possibilities of control) and are typically more than 10 times expensive and have much more complicated design assembly (with numerous parts) as compared to EGMs. Therefore, the industry and academia have dedicated significant research efforts (as described in Section 1.4) in finding a novel design of EGM which are capable of varying the displacement while simultaneously preserving the advantages of low cost, compactness, reliability and efficiency.

Although a new cost-effective hydrostatic unit capable of achieving a full (0-100%) displacement regulation would be ideal to replace current expensive VD machines; the proposition and development of a partially variable displacement unit (such as from 50%-100%) will be capable of substituting current fixed displacement units with significant energy advantages. As a matter of fact, in many fluid power systems the fixed displacement hydrostatic unit is sized for the peak demands of flow, and consequently the unit idles for significant intervals of the machine operation. Therefore, introducing a unit of partial VD-EGM in such circuits will appreciably reduce the energy consumption of the system.

1.2. Introduction to External Gear Machines

The well know advantages of external gear machines (EGMs) such as low cost, ease of manufacture, compactness, operating efficiency and reliability make them as one of the most popular and widely used positive displacement machines. In many applications where EGMs are used as main flow supply units include: fuel injection systems, small mobile applications such as micro-excavators, turf and gardening machines, fixed applications such as: forging machines, hydraulic presses etc. In most of the other applications, they are principally used as auxiliary flow supply components such as hydraulic power steering systems, fan drive systems, and as charge pumps in hydrostatic transmissions. The principal components of a typical EGM are shown in Figure 3.

EGMs are known to have a very simple principle of operation. The gears are driven by mechanical power provided (by a prime mover) to the shaft and converts the mechanical energy to fluid energy. The fluid is transferred from the inlet to the outlet due to the

rotation of the gears and the displacement of the fluid is achieved by the meshing of the gears (as shown in Figure 4).

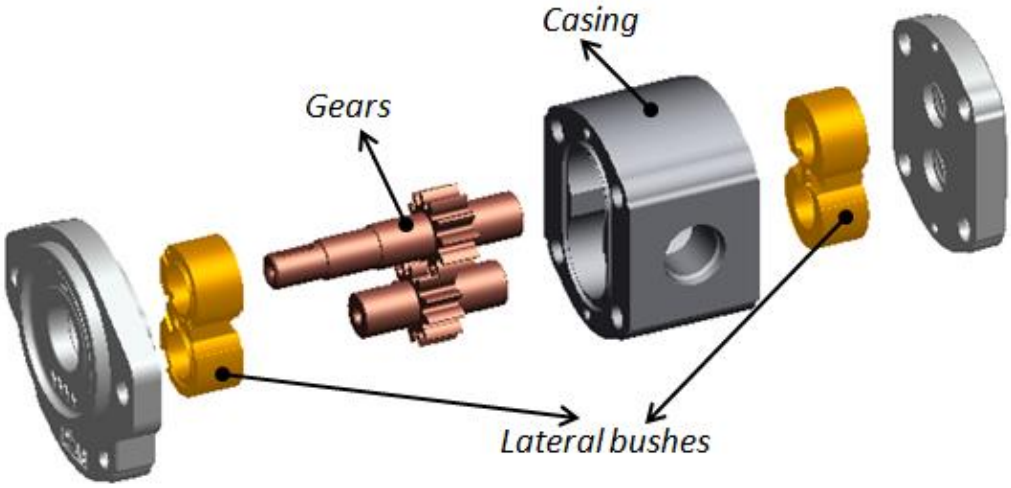

Figure 3: Main elements of a typical EGM for high pressure applications.

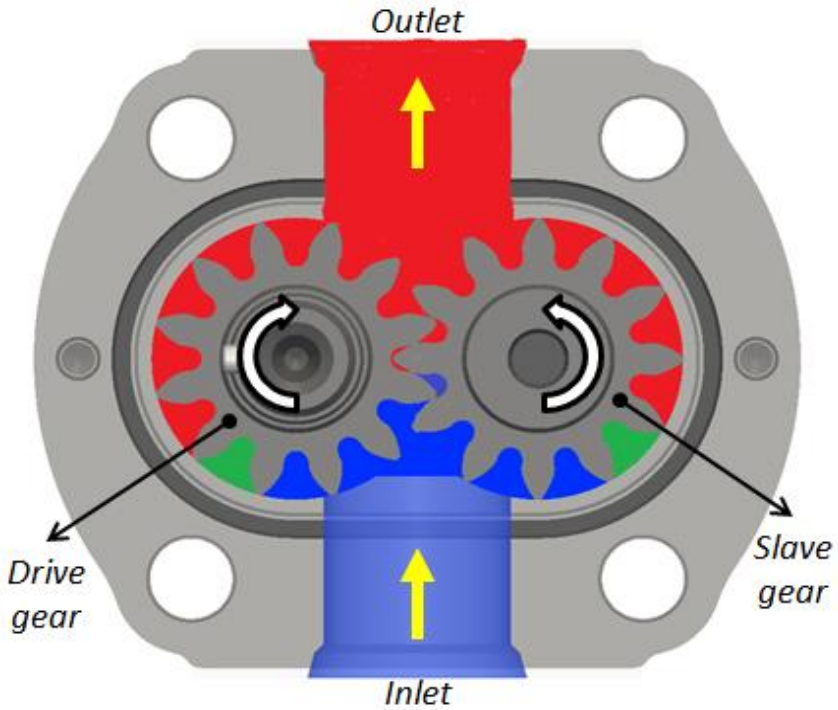

Figure 4: Principle of working of EGMs. (blue, green and red qualitatively represent the pressure (low, intermediate and high respectively) of the fluid while it is being displaced inside the pump.

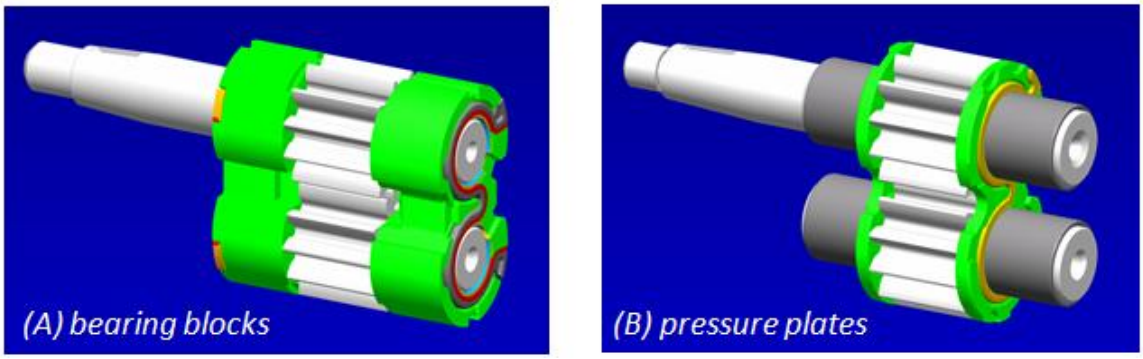

Figure 5: (A) Lateral bushings as bearing blocks; (B) Lateral bushings as pressure/thrust plates.

The lateral bushings form one of the most important parts in an EGM. Typically, they are known as bearing blocks (they possess journal bearings which support the shaft) or thrust/pressure plates (the journal bearings are housed in the casing) as shown in Figure 5. The lateral bushings have relief grooves (for EGMs with no pressure compensation, the relief grooves are machined on the casing) such as inlet and outlet grooves facing the gears, perform the timing function of connecting the displacement chambers (tooth space volumes (TSVs)) to the inlet/outlet ports, thereby avoiding the TSVs to be isolated between the contact points of the gears. Hence these grooves optimize the performance of the machine in terms of internal pressure overshoots and localized cavitation (which introduce pulsations of flow at the outlet, noise emissions, instabilities etc.) which occurs due to the meshing process as shown in Figure 6(A) The other side of the lateral bushings facing the gears has inlet and outlet grooves as shown in figure 4(B). The lateral bushings also take care of sealing the TSVs so as to prevent leakages from the outlet (delivery or high pressure (HP)) port to the inlet (suction or low pressure (LP)). Therefore, design of the grooves is of utmost importance in determining the performance of the machine particularly in terms of displaced flow as well as noise emissions

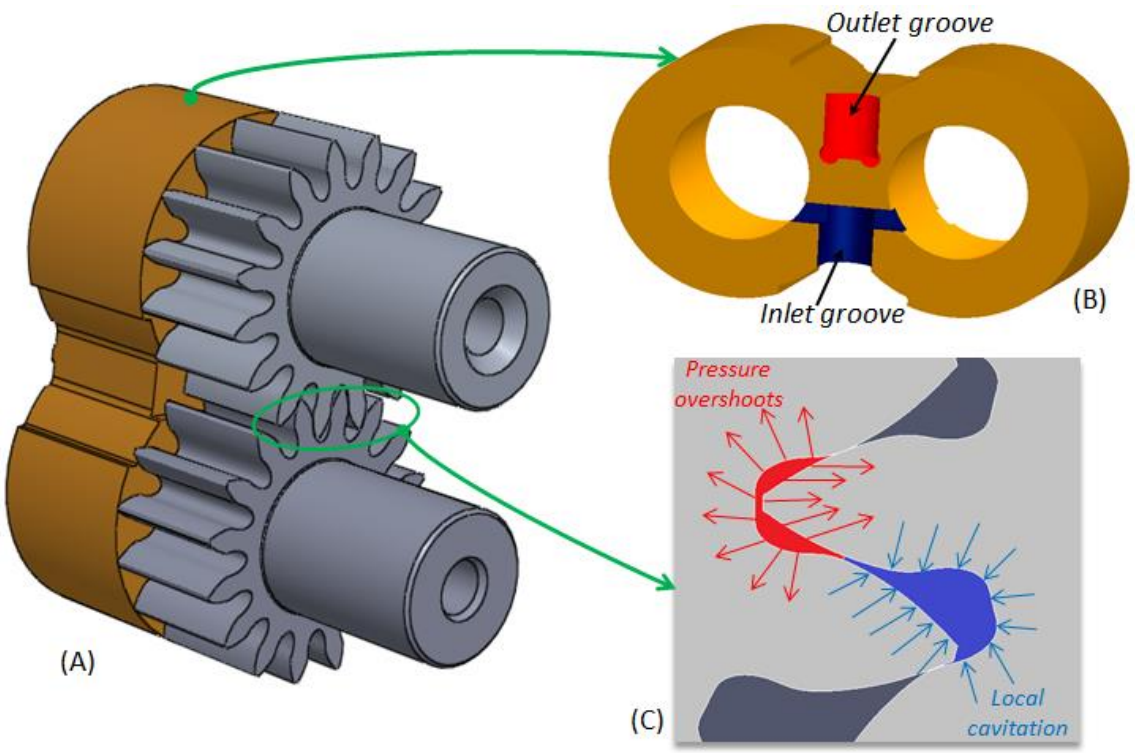

Figure 6: (A) Gears meshing with each other; (B) Detail of the grooves in the lateral bushings; (C) Detail of the meshing process showing the regions of pressure peaks and local cavitation.

The space between the lateral bushings and gears is called the lateral lubricating gap, which poses as one of the main sources of power loss in EGMs, particularly, volumetric losses due to leakages as well as mechanical losses due to viscous shear. Typically, EGMs are designed using lateral bushings which are axially balanced. In Figure 7(B), the pressure distribution in the lateral gap of a gear machine is represented. This distribution of pressure acts on one side of the lateral bushings pushing it outwards away from the gears axially. The side of the lateral bushings which face away from the gears (also known as balance side) has a distribution of the pressures as shown in Figure 7(A), which pushes the lateral bushings inwards towards the gears axially. The fluid for pressurizing this side is obtained through small channels machined on the lateral bushings which have high pressure (equal to the outlet) or low pressure (equal to the inlet) separated by a seal. An axial balance of the lateral bushings is obtained based on pressure distribution on both of its sides. Thus, an optimal lubricating gap height is necessary for obtaining reliable and efficient performance.

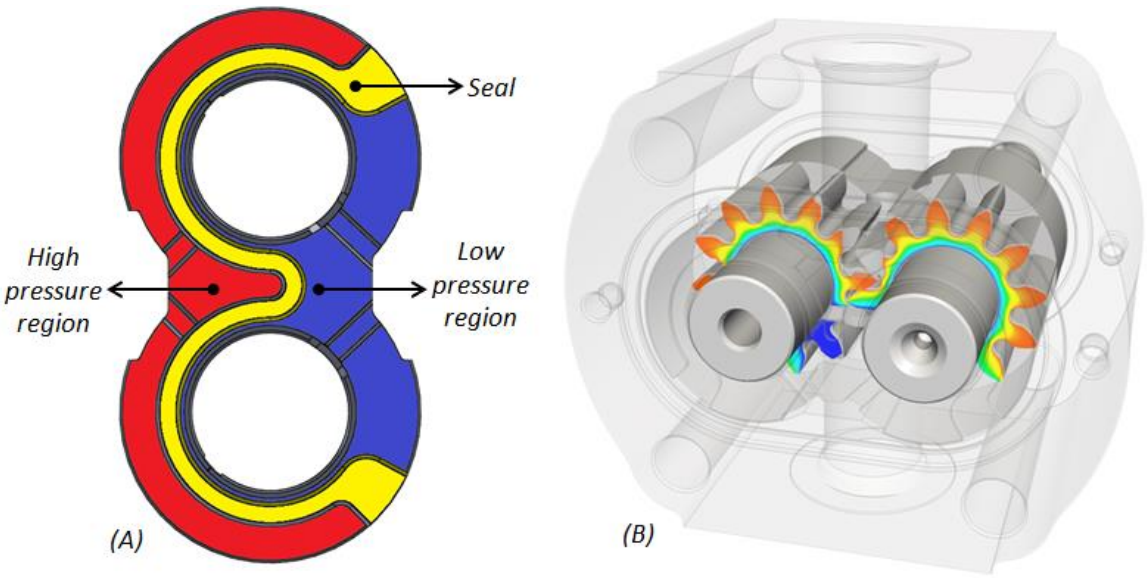

Figure 7: (A) Detail of the balance side of lateral bushings; (B) Qualitative representation of pressure distribution in the lateral gap (blue to red represent low to high pressures respectively).

Since the different tooth space volumes have different pressures at each instant of time similar to the pressure distribution in Figure 4, there is a net force acting on the gears in the radial plane. This net radial force pushes the gears away from the high pressure side to the low pressure (LP) side as shown in Figure 8. Therefore, during the operation of the machine, the gear teeth are in contact with the casing on the low pressure side and having a larger clearance at the high pressure side, thus, showing an eccentricity in their position. The resultant eccentric position of the gears causes a region of "good sealing" in the low pressure side and a "weak sealing" region at the high pressure side, considering the radial leakages during the operation of the machine.

During the initial parts of the operation of the machine, the eccentricity in the position of the gears causes the wear of the casing in the low pressure side. This initial wearing of the casing in the low pressure side is desirable since it improves the sealing between the TSVs and the casing, thereby controlling the radial leakages and hence improving the performance of the EGM. This process also popularly known as the "breaking in" is performed by the EGM manufactures for a specified number of hours at varying speed and pressures before it is being shipped to the consumer.

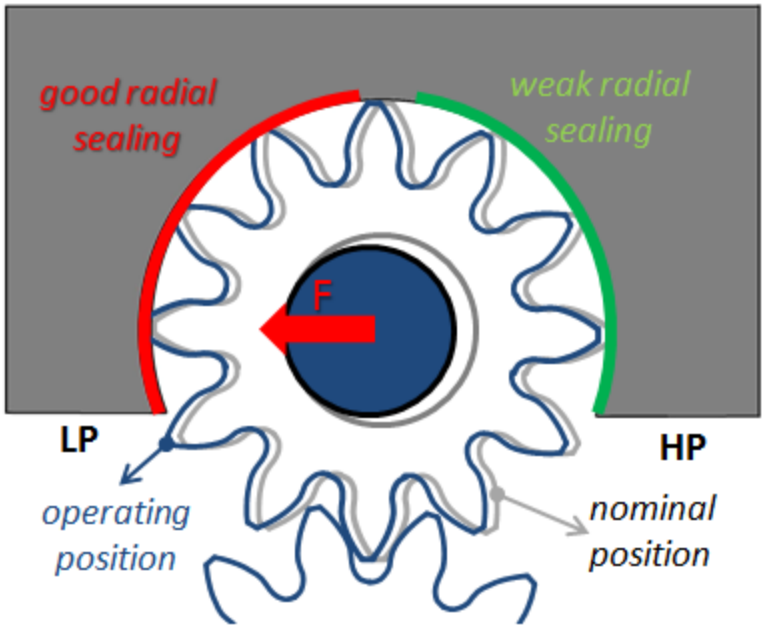

Figure 8: Radial movement of gears during the operation of the machine.

Even though the principle of working of EGMs is not complicated, all the important functions of a positive displacement machine as explained previously are concentrated on the only few parts of the EGM. Therefore, the design/study of the machine as a "whole" needs to consider all the functions and their mutual interactions simultaneously. Hence the design process becomes intricate and complicated.

1.3. Research Objectives

The main aim of the current work is to formulate and construct a variable delivery (VD) concept implementable in traditional external gear machines (EGMs). In order to achieve the overall goal of conceiving a working concept of VD-EGM, the following sub-goals need to be accomplished:

- Devise a working concept based on the variable timing of the connection of the TSVs with the suction/delivery for achieving VD in EGMs
- Identify novel design of gears which are beneficial for achieving VD in an EGM

- Develop a robust tool for designing gears (asymmetric, cycloidal etc.) as well as a geometrical model for HYGESim simulation tool
- Development of an optimization tool, capable of optimizing the gear geometry in terms of displacement reduction
- Development of a multi-level, multi-objective genetic algorithm based optimization method for determining the design of the important parts of the EGM – gears and the lateral bushings.
- Propose optimal designs which can be prototyped and perform steady-state measurements to validate the findings in simulation
- Formulate and prototype an automatic actuation system for changing the displacement in the EGM

The primary aim of the design tool for modeling different gear profiles is to understand the benefits of using the specific gear design in an EGM in terms of VD applicability, noise emissions, volumetric efficiency etc. A significant amount of research effort was dedicated to the creation of a version of HYGESim (a simulation tool limited to only classic EGM geometry, previously existing in the team) to be capable of simulating EGMs with novel gear profiles in a robust manner so that it can be used for optimization purposes.. The optimization tool developed in this work will be used to optimize the design of gear and the lateral bushings and the particular design chosen would be prototyped and experimental measurements will be performed to prove the concept of working of VD in EGMs. Once the operating concept of VD EGM is proved, a novel and compact actuation system will be designed to vary the displacement both manually as well as automatically.

The optimization tool developed can not only be used to identify the design for VD-EGM but also for traditional FD-EGM. Thus, promoting the generalization of the design process of EGMs (which were traditionally designed based on expensive and prolonged trial and error experimental design process) computationally.

1.4. Literature Overview

In the past there has been only few works which are directly related to the design of EGMs for VD. These works can be broadly classified two categories of achieving VD: 1) at the system level and 2) at the component level as described in section 1.4.1. Specific efforts in the literature related to the modeling and simulation of EGMs are described in section 1.4.2. The very few works related to the optimization of the design of EGMs are described in section 1.4.4.

1.4.1. Principle of Achieving Variable Displacement in External Gear Machines

In the past research on implementing VD in EGMs can be broadly classified into two different paths:

- Design modification at the component level – in which the design of the pump is modified to achieve a change in displacement geometrically
- Design modification at the system level – in which the hydraulic layout of the system is acted upon to simulate variable displacement while using fixed displacement pumps

1.4.1.1. Design Modification at the Component Level

The displacing action of a pump is achieved due to the change in volume of the displacement chambers: TSVs in the case of EGMs. The TSV increases when it is connected to the inlet/suction with a consequent influx of fluid into the displacement chamber. Subsequently, when the TSV reaches the delivery, the TSV decreases the fluid is forced out of the displacement chambers into the outlet/delivery of the pump. The displacement contribution by a single TSV is thus the difference between its maximum and the minimum volumes as shown in Figure 9. The TSVs achieve the maximum value when it is out of the meshing zone and is close to the casing of the pump. The minimum value is achieved in the meshing zone (where the volumes are changing) as can be seen from the Figure 9. The volume displaced by a single TSV can be written as,

$$V = (A_{max} - A_{min}) \cdot b, \tag{1.3}$$

where A is the cross section area of the TSV and b is the facewidth of the gears. The total displacement of the pump can be written as,

$$V_d = V \cdot z = (A_{max} - A_{min}) \cdot b \cdot z, \tag{1.3}$$

where z is the number of TSVs in action.

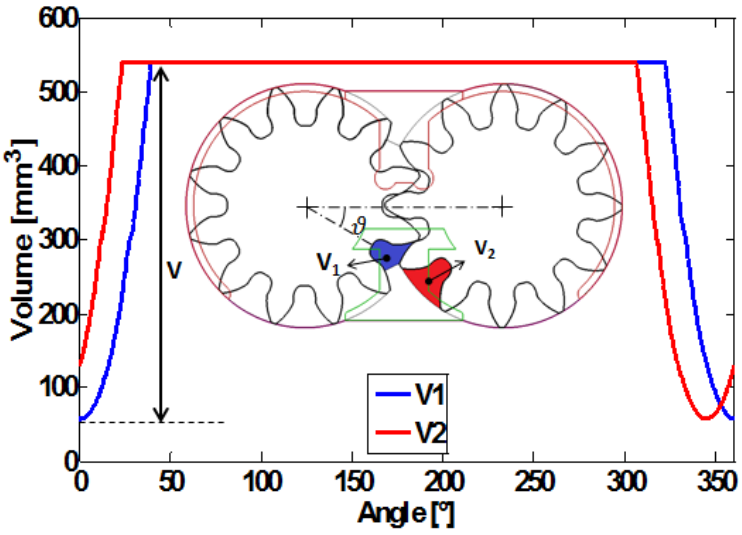

Figure 9: Propagation of the TSVs (V1 for drive gear and V2 for slave gear) for one complete revolution.

For varying the displacement at the component level, in the past, efforts were made to act on the different terms in Eq. (1.3). Firstly, VD was achieved by moving the gears in the radial direction away from each other, thus changing the area of cross-section of TSVs in the meshing zone. Secondly, the variation of the displacement is achieved by changing the gears effective meshing length, b.

In an EGM, changing the inter-axis distance between the gears as shown in Figure 10, allows for changing the minimum volume in the meshing zone. Particularly, decreasing the wheel base results in a decrease of the minimum volume, therefore an increase in displacement and an increase in the inter-axis distance allows for the opposite effect by reducing the displacement of the pump.

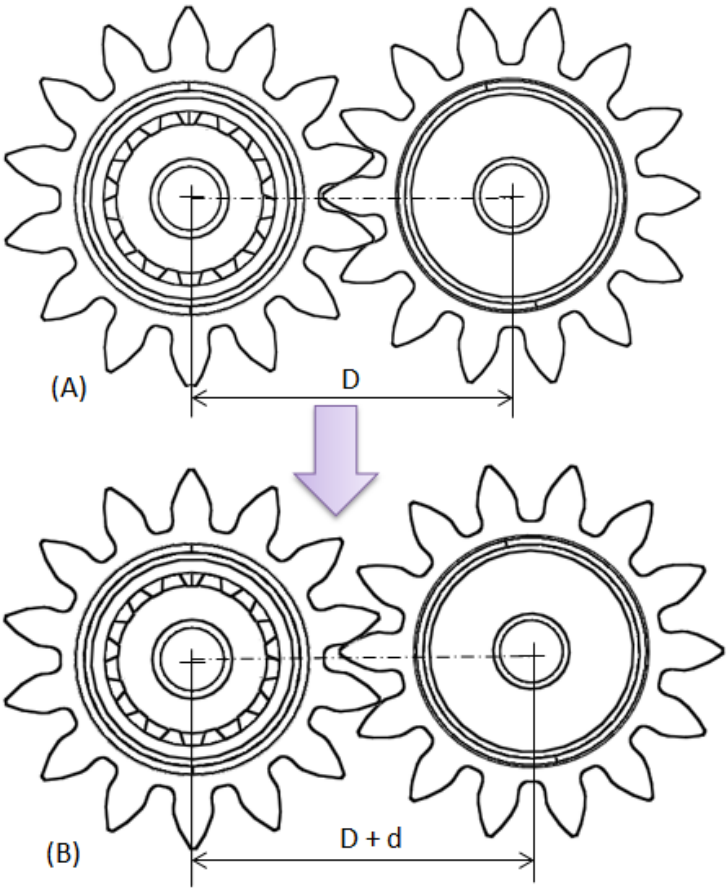

Figure 10: (A) Gears in the nominal inter-axis, D, position to achiecve max displacement;(B) Gears at a larger interaxis disance (D+d) to achieve partial displacement.

There has been just two patents which implement complicated procedures to achieve VD by moving the gears radially as described as follows. In (Yang & Zhong, 1987), one of the gears is mounted on a stator which ic capable of moving it radially, however, the design does not include any mechanism to seal the TSVs within the housing when the gears are moved farther away. (Reiners & Wiggermann, 1960) describes a technique in which an intermediate gear mounted on an eccentric shaft is used. Movement of this eccentric shaft offers different degress of meshing of the gears and hence varies the displacement volume.

Another mechanism of changing the displacement of the EGM can be attained by acting on the effective meshing length, b of the gears as can be seen from Eq. (1.3). In traditional EGMs, the design of the casing corresponds to the facewidth of the gears as

shown in Figure 3, however in order to translate the driven/slave gear axially additional elements need to be intoduced as described which tremendously increase the complexity and number of additional parts.

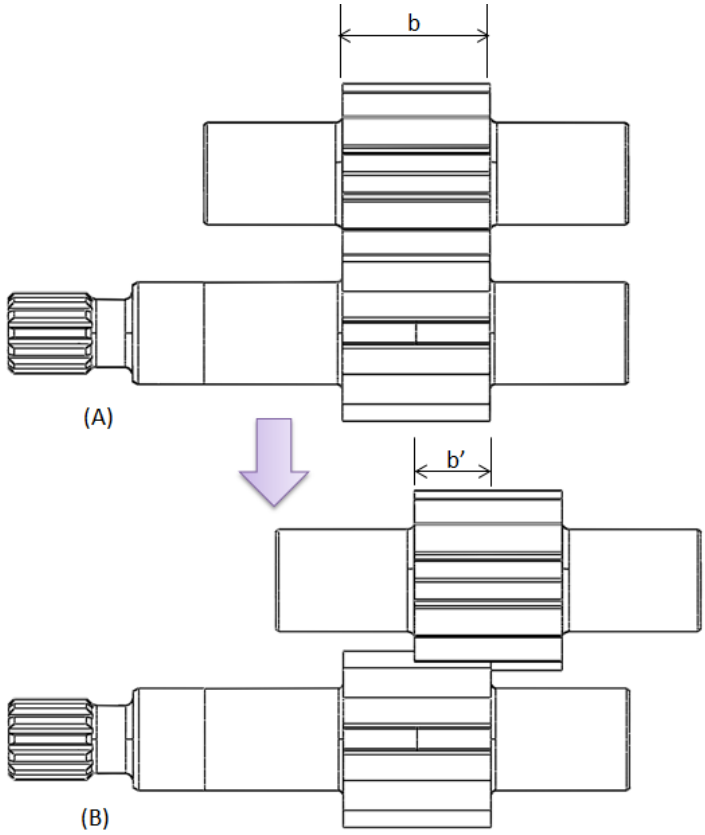

Figure 11: (A) Gears meshing the entire facewidth, b, achieving max displacement; (B) Gears meshing only a fraction of the facewidth, b', achieving partial displacement.

The design proposed in (Winmill, 2001) shows gears which are staggered axially and engage only a portion of the width. The remaining parts of the gears engage with other elements of the machine which have internal teeth. These internal gears rotate inside shims which allow axial movement and hence varying the width of the driven gear engaging with the driver gear hence varying the displacement. One significant advantage of this design is the possibility of achieving zero displacement by ensuring that the driven gear does not engage with the driver at all. A similar design is presented in (Bussi, 1992) however, the design is claimed to be more compact and economical.

In (Hoji, Nagao, Shinozaki, 2008), a pressure compensated design for translating the axial meshing length of the driven gear. The driver gear is not allowed to move axially and has perfect sealing with the casing, but a suitable arrangement of rings allow for the correct meshing of the desirable length of the driven gear. An arrangement of springs supporting the driven gear against the pressure at the delivery of the pump brings about the variation in displacement. (Clarke, 2002) presents a similar approach for changing the displacement of the pump; however it also extends the design to consider a hydraulic transformer.

However, both these categories were not successful because the solutions were dependent on moving the most loaded parts of the machine (mainly the gears). Therefore, the solutions introduced many additional components making the design complicated and difficult to manufacture or successfully function.

Differently from the previously described methods of changing the displacement, (Bowden, 1989 - 1990) introduce a mechanism for achieving variable discharge flow in an EGM with the help of an adjustable spool that provides pressurized fluid from the outlet to selected portions of the TSV in the de-meshing zone to vary the discharge flow of the pump. The proposed design also claims energy recovery in the process of varying the displacement. This concept was also not put into production since the design of the gear were restricted to symmetric teeth and hence the reduction in displacement would have been limited to very low values (100% to 95%).

In (Zavadinka & Grepl, 2014) a design for a variable charge pump of internal gear type is presented. Variation in discharge flow is achieved by changing the eccentricity between the rotor-cam rings. It also presented that the displacement of this kind of variable charge pump cannot go below a certain minimum limit. Energy savings for different operating cycles have also been presented, hence purporting the research on partially variable displacement units.

1.4.1.2. Design Modification at the System Level

In many applications which require high speeds of the actuator at specific instants of operation, it is possible to adapt a flow system which is capable of delivering discrete values of flow rate. As a first example, the system can provide two different speed values based on the usage of commercially available duplex pumps (Parker®, Casappa®). These duplex pumps are used in many industrial machines which require a high piston speed in the return stroke of an actuator, while during the working stroke high loads need to be handled were the speed is restricted. Representative circuits with double pumps are show in Figure 12.

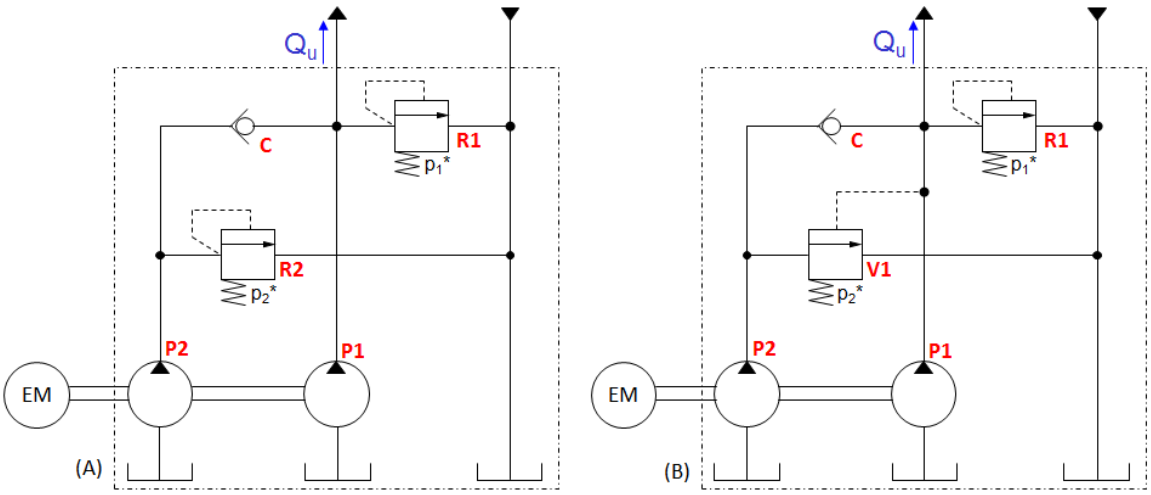

Figure 12: (A) Schematic of a hydraulic circuit for discrete flow using 2 pumps and 2 relief valves; (B) Schematic of a hydraulic circuit for discrete flow using 2 pumps, 1 relief valve and a drain valve[12].

In Figure 12(A), both the pumps are mounted on the same shaft hence generating flow to their full capacity. The first relief valve R2, is set at p_2* which is lesser than p_1* which is set by R1. Until the pressure set by the load reaches p_2*, the resultant flow is the sum of the flow provided by both P1 and P2. When the pressure reaches more than p_2* and less than p_1*, R2 regulates the flow by P2 into the tank and the resultant flow is only due to the flow provided by P1. During this instance, the check valve closes and isolates P2 from the system directly. The flow provided by P1 will continue to be the outlet flow until the pressure reaches p_1*. After which R1 opens and directs the flow to the tank, thereby reducing the resultant flow to zero. A more efficient system is shown in Figure

12(B), where the relief valve R2 is replaced by a drain valve which operates with the pressure at the delivery of the system. However, in both these cases, both the pumps consume equal amounts of power at all instants of operation, thereby not converting the input power into useful power while operating at partial displacement (Nervegna, 2003).

Another method of achieving VD is known as virtual variable displacement (VVD), where a pulse width modulation (PWM) control of a two-way two position solenoid valve (V1) connecting to the tank as shown in Figure 13(A). In actuality, the valve is operated at a very high frequency pulse signal, which would correspond to the flow rate signal (Nieling, Fronczak, & Beachley, 2005), (Mahrenholz, Lumkes, 2009), (Rannow, Tu, 2006), (Rannow, Li, 2009), (Tomlinson, Burrows, 2009). Therefore, the mean flow rate depends on the ratio of time in which the valve is open to the entire time per duty cycle. Figure 13(B), shows an efficient system which uses a compact open center valve (V1) with a non-return valve, (C1) which ensures no back flow from the system to the tank during the fast switching of the valve.

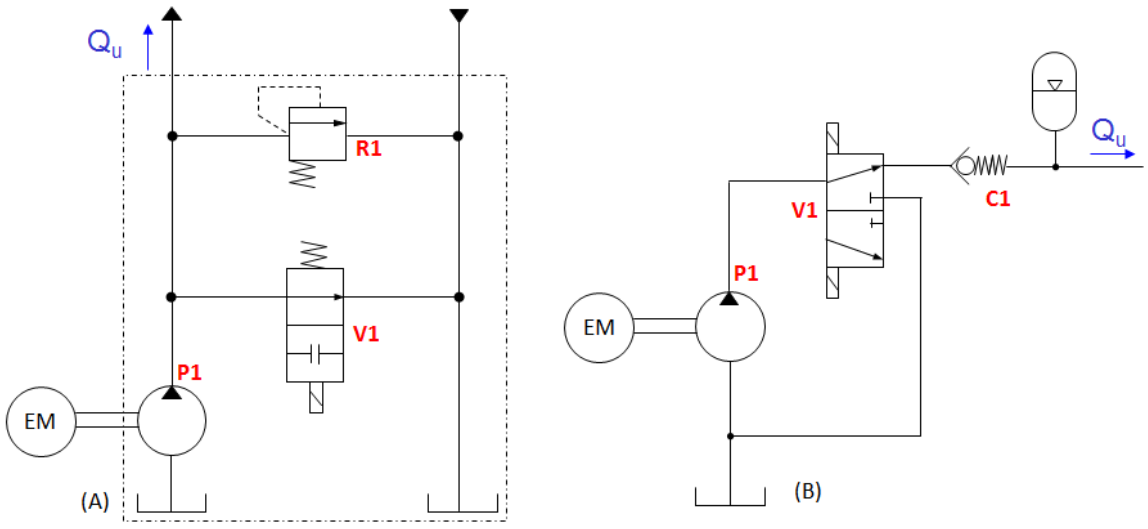

Figure 13: (A) VVD system with a solenoid valve; (B) VVD system with an open center valve and a non-return valve [13].

The patents, (Ikeda, 2002), (Svenson, 1930), implement a solution which is a combination of the design modification at the component and system level. These designs change the amount of flow delivered by varying the amount of leakages from the high pressure to the low pressure side.

In (Ivantysynova, 1998), (Grabbel & Ivantysynova, 2005), (Williamson, Zimmerman & Ivantysynova, 2008), researchers have implemented separate VD units (axial piston type) for controlling the actuator using displacement control. These works show how the use of VD units significantly reduces the energy consumption by removing the metering losses introduced by valves.

1.4.2. External Gear Machine Analytical Models

In this section, the few studies available in literature which focuses on using analytical methods to study the performance of an EGM are discussed briefly.

(Beacham, 1946) used simplified graphical approach in understanding the effect of grooves lateral bushing on the flow ripple at the delivery. Also, this study discusses in detail the impact of casing wear on the volumetric performance of the EGM as well. (Bonacini, 1961), (Ivantysyn & Ivantysynova, 2003) used an extensive analytical approach based on the geometry of the EGM to derive expressions for geometric displacement, flow rate and input torque required. (Manring, Kasaragadda, 2005) analyzed the performance of an EGM in terms of the flow ripple theoretically for EGMs with different number of teeth on the driver and driven gears. The study concludes that the number of teeth on the driver gears dictates the flow ripple at the delivery and hence a higher number of teeth on the driver gear are recommended to reduce flow pulsations. (Fielding, Hooke, Foster & Martin, 1977), present a model which analyzes the generation and propagation of pressure waves in the high pressure delivery.

Even though, all the previously mentioned studies have been valuable in itself, none of them have been used to study the performance of an EGM with asymmetric gears nor they have discussed the principle of achieving variable displacement in EGMs.

1.4.3. External Gear Machine Simulation Models

In order to understand the performance of an EGM and to radically change their design, a robust simulation tool which is capable of considering the different functions in an EGM is of utmost necessity and importance. In this section, the different simulation models available in the literature are described briefly.

In (Castellani, 1967), (Eaton & Edge, 2001), (Borghi, Milani, Zardin & Patrinieri, 2006), (Manco & Nervegna, 1993), (Casoli, Vacca, Franzoni, & Guidetti, 2008), (Casoli, Vacca & Berta, 2008), (Zardin, Borghi, Paltrinieri & Milani, 2004) the performance of the machine, specifically concerning the efficiency, internal pressure peaks and cavitation, was analyzed on the bases of the recesses machines on the lateral bushings. Recently in (Nagamura, Ikejo & Tutulan, 2004), (Kollek & Osinski, 2009) analysis has been extended to non-standard profile of the gears.

Apart from the analysis of flow through the machine, another factor that affects the operation of machines are the different forces acting on the moving parts of the unit Analytical solutions for the compensation of radial forces which occur due to the unbalanced pressure field in the radial cross-section are discussed in (Ivantysyn & Ivantysynova, 2003), while numeric solutions predicting the effect of radial forces were modeled in (Falfari & Pelloni, 2007), (Zardin & Borghi, 2008). The pressures in the lateral gaps (between the gear face and the sliding elements) contribute towards the axial forces which act on the lateral bushings and on the gears. In current designs which are balanced, these forces are compensated by high pressure zones on the other side of the lateral bushings. In this way, the lateral gap and the leakages can be controlled reasonably for different operating pressures. (Koç, Kurban & Hooke, 1997), (Koc & Hooke, 1997) experimentally validate that the balance is normally achieved with a relative tilt between gears and the bushings and hence leading to hydrodynamic pressure generation in the gaps. (Borghi, Milani, Zardin & Patrinieri, 2005), (Casoli, Vacca, Berta & Zecchi, 2009), (Zecchi, Vacca & Casoli, 2010) present simplified numerical solutions to the leakage flow in the lateral lubricating gap.

All of the previously mentioned works focused on the modeling of several different aspects separately. But all these models did not take into consideration the interaction between the different aspects simultaneously. The complete evaluation of the operation of the gear machine can be obtained by an all-embracing model which takes into account all the different effects simultaneously. The different instantaneous geometric configuration of the various connections between the displacement chamber and the suction and the delivery ports has to be accurately modeled for a precise analysis of the flow through the

machine. Due to the action of various forces on the gears, the micro-motion of the gears needs to be predicted as well, since they play a vital role in determining the performance of the machine. The omni-comprhensive approach which encompasses all these different aspects of modeling is the motivation behind the simulation tool HYGESim (HYdraulic GEar machines Simulator) as described in 4.

1.4.4. Design Optimization of External Gear Machines

There are several different designs of EGMs which are successful commercially. In this section, a brief description of the different designs of EGMs successfully implemented in the recent years and efforts done by researchers in using automatic numerical procedure for the optimization of the design of positive displacement machines is provided.

As described in the previous section quite a lot of literature exists in the modeling and simulation of gear machines. Few works exists on the design optimization of other positive displacement machines especially, axial piston machines are described in (Seeniraj & Ivantysynova, 2008 - 2011), (Kim & Ivantysynova, 2012). These works focused on optimization of specific parts of the axial piston machines for reducing noise emissions and maintaining high volumetric efficiency. However, these works considered only a few specific objective functions for the design optimization. On the contrary the only few works which are dedicated to the optimization of components of the gear machines are described in this section. In (Huang, Chang & Lian, 2008) an optimization procedure was used to determine the optimal design of gear pumps which maximized the displacement volume using an analytical expression. (Huang & Chen, 2008) Focuses on the optimization of the displacement volume of the pump using a closed form solution for helical gears. However, in both these works, the performance of the machine in terms of delivery flow pulsation, maximum pressure in the tooth space volumes, internal cavitation effects have been neglected and only the volumetric performance of the unit was optimized. Also the performance of the machine was evaluated on the basis of the design of the gears without any considerations regarding the influence of the design of the lateral bushings. In (Wang, Sakurai & Kasarekar, 2011) the nonlinear equations which govern the instantaneous flow areas connecting the tooth space volumes and the

suction/delivery grooves have been used to just minimize the pressure overshoots while noise emissions due to the delivery flow pulsations have not been considered. Nevertheless, design of the gears is made neglecting the important effects of the lateral grooves on the timing of the connections. In (Casoli, Vacca & Berta, 2008), (Vassena & Vacca, 2010) HYGESim was utilized for the first time for optimization purposes, considering the design of the grooves of the lateral pressure plates of a particular pump, considering a fixed gear profile. From this work, it is clear that the recesses (suction, delivery and backflow) machined on the bearing block have a strong influence on the operation of the machine and even a small modification of their geometry can significantly affect the unit performance.

In the past, there have been only a few research efforts on the changing the design of the gears in order to reduce noise emissions. Dual-flank configuration of gears with zero backlash was implemented by commercial EGM companies as described in (Schwuchow, 2002), (Negrini, 1996). Both these works focused on the traditional symmetric involute profiles of the teeth, which provide high effectiveness in smooth transmission of forces but presents some limits concerning noise emissions. A more radical change in the design of EGMs was presented in (Lätzel, Schwuchow, 2012), where helical gear design with cycloidal teeth was used for noise abatement up to 75% in terms of delivery flow pulsations. In (Nagamura, Ikejo & Tutulan, 2004), the influence of different gear profile (involute, cycloid, involute-cycloid composite and modified-cycloid) on the flow oscillations at the outlet of the machine. But the study did not involve an optimization process to determine the optimal design of the gears. The performance of asymmetric teeth profile was analyzed in terms of mechanical power transmission in (Kumar, Muni, & Muthuveerappan, 2008), (Kapelevich, 2000) describes the design and optimization procedure for gears which can improve the fillet load carrying capacity in bending for applications other than in hydraulic gear machines. (Kumar, Muni & Muthuveerappan, 2008) illustrates the design process of asymmetric teeth, showing also the potentials of this design for reducing the vibration levels, increasing the load capacity. The application of asymmetric teeth in EGMs for fluid power applications was never analyzed before,

and the related potentials on machine performance are still unexplored in terms of their benefits in VD as well as fluid-borne-noise emissions.

2. PRINCIPLE OF ACHIEVING VARIABLE TIMING IN EXTERNAL GEAR MACHINES

In this chapter, an innovative solution that implements a variable timing and hence VD in EGMs is described in detail graphically. The principle has been described starting from the meshing process of the gears and the concept for achieving maximum and minimum displacement has been explained.

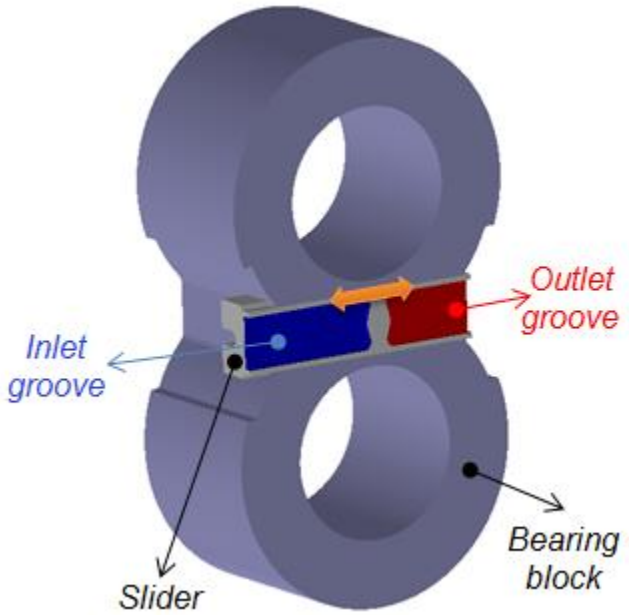

Figure 14: Slider placed inside the bearing block for achieving VD in an EGM.

The novel concept for achieving variable displacement in EGMs is based on the optimal variable timing of the connections of the TSVs with the inlet/outlet grooves. The variation in the timing of the connections can be achieved by introducing a movable element, called the “slider” in the lateral bushings as shown in Figure 14 (the slider can also be implemented direclty inside the casing for designs without pressure compensation of the lateral bushings). The slider also contains the grooves which realize the

communication between the TSVs and the inlet/outlet ports. The position of the slider determines the amount of flow displaced by the unit per revolution, for the case of pump and motors.

In order to have a better understanding of the working principle of achieving variable displacement in an EGM, a detailed description of the displacing action is provided in Figure 15. Figure 15(A) represents a generic displacement chamber (TSV) with dual flank configuration (points of contact on both flanks of the gears as shown in Figure 15(B)) in an EGM, showing the angular region θ, where the meshing process takes place and hence the displacing action is realized.

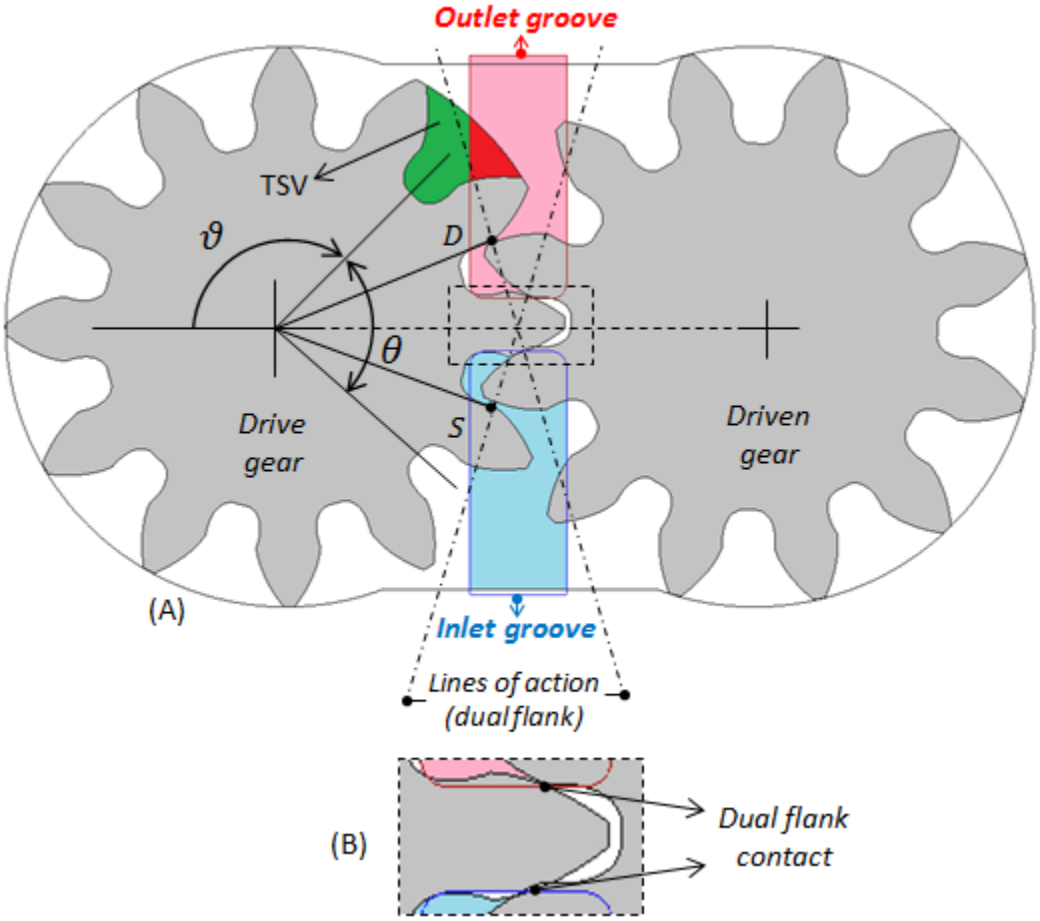

Figure 15: (A) Generic TSV representing the angular interval in which the meshing process takes place; (B) TSV with dual flank contact configuration.

In Figure 16, a representative trend of the progression of the TSV over an entire shaft revolution is represented. Unlike other displacement machines like axial piston machines,

where the displacing action takes place over 180° , the displacing action of an EGM occurs only in the angular interval represented by, θ which represents the meshing region. As can be seen from Figure 16, this angular interval, θ is much smaller than 180°. Within the meshing region, there exists, points D and S along the line of action of the gears, which represent the angular region within which the fluid in the TSV is trapped between the points of contact. Therefore, in this region, the fluid is displaced by means of the inlet and outlet grooves. A simplified representation of the grooves is represented by traces (red represents the outlet groove and blue represents the inlet groove) in Figure 15(A).

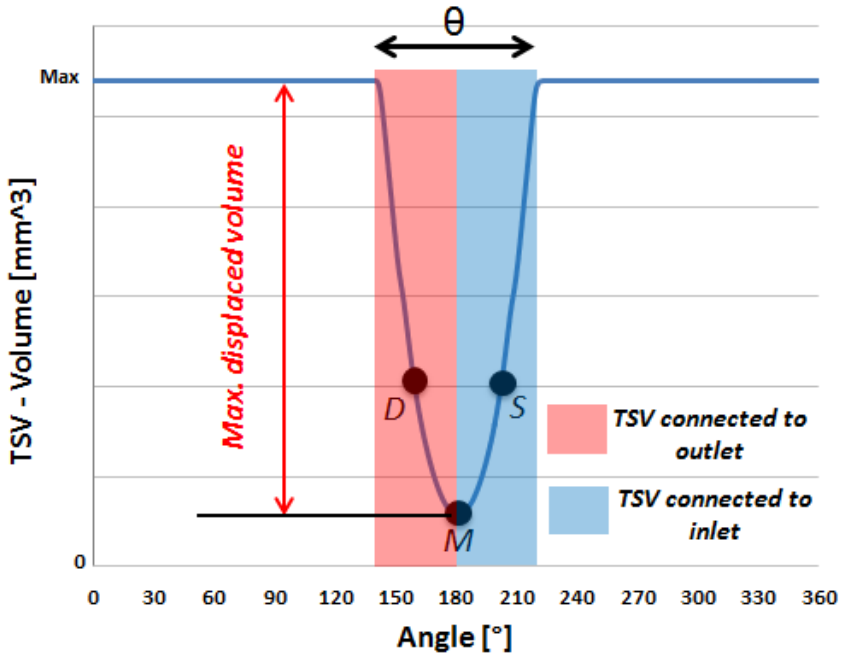

Figure 16: TSV as a function of shaft angle showing the angular interval in which the TSV is connected to the outlet (red) and the inlet (blue) for achieving maximum displacement.

In standard EGMs, the commutation of the trapped TSV between the inlet and the outlet groove is realized when the volume is at its minimum, depicted by point M in Figure 16 and Figure 17. In this configuration, the TSV is connected to the inlet or to the outlet for equal angular intervals, depicted by the red and blue boxes of equal dimensions in Figure 16. Therefore, the maximum volumetric capacity of the pump is utilized and hence maximum flow is displaced by the unit. Ideally, the commutation occurs without any crossporting (simultaneous connection of the TSV with the inlet and outlet) so that for

each TSV, the maximum volume shown in Figure 16 can be displaced. However, the optimal performance in terms of noise emissions, reducing internal pressure peaks and cavitation is realized usually with a help of an optimized profile of the grooves which allow for an optimal crossport.

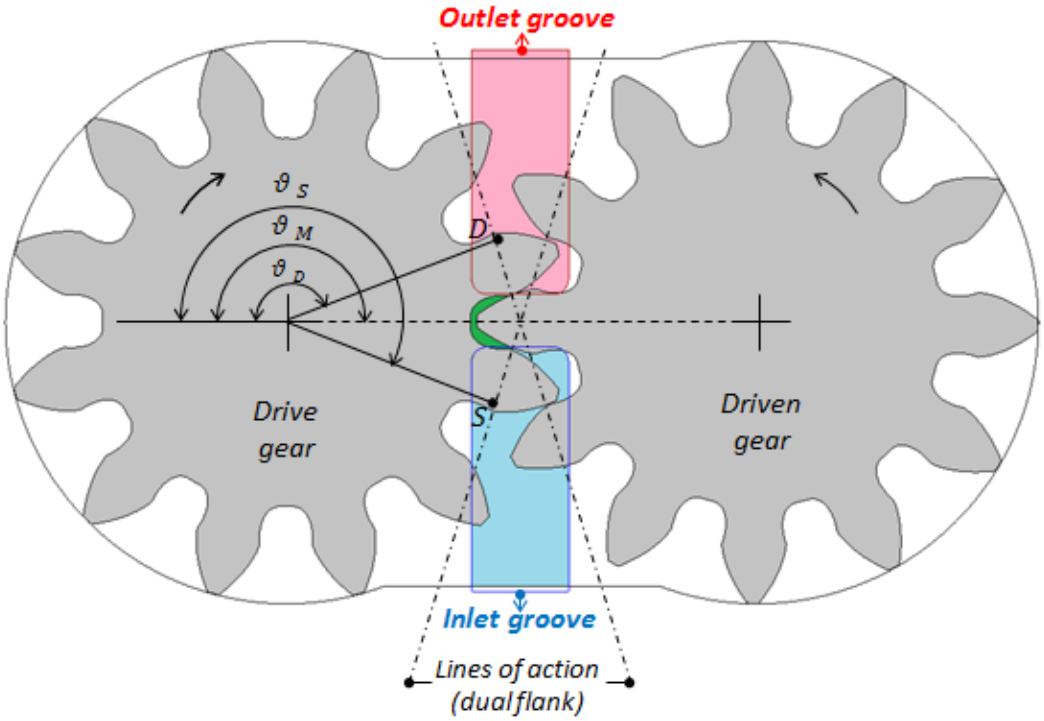

Figure 17: Position of the grooves in the slider to achieve maximum displacement (outlet in red, inlet in blue).

In traditional standard EGMs for high pressure applications the grooves (inlet and outlet) are machined on the lateral bushings (bearing blocks/pressure plates) and in the unit housing for low pressure, non-pressure compensated designs. In the current design, for achieving variable displacement, the grooves are machined on the slider, which is permitted to have a one degree of freedom of motion. Therefore, moving the slider introduces a variation of the angular position at which the commutation between the connection of each TSV with the inlet and outlet ports.

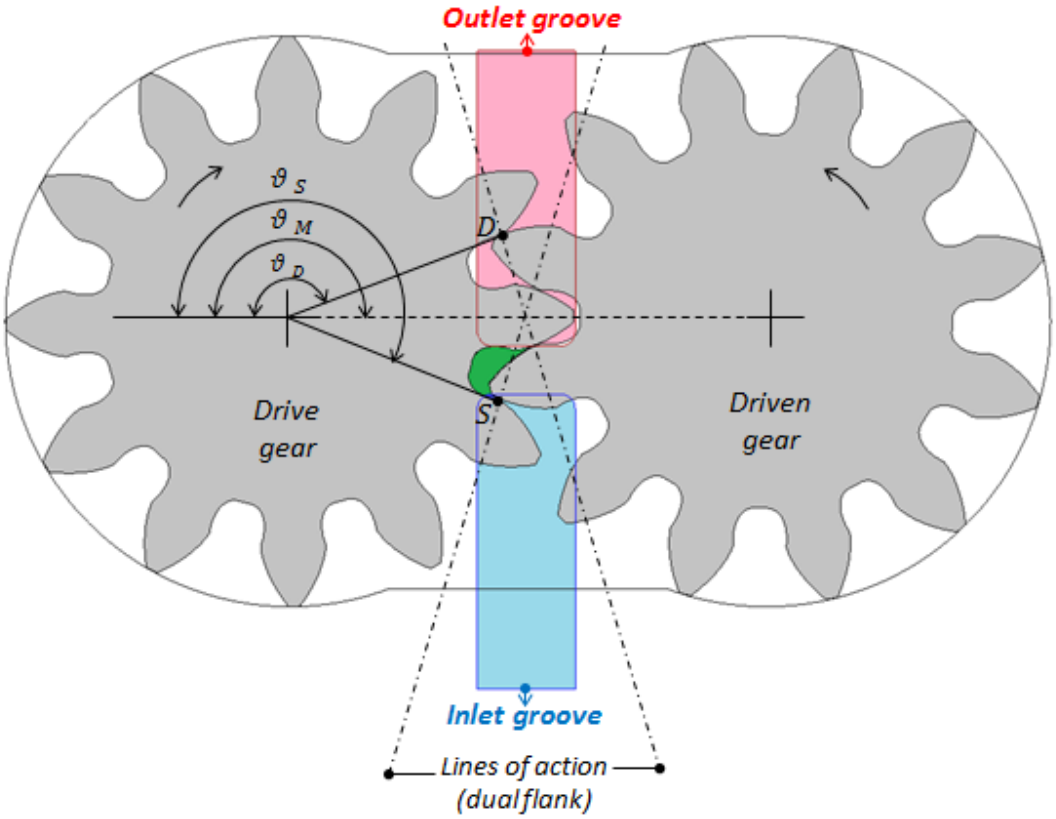

Figure 18: Position of the grooves in the slider to achieve minimum displacement (outlet in red, inlet in blue).

On the contrary to Figure 16 and Figure 17, a reduced displacement can be achieved if the slider is positioned closer to the inlet port as shown in Figure 18. In this configuration, each TSV remains connected to the outlet via the outlet groove for a first portion of the filling process (after it reaches the minimum volume at point M, 180°), wherein a part of the fluid which has been already delivered to the outlet is taken back into the TSV which acts a fluid "virtual dead volume". Due to this dead volume, each TSV is capable of displacing an effective reduced volume of fluid to the outlet.

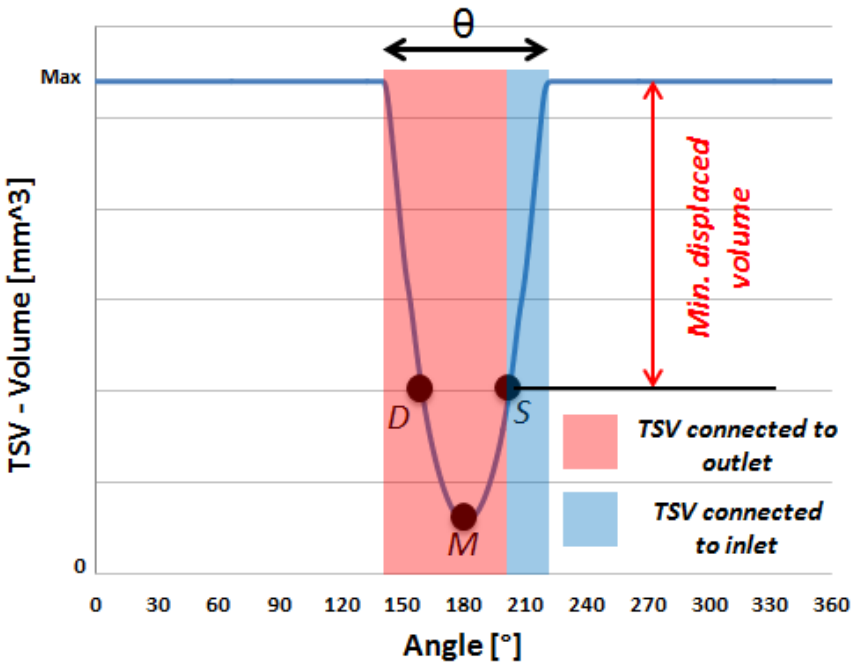

Figure 19: TSV as a function of shaft angle showing the angular interval in which the TSV is connected to the outlet (red) and the inlet (blue) for achieving minimum displacement.

Graphically, the principle for achieving reduced displacement is represented in Figure 19. In Figure 19, a larger red box (as compared to Figure 16) represents a larger angular period for which the TSV is connected to the delivery and a smaller blue box (as compared to Figure 16) represents a smaller angular period for which the TSV is connected to the inlet. The virtual fluid dead volume can be represented by the difference between the volumes at points S and M, therefore the effective fluid displaced to the outlet is equal to the difference between the maximum volume and the volume at point S.

To realize delivery flow variation, the slider can move either towards the inlet port (as shown in Figure 18) or towards the outlet port. Since the fluid at the inlet port is often close to saturation pressure conditions (for the case of a pump) it is advisable to consider the motion of the slider towards the inlet, so that cavitation effects due to fluid aeration are limited. However, for the case of the motor, the opposite considerations apply.

It is also important to observe how the variation of the achieved displacement as a result of change in slider position is effective only when the switching point between the

inlet/outlet connections is realized between the points D and S. By moving the slider outside the limits D-S, in which the TSV is not trapped between points of contact of the gears, a direct bypass connection between the outlet and the inlet is realized, hence significantly reducing the volumetric efficiency of the EGM. In this case, the machine acts like a relief valve by directing flow from the outlet to the inlet.

Since the description of the TSVs have been pertaining to gears with dual flank contact configuration, considerations of the TSV for drive gear and slave gear are similar to the ones represented in the figures before. However, for the case of gears with single flank contact configuration, due to the presence of a backlash between the gears, each TSV of the drive gear is connected to the corresponding TSV of the slave gear. Hence, the calculation of the displaced volume of the unit should be considered as a sum (or union) of the TSV pairs (as shown in Figure 20), rather than being considered separately as described previously.

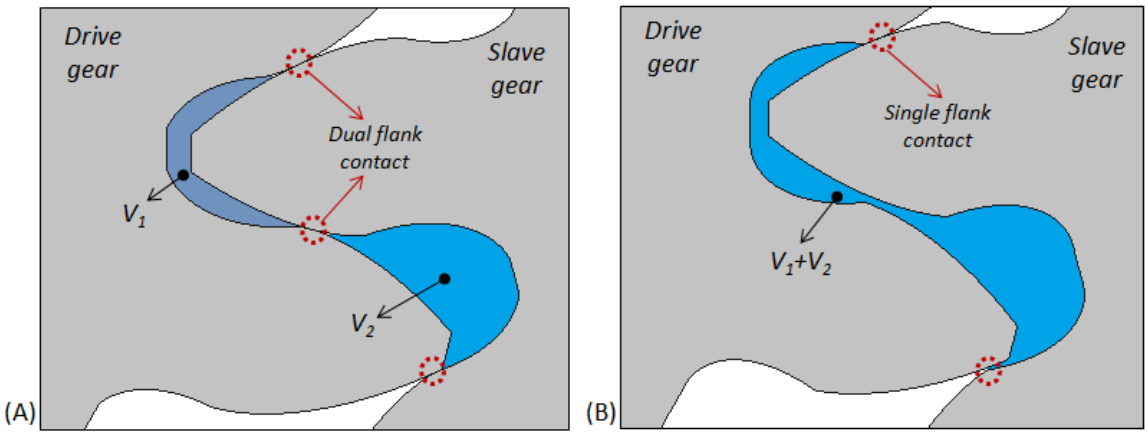

Figure 20: (A) Consideration of TSVs for dual flank contact configuration; (B) Consideration of TSVs for single flank contact configuration.

As evident from Figure 16 and Figure 19, the meshing zone for conventional EGMs with traditional gears having symmetrical involute profiles, is limited to an angular amplitude of ~ 60°. The angular range of the points D-S is even smaller and usually of the order of a few degrees. Therefore, it was only possible to achieve maximum displacement variation between just 100%-83% using dual flank design of standard symmetric involute profile (as explained by the past research by one of the previous member of the team in

[56]). In order to maximize the reduction in displacement, the point D-S should be ideally farther away from point M, Consequently, novel gear profiles need to be identified which not only maximizes the angular span of the trapped volume, but also simultaneously preserves all the other important performance features of the EGM. Due to the inherent nature of design of the gears and hence the propagation of TSVs in the meshing zone, it is highly unlikely to achieve zero displacement; however the goal is to achieve a variation from 100% to 50% which would still be challenging.

3. ANALYTICAL MODEL FOR VARIABLE TIMING IN EXTERNAL GEAR MACHINES

In this chapter, an effort has been made to analytically derive the working of the proposed principle of achieving variable timing in EGMs. Firstly, analytical expressions for the locations of the contact points (D and S) of the gears have been derived based on the geometry of the gears, as they define the extent to which the displacement can be reduced. Secondly, analytical derivations for geometric displacement, flow delivered and shaft torque required during operation has been provided both for max and min displacement. Lastly, the non-uniformity/pulsations in flow rate and hence torque has also be derived for max and min displacement.

3.1. Analytical Determination of Points of Contact

The points of contact which define the angular region within which the volume of the fluid is trapped can be determined using the geometry of the involute curves and the line of action. In this section a generalized approach for identifying the points of contact for an asymmetric teeth profile is considered.

The asymmetric teeth profile is defined on the basis of two different pressure angles which control the shape of the tooth. A detailed description of the generation of the asymmetric tooth is provided in section 5.1, but this section focuses on the calculation of the points of contact based on trigonometric functions and gear geometry. Representative gears with asymmetric teeth in mesh with dual flank contact configuration are shown in Figure 21. Each tooth can be differentiated as drive side and coast side based on two different pressure angles, with the drive side pressure angle always considered to be larger than the coast side, since power is transmitted from the drive gear to the slave gear via the drive side of the tooth. The addendum/outside circle of the gears is represented in

green, the pitch circle in black and the base circles (drive side and coast side) are represented in blue. The drive side base circle radius can be expressed as,

$$r_{bd} = r_0 \cdot \cos \alpha_{0d}, \tag{3.1}$$

and the coast side base circle radius can be expressed as,

$$r_{bc} = r_0 \cdot \cos \alpha_{0c}. \tag{3.2}$$

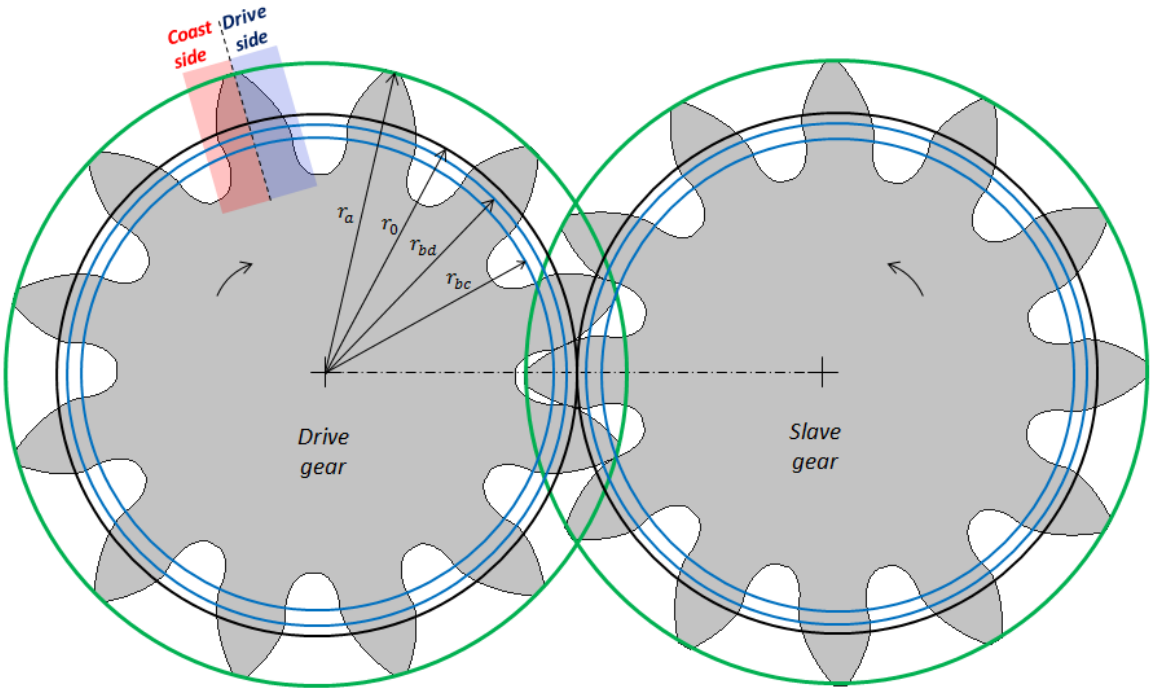

Figure 21: Representative asymmetric gears in mesh, detailing the coast and drive side of the teeth.

In order to have a better understanding of the different curves, a magnified representation of the all the curves showing the line of action is shown in Figure 22. Since the gears are assumed to be of having dual flank contact configuration, there are two lines of action corresponding to the drive and coast pressure angles. The drive side line of action is represented by the red line K_1L_1, formed by the common tangent between the drive side base circles. Similarly, the coast side line of action is represented by the red line K_2L_2 formed by the common tangent between the coast side base circles.

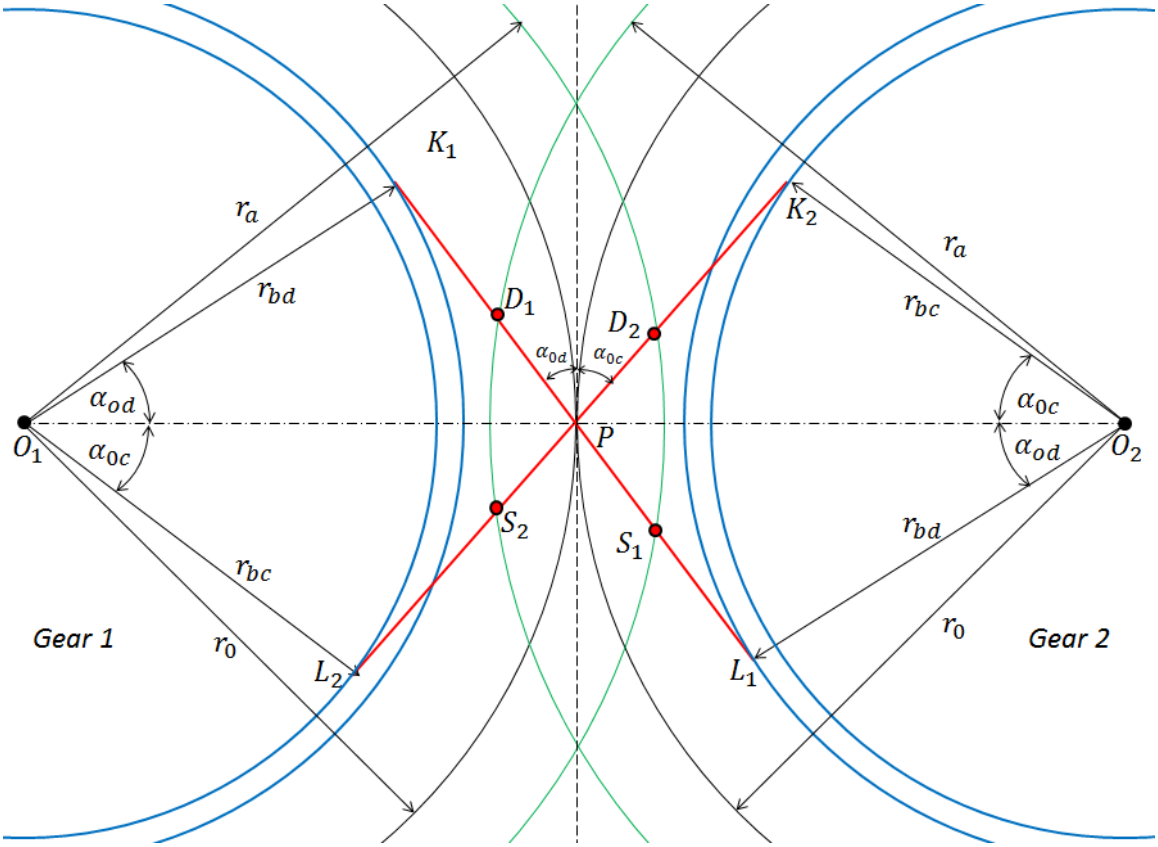

Figure 22: Meshing of the gears showing the detail of the lines of action.

However, for a particular tooth pair, the active/working part of the line of action can be defined as the part of the line of action which is enveloped by the addendum circles of both the gears. Therefore, for the drive side, the active/working part of the line of action is defined as D_1S_1 and for the coast side as D_2S_2.

Let l_d and l_c be the lengths of the working part of the drive side and coast side lines of action respectively. With reference to Figure 22, the line of action from the drive side and coast side can be written as,

$$K_1S_1 + D_1L_1 = K_1L_1 + l_d \text{ and } K_2S_2 + D_2L_2 = K_2L_2 + l_c. \quad (3.3)$$

Eq. (2.3) can be re-arranged as,

$$l_d = K_1S_1 + D_1L_1 - K_1L_1 \text{ and } l_c = K_2S_2 + D_2L_2 - K_2L_2. \quad (3.4)$$

Considering the triangles $\Delta O_1K_1S_1$and $\Delta O_2D_1L_1$ (henceforth in this document a triangle will be represented in short as Δ),

$$K_1S_1 = D_1L_1 = \sqrt{r_a^2 - r_{bd}^2}. \tag{3.5}$$

Similarly considering $\Delta O_2K_2S_2$ and $\Delta O_1D_2L_2$,

$$K_2S_2 = D_2L_2 = \sqrt{r_a^2 - r_{bc}^2}. \tag{3.6}$$

Considering ΔO_1K_1P and ΔO_2PL_1,

$$K_1P = PL_1 = r_0 \cdot \sin\alpha_{0d} = r_{b1} \cdot \tan\alpha_{0d}. \tag{3.7}$$

Considering ΔO_2K_2P and ΔO_1PL_2,

$$K_2P = PL_2 = r_0 \cdot \sin\alpha_{0c} = r_{b2} \cdot \tan\alpha_{0c}. \tag{3.8}$$

Substituting, Eqs. (2.5) - (2.8) into Eq. (2.4) yields the expressions for l_d and l_c as,

$$l_d = 2 \cdot \sqrt{r_a^2 - r_{bd}^2} - 2 \cdot r_0 \cdot \sin\alpha_{0d}, \tag{3.9}$$

$$l_c = 2 \cdot \sqrt{r_a^2 - r_{bc}^2} - 2 \cdot r_0 \cdot \sin\alpha_{0c}. \tag{3.10}$$

Since the points, K_1, D_1, S_1 and L_1 are collinear,

$$K_1P = K_1D_1 + D_1P. \tag{3.11}$$

Similarly, K_2, D_2, S_2 and L_2 are collinear, hence,

$$K_2P = K_2D_2 + D_2P. \tag{3.12}$$

The pitch point ‘P’ divides the drive side line of action into two equal parts, therefore,

$$D_1P = PS_1 = \frac{D_1S_1}{2} = \frac{l_d}{2} = \sqrt{r_a^2 - r_{bd}^2} - r_0 \cdot \sin\alpha_{0d}, \tag{3.13}$$

$$D_2P = PS_2 = \frac{D_2S_2}{2} = \frac{l_c}{2} = \sqrt{r_a^2 - r_{bc}^2} - r_0 \cdot \sin\alpha_{0c}. \tag{3.14}$$

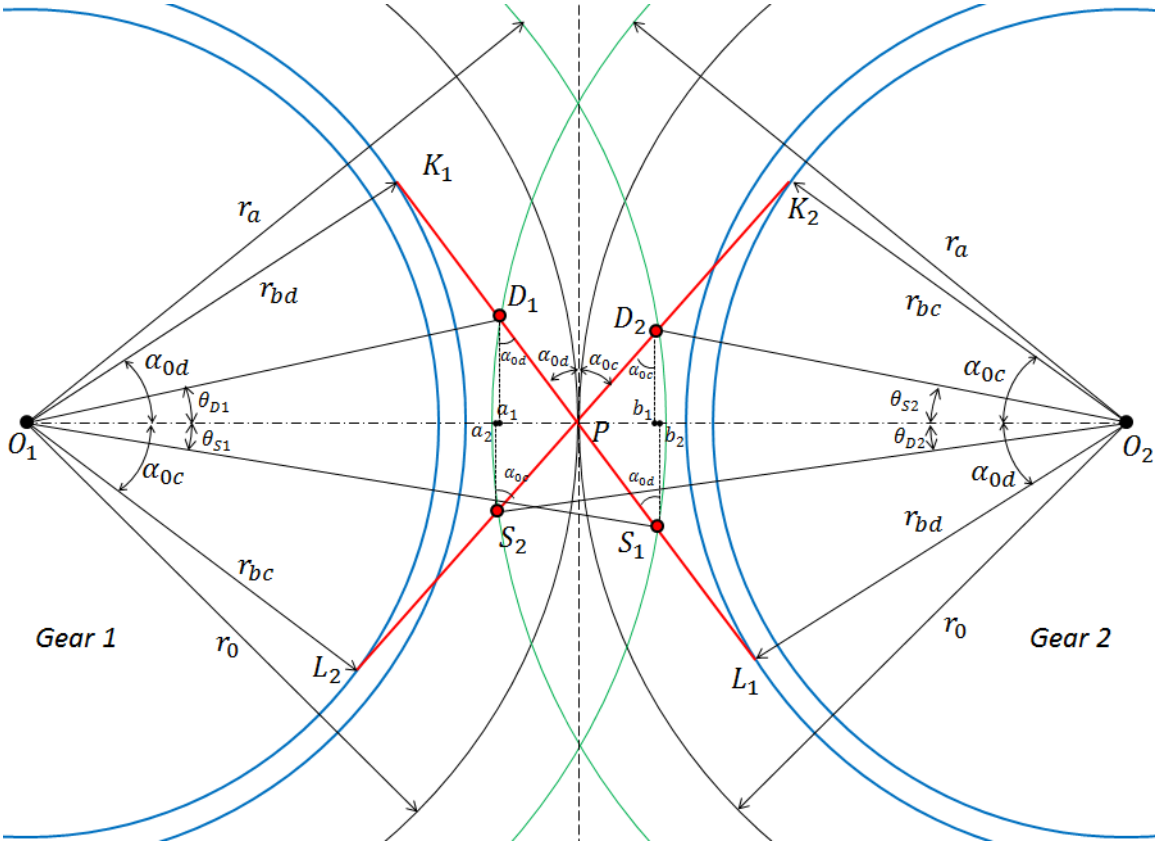

Figure 23: Meshing of the gears showing the detail of the triangles required to calculate the angular location of the points of contact.

Considering $\Delta D_1 a_1 P$ in Figure 23,

$$a_1P = D_1P \cdot \sin\alpha_{0d} = \left(\sqrt{r_a^2 - r_{bd}^2} - r_0 \cdot \sin\alpha_{0d}\right) \cdot \sin\alpha_{0d}, \tag{3.15}$$

$$D_1a_1 = D_1P \cdot \cos\alpha_{0d} = \left(\sqrt{r_a^2 - r_{bd}^2} - r_0 \cdot \sin\alpha_{0d}\right) \cdot \cos\alpha_{0d}. \tag{3.16}$$

Therefore,

$$O_1a_1 = O_1P - a_1P = r_p - \left(\sqrt{r_a^2 - r_{bd}^2} - r_0 \cdot \sin\alpha_{0d}\right) \cdot \sin\alpha_{0d}. \tag{3.17}$$

Hence, the angular position at which the drive side of a particular tooth of gear 1 comes in contact with the corresponding drive side of a tooth of gear 2, θ_{D1} can be represented as,

$$\theta_{D1} = \tan^{-1}\left(\frac{D_1 a_1}{O_1 a_1}\right) = \tan^{-1}\left(\frac{\left(\sqrt{r_a^2 - r_{bd}^2} - r_0 \cdot \sin\alpha_{0d}\right) \cdot \cos\alpha_{0d}}{r_p - \left(\sqrt{r_a^2 - r_{bd}^2} - r_0 \cdot \sin\alpha_{0d}\right) \cdot \sin\alpha_{0d}}\right). \quad (3.18)$$

Considering $\Delta D_2 b_1 P$ in Figure 23,

$$b_1 P = D_2 P \cdot \sin\alpha_{0c} = \left(\sqrt{r_a^2 - r_{bc}^2} - r_0 \cdot \sin\alpha_{0c}\right) \cdot \sin\alpha_{0c}, \quad (3.19)$$

$$D_1 b_1 = D_2 P \cdot \cos\alpha_{0c} = \left(\sqrt{r_a^2 - r_{bc}^2} - r_0 \cdot \sin\alpha_{0c}\right) \cdot \cos\alpha_{0c}. \quad (3.20)$$

Therefore,

$$O_2 b_1 = O_2 P - b_1 P = r_p - \left(\sqrt{r_a^2 - r_{bd}^2} - r_0 \cdot \sin\alpha_{0d}\right) \cdot \sin\alpha_{0d}. \quad (3.21)$$

Hence, the angular position at which the coast side of a particular tooth of gear 1 comes in contact with the corresponding coast side of a tooth of gear 2, θ_{D2} can be represented as,

$$\theta_{D2} = \tan^{-1}\left(\frac{D_2 b_1}{O_2 b_1}\right) = \tan^{-1}\left(\frac{\left(\sqrt{r_a^2 - r_{bc}^2} - r_0 \cdot \sin\alpha_{0c}\right) \cdot \cos\alpha_{0c}}{r_p - \left(\sqrt{r_a^2 - r_{bc}^2} - r_0 \cdot \sin\alpha_{0c}\right) \cdot \sin\alpha_{0c}}\right). \quad (3.22)$$

Considering $\Delta b_2 P S_1$ in Figure 23,

$$b_2 P = P S_1 \cdot \sin\alpha_{0d} = \left(\sqrt{r_a^2 - r_{bd}^2} - r_0 \cdot \sin\alpha_{0d}\right) \cdot \sin\alpha_{0d}, \quad (3.23)$$

$$b_2 S_1 = D_1 a_1 = \left(\sqrt{r_a^2 - r_{bd}^2} - r_0 \cdot \sin\alpha_{0d}\right) \cdot \cos\alpha_{0d}. \quad (3.24)$$

Therefore,

$$O_1 b_2 = O_1 P - b_2 P = r_p + \left(\sqrt{r_a^2 - r_{bd}^2} - r_0 \cdot \sin\alpha_{0d}\right) \cdot \sin\alpha_{0d}. \quad (3.25)$$

Hence, the angular position at which the drive side of a particular tooth of gear 1 moves away from being in contact with the corresponding drive side of a tooth of gear 2, θ_{S1} can be represented as,

$$\theta_{S1} = \tan^{-1}\left(\frac{b_2 S_1}{O_1 b_2}\right) = \tan^{-1}\left(\frac{\left(\sqrt{r_a^2 - r_{bd}^2} - r_0 \cdot \sin\alpha_{0d}\right) \cdot \cos\alpha_{0d}}{r_p + \left(\sqrt{r_a^2 - r_{bd}^2} - r_0 \cdot \sin\alpha_{0d}\right) \cdot \sin\alpha_{0d}}\right). \quad (3.26)$$

Considering $\Delta P a_2 S_2$ in Figure 23,

$$a_2 P = P S_2 \cdot \sin\alpha_{0c} = \left(\sqrt{r_a^2 - r_{bc}^2} - r_0 \cdot \sin\alpha_{0c}\right) \cdot \sin\alpha_{0c}, \quad (3.27)$$

$$a_2 S_2 = D_2 b_1 = \left(\sqrt{r_a^2 - r_{bc}^2} - r_0 \cdot \sin\alpha_{0c}\right) \cdot \cos\alpha_{0c}. \quad (3.28)$$

Therefore,

$$O_2 a_2 = O_2 P + a_2 P = r_p + \left(\sqrt{r_a^2 - r_{bd}^2} - r_0 \cdot \sin\alpha_{0d}\right) \cdot \sin\alpha_{0d}. \quad (3.29)$$

Hence, the angular position at which the coast side of a particular tooth of gear 1 moves away from being in contact with the corresponding coast side of a tooth of gear 2, θ_{S2} can be represented as,

$$\theta_{S2} = \tan^{-1}\left(\frac{a_2 S_2}{O_2 a_2}\right) = \tan^{-1}\left(\frac{\left(\sqrt{r_a^2 - r_{bc}^2} - r_0 \cdot \sin\alpha_{0c}\right) \cdot \cos\alpha_{0c}}{r_p + \left(\sqrt{r_a^2 - r_{bc}^2} - r_0 \cdot \sin\alpha_{0c}\right) \cdot \sin\alpha_{0c}}\right). \quad (3.30)$$

Since, the angular positions at which both the sides of the tooth comes in contact and moves away from contact have been defined. The angular range within which the TSV of gear 1 (drive) and gear 2 (slave) are trapped can be described easily.

For gear 1, the angular range within which the TSV of gear 1 is trapped between the points of contact can be represented as,

$$\theta_{TR1} = \theta_{D1} + \theta_{S2}. \quad (3.31)$$

Similarly for gear 2, the angular range within which the TSV of gear 2 is trapped between the points of contact be represented as,

$$\theta_{TR2} = \theta_{D2} + \theta_{S1}. \quad (3.32)$$

Eqs. (2.32) - (2.33) hold only for the case of assuming dual flank contact configuration of the gears. However, for the case of gears operating with single flank contact

configuration due to the presence of backlash between the gears, the consideration of the trapped TSV can be represented as,

$$\theta_{TR} = \theta_{D1} + \theta_{S1}. \tag{3.33}$$

3.2. Analytical Determination of Geometric Displacement, Flow Rate and Input Torque

With reference to the energy method described in [23] and [24], a similar approach has been followed in this section to derive the expressions for displaced volume, flow rate and input torque. Consider an EGM with symmetrical teeth in the configuration shown in Figure 24. The red curves show the initial position of the gears and the black curves represents their final position after both gears rotate by a small angle, $d\phi$. As shown in Figure 24, an assumption of the pressure distribution around the gears is assumed with the pink and blue colors representing the regions of high pressure and low pressure respectively. Even if a gradual pressure variation can be expected around the gears, the described method will still hold good for deriving the various expressions.

Consider the pump shown in Figure 24, to be operating at a inlet pressure of $P_{in} = 0$ and an outlet pressure of P_{out}. Therefore the pressure difference across the pump is $\Delta p = P_{out}$. Assuming, that the operating fluid of the machine is incompressible, the work done by the pump to displace a volume, dv over a pressure barrier of Δp can be written as,

$$dW = dv \cdot \Delta p. \tag{3.34}$$

Hence, the amount of work/energy to be input to the pump, can be written as,

$$dW = (M_1 + M_2) \cdot d\phi, \tag{3.35}$$

where M_1 and M_2, are respectively torques acting on gear 1 and 2, with respect to their axis of rotation and opposite to the direction of rotation. Taking the time derivate of Eqs. (3.35) - (3.36) gives,

$$\frac{dv}{dt} \cdot \Delta p = (M_1 + M_2) \cdot \frac{d\phi}{dt} = Q \cdot \Delta p = (M_1 + M_2) \cdot \omega. \tag{3.36}$$

where ω is the angular velocity of gear 1 and Q is the flow rate delivered by the pump [23].

Considering the pressure distribution as shown in Figure 24, the torque acting on gear 1 can be written as [23],

$$M_1 = \left(\frac{r_a^2 - r_r^2}{2} - \frac{r_1^2 - r_r^2}{2}\right) \cdot b \cdot \Delta p = \left(\frac{r_a^2 - r_1^2}{2}\right) \cdot b \cdot \Delta p, \tag{3.37}$$

where, b is the facewidth of the gears, r_1 is the distance O_1C' of the point of contact C' from the center of the gear 1, O_1 as shown in Figure 24.

Similarly the torque acting on gear 2 can be written as [23],

$$M_2 = \left(\frac{r_a^2 - r_2^2}{2}\right) \cdot b \cdot \Delta p. \tag{3.38}$$

Where, $r_2$is the distance O_2C' of the point of contact C' from the center of gear 2, O_2 as shown in Figure 24.

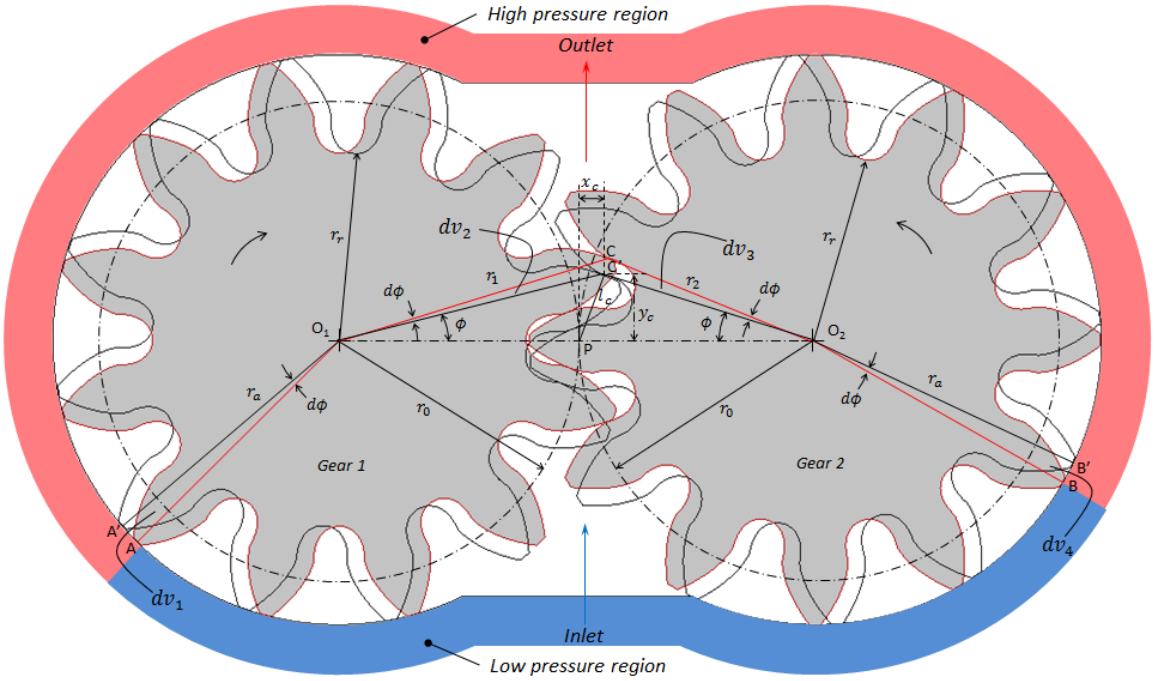

Figure 24: Determination of the displacement of the pump with symmetric teeth. [red] represents the initial position of the gears and [black] represents the final position of the gears.

Substituting Eqs. (3.37) - (3.38) into Eq. (3.36) and re-arranging yields,

$$Q = b \cdot \omega \cdot \left(\left(\frac{r_a^2 - r_1^2}{2} \right) + \left(\frac{r_a^2 - r_2^2}{2} \right) \right). \tag{3.39}$$

Eq. (3.39) provides an expression for calculating the flow rate, provided the information of r_1 and r_2 are readily available. To understand the meaning of the expression in Eq. (3.39) geometrically, the following discussion in the remainder of this section has been made.

In order to make the geometric interpretation a little easier, it is assumed that the instantaneous points in the line of action, l_c (which is the loci of the points of contact in the meshing zone of the gears), separates the high pressure from the low pressure at each angular position. Therefore, in the meshing zone, the region above line O_1C' for gear 1 and above line O_2C' for gear 2 are at high pressure and the regions below these lines are at low pressure. On the other hand, the line O_1A' for gear 1 and above line O_2A' for gear 2 represent regions of high pressure and the regions below these lines are at low pressure.

With reference to Figure 24, consider the control volume, $O_1O_2BAO_1$ (also encompassed by the pink color), which basically represents the entire region in high pressure. Due to a small angular rotation of both the gears by an angle, $d\phi$, the control volume changes to $O_1O_2B'A'O_1$ (also encompassed by the pink color). The change in volume or displaced volume, dv can be represented as,

$$dv = volume\ O_1O_2B'A'O_1 - volume\ O_1O_2BAO_1. \tag{3.40}$$

In achieving this change in the control volume, the volumes, $dv_1$and dv_4 enter the control volume, and the volumes, $dv_2$and dv_3 leave the control volume as shown in Figure 24. Therefore, the displaced volume, dv can be represented as,

$$dv = dv_1 + dv_4 - dv_2 - dv_3. \tag{3.41}$$

Since the angle through which the gears rotate are considered to be infinitesimally small, the volumes which enter and leave the control volume can be written as,

$$dv_1 = b \cdot \frac{r_a^2}{2} \cdot d\phi, \tag{3.42}$$

$$dv_2 = b \cdot \frac{r_1^2}{2} \cdot d\phi, \tag{3.43}$$

$$dv_3 = b \cdot \frac{r_2^2}{2} \cdot d\phi, \tag{3.44}$$

$$dv_4 = b \cdot \frac{r_a^2}{2} \cdot d\phi, \tag{3.45}$$

Substituting Eqs. (3.42) - (3.45) in Eq. (3.41) yields,

$$dv = b \cdot \frac{r_a^2}{2} \cdot d\phi + b \cdot \frac{r_a^2}{2} \cdot d\phi - b \cdot \frac{r_1^2}{2} \cdot d\phi - b \cdot \frac{r_2^2}{2} \cdot d\phi. \tag{3.46}$$

Re-arranging Eq. (3.46) yields,

$$dv = b \cdot \left(r_a^2 - \frac{r_1^2}{2} - \frac{r_2^2}{2} \right) \cdot d\phi. \tag{3.47}$$

If the origin is translated to the pitch point P, of the gears, the co-ordinates of the point C' can be represented by x_c and y_c as shown in Figure 24. The distance of point C from the origins of gears 1 and 2 can be written as [24],

$$r_1^2 = (r_0 + x_c)^2 + y_c^2 = r_0^2 + 2 \cdot r_0 \cdot x_c + x_c^2 + y_c^2, \tag{3.48}$$

$$r_2^2 = (r_0 - x_c)^2 + y_c^2 = r_0^2 - 2 \cdot r_0 \cdot x_c + x_c^2 + y_c^2. \tag{3.49}$$

Also from Figure 24, l_c can be written as,

$$l_c^2 = x_c^2 + y_c^2. \tag{3.50}$$

Substituting Eq. (3.50) in Eq. (3.48) and Eq. (3.49) yields,

$$r_1^2 = r_0^2 + 2 \cdot r_0 \cdot x_c + l_c^2, \tag{3.51}$$

$$r_2^2 = r_0^2 - 2 \cdot r_0 \cdot x_c + l_c^2. \tag{3.52}$$

Substituting Eq. (3.51) and Eq. (3.52) into Eq. (3.47) gives [23] and [24],

$$dv = b \cdot (r_a^2 - r_0^2 - l_c^2) \cdot d\phi. \tag{3.53}$$

It should also be noticed that l_c, varies with the angular position of the gears and hence it is a function of ϕ .For small angle ϕ, l_c can be approximated as,

$$l_c = r_0 \cdot \phi \cdot \cos\alpha = r_b \cdot \phi, \tag{3.54}$$

Where, α is the pressure angle of the symmetric gears considered and r_b is the base radius of the gears.

The Eq. (3.53) is however valid for the assumption of symmetric gears because it depends only on one pressure angle. Therefore, when applying such an expression for deriving the displaced volume using asymmetric gears, the pressure angles corresponding to both the sides of the teeth need to be carefully incorporated into Eq. (3.53) to have an accurate evaluation of the displaced volume.

Consider Figure 25 and Figure 26, in which the meshing of asymmetric gears have been depicted in a similar fashion as in Figure 24. In Figure 25, the point of contact has been represented on the coast side and hence the loci of the point of contact lie along the coast side line of action, l_c. On the other hand in Figure 26, the point of contact has been represented on the drive side and hence the loci of the point of contact lie along the drive side line of action, l_d. Due to the presence of two different pressure angles forming the asymmetric teeth, the angular position at which the coast side of a particular tooth of gear 1 comes in contact with the corresponding coast side of a tooth of gear 2, θ_{D2} and the angular position at which the drive side of a particular tooth of gear 1 comes in contact with the corresponding drive side of a tooth of gear 2, θ_{D1} are different as explained in detail in section 3. Hence the lines of action, l_c and l_d are different for any angular position ϕ, as shown in Figure 25 and Figure 26. Since the number of teeth for both the gears are the same, it is safe to conclude that the displaced volume is an average of the volume displaced calculated using l_c and l_d.

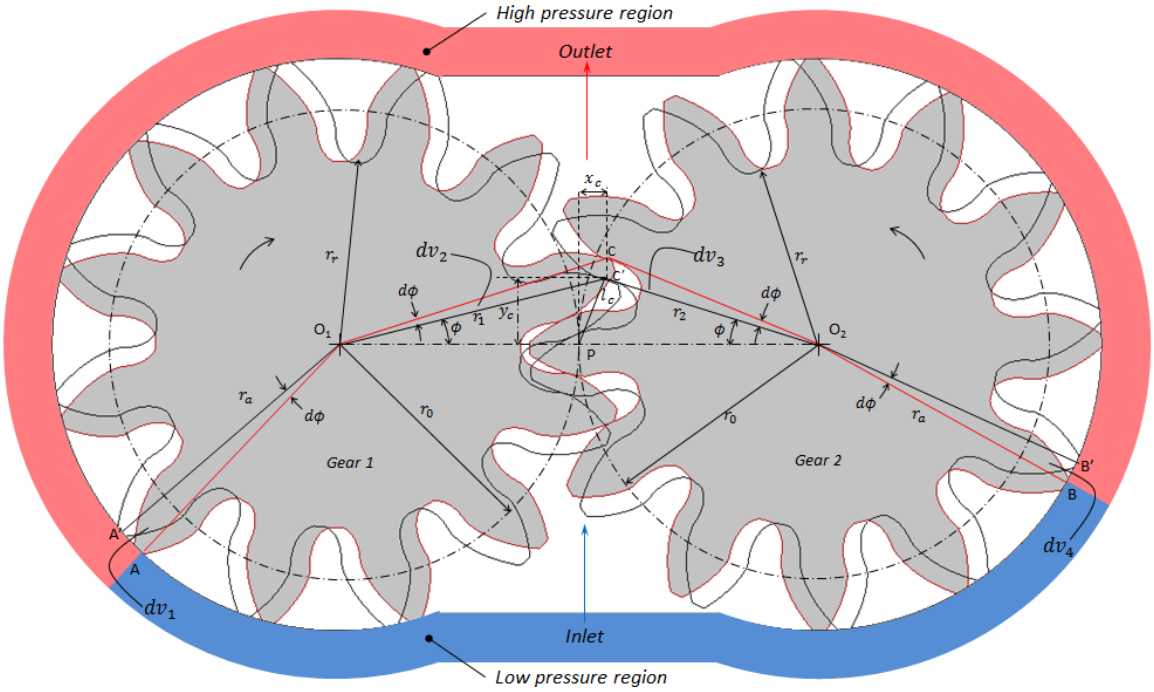

Figure 25: Determination of the displacement of the pump with asymmetric teeth showing the point of contact (C) on the coast side of the teeth. Red lines represent the initial position of the gears and black lines represent the final position of the gears.

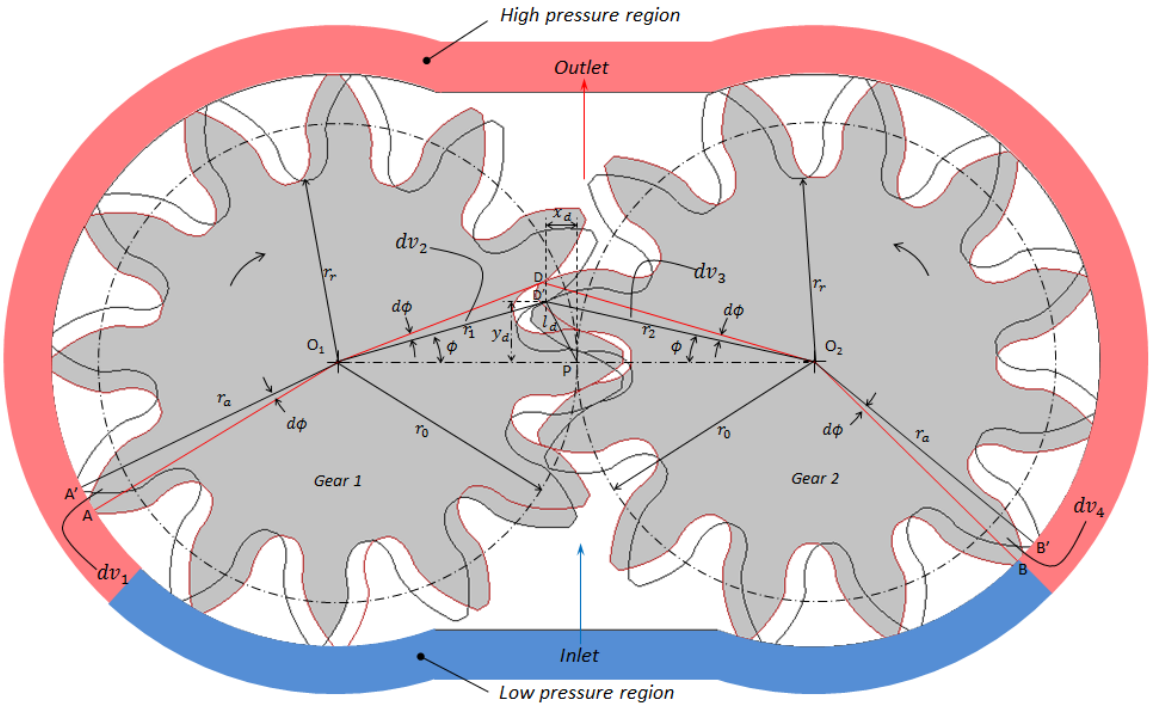

Figure 26: Determination of the displacement of the pump with asymmetric teeth showing the point of contact (D) on the drive side of the teeth. [red] represents the initial position of the gears and [black] represents the final position of the gears.

Therefore, for gears with asymmetric teeth, the displaced volume, dv, can be represented as,

$$dv = \frac{1}{2} \cdot b \cdot (r_a^2 - r_0^2 - l_c^2) \cdot d\phi + \frac{1}{2} \cdot b \cdot (r_a^2 - r_0^2 - l_d^2) \cdot d\phi. \tag{3.55}$$

Rearranging, Eq. (3.55) yields,

$$dv = b \cdot (r_a^2 - r_0^2) \cdot d\phi - \frac{1}{2} \cdot b \cdot (l_c^2 + l_d^2) \cdot d\phi. \tag{3.56}$$

where,

$$l_c = r_0 \cdot \phi \cdot \cos \alpha_{0c} = r_{bc} \cdot \phi, \tag{3.57}$$

$$l_d = r_0 \cdot \phi \cdot \cos \alpha_{0d} = r_{bd} \cdot \phi, \tag{3.58}$$

assuming a small angular rotation, ϕ.

The instantaneous flow rate delivered by the pump can be written as,

$$Q = \frac{dv}{dt} = b \cdot (r_a^2 - r_0^2) \cdot \frac{d\phi}{dt} - \frac{1}{2} \cdot b \cdot (l_c^2 + l_d^2) \cdot \frac{d\phi}{dt}. \tag{3.59}$$

Therefore,

$$Q = b \cdot (r_a^2 - r_0^2) \cdot \omega - \frac{1}{2} \cdot b \cdot (l_c^2 + l_d^2) \cdot \omega, \tag{3.60}$$

where (for small angle ϕ,),

$$l_c = r_0 \cdot \phi \cdot \cos \alpha_{0c} = r_{bc} \cdot \phi, \tag{3.61}$$

$$l_d = r_0 \cdot \phi \cdot \cos \alpha_{0d} = r_{bd} \cdot \phi. \tag{3.62}$$

Substituting Eqs. (3.61) - (3.62) in Eq. (3.60) yields,

$$Q = b \cdot (r_a^2 - r_0^2) \cdot \omega - \frac{1}{2} \cdot b \cdot (r_{bc}^2 + r_{bd}^2) \cdot \phi^2 \cdot \omega. \tag{3.63}$$

3.2.1. Maximum Displacement

Using the expression in Eq. (3.63), the mean flow rate delivered at maximum displacement to the outlet can be written as, Q_m,

$$Q_m^{max} = \frac{z}{\pi} \cdot \int_{-\frac{\pi}{2 \cdot z}}^{\frac{\pi}{2 \cdot z}} \left(b \cdot (r_a^2 - r_0^2) \cdot \omega - \frac{1}{2} \cdot b \cdot (r_{bc}^2 + r_{bd}^2) \cdot \phi^2 \cdot \omega \right) d\phi, \tag{3.64}$$

Notice that, in Eq. (2.62) the integration has been performed within the limits within which the displacement chamber or the TSV changes its connection from the high pressure outlet to the low pressure inlet (based on the position of the simplified grooves shown in Figure 27). The integration limits represent the region within which the trapped TSV crosses the pressure barrier defined by the difference between outlet and inlet pressures, to be consistent with the assumption for Eq. (3.34). This approach is similar to the one presented in [23] and [24], but nevertheless the analytical derivation considered in the mentioned gears only with symmetrical teeth.

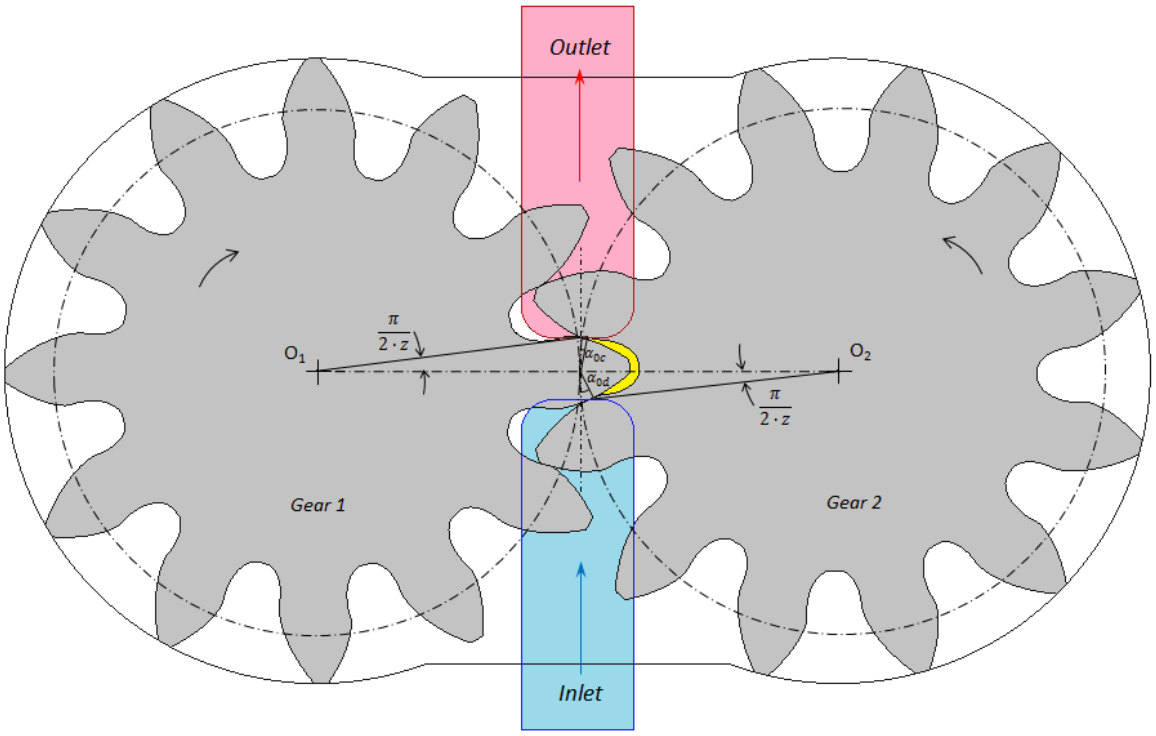

Figure 27: Position of the asymmetric gears and grooves showing the integration limits for maximum displacement.

Integrating Eq. (3.64), yields,

$$Q_m^{max} = b \cdot \omega \cdot \left(r_a^2 - r_0^2 \cdot \left(1 + \frac{\pi^2}{24 \cdot z^2} \cdot (\cos {\alpha_{0c}}^2 + \cos {\alpha_{0d}}^2) \right) \right). \tag{3.65}$$

For the case of symmetric gears, Eq. (3.65) can be re-written by equating $\alpha_{0c} = \alpha_{0d} = \alpha$, therefore it boils down to the equation as shown in [23],

$$Q_{m,sym}^{max} = b \cdot \omega \cdot \left(r_a^2 - r_0^2 \cdot \left(1 + \frac{\pi^2}{12 \cdot z^2} \cdot (\cos \alpha^2) \right) \right). \tag{3.66}$$

The mean value of the geometric maximum displacement for asymmetric gears can be evaluated using,

$$\begin{aligned} V^{max} &= \frac{Q_m^{max}}{\omega / 2 \cdot \pi} \\ &= 2 \cdot \pi \cdot b \cdot \left(r_a^2 - r_0^2 \cdot \left(1 + \frac{\pi^2}{24 \cdot z^2} \cdot (\cos {\alpha_{0c}}^2 + \cos {\alpha_{0d}}^2) \right) \right). \end{aligned} \tag{3.67}$$

The total torque input to the shaft for maximum displacement can be written using Eq. (3.36) as,

$$\begin{aligned} M^{max} &= \frac{Q_m^{max} \cdot \Delta p}{\omega} \\ &= b \cdot \left(r_a^2 - r_0^2 \cdot \left(1 + \frac{\pi^2}{24 \cdot z^2} \cdot (\cos {\alpha_{0c}}^2 + \cos {\alpha_{0d}}^2) \right) \right) \cdot \Delta p. \end{aligned} \tag{3.68}$$

3.2.2. Minimum Displacement

In a similar approach as considered in the previous section, the mean flow rate delivered at minimum displacement can be calculated. However, the integration limits for this case is more complicated than the previous case, due to the fact that the two different lines of action: the drive side (l_d) and the coast side (l_c) end at two different asymmetric locations represented by θ_{S2} and θ_{S1} respectively (as previously explained in Section 3.1), hence the integration limits have to be considered taking into account θ_{S2} and θ_{S1} separately. The integration limits for the drive side line of action is represented in Figure 28. A

similar representation for the limits for the coast side line of action can also be made (not shown in figure).

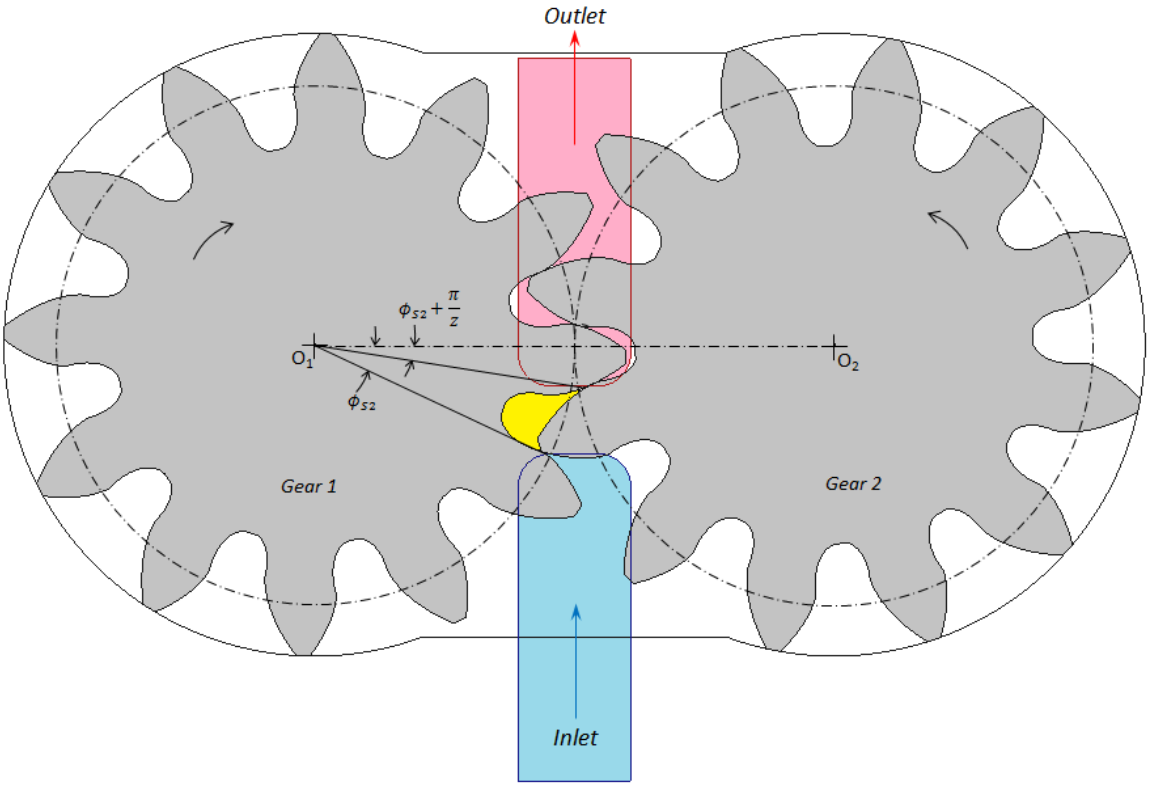

Figure 28: Position of the asymmetric gears and grooves showing the integration limits for minimum displacement.

Mathematically, the limits of integration considering the drive side line of action can be represented as,

$$-\phi_{S2} \leq \phi \leq -\phi_{S2} + \frac{\pi}{z}. \tag{3.69}$$

Similarly, the limits of integration considering the coast side line of action can be represented as,

$$-\phi_{S1} \leq \phi \leq -\phi_{S1} + \frac{\pi}{z}. \tag{3.70}$$

The mean flow rate delivered at minimum displacement can be expressed by re-arranging Eq. (3.63) and applying the appropriate integration limits as,

$$Q_m^{min} = \frac{z}{\pi} \cdot \int_{-\phi_{S2}}^{-\phi_{S2}+\frac{\pi}{z}} \left(\frac{1}{2} \cdot b \cdot (r_a^2 - r_0^2 - r_{bd}^2) \cdot \omega\right) d\phi + \frac{z}{\pi} \cdot \int_{-\phi_{S1}}^{-\phi_{S1}+\frac{\pi}{z}} \left(\frac{1}{2} \cdot b \cdot (r_a^2 - r_0^2 - r_{bc}^2) \cdot \omega\right) d\phi. \quad (3.71)$$

Integrating, Eq. (3.71) and rearranging the terms yields,

$$Q_m^{min} = b \cdot \omega \cdot \left(r_a^2 - r_0^2 \cdot \left(1 + \frac{\cos \alpha_{0d}{}^2}{6} \cdot \left(\frac{\pi^2}{z^2} - 3 \cdot \phi_{S2} \cdot \frac{\pi}{z} + 3 \cdot \phi_{S2}^2\right) + \frac{\cos \alpha_{0c}{}^2}{6} \cdot \left(\frac{\pi^2}{z^2} - 3 \cdot \phi_{S1} \cdot \frac{\pi}{z} + 3 \cdot \phi_{S1}^2\right)\right)\right). \quad (3.72)$$

The mean value of the geometric minimum displacement for asymmetric gears can be evaluated using,

$$V^{min} = \frac{Q_m^{min}}{\omega / 2 \cdot \pi} = 2 \cdot \pi \cdot b \cdot \left(r_a^2 - r_0^2 \cdot \left(1 + \frac{\cos \alpha_{0d}{}^2}{6} \cdot \left(\frac{\pi^2}{z^2} - 3 \cdot \phi_{S2} \cdot \frac{\pi}{z} + 3 \cdot \phi_{S2}^2\right) + \frac{\cos \alpha_{0c}{}^2}{6} \cdot \left(\frac{\pi^2}{z^2} - 3 \cdot \phi_{S1} \cdot \frac{\pi}{z} + 3 \cdot \phi_{S1}^2\right)\right)\right) \quad (3.73)$$

The total torque input to the shaft for minimum displacement can be written using Eq. (3.36) as,

$$M^{min} = \frac{Q_m^{min} \cdot \Delta p}{\omega} = b \cdot \left(r_a^2 - r_0^2 \cdot \left(1 + \frac{\cos \alpha_{0d}{}^2}{6} \cdot \left(\frac{\pi^2}{z^2} - 3 \cdot \phi_{S2} \cdot \frac{\pi}{z} + 3 \cdot \phi_{S2}^2 \right) + \frac{\cos \alpha_{0c}{}^2}{6} \cdot \left(\frac{\pi^2}{z^2} - 3 \cdot \phi_{S1} \cdot \frac{\pi}{z} + 3 \cdot \phi_{S1}^2 \right) \right) \right) \cdot \Delta p. \quad (3.74)$$

Based on the expressions derived previously for maximum and minimum displacement, the resultant reduction in displacement can be written as,

$$\beta = \frac{V^{min}}{V^{max}}. \quad (3.75)$$

3.3. Analytical Determination of Non-Uniformity in Flow Rate and Input Torque

In this section, the non-uniformity/pulsations in the flow rate and torque at max and min displacement has been determined analytically starting from the equation for instantaneous flow rate as described in the following sub-sections.

3.3.1. Maximum Displacement

In order to understand the non-uniformity of the flow rate delivered at the outlet, the maximum and minimum value of the instantaneous flow rate need to be determined. For the configuration of grooves to attain maximum displacement, Eq. (3.63) is applicable to the region represented by,

$$-\frac{\pi}{2 \cdot z} \leq \phi \leq \frac{\pi}{2 \cdot z}. \quad (3.76)$$

Within this region, the maximum value of the instantaneous flow rate is achieved when $\phi = 0$ and the minimum value of the instantaneous flow rate is achieved when $\phi = \frac{\pi}{2 \cdot z}$.

Therefore, the maximum value of the instantaneous flow rate for maximum displacement configuration can be written as,

$$Q_{i,max}^{max} = b \cdot (r_a^2 - r_0^2) \cdot \omega. \tag{3.77}$$

And, the minimum value of the instantaneous flow rate for minimum displacement configuration can be written as,

$$Q_{i,min}^{max} = b \cdot (r_a^2 - r_0^2) \cdot \omega - \frac{1}{2} \cdot b \cdot (r_{bc}^2 + r_{bd}^2) \cdot \frac{\pi^2}{4 \cdot z^2} \cdot \omega. \tag{3.78}$$

Hence, the non-uniformity in the flow rate (or outlet flow pulsations) for maximum displacement can be represented as the difference between the maximum and minimum values of the instantaneous flow rate as,

$$\delta_Q^{max} = Q_{i,max}^{max} - Q_{i,min}^{max} = \frac{1}{8} \cdot b \cdot (r_{bc}^2 + r_{bd}^2) \cdot \frac{\pi^2}{z^2} \cdot \omega. \tag{3.79}$$

Similar to the non-uniformity in the flow rate, non-uniformity of input shaft torque (or input shaft torque pulsations) can be represented as,

$$\delta_M^{max} = \frac{\delta_Q^{max} \cdot \Delta p}{\omega} = \frac{1}{8} \cdot b \cdot (r_{bc}^2 + r_{bd}^2) \cdot \frac{\pi^2}{z^2} \cdot \Delta p. \tag{3.80}$$

3.3.2. Minimum Displacement

Considering the limits of integration as shown in Eq. (3.71), the maximum value of the instantaneous flow rate for minimum displacement configuration can be calculated by substituting $\phi = -\phi_{S2}$ and $\phi = -\phi_{S1}$ respectively in the drive side and coast side line of action in Eq. (3.60). Therefore,

$$Q_{i,max}^{min} = b \cdot (r_a^2 - r_0^2) \cdot \omega - \frac{1}{2} \cdot b \cdot (r_{bc}^2 \cdot \phi_{S1}^2 + r_{bd}^2 \cdot \phi_{S2}^2) \cdot \omega. \tag{3.81}$$

Similarly, the minimum value of the instantaneous flow rate for minimum displacement configuration can be calculated by substituting $\phi = -\phi_{S2} + \frac{\pi}{z}$ and $\phi = -\phi_{S1} + \frac{\pi}{z}$ respectively in the drive side and coast side line of action in Eq. (3.60). Hence,

$$Q_{i,min}^{min} = b \cdot (r_a^2 - r_0^2) \cdot \omega - \frac{1}{2} \cdot b \cdot \left(r_{bc}^2 \cdot \left(\phi_{S1}^2 - 2 \cdot \phi_{S1} \cdot \frac{\pi}{z} + \frac{\pi^2}{z^2} \right) + r_{bd}^2 \cdot \left(\phi_{S2}^2 - 2 \cdot \phi_{S2} \cdot \frac{\pi}{z} + \frac{\pi^2}{z^2} \right) \right) \cdot \omega. \tag{3.82}$$

Therefore, the non-uniformity in the flow rate (or outlet flow pulsations) for minimum displacement can be represented as the difference between the maximum and minimum values of the instantaneous flow rate as,

$$\delta_Q^{min} = Q_{i,max}^{min} - Q_{i,min}^{min} = \frac{1}{2} \cdot b \cdot \left(r_{bc}^2 \cdot \left(\frac{\pi^2}{z^2} - 2 \cdot \phi_{S1} \cdot \frac{\pi}{z} \right) + r_{bd}^2 \cdot \left(\frac{\pi^2}{z^2} - 2 \cdot \phi_{S2} \cdot \frac{\pi}{z} \right) \right) \cdot \omega. \tag{3.83}$$

Comparing, Eq. (3.83) and Eq. (3.79), the difference between the non-uniformity between the maximum and minimum displacement can be written as,

$$\delta_Q^{min} - \delta_Q^{max} = \frac{3}{8} \cdot b \cdot (r_{bc}^2 + r_{bd}^2) \cdot \frac{\pi^2}{z^2} \cdot \omega + b \cdot (r_{bc}^2 \cdot \phi_{S1} + r_{bd}^2 \cdot \phi_{S2}) \cdot \frac{\pi}{z} \cdot \omega. \tag{3.84}$$

It can be clearly seen that the non-uniformity in the flow rate is higher at minimum displacement than that at maximum displacement, which is inherent to the concept with which displacement variation is achieved.

Similar to the non-uniformity in the flow rate, non-uniformity of input shaft torque (or input shaft torque pulsations) can be represented as,

$$\delta_M^{min} = \frac{\delta_Q^{min} \cdot \Delta p}{\omega} = \frac{1}{2} \cdot b \cdot \left(r_{bc}^2 \cdot \left(\frac{\pi^2}{z^2} - 2 \cdot \phi_{S1} \cdot \frac{\pi}{z} \right) + r_{bd}^2 \cdot \left(\frac{\pi^2}{z^2} - 2 \cdot \phi_{S2} \cdot \frac{\pi}{z} \right) \right) \cdot \Delta p. \tag{3.85}$$

In a similar manner to the non-uniformity in flow rate, the input shaft torque pulsations at minimum displacement are higher than that at maximum displacement.

In short, in this chapter an effort was made to analytically derive the displacement of the pump based on the geometry of the pump. Expressions pertaining to mean flow rate, input shaft torque and non-uniformity were derived both maximum and minimum displacement. However, it should be noted that these derivations were made on the assumption of small angles and hence these expressions may over predict the particular quantities. Nevertheless, a general understanding of the phenomenon can be obtained using these equations. A robust geometrical model capable of numerically predicting the displacement values is therefore, necessary to accurately predict the geometric displacement considering the actual profile of the gears as described in 5.

4. OVERVIEW OF THE HYGESIM SIMULATION TOOL

In order to have a complete understanding of the performance of the EGM, a robust simulation tool which is capable of predicting the detailed operation of the EGM is necessary. In this study a tool named HYGESIM - HYdraulic GEar machine Simulator which is being developed by the members of the lab will be used to predict the performance of the VD-EGM as well as to optimize the design. In this chapter, a brief description of the important submodels of HGESIM tool is provided.

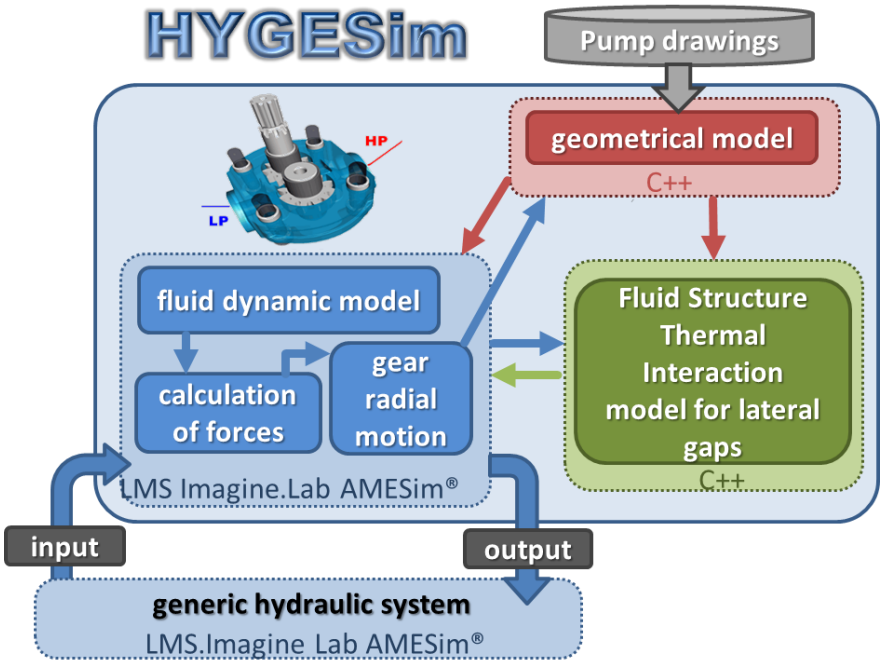

Figure 29: Structure of HYGESim. Sub-models of HYGESim and their interactions are shown.

HYGESim, represents a state-of-the-art EGM simulator tool that has been developed over several years of research [57] to [64]. HYGESim is capable of predicting almost all of the

important aspects of EGMs, such as features of the meshing process: internal pressure peaks and cavitation, port flow oscillations, the displacement of fluid through the TSVs, radial motion of the gears, radial balance of forces, flow features in the lateral gaps accounting for the axial balance of the floating bushings considering the deformation due to pressure and thermal effects of the gears and bushings. The Geometrical model of HYGESim forms the prime focus of this work, and will be described in detail in the following chapter.

As can be seen from Figure 29, HYGESim has several submodels which work together in cosimulation and the flux of data such as rate of flow between the CVs, pressures in the TSVs etc. between the several models are shown. In the present section an overview will be provided of the fluid dynamic model which is responsible for the simulation of the flow through the TSVs of the EGM. In addition, a short description of the mechanical model responsible for radial motion of the gears and as well as the fluid structure thermal interaction (FSTI) model for the lateral gaps will also be described briefly. The fluid dynamic model and the evaluation of the gear micro-motion were created inside the LMS.Imagine Lab AMESim® environment using custom built component libraries combined with the standard libraries of the code in C language, while the geometric model and FSTI models are standalone applications developed using C++.

4.1. Fluid Dynamic Model

The principal component of HYGESim is the fluid dynamic model which strongly influences the functioning and the evaluation in the other submodels. A lumped parameter approach is used to analyze the flow entering and exiting the tooth space volumes at a macro level to reduce considerably the simulation time and simplify the interaction between the other sub-models. Thanks to the accurate evaluation of the different geometrical features (by the Geometrical model as described in Chapter 5) for the calculation flow during one complete revolution of the machine, the lumped parameter model predicts the flow through the machine accurately [59].

The gear machine is divided into several control volumes (CV) corresponding to each tooth space volume (TSV) and the inlet and the delivery volume as shown in Figure 30. It is assumed that the fluid properties remain uniform in each of the CVs. The fluid properties such as the density and bulk modulus are predicted according to the change in pressure of the fluid in the CV. HYGESim uses the fluid properties model which takes into consideration the cavitation features with a simplified continuum model that assumes a uniform mixture of different phases (liquid/gas) to evaluate the fluid properties, especially the density and the bulk modules as a function of pressure [65][66][67].

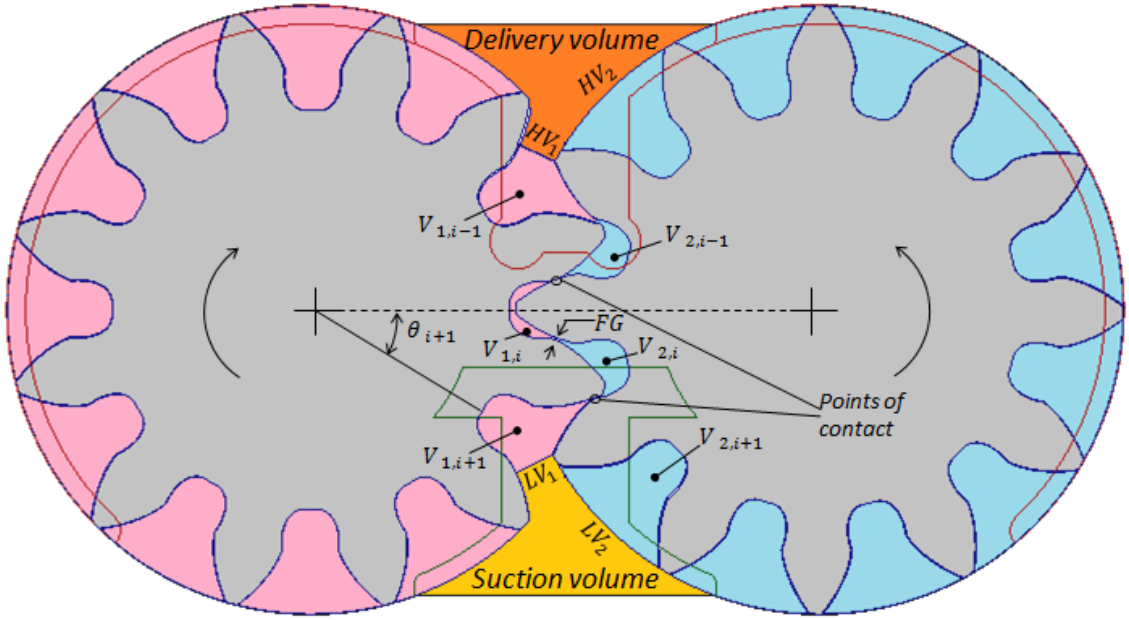

Figure 30: Control volumes defined in the fluid dynamic model of HYGESim (representation of the TSVs and the connections between each other).

Based on the flow between the adjacent TSVs, assuming conservation of mass and fluid state equation, the rate of change of pressure in the CV can be obtained using a pressure build-up equation,

$$\frac{dp_i}{dt} = \frac{1}{V_i}\frac{dp}{d\rho}\Big|_{p=p_i} \cdot \left[\sum \dot{m_{in,\iota}} - \sum \dot{m_{out,\iota}} - \rho|_{\rho=\rho_i}\left(\frac{dV_i}{dt} - \frac{dV_{var,i}}{dt}\right)\right], \tag{4.1}$$

$$\dot{m_{\iota,J}} = \frac{(p_i - p_j)}{|(p_i - p_j)|} \cdot \rho|_{P=\overline{P_{i,j}}} \cdot \alpha \cdot \Omega_{i,j} \cdot \sqrt{\frac{2 \cdot (p_i - p_j)}{\rho|_{P=\overline{P_{i,j}}}}}. \tag{4.2}$$

Eq. (4.2) represents the turbulent flow orifice equation for calculating the flow rate, $\dot{m}_{i,j}$ from ith TSV to the jth TSV and $\Omega_{i,j}$indicates the orifice area of the connections between the two TSVs. In particular, in Eq. (4.1), the terms V_i correspond to the instantaneous volume of the ith CV as the volume continuously changes to achieve the displacing action. The term $V_{var,i}$ takes account of the additional variable volume which occurs at the suction and the delivery due to the nature of definition of the i^{th} CV during the rotation of the gears .

A laminar flow equation (fully developed laminar flow, considering the relative motion between surfaces) is used to calculate the leakages across the tooth – tip,

$$\dot{m}_{i,j} = \rho \left[-\frac{h^3}{12\mu} \frac{(p_i - p_j)}{L} + \frac{h \cdot u}{2} \right] \cdot b, \tag{4.3}$$

where, $\dot{m}_{i,j}$is the laminar flow from the i^{th} to the j^{th} TSV of the same gear through the gap between the tooth tip and the casing, u is the velocity of the wall, L is the gap length, h is the gap height and b is the gap width.

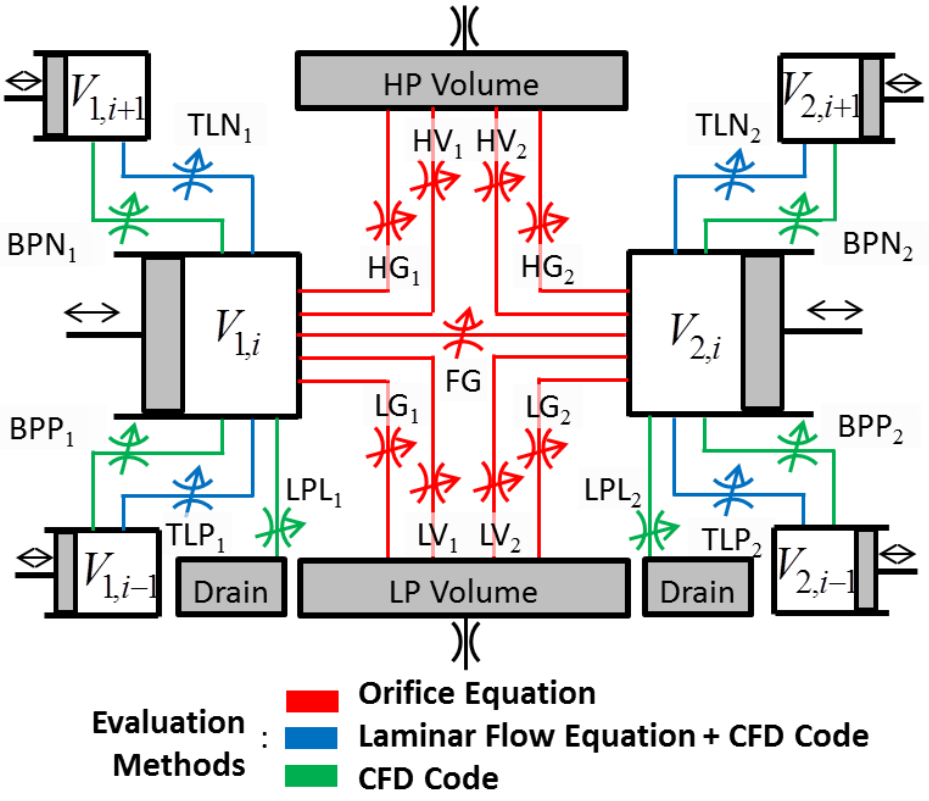

Figure 31: Framework of connections between a pair of corresponding CVs.

In Figure 31, the framework of connections between a pair of teeth which are meshing together have been depicted. Figure 30 and Figure 32, show the same connections considering the gears and the relief grooves in the EGM. Each of these connections evaluates flow between the corresponding CVs using the correct approaches as summarized in Table 1.

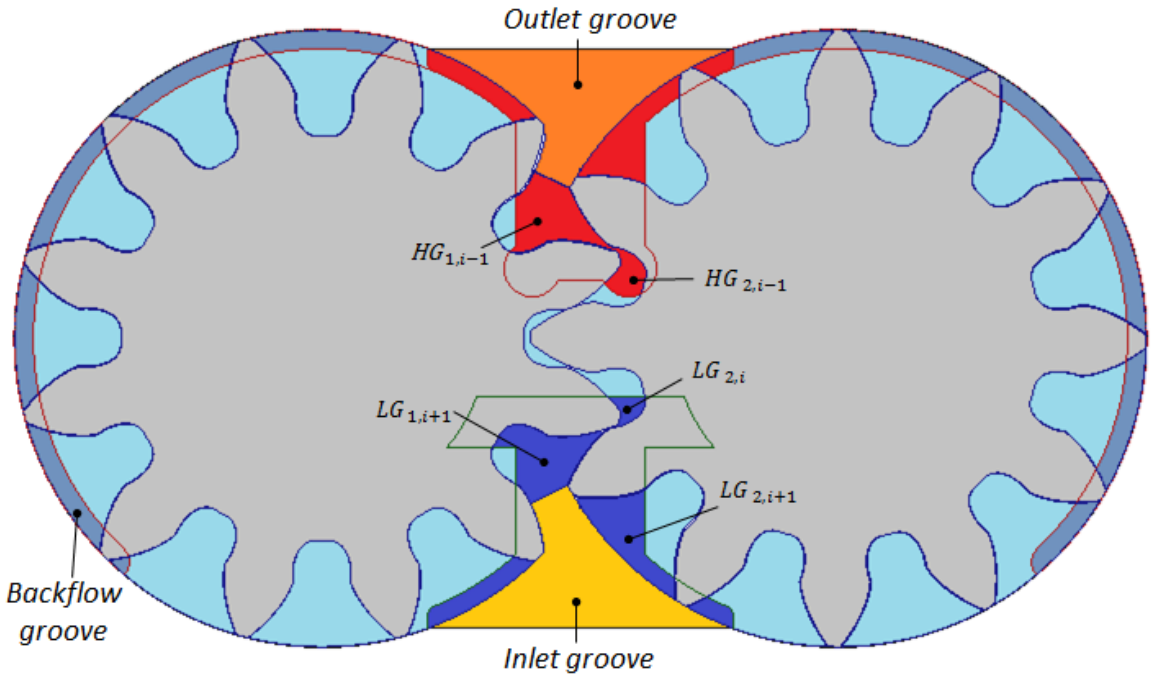

Figure 32: Representations of the connections HG_1, HG_2, LG_1, LG_2.

Table 1: Descriptions of orifice connections between control volumes used in HYGESim fluid dynamic model.

	Description
FG	connection between the two corresponding TSVs (Figure 30) (the connection is closed outside the meshing zone)
HV	connection between the TSV and the HP volume through the gear whole depth (examples are displayed in Figure 30)
LV	connection between the TSV and the LP volume through the gear whole depth (Figure 30)
HG	connection between the TSV and the HP port through the recesses machined on the lateral sliding elements (Figure 32).
LG	connection between the TSV and the LP port through the recesses machined on the lateral sliding elements (Figure 32).

The leakages due to the clearances between the gears tooth tip are represented by TLP and TLN which correspond to the connection between the previous and following TSV respectively with the current TSV. In a similar fashion, the lateral leakages through the gap (lateral gap) between the gears and the lateral bushings are represented by BPP and

BPN which correspond to the connection between the previous and following TSV respectively with the current TSV A simplified approach is used for calculating the lateral leakages by assuming a constant gap height and using Eq. (3.3). However a more accurate evaluation is performed by the FSI model for the later gap as described in section 2.3.

4.2. Mechanical Model

The mechanical model of HYGESim deals with the evaluation of forces acting on the gears in the radial plane, perpendicular to the axes of rotation. It is also capable of calculating the torque required/provided to the drive gear. The calculation of the forces allows for the calculation of the equilibrium of forces in the radial plane and also to predict the movement of the gears as a function of the operating conditions of the machines.

The evaluation of the pressure acting on each TSV by the fluid dynamic model, provides the pressure distribution acting on the gear. Since considering a single tooth will involve the presence of different pressures on its sub-surfaces corresponding to the different CVs defined by the fluid dynamic model, a single surface can be affected by several different CVs (maximum three) in the meshing zone. While outside the meshing zone, it is attributed to just one CV as shown in Figure 33.

In Figure 33(A), the forces acting on the tooth surface due to the pressure inside the TSV is depicted. The resultant force in the x-direction acts on the projected area Ω_{yz} perpendicular to the x-axis. Similarly, the resultant force in the y-direction acts on the projected area Ω_{xz} perpendicular to the y-axis. The resultant forces can be calculated using,

$$F_{p,x}(\vartheta) = \sum_{i=1}^{z} \sum_{k=1}^{Ns} f_{x,i,k}(\vartheta) \quad where\ Ns = 1\ or\ 3 \tag{4.4}$$

and,

$$F_{p,y}(\vartheta) = \sum_{i=1}^{z}\sum_{k=1}^{Ns} f_{y,i,k}(\vartheta) \quad where\ Ns = 1\ or\ 3. \tag{4.5}$$

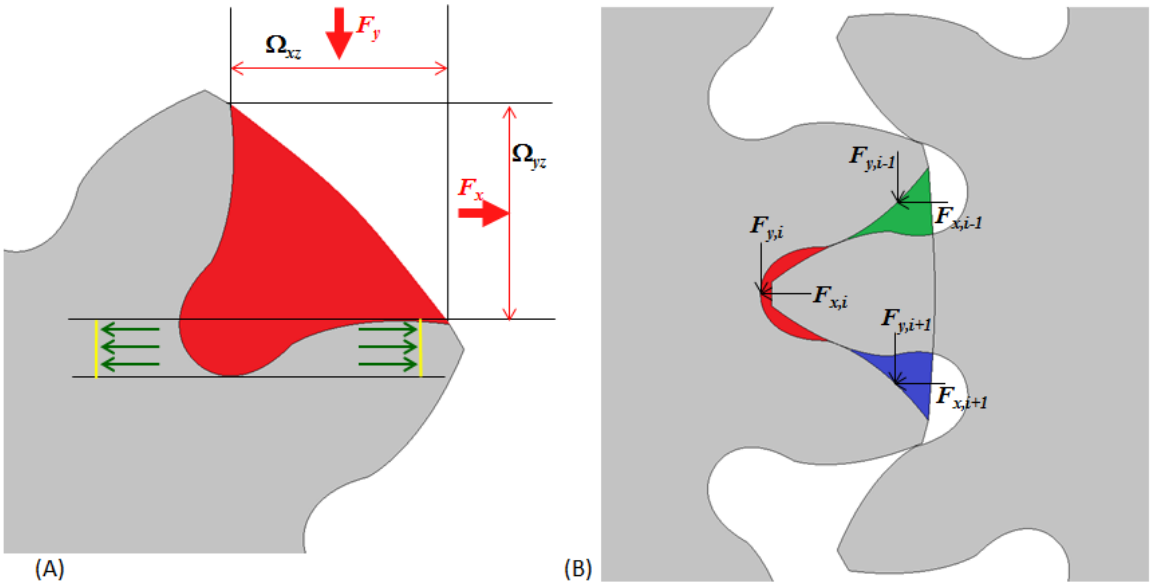

Figure 33: (A) Forces acting on the horizontal and vertical plane for a TSV; (B) Forces acting on different tooth surfaces due to the pressure in the different CVs.

For each of the gears, the resultant forces $F_{p,x}(\vartheta)$ and $F_{p,y}(\vartheta)$ act at a distance $Y(\vartheta)$ and $X(\vartheta)$ from the gear center which can be determined by using,

$$X(\vartheta) = \frac{\sum_{i=1}^{z}\sum_{k=1}^{Ns}\left(f_{y,i,k}(\vartheta)\cdot x_{i,k}(\vartheta)\right)}{F_{p,y}(\vartheta)} \quad Ns = 1\ or\ 3 \tag{4.6}$$

and,

$$Y(\vartheta) = \frac{\sum_{i=1}^{z}\sum_{k=1}^{Ns}\left(f_{x,i,k}(\vartheta)\cdot y_{i,k}(\vartheta)\right)}{F_{p,x}(\vartheta)} \quad Ns = 1\ or\ 3. \tag{4.7}$$

The entire system of forces due to the pressure inside the different CVs can be transferred to a resultant force and torque acting on the gear center as shown in Figure 34: Resultant forces due to pressure, contact forces and total torque acting on the gears. The contact forces between the two gears have also been modeled assuming that at least one pair of teeth is always in contact with each other and hence the load is being shared. Details of the contact force modeling are represented in [59]. Based on the resultant of the forces acting on the gears and with the implementation of the hydro-dynamic journal bearing

model as in [59] the movement of the gears can be predicted. This allows for a simplified, but accurate, prediction of the wear in the casing, which allows HYGESim to accurately simulate the performance of an EGM that has been through the so called, "breaking in" process which is a proprietary operation performed on all EGMs by the manufacturers. More details regarding the modeling of the radial forces and comparison with measurements are shown in [59].

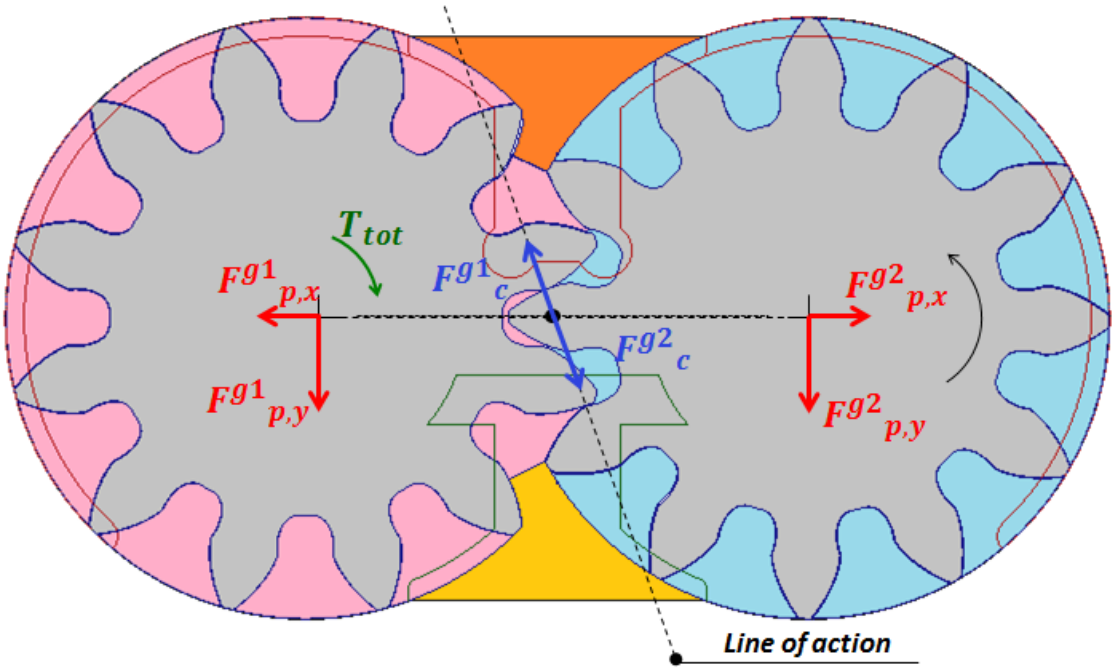

Figure 34: Resultant forces due to pressure, contact forces and total torque acting on the gears.

4.3. Fluid Structure Interaction Model

The Fluid Structure Interaction (FSI) model of HYGESim studies the lateral lubricating gap (as shown in Figure 35) between the sliding lateral bushings and the gears in an EGM. The model represents a state-of-the-art tool that can predict the lateral lubricating gap features, accounting for the main features of machine operation. A Computational Fluid Dynamics solver that solves for the flow field in the lubricating gap is coupled with a model for evaluating the mechanical equilibrium of the lateral bushings to determine the lubricating gap heights. The model also interacts closely with a lumped parameter fluid

dynamic model as well as the geometric model of gear teeth control volumes, and therefore provides a tool for a "complete simulation" of the unit. The forces acting on the lateral bushing are seen to lead to an axially balanced condition. The model is capable of accounting for elasto-hydrodynamic effects in the lubricant film by taking into consideration the deformation of the different parts due to pressure forces and also due to thermal effects, and can predict the lubricant film thickness.

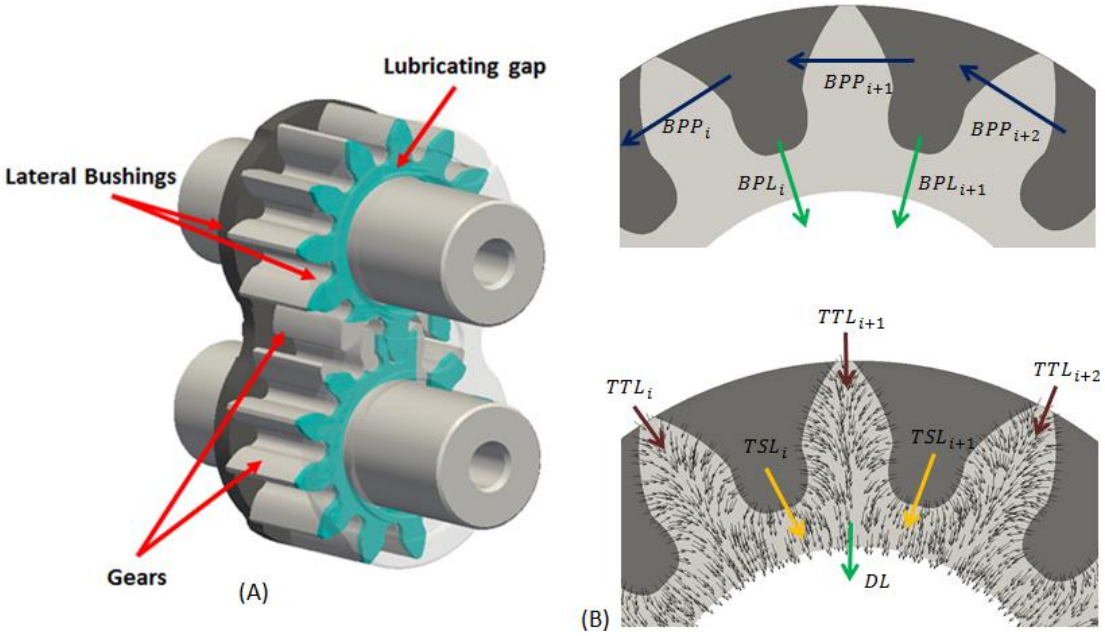

Figure 35: (A) Lateral lubricating gap between the gears and the lateral bushings; (B) Lateral leakage flow calculated by the FSI model.

The fluid dynamic model provides the pressure boundary conditions for all the gap boundaries to the FSI model [60]. The pressure field in the lateral gap is determined by solving the Reynolds equation. The different leakages which are being calculated in the FSI model include: TTL which represent the leakage flow from the radial gap from the tooth tip. TSL represents the leakage flow from the CV into the lateral gap. LPL represents the leakage from suction side into the lateral gap and HPL represents the leakage from the high pressure into lateral gap and DL includes the leakage from the lateral gap into the drain. There is a two way interaction between the fluid dynamic model and the FSI model in such a way that the FSI model receives the pressure at the boundaries as inputs and it provides the fluid dynamic model with the evaluation of the

mentioned leakages. This exchange of information between the two sub-models (co-simulation) is performed iteratively until a converged solution is achieved. The details of the FSI model which deals with the determination of the different part as well as the axial balance of the lateral bushings are can be found in [62],[63] and [64].

5. DESCRIPTION OF THE GEOMETRICAL MODEL

The development of the geometrical model of HYGESim was one of the major focuses of the present study. An accurate description of the different geometrical features is an important requirement to precisely predict the performance of the EGM. The geometrical model precisely satisfies this goal by providing the necessary information to all the other sub-models of HYGESim. In this section the details of the different parts of the geometrical model will be discussed.

The novel geometrical model developed in this work, represents a step forward with respect to the model (which was capable of handling only gears with tooth of symmetric involute profile) prior to the present work, wherein there is an in-built gear and groove designer and also a sub-model to evaluate the different features required by the fluid dynamic model. The new geometrical model is completely implemented in C++ and consists of three sub-models as described below:

1. **Gear generator**- Capable of designing symmetrical and asymmetrical involute profile gears assuming a particular manufacturing process.
2. **Lateral bushings designer**- Capable of designing the inlet and outlet grooves on the lateral bushings.
3. **Geometrical features evaluation** – Capable of evaluating the TSVs, orifice areas of interaction between the TSVs and the delivery and suction volumes and the different projections required for the calculation of forces.

Although the geometrical model is capable of designing the gears and the grooves per se, it is also capable of accepting the 3D drawing of the various parts of the gear machine to evaluate the TSVs. The following subsections describe the details of the sub-models of the geometrical model.

5.1. Gear Generator

In this study, the novel tool for generating gears with asymmetric teeth has been developed. In order to model the gear profiles accurately, the particular gear manufacturing process needs to be understood so that the parameters which will be used to create the gears (as described in Section 5.1.3) are well-defined; therefore a brief description of the different manufacturing methods of the gears is provided. Followed by the description of how the different parts of the teeth are generated.

5.1.1. Gear Manufacturing Methods

Gears can be manufactured by most of manufacturing processes most of the commonly used machining processes, like casting, forging, molding, forming etc. But in almost all of the cases, some sort of machining is applied to obtain the required surface finish, shape and the final dimensions. The two widely used methods for manufacturing gears are:

1. Gear forming
2. Gear machining

In *Gear forming* operation, the teeth on the gear are formed all at once from a mold or die into which the tooth shapes have been machined. The accuracy of the shape and the dimensions are totally dependent on the quality of the die or mold and are usually much lower than those obtained by other machining and finishing operations. The kinds of processes which are included in the forming operations are: Casting, sintering, injection molding forging etc.

Usually, the gear forming processes are used for manufacturing gears which are used for a wide variety of applications which do not require gears produced to a very high accuracy. For manufacturing gears with non-metallic materials such as polymers, nylon, plastic, etc. injection molding is used, because of their applications to low precision gears which are small in size and are not expensive. However, the most commonly used manufacturing methods for producing gears with better accuracy and surface finish are the machining processes which include, form milling, rack generation, shaping, hobbing etc. as described below.

In *form milling*, the form cutter travels axially along the facewidth of the gears to produce the gear tooth. Only one tooth is cut at a time. Once a tooth is generated, the cutter is moved back to the initial/starting position and the gear blank is rotated or indexed (evenly dividing the circumference of a gear blank into equally spaced divisions, which enables the rotation of the gear blank by specific angular steps for cutting a new tooth) and then the cutter proceeds to cut another tooth. This process continues until all teeth are cut. A schematic of this process is shown in Figure 36(A).

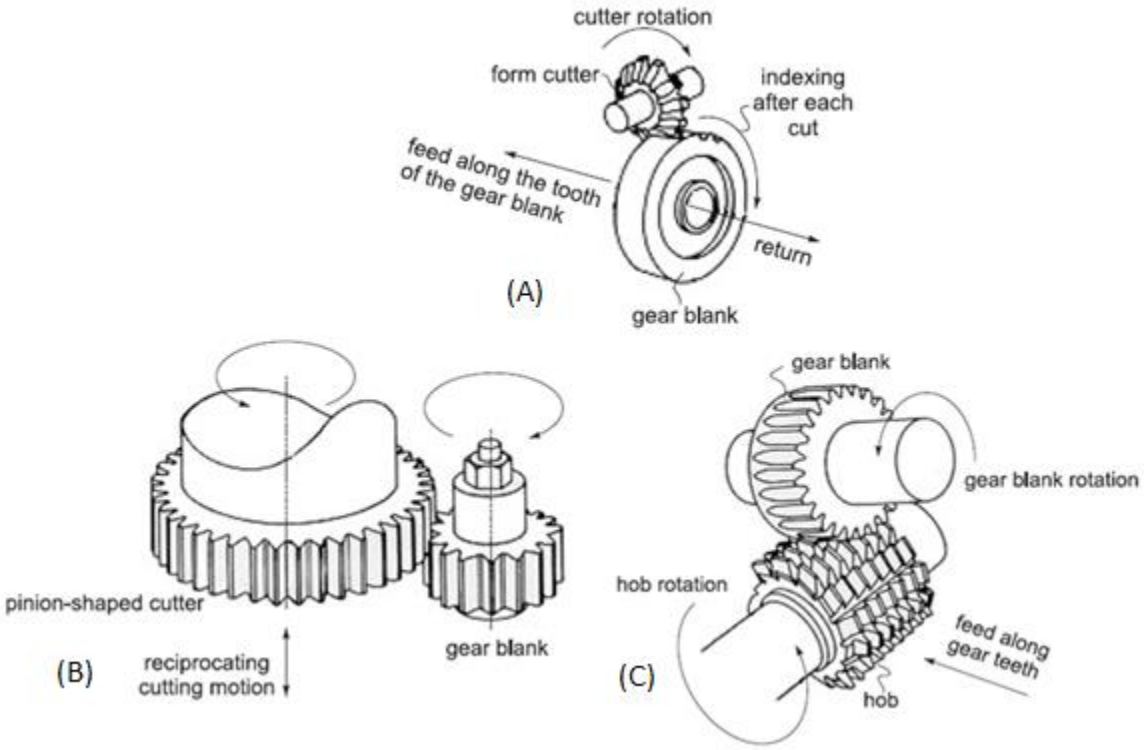

Figure 36: (A) Form milling process; (B) Gear shaping with pinion shaped cutter; (C) Gear hobbing [70].

In *shaping with a pinion-shaped cutter*, a pinion-shaped cutter is both reciprocated and rotated at the same time to generate gears (as shown in Figure 36(B)). The axis of the cutter and the gear blank are made parallel to each other and the cutter is made to rotate in a similar fashion like the gear blank with the same pitch-cycle velocity. At the same time, an axial reciprocating motion is provided to the cutter to produce the gear teeth with the desired facewidth.

A slight variation to shaping using a pinion cutter is *gear shaping with a rack cutter*, gear teeth are generated by cutting tool called a rack shaper/cutter. The rack cutter reciprocates parallel to the gears axis of rotation. It is made to move slowly in a linear manner with the gear blank rotation at the same pitch velocity.

Gears manufactured by this method usually have a very high dimensional accuracy. This process can be also be used to manufacture a wide variety of gears with different number of teeth, pressure angle, tooth thickness etc. just by altering the position of blank with respect to the cutter.

Another type of widely used gear generation methods is *gear hobbing*, in which the gear teeth are progressively generated by a series of cuts with a helical cutting tool called the hob. In this method of manufacturing, all the motions are rotary; therefore, the hob and the gear blank rotate continuously until all the teeth are cut as shown in Figure 36 (C).

5.1.2. Geometry of Involute Curves

A planar curve, *I* is shown in Figure 37(A). The different segments M_iN_i (i = 1,2,….N) represent the radii of curvature of curve I at the different points M_i, where N_i is the corresponding curvature center. The locus of these curve centers N_i is the evolute E to curve I. Particularly, the normal M_iN_i at point M_i of curve I is the tangent to the evolute E and the evolute to a regular curve I is the envelope to the family of normal M_iN_i to I. Considering E as given, the involute curve I for E can be determined from E. In simple words, the involute curve I can be imagined to be the trace out of point M, of an inextensible thread MN that is wrapped on a curve E.

When the evolute curve becomes a circle, the involute curve for such a case is the tooth profile for a spur gear. As shown in Figure 37 (B), considering the evolute curve as the base circle with radius, r_b, an involute curve is generated by the locus of point M_0 of the straight line that rolls over the base circle in the clockwise direction (shown in Figure 37 (B)). Another involute curve can be generated by the counter clockwise rolling of the straight line (not shown in figure).

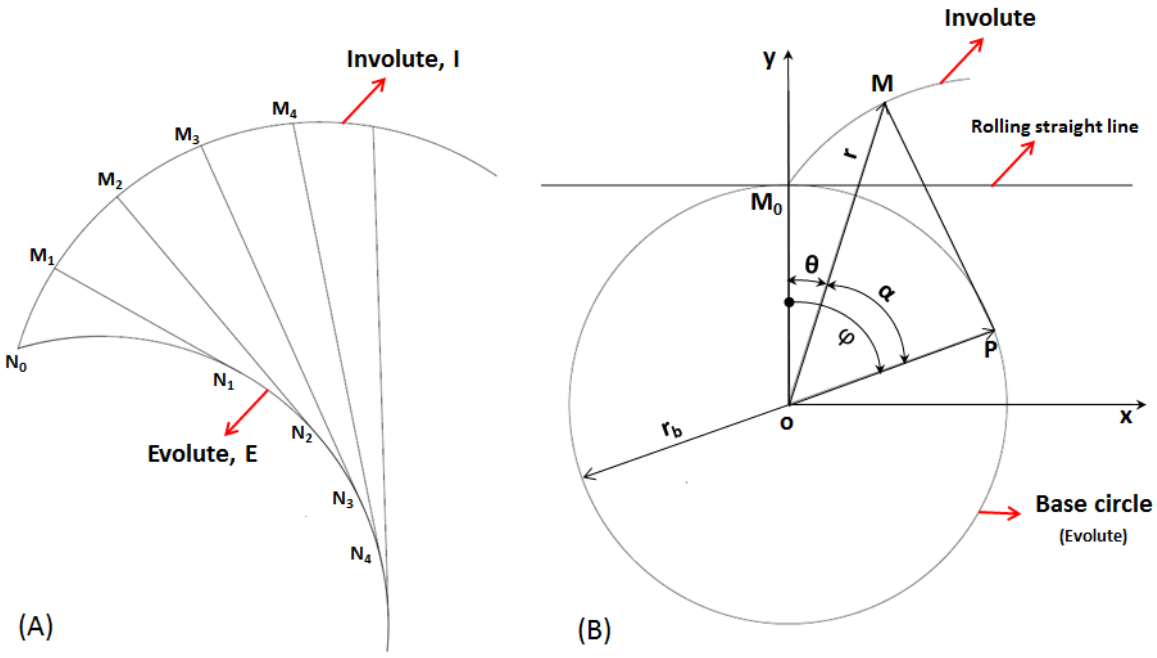

Figure 37: (A) Involute and evolute curves; (B) Involute curve for spur gears.

The point M of the involute curve can be determined by the vector equation,

$$\overline{OM} = \overline{OP} + \overline{PM}, \tag{5.1}$$

where,

$$\overline{OP} = r_b[\sin\emptyset \quad \cos\emptyset]^T, \tag{5.2}$$

$$\overline{PM} = PM[-\cos\emptyset \quad \sin\emptyset]^T. \tag{5.3}$$

In order to have rolling without sliding,

$$PM = \widehat{M_0P} = r_b\emptyset. \tag{5.4}$$

Therefore, using the Eqs. (5.1) - (5.4), the x and y coordinate of the involute curve can be determined using,

$$x = r_b(\sin\emptyset - \emptyset\cos\emptyset), \tag{5.5}$$

$$y = r_b(\cos\emptyset + \emptyset\sin\emptyset). \tag{5.6}$$

A similar representation of the involute curve can be obtained using the variables r and θ as,

$$x = r \cdot \sin\theta, \tag{5.7}$$

$$y = r \cdot \cos\theta. \tag{5.8}$$

Using simple trigonometry, and from the different triangles represented in Figure 37 (B), it can be written that,

$$r = \frac{r_b}{\cos\alpha}, \tag{5.9}$$

$$MP = \widehat{M_0P} = r_b(\theta + \alpha) = r_b \tan\alpha \tag{5.10}$$

Therefore, from Eq. (23) it follows that,

$$\theta = tan\alpha - \alpha. \tag{5.11}$$

If $\theta(\alpha)$ is designated as inv α, then,

$$x = \frac{r_b}{\cos\alpha}\sin(inv\ \alpha), \tag{5.12}$$

$$y = \frac{r_b}{\cos\alpha}\cos\ (inv\ \alpha), \tag{5.13}$$

where,

$$inv\ \alpha = \tan\alpha - \alpha \tag{5.14}$$

can be determined directly from the value of α.

With the help of gears with involute profiles meshing together, it is possible to achieve a constant angular velocity ratio between the gears which is important for smooth transmission of power with minimal speed or torque variations, hence, supporting the success of gears with involute profiles for gear machines in general.

5.1.3. Construction of Asymmetric Teeth

As already mentioned, it is of utmost importance to identify novel gear profiles which maximize the angular range of the trapped volume hence providing advantages in terms of reduction in displacement, while maintaining all the other important performance features of the EGM at an optimum. In this work, the design of the gears is assumed to be comprised of involute and trochoid profiles above and below the base circle respectively. In the past there has been very few works on the novel design of gears, particularly [50]-

[52] focus on the unconventional gears for gear machines only to reduce noise emissions. In order to accomplish the goal of designing asymmetric teeth, two different pressure angles are considered respectively for the drive and coast side of the tooth as shown in Figure 38(A). In order to ensure that the asymmetrical teeth gear profile is physically manufacturable using conventional manufacturing processes like hobbing, shaping, rack-cutting described previously, an asymmetrical cutter profile is assumed first and the teeth profile is derived based on the parameters that determine the shape of the asymmetric cutter as shown in Figure 38(B).

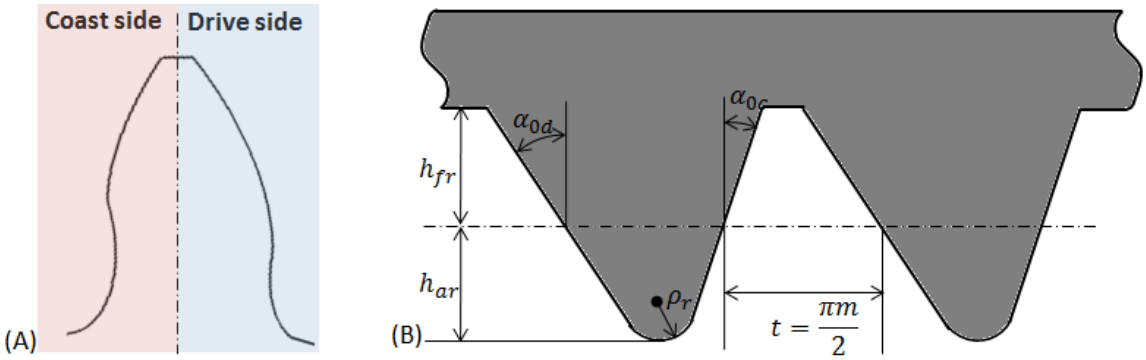

Figure 38: (A) Asymmetric tooth representing the drive and coast sides; (B) Asymmetric tool profile taken as a reference for generating gears.

The basic design variables which govern the shape of the asymmetric gear profile are depicted in Table 2. The range of variation of these parameters and the steps used for the optimization of the gear design (described in the following sections) is also included in the table.

Table 2: Design variables governing the shape of the gear cutter.

Variable	***Description***	***Unit***	***Range***		***Step***
			min	***max***	
m	Normal module	mm	1.0	3.6	0.1
z	Number of teeth	-	9.0	30	1
α_{0d}	Drive pressure angle	°	5.0	30.0	0.1
α_{0c}	Coast pressure angle	°	5.0	30.0	0.1

Based on the design variables, the parameters which govern the shape of the asymmetric cutter are obtained using Eqs. (5.15) – (5.18),

$$h_{ar} = 1.25 \cdot m, \tag{5.15}$$

$$h_{fr} = 1 \cdot m, \tag{5.16}$$

$$\rho_r = \frac{(\pi \cdot m/2) - (\tan\alpha_{od} + \tan\alpha_{oc}) \cdot h_{ar}}{(1/\cos\alpha_{0d}) + (1/\cos\alpha_{oc}) - (\tan\alpha_{od} + \tan\alpha_{oc})}, \tag{5.17}$$

$$h_0 = h_{ar} - \rho_r. \tag{5.18}$$

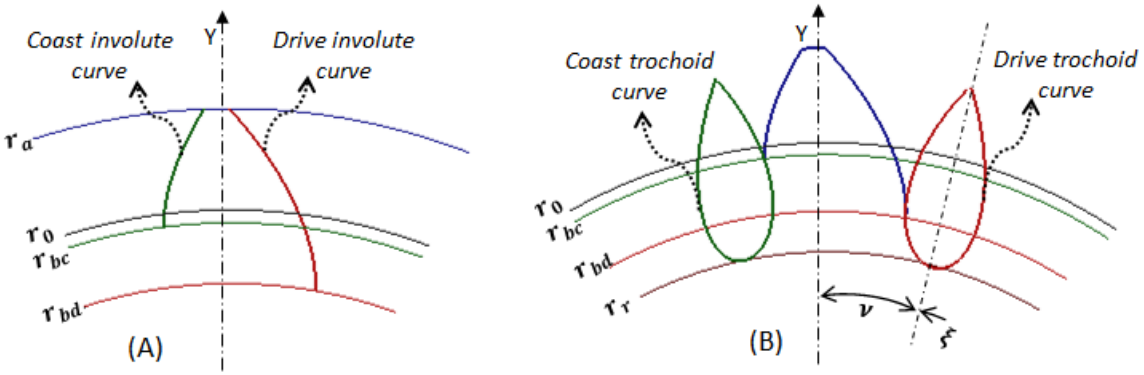

Figure 39: (A) Drive and coast involute curves; (B) Drive and coast Trochoid curves.

The involute profiles for the drive and coast side of the teeth can be obtained using the Eqs. (5.19) – (5.20) [[53]-[55], [68][69][71]].

$$x = (\sin\theta - \theta \cdot \cos\theta) \cdot r_b \cdot \cos\vartheta - (\cos\theta + \theta \cdot \sin\theta) \cdot r_b \cdot \sin\vartheta, \tag{5.19}$$

$$y = (\sin\theta - \theta \cdot \cos\theta) \cdot r_b \cdot \sin\vartheta + (\cos\theta + \theta \cdot \sin\theta) \cdot r_b \cdot \cos\vartheta, \tag{5.20}$$

where,

$$\vartheta = \text{inv}\,\alpha_0 + \frac{\pi}{2 \cdot z}. \tag{5.21}$$

These equations are represented in a generic form for any involute side of the teeth, changing the values of r_b and ϑ for the drive or coast yields respectively the corresponding involute profiles as shown in Figure 39(A) (green curve represents the coast and the red curve represents the drive). It should be noted that the parts of the curves above the addendum circle has been neglected to construct a proper profile above the base circle.

Similar to the construction of the involute profiles, the trochoid profiles of the teeth are obtained using the generic Eqs. (5.22) – (5.23). [53][54][55][68][69]

$$x = (r_0 - h_0) \cdot \sin(\xi + v) - r_0 \cdot \xi \cdot \cos(\xi + v) - \left[\frac{r_0 \cdot \xi + h_0}{\sqrt{h_0^2 + r_0^2 \cdot \xi^2}}\right] \cdot \rho_r \cdot \sin(\xi + v), \quad (5.22)$$

$$y = (r_0 - h_0) \cdot \cos(\xi + v) + r_0 \cdot \xi \cdot \sin(\xi + v) + \left[\frac{r_0 \cdot \xi - h_0}{\sqrt{h_0^2 + r_0^2 \cdot \xi^2}}\right] \cdot \rho_r \cdot \sin(\xi + v), \quad (5.23)$$

where,

$$v = \frac{\pi}{2 \cdot z} + \frac{h_0 \cdot tan\alpha_0}{r_0} + \frac{\rho_r + b_n}{r_0 \cdot cos\,\alpha_0}. \quad (5.24)$$

The value of b_n, controls the backlash in the gear pear generated, therefore setting to zero yields gears with zero backlash or dual flank contact as depicted in Figure 40.

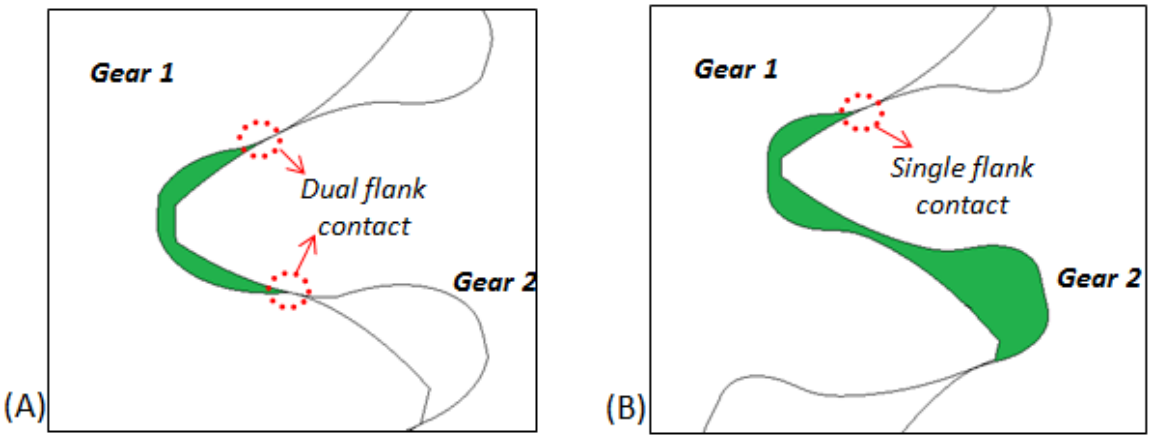

Figure 40: (A) Gears with dual flank contact; (B) Gears with single flank contact.

A complex optimization procedure is used to identify the optimal design of the gears as described in further sections.

5.2. Lateral Bushing Designer

In this section the design of the inlet and outlet grooves is explained briefly. As explained previously in Section 1.2, the grooves in the lateral bushings perform the important timing function of connecting the volume of the fluid trapped in the TSVs between the points of contact of the teeth to the inlet and outlet, hence playing an important role in

controlling the amount of fluid displaced. These grooves are also necessary to ensure that the trapped volume of the fluid between the two contact points of the teeth is connected to the inlet (suction) or the outlet(delivery) (as shown in Figure 41) to guarantee minimal internal pressure overshoots and localized cavitation effects.

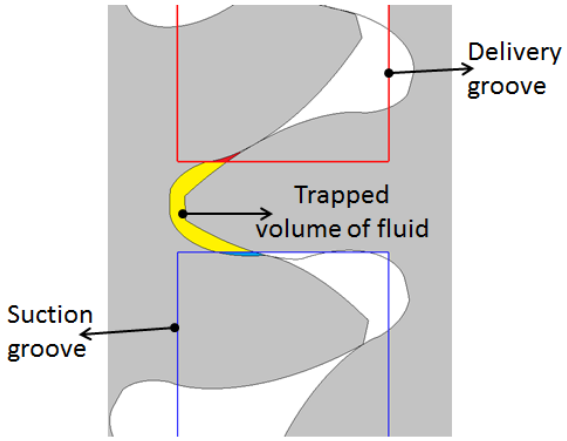

Figure 41: Trapped volume (in yellow) connected to the suction (shown in blue) and delivery (shown in red).

The lateral bush designer is capable of handling any complicated groove geometry, but the one which is considered in this research is of a two-wing structure as shown in figure 12. The design variables governing the shape of the suction and delivery grooves are represented in Table 3.

Particular emphasis is placed on the feasibility of machining the grooves using the conventional milling process for prototyping. As can be seen from Figure 42 (B) and (C), the radius ‘R’ of the milling tool is taken into consideration, so that the results the optimal design out of the optimization process can be directly prototyped without any additional contemplation based on the manufacturability.

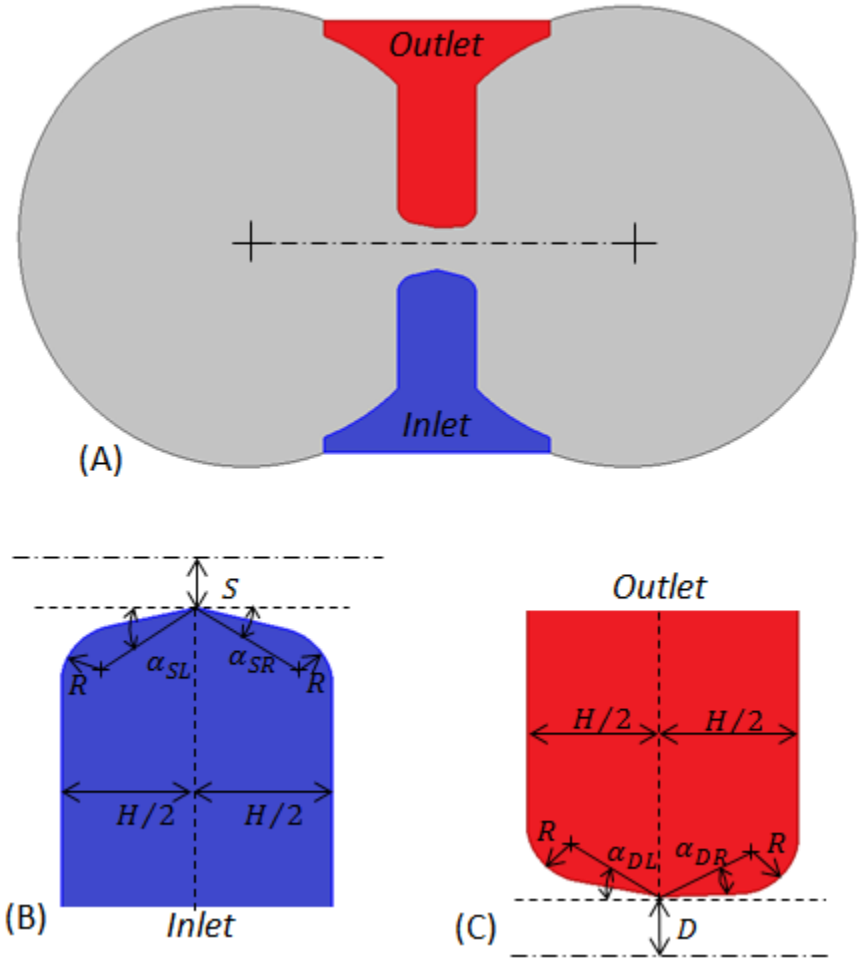

Figure 42: (A) Lateral bush with a representative inlet and outlet groove; (B) Detail of inlet groove; (C) Detail of outlet groove.

Table 3: Design variables governing the shape of the grooves.

Variable	***Unit***	***Range***		***Step***
		min	***max***	
D	mm	0.0	3.6	0.1
S	mm	0.0	3.6	0.1
α_{DL}	°	-45.0	45.0	1
α_{DR}	°	-45.0	45.0	1
α_{SL}	°	-45.0	45.0	1
α_{SR}	°	-45.0	45.0	1

5.3. Geometrical Features Evaluation

The last part of the Geometrical model is the geometrical features evaluation. This sub-model evaluates the tooth space volume of both the gears and the various orifice connections for an entire revolution of operation of the machine. A flowchart showing the details of the operation of the geometrical model is shown in figure 17. The model is implemented in C++ language and once the inputs design variables/CAD drawings are provided to the model, the entire model operates automatically and at the end all the information required by the other sub-models of HYGESim are written in a specific file format readable by HYGESim.

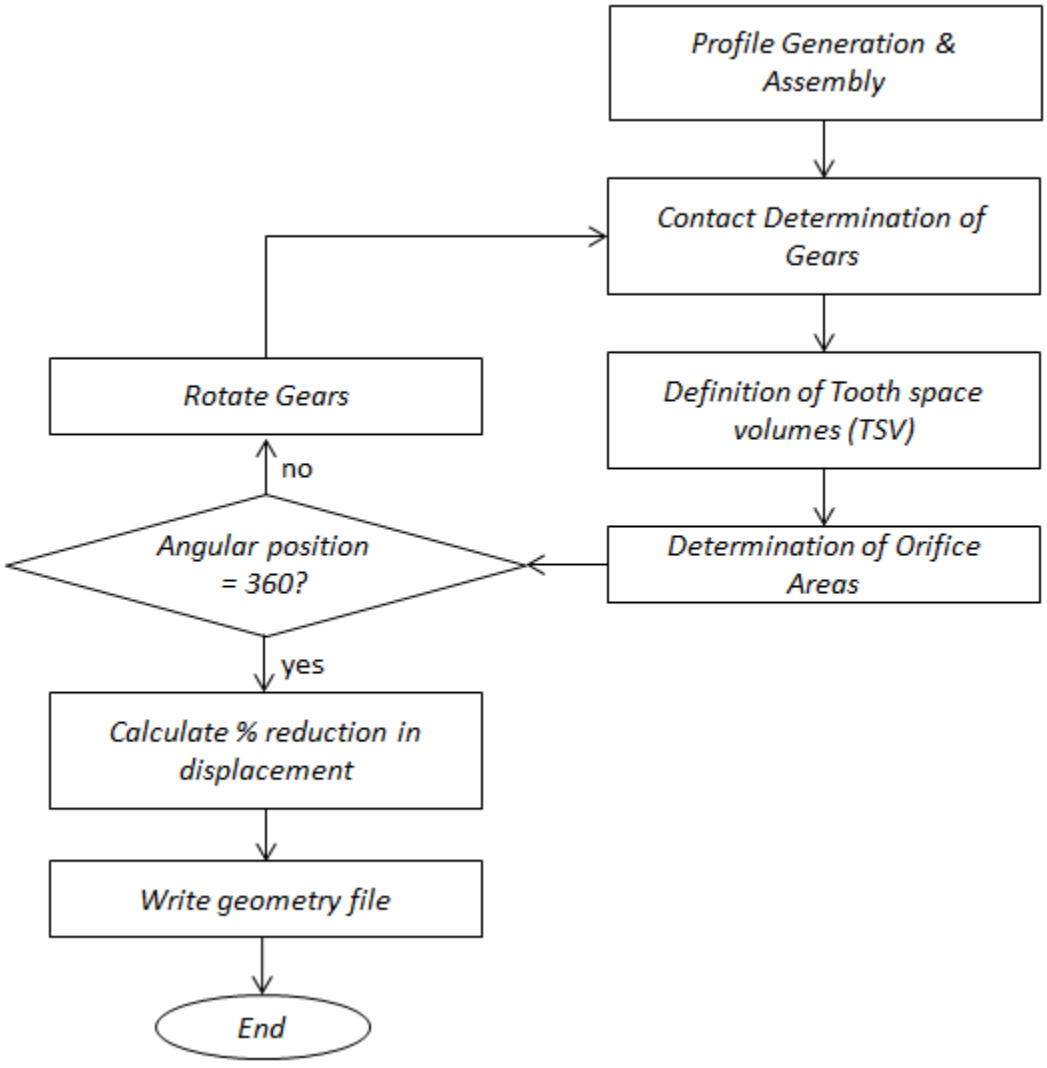

Figure 43: Flowchart for the geometrical model of HYGESim.

5.3.1. Profile Generation & Assembly

In this step, the different parts of the EGM are created within the model starting from:

1. design variables which govern the shapes of the gears and the grooves on the lateral bushings as described in the sections
2. CAD drawings of the parts (bearingblock, grooves – suction, delivery, high speed and half tooth of the gears) of the EGM in Stereo Lithography (STL) or text format. Representative inputs for a typical conventional EGM are shown in

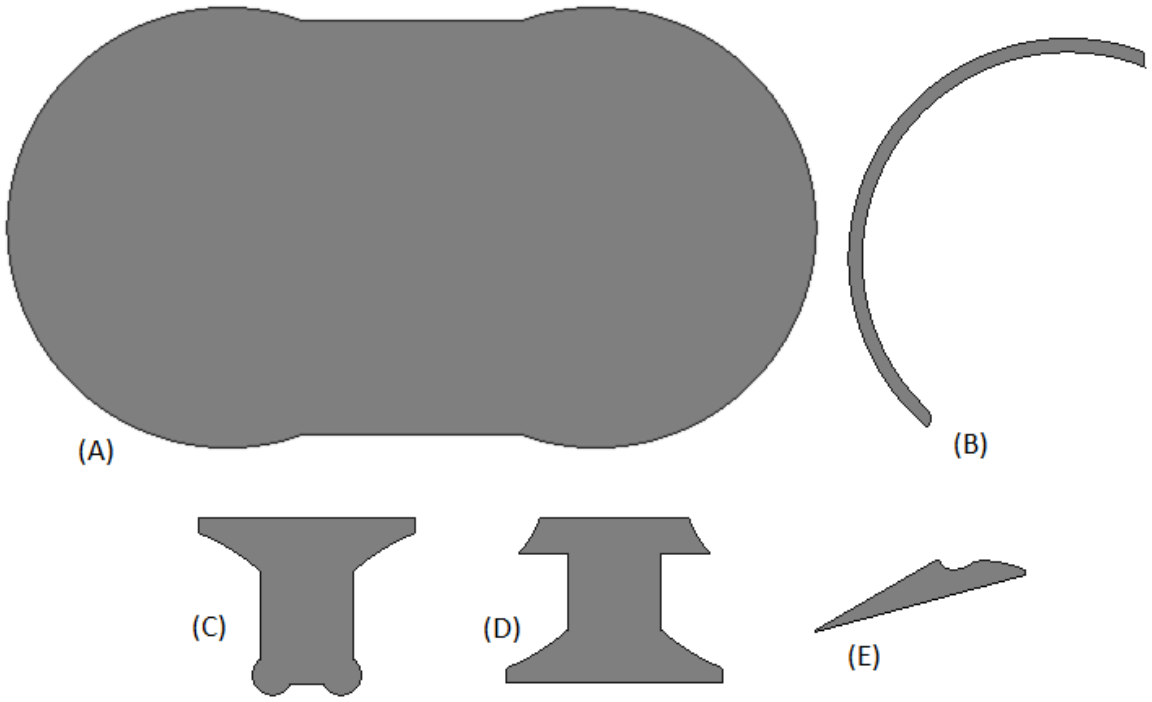

Figure 44: CAD inputs used by the geometrical model: (A) bearing block; (B) high speed groove; (C) delivery groove; (C) suction groove.

Having the capability of using both the approaches, described previously makes the geometry model robust enough for performing complex optimization.

The geometrical model also has an in-built STL file reader, which reads the complicated CAD drawings in STL format and transforms them into 2-D profiles which are constructed based on the X and Y coordinates of all the points based off of the STL files. This serves as a preprocessor for all the calculation of the different features for flow and forces. Since all the different parts of the lateral bushings exists as different entities. The

individual parts generated by the model need to be assembled back again carefully to replicate the real geometry of the bushings and the gears. Using simple translation and rotation techniques, the different grooves are positioned exactly at their precise locations.

The gears are generated from the tooth slice in case of a symmetric tooth, or from a tooth profile in case of an asymmetric tooth. Based on a controlled set of reflections, about the straight edges (which connect to the center) of the tooth or the slice the entire drive gear can be generated. The slave gear is obtained by moving the drive gear through a distance equal to the specified inter-axis distance. The translated gear profile is rotated by an,

$$angle = 180 - \frac{360}{(2 \cdot Z)}. \tag{5.25}$$

(where Z is the total number of teeth in one gear) to ensure that the drive and the slave gear are meshing with each other.

5.3.2. Contact Determination of Gears

To ensure that the drive and the slave gear are maintained in contact throughout the entire 360 degree of rotation, the model uses a contact finding algorithm specifically developed for identifying the point of contact between the gears as shown in Figure 45. Essentially the algorithm uses a set of rotations of the slave gear in the clock wise (CW) and counter clock wise (CCW) direction to ensure that the gears are in contact. Since the drive and slave gear profiles comprise of a closed profile of points in the X-Y plane, the contact is assumed to be achieved when both the closed profiles of the gears are intersecting with each other (as shown in figure 25(B)). The model uses, open source General Polygon Clipper (GPC) library for predicting the intersection of two closed profiles [72].

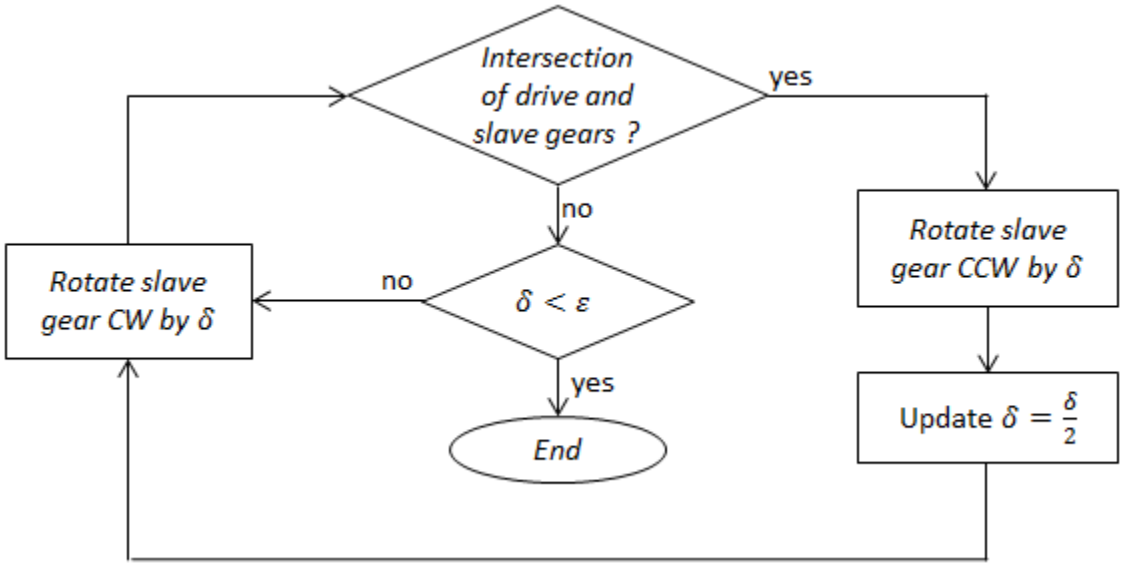

Figure 45: Contact determination algorithm.

As shown in Figure 46(A), there is no contact between the drive and the slave gear initially when the gears are positioned. The model checks if there is intersection between the profiles of the drive and the slave gear. If there is no intersection then the slave gear profile is rotated CW by an angle, δ, a small angle usually of the order of 0.1°. This rotation of the slave gear in CW direction continues until an intersection of the gear profiles is detected.

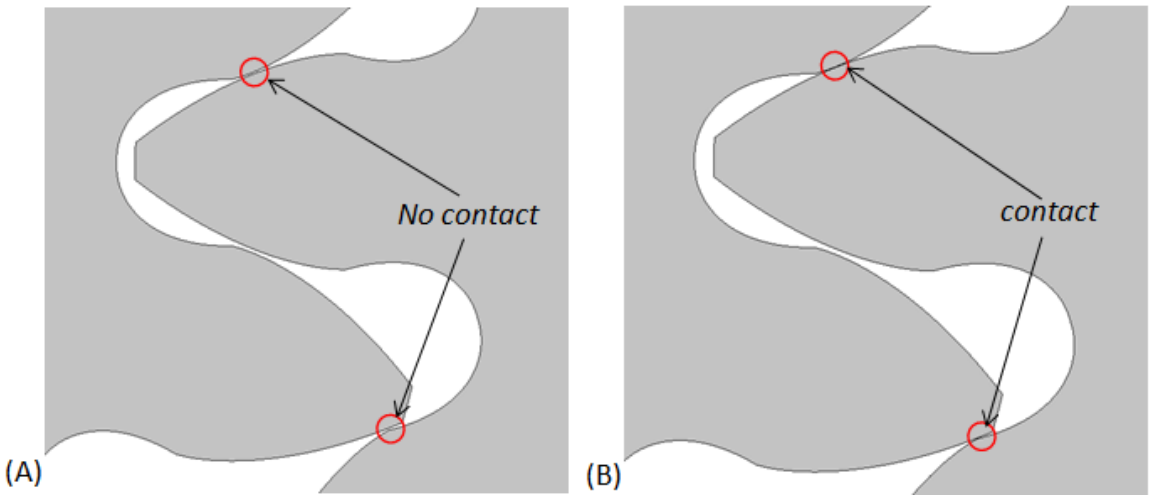

Figure 46: (A) Drive and slave gear without contact in the meshing zone; (B) Drive and slave gear with contact in the meshing zone.

Once an intersection is detected, the slave gear is rotated in the opposite (CCW) direction, by the same angle δ, so that the gears are not in contact any more. The angle δ is updated by dividing it by 2 as shown in Figure 45. The slave gear is rotated by the updated angle, δ in the CW direction to detect the intersection of the profiles again. This process continues until the angle δ reaches a very small value,ε, usually less than 0.05° for a starting angle δ of 0.1°. It is assumed that the contact occurs when the angular step reaches a value less than 0.0125° as shown in Figure 46 (B). In this manner the contact finding algorithm ensures that there is contact between the corresponding teeth of the drive and the slave gear throughout its one complete revolution.

5.3.3. Definition of Tooth Space Volumes

Due to the symmetry of the gears, the definition of the TSVs can be performed by only five slices (slices 0 through 4) of the gear as shown in Figure 47. The definition of TSVs and the orifices (LV1, LV2, HV1, HV2 and FG) are based on the shortest distance of the surfaces between the corresponding teeth profiles of the drive and slave gear profiles. With reference to Figure 47, and a particular angular position, the point of contact is obtained at point ‘A’ corresponding to the drive gear profile and point ‘F’ corresponding to the slave gear profile. The orifice connection FG between the drive and the slave gear TSVs in the meshing zone is represented by the shortest distance between the slice 2 of the drive gear and slice 2 of the slave gear. This connection is shown by the line BE in Figure 47. The drive TSV is defined as the profile with all the points of the drive gear between points ‘A’ and ‘B’ corresponding to the slices 1 and 2 (shown by the yellow curve on the drive gear), the line BE and all the points of the slave gear between points E and F corresponding to slices 2 and 1 (shown by the yellow curve on the slave gear). The drive TSV is depicted in red by a closed profile ABEFA. The connection LV2, between the slave TSV and the suction/low pressure port is determined by the shortest distance between the slice 3 of the drive and slice 3 of the slave gear as depicted by the line CD in Figure 47.

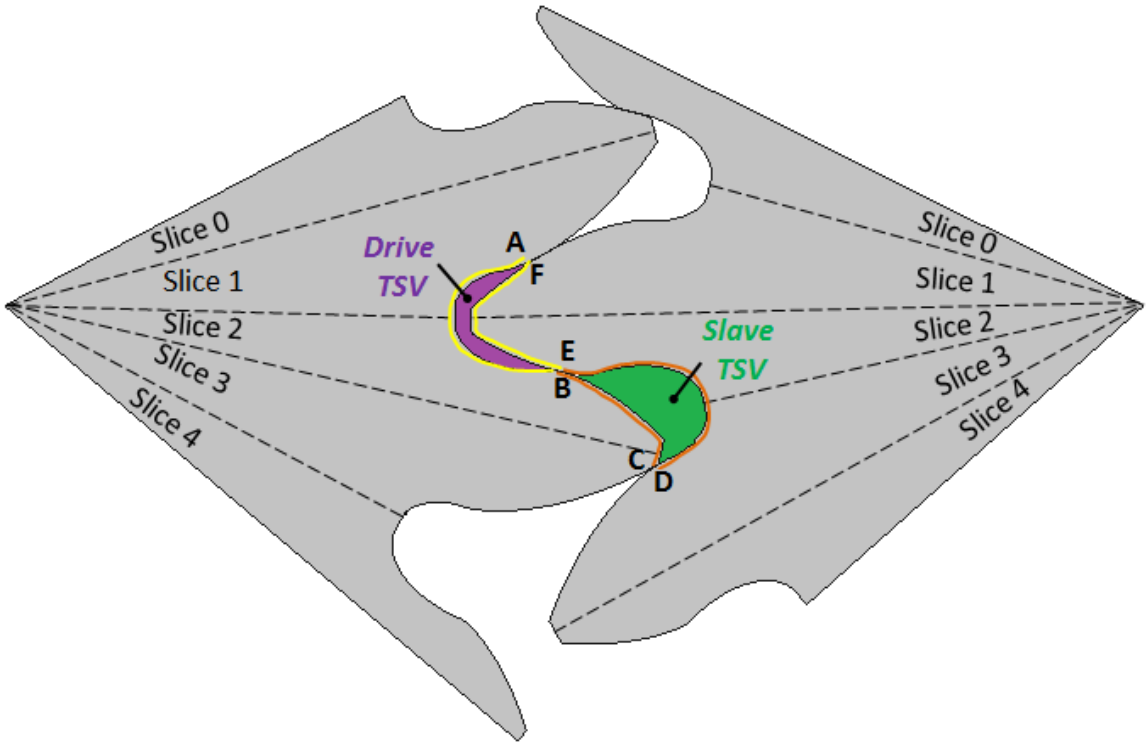

Figure 47: Definition of tooth space volumes.

The slave TSV is defined is a similar method as compared to the drive TSV. It is bounded by the two connections basically FG and LV2 in the meshing zone as depicted by the lines BE and CD. At the particular angular position shown in Figure 47, the slave TSV includes all the points of slice 2 and 3 of the drive gear between points 'B' and 'C' (shown by white curve on the drive gear), the line CD, all the points between 'D' and 'E' of slices 3 and 2 of the slave gear (shown by the white curve on the slave gear) and finally the line EB hence making a closed profile, BCDEB, as depicted in blue in Figure 47.

The TSV is obtained by the product of the profiles represented by ABEFA and BCDEB respectively for the drive and the slave gear with the face width of the gears. The area of these irregular shaped polygons is obtained by,

$$Enclosed\ area = \frac{1}{2}\sum_{i=1}^{n}(x_i y_{i+1} - x_{i+1} y_i), \tag{5.26}$$

where, the x and y co-ordinates of the points forming the polygon are represented by x_i and y_i respectively.

The propagation of the TSVs for an entire 360° operation is depicted in Figure 48(A). the TSVs increases since the gears are moving out of the meshing process, firstly the slave TSV reaches its maximum value as it is offset by an angle of 180/z° (where z is the number of teeth on a gear) with respect to the drive TSV. Eventually the drive TSV also reaches its maximum value and both of them remain at the maximum value until they start meshing again after around 300°. Therefore the TSV decreases again.

5.3.4. Determination of Orifice Areas

The connection FG which exists only during the meshing process is shown in Figure 48 (B), therefore the value of the area outside the meshing zone is equal to zero. The connections, LV and HV respectively represent the connection between the TSV with the suction and delivery through the facewidth of the gears as represented in Figure 48(C). With the TSVs defined accurately, the different orifice connections such as LG and HG which are the connections of the TSVs with the suction and the delivery grooves/recesses can be obtained by taking the intersection of the TSVs with the groove profiles as previously described in Figure 31 and Figure 32. The intersection of the delivery/outlet groove with the drive TSV is known as HG1, similarly the intersection of the delivery/outlet groove with the slave TSV is known as HG2 (Figure 48(D)). LG1 and LG2 are analogous to HG1 and HG2 except that the TSVs intersect with the inlet/suction groove (Figure 48(D)).

Similarly, all the different features for the calculation of flow through the machine are determined. The definition of TSVs is one of the important and which involves a lot of complexity. Once the TSVs have been defined accurately, the calculation of all the other features follows without much intricacy. The calculation of the different areas of projections needed to calculate the forces acting on the gears is as also performed in a similar manner as described previously in section 4.2.

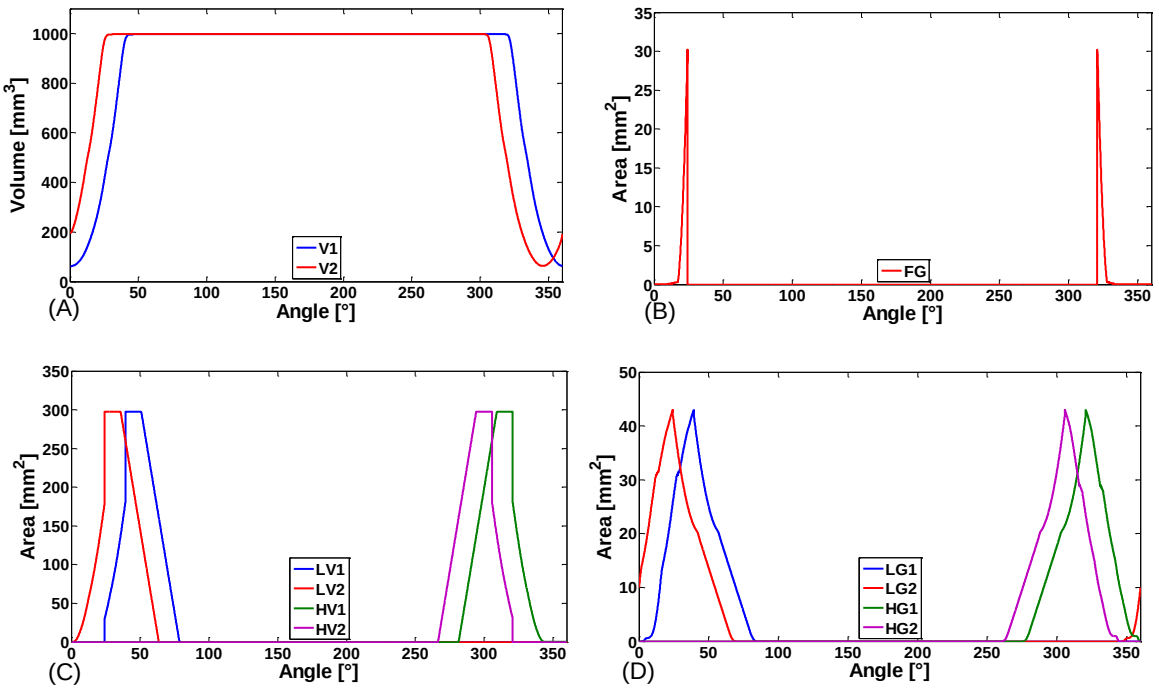

Figure 48: (A) Drive and slave TSVs (V1 and V2); (B) FG. (C) LV1, LV2, HV1, HV2; (D) LG1, LG2, HG1, HG2.

After the successful definition of the TSVs and the evaluation of the different orifice connections, the drive gear is rotated clockwise, and the slave gear is rotated counter-clockwise the procedure is repeated until one complete rotation of the gears is performed.

5.3.5. Calculation of Reduction in Displacement

With the information of the TSVs and the propagation of the contact points between the gears, it is now possible to calculate the maximum reduction in displacement, which can be achieved with the designed gear pair.

Due the asymmetric nature of the gears, the location of the points ‘D’ and ‘S’ (which represent the angular location when the TSV is trapped) are not symmetric about the point ‘M’ (angular location which the trapped TSV is at a minimum) unlike gears with symmetric involute teeth (as shown in Figure 49). It can be seen however that the angular range remains the same point ($\theta_{D2} - \theta_{S2} = \theta_{D1} - \theta_{S1}$) though the actual position at which these points occur differs as seen from Figure 49.

Since dual flank configuration is imposed on all the gears, in order to expand further the angular range of the trapped volume, both the drive TSV and slave TSV behave as

independent pumping chambers. Therefore, in order to maximize the full potential in achieving the reduction in displacement, the switch of the connection of the drive TSV from the delivery to suction should occur at point S1, and at point S2 for gear 2's TSV since both TSVs. The minimum displacement achievable from the drive TSV as a percentage can be expressed as,

$$\beta_{drive} = \frac{V_{S1}}{V_M} \tag{5.27}$$

Similarly, the minimum displacement achievable from the drive TSV as a percentage can be expressed as,

$$\beta_{slave} = \frac{V_{S2}}{V_M} \tag{5.28}$$

The resultant minimum displacement achievable is an average of the ones provided by drive and slave TSVs independently. Therefore, the minimum displacement achievable can be calculated using the expression in Eq. (5.28),

$$\beta_{resultant} = \frac{\beta_{drive} + \beta_{slave}}{2} = \frac{V_{S2} + V_{S1}}{2 \cdot V_M}. \tag{5.29}$$

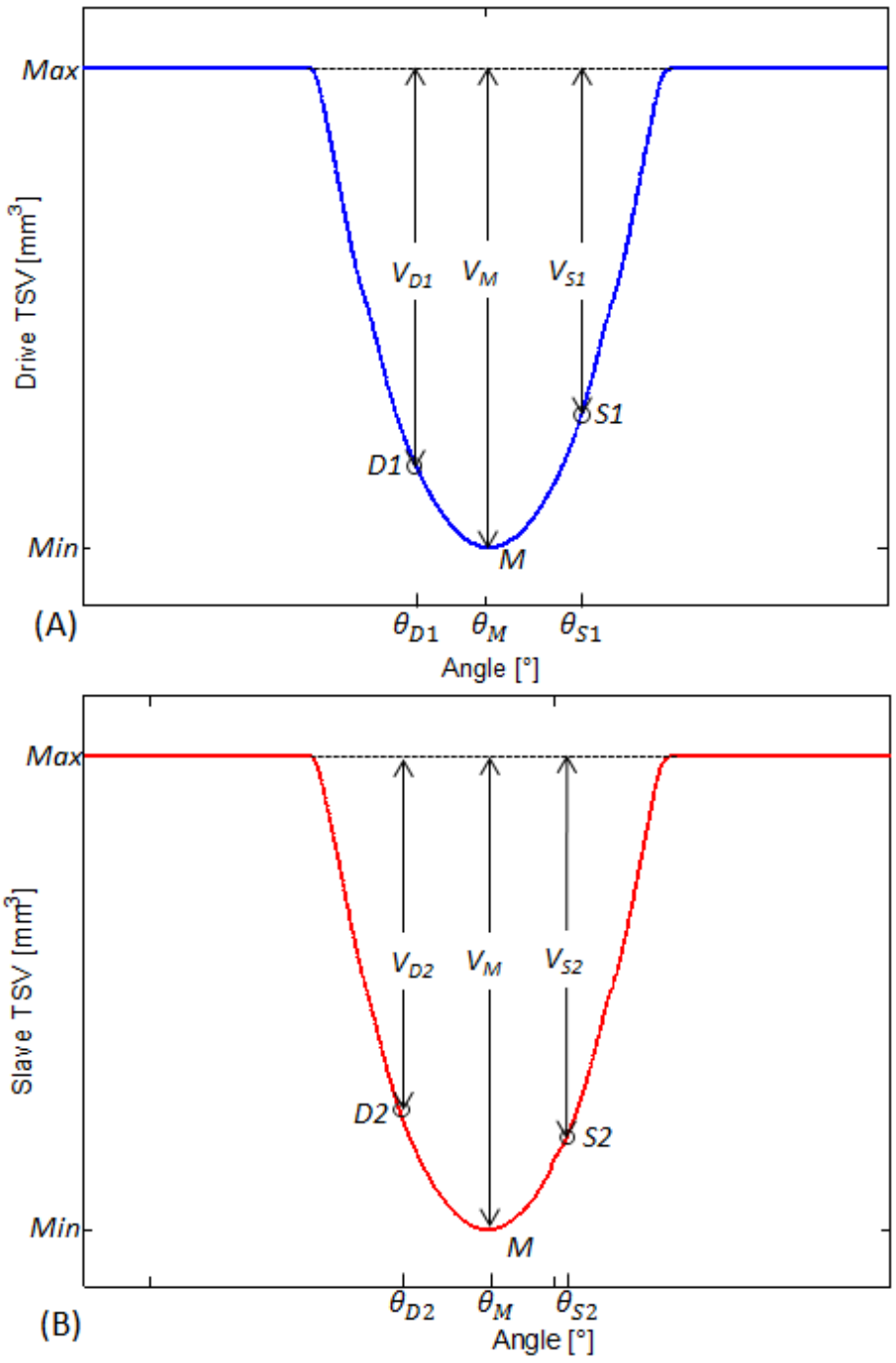

Figure 49: (A) Drive TSV for asymmetric gears; (B) Slave TSV for asymmetric gears.

6. OPTIMIZATION METHODOLOGY

Many problems of both practical and theoretical importance concern themselves with the choice of a "best" configuration or set of parameters to achieve a certain goal. The process of determining the "best" configuration is called optimization. Over the past few decades several hierarchies of such problems has emerged, together with a corresponding collection of techniques for their solution. In simple mathematical terms, optimization can be represented as,

$$Minimize: f(x), \tag{6.1}$$

$$Subject\ to: g_i(x) \geq 0, \quad i \in [1, n], \tag{6.2}$$

$$h_j(x) = 0, \quad j \in [1, p]. \tag{6.3}$$

where f(x) is the objective function which is intended to be minimized subject to the in-equality constraints represented by g(x) and equality constraints represented by h(x). The optimization process becomes easier if there is just one objective function. But the optimization process considered in this research considers five basic objective functions such as maximize reduction in displacement, maximize volumetric efficiency, minimize pressure ripple, minimize pressure overshoots and minimize local cavitation This makes it a multi-objective problem, with no definitive analytic functions readily available for these objective functions in terms of the design variables. Since there are no analytical functions available, conventional optimization methods like, linear programming, quadratic programming, golden-section search etc. cannot be used for the intended design process. Therefore, more complicated methods like genetic algorithms with response surfaces need to be used to determine the optimal design of the machine. Especially since the search space is complex, large and lacks proper understanding. However, genetic algorithm solves the problem providing multiple optimal solutions, from which a

particular design can be identified based on the requirements. But there is no absolute assurance that the genetic algorithm will find a global optimum. Therefore, the procedure should be simulated for a sufficiently long time to obtain results which are close to the global optima.

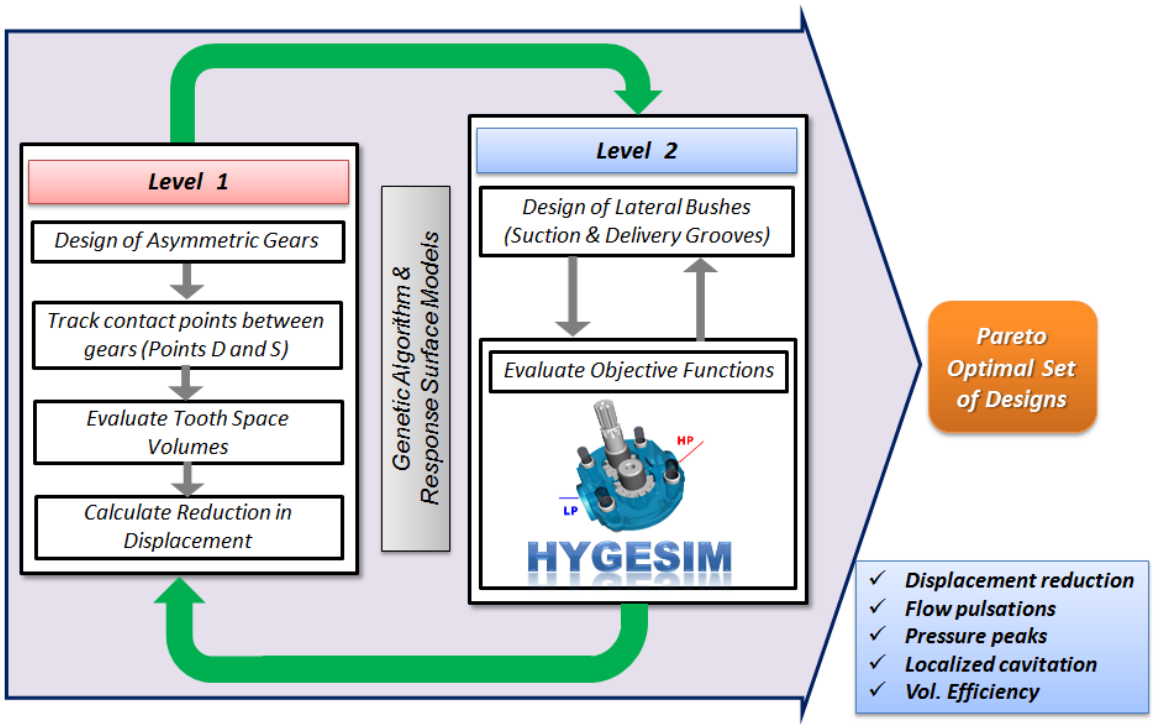

Figure 50: Schematic of the multi-level optimization process.

In this research the optimal design of the asymmetric gears along with their grooves is determined using a multi-level-multi-objective genetic algorithm based optimization process. A schematic of the complete optimization workflow is shown in Figure 50. As depicted in Figure 50, *Level 1* deals entirely with the design of asymmetric gears and *Level 2* deals with the optimization of the grooves in the lateral bushings. Due to the inherent inter-relationship existing between the design of the gears and the grooves, a design process considering an optimization within an optimization is of extreme importance and necessity. Once the gears are designed in *Level 1*, the contact points between the gear teeth are tracked throughout an entire evolution of the gears. Particularly, the location of the points D and S (defining the angular locations at which the fluid in the TSV is trapped between the contact points between the gears) is identified,

followed by the geometric evaluation of the progress of the TSV. Finally, the amount of displacement reduction that can be achieved with the design of the gears is evaluated based on the information on the points of contact and the progress of TSV.

Following the design of the gears, the optimization algorithm moves automatically into *Level 2*: entirely dedicated to the determination of the optimal design of the grooves for the particular gear designed in *Level 1*. In *Level 2*, the simulation tool HYGESim is used as a "virtual test rig" to evaluate the performance of the machine in a particular hydraulic test circuit required by the user. Post processing the results of HYGESim, yields the values of the different objective functions (as described in later parts of this section). Level 2, automatically performs enough number of iterations until an optimal design of the grooves is determined. The objective functions corresponding to the particular combination of the gears and the grooves is conveyed to Level 1 for enabling comparison with other gear designs also operating with their optimal groove counterparts. This procedure, thus enables the determination of the optimal design of the machine as a "whole". The described optimization procedure derives its motivation from [68],[69] however, mentioned works did not consider the evaluation of the reduction in displacement along with the other performance features. Also, they dealt only with the design of gears with symmetric involute profiles. Therefore, the optimization workflow represents a state-of-the-art method, for designing gears and grooves for the novel VD-EGM, starting from simple design parameters which control the model of the gears and the grooves.

The following sub-sections deal with the description of the optimization problem in terms of the objective function, design constraints etc.

6.1. Objective Functions

The performance of the machine is evaluated based on five important features: possible reduction in displacement, delivery flow pulsations, internal pressure overshoots, localized cavitation effects and volumetric efficiency. These objective functions depend greatly on the operating condition of the machine and serve as a criterion to understand

the performance variation between different design configurations of gears and lateral bushings.

6.1.1. Maximize Reduction in Displacement (OF_1)

As described in section 5.3.5, the minimum displacement that can be achieved from a specific gear design can be represented by, β. In order to maximize the reduction in displacement, the objective function can be expressed as,

$$Maximize: OF_1 = 1 - \beta_{resultant} \tag{6.4}$$

This objective function in turn will ensure that the angular range of trapped volume ($\theta_{D2} - \theta_{S2} = \theta_{D1} - \theta_{S1}$) is also maximized.

6.1.2. Minimize Delivery Flow Ripple (OF_2)

The fluctuation of the flow at the delivery is one of the major contributions to the fluid borne noise **Error! Reference source not found.**,[73],[74]. An estimate of the delivery flow pulsations can be taken as the peak to peak amplitude of the delivery flow ripple. But, a more accurate estimation of the pressure ripple can be derived from the energy possessed by the flow ripple signal. An evaluation of the energy of the flow can be evaluated by moving to a frequency domain which helps in determining the major harmonics which contribute to the fluid-borne-noise emission.

The flow ripple in frequency domain can be obtained by using the Fast Fourier Transform (FFT) of the signal in time domain. A representative delivery flow pulsation is shown in Figure 51 and the corresponding FFT is shown in Figure 52. An estimate of energy of the pressure ripple signal can be calculated using Parseval's identity, which can be applied to both continuous and discrete functions, which states that, energy contained in a waveform $L(t)$, integrated across all the sampling time, equals the total energy of the waveforms Fourier Transform $L(f)$. Mathematically, the total energy of the wave form, can be expressed as,

$$E = \sum_{k=1}^{N} \pi_k, \tag{6.5}$$

where,

$$\pi_k = \sum_{f_k-\Delta f}^{f_k+\Delta f} L(f)^2, \tag{6.6}$$

Where, N is the total number of fundamental harmonics of interest. π_k is the total energy of k^{th} fundamental frequency about a frequency resolution or an opportune interval, Δf and $L(f)$ is the FFT of the flow ripple signal.

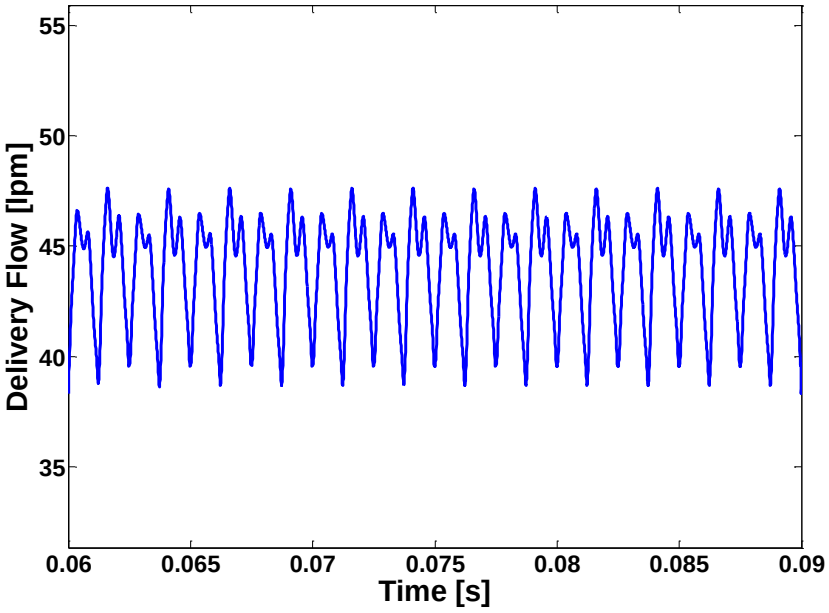

Figure 51: Simulated delivery flow ripple in time domain.

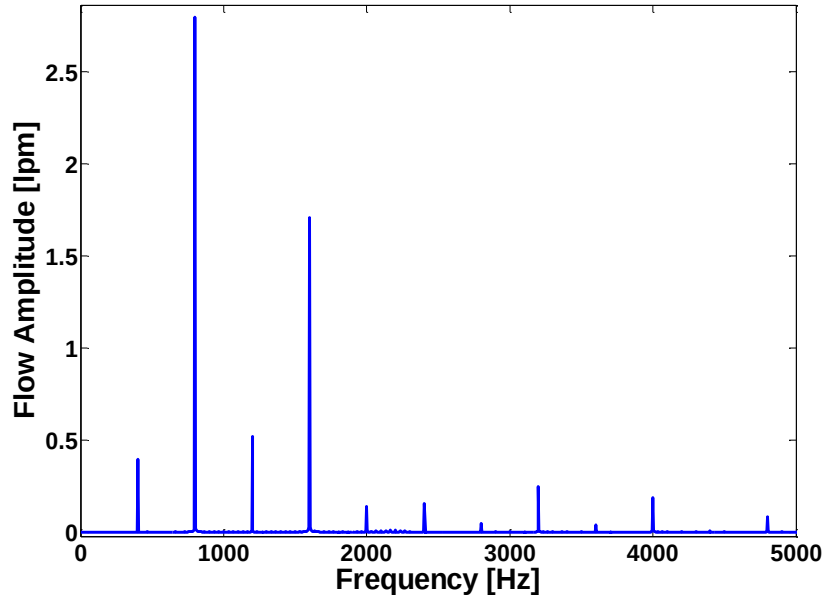

Figure 52: Simulate delivery flow ripple in frequency domain.

Therefore, the objective function for minimizing the flow ripple [68],[69] can be written as,

$$Minimize: OF_2 = E \tag{6.7}$$

6.1.3. Minimize Internal Pressure Peaks (OF_3)

During the meshing process of the gears, a certain amount of fluid is trapped between the points of contact between the two gears. In the initial phase of the meshing process this volume decreases and hence the pressure of the trapped fluid shoots to a very high value as shown in Figure 53.

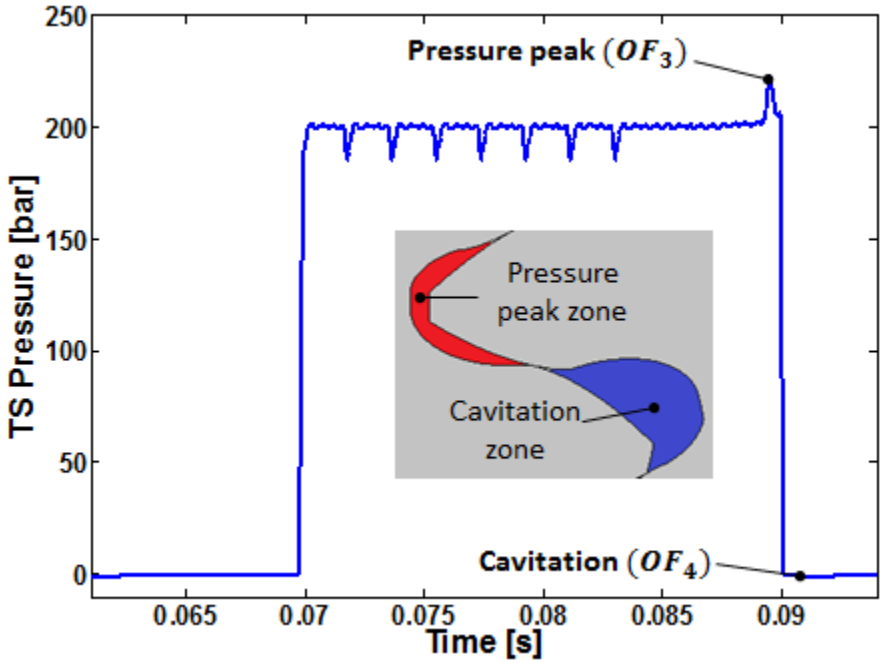

Figure 53: Tooth space pressure detailing the zones of internal pressure peaks and internal cavitation.

This phenomenon has been highlighted in Figure 53 where the pressure in the TSV of the gear reaches a high value. These pressure peaks in the meshing zone cause noise during the operation of the machine as well as they induce structural damage to the parts of the machine, if an optimal design of the grooves is not considered. OF_3 is expressed as a non-dimensional value [68],[69] given by,

$$Minimize: OF_3 = \frac{P_{TSV,peak} - P_{D,avg}}{P_{D,avg}} \tag{6.8}$$

Where, $P_{TSV,peak}$ is maximum pressure reached inside the TSV during the meshing process and $P_{D,avg}$ is the average delivery pressure of operation. Since, the pressure peaks inside the drive and slave TSV can be different, the calculation is applied for both the TSVs and the minimum of the both is taken as the objective function to be minimized.

6.1.4. Minimize Localized Cavitation (OF_4)

During the end of the meshing process, the fluid is still trapped between the contact points of the teeth but the TSV starts increasing. This leads to the pressure in the TSVs to fall below the saturation pressure of the fluid (as shown in Figure 53). This effect can also be reduced by using an optimal design of the grooves machined on the lateral bushings. OF_4 is expressed as the area of the tooth space pressure curve which falls below the saturation pressure of the fluid [68],[69].

$$Minimize: OF_4 = \int P_{TSV}\, d\theta\ , \qquad \forall\ P_{TSV} < P_{sat} \tag{6.9}$$

6.1.5. Maximize Volumetric Efficiency (OF_5)

The volumetric performance of the unit has to be maximized in the optimal design. While backflows and radial leakages are accurately evaluated, an evaluation of lateral leakages is made by assuming a constant gap height of the fluid film between the gears and the lateral bushes. For reducing the simulation time for the optimization process, the FSI model of HYGESim usually used to determine the axial balance of the EGM was not used, assuming a good balance of the design. However, once the optimal design of the machine is determined, the FSI model can be used to find the actual balance of the lateral bushings. The optimization algorithm in itself is very time consuming to analyze numerous designs, therefore, these assumptions made the process much faster. More details concerning the radial leakages evaluation can be found **Error! Reference source not found.**, while [63][64] report details about the evaluation of the axial leakages. The expression for OF_5 is given by,

$$Maximize: OF_5 = \eta_v = \frac{Q_{avg}}{n \cdot V_d} \tag{6.10}$$

Where, Q_{avg} is the mean flow provided by the machine at its delivery while operating at a speed of '*n'* rpm and V_d is the displacement of the machine.

The objective functions described in sections 6.1.2 through 6.1.5 are evaluated for both maximum and minimum displacement configurations of the pump at a representative operating condition.

6.2. Design Constraints

Due to the wide range of variability of the values of the design variables, designs of gears and bushings which are unfeasible or impractical could be generated by the optimization algorithm. To eliminate such designs, several constraints were identified to define the feasible design space. As already stated, in this work only gears with involute profiles are taken into consideration. The various constraints pertaining to the gear profile have been broadly classified into three different categories as: meshing constraints, failure constraints and geometrical constraints. The constraints for the design of the grooves in the lateral bushings are also discussed in the later parts of this section.

6.2.1. Meshing Constraints

Meshing constraints enable a pair of spur gears to be matched in such a way that there is smooth operation of the pump when the gears are meshing. Three different constraints which fall in this category are described below.

Contact ratio

The contact ratio between a pair of gears is one of the most important parameters which determine if there is a continuous and smooth transmission of power/force between the gears. In order to ensure the smooth transmission of forces between the gears, there should be at least one pair of teeth which is always in contact with each other (for load sharing) during the working of the machine [71]. Therefore the contact ratio for both the sides of the gears, (namely the drive and the coast) should always be greater than one (a thumb rule is to use this value as 1.1). Since the drive side of the gear tooth plays a more important role in transmission of forces compared to the coast side. It is ensured that the

drive side contact ratio is higher than that of the coast side. The expression for contact ratio for both the sides of the tooth can be written as,

$$\varepsilon = \frac{2 \cdot \sqrt{r_a^2 - r_b^2} - m \cdot z \cdot \sin\alpha}{\pi \cdot m \cdot \cos\alpha} > 1.1 \tag{6.11}$$

Interference

Interference is the phenomenon by which the involute portion of one gear digs into the flank of the other member of the pair. Particularly, the involute portion of one mating gear is meshing or intersecting with the fillet of the other gear as shown in figure 45. Thus resulting in the removal of involute portions of the gear near the base circle and hence weakening the teeth.

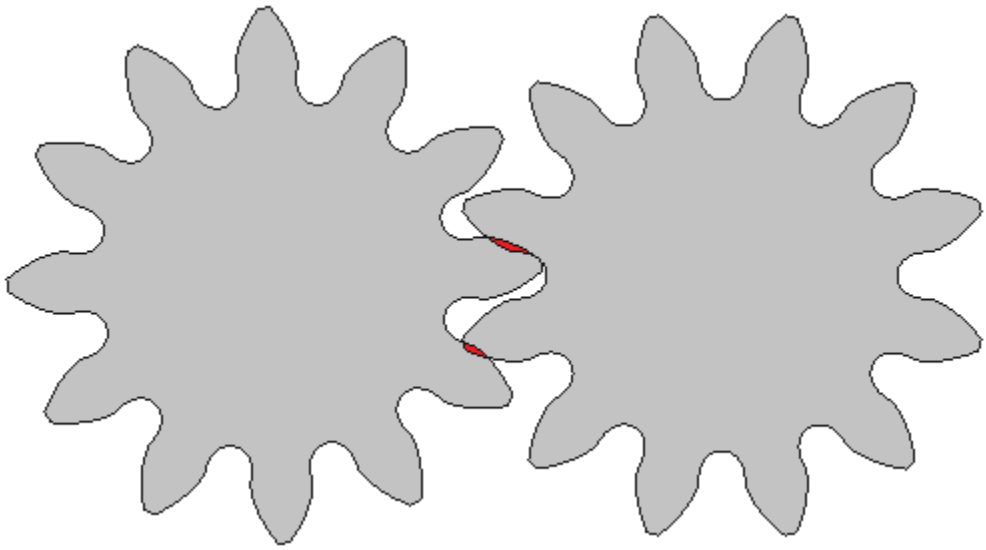

Figure 54: Gears meshing with interference (highlighted in red).

Since origin of involute tooth profile is the base circle of the gear, the active profile of the gear teeth is restricted to a comparatively small section of the involute curve in close proximity to its origin at the base circle. Also, the active profile of the involute gear is influenced, not only by its own proportions, but by the proportions of all the mating gears in the general case [75]. The gears will mesh freely when the point of contact between the meshing gears falls on the tip circle of the other gear member. But, interference occurs when the point of contact falls within the tip circle of the other gear member. Therefore, this serves as the limiting condition to prevent interference between the gears. Based on

the limiting case of interference when the tip circle of one gear is below the base circle of the other gear, the generic expression for this constraint for both the drive and coast sides of the teeth are derived as,

$$r_a^2 < r_b^2 + 4 \cdot r_0^2 \cdot \sin^2 \alpha \tag{6.12}$$

Tip-to-Root Clearance

The tip to root clearance is the clearance or the distance between the top land/tip of one gear and the root/bottom land of the other gear. If the inter-axis distance between the gears is not large enough then this clearance would be very small and hence the tip of one gear may dig into the bottom land of the other gear as shown in Figure 55.

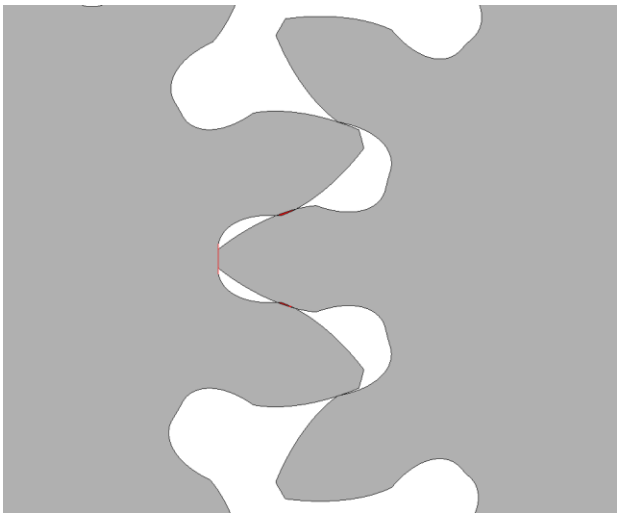

Figure 55: Gears with zero tip-to-root clearance thereby causing interference (highlighted in red) between the gears.

In order to prevent the extreme condition, the sum of the radii of the tip circle and the root circle should be less than the nominal inter-axis distance which is specified by twice the pitch radius of the gears. Therefore, the constraint can be written as,

$$r_o + r_r < 2 \cdot r. \tag{6.13}$$

Pointed Teeth

The *Pointed teeth* constraint restricts the optimization algorithm to generate gear designs which have very pointed tooth tips as shown in Figure 56. Hence this constraint prevents the wear and tear of the casing due to the sharp gears.

The expression for the preventing pointed teeth can be written as,

$$r_a \cdot \left(\frac{\pi}{z} + inv\ \alpha_d + inv\ \alpha_c - 2 \cdot inv\ \alpha_a\right) > 0.30 \tag{6.14}$$

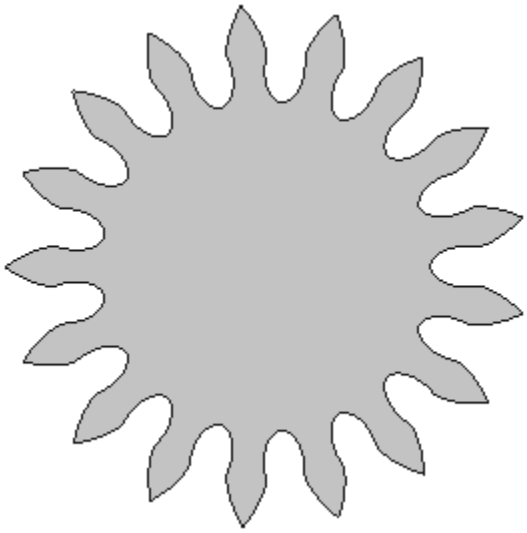

Figure 56: Gear with very sharp and pointed tooth tip.

6.2.2. Failure Constraints

In this section, specific constraints which relate to the strength and durability of the gears are considered. Bending failure and pitting of the teeth are the two main failure modes which can occur in an EGM as described briefly in this section.

Bending Stress

The bending stress in spur gears poses an interesting failure. When the loads are too large, bending failure may occur. Bending failure in gears is predicted by comparing the calculated bending stress to the maximum allowable stress values [76]

The bending stress number for a gear can be calculated as,

$$S_t = \frac{W_t \cdot K_a}{K_v} \cdot \frac{1.0}{b \cdot m} \cdot \frac{K_s \cdot K_m}{J}. \tag{6.15}$$

Where, S_t is the bending stress number (MPa), W_t is the maximum transmitted load (N), K_a is the application factor (a value of 1.15 for uniform application of load is used), K_s is the size factor (a value of 1.0 is used), K_m is the load distribution factor (a value of 1.1 corresponding to 95% facewidth contact at full torque is used), K_v is the dynamic factor

(a value of 1.0 is used), J is the geometry factor (a value of 0.30 is used), b is the facewidth of the gears, and m is the module of the gears. The values for the different factor correspond to those for bending stress number evaluation as described in [76].

The bending stress number,S_t, in Eq. (6.15) is related to the allowable bending stress number, S_{at} by,

$$S_t \leq \frac{S_{at} \cdot K_L}{K_T \cdot K_R}, \tag{6.16}$$

where, K_L is the life factor (a value of 0.90 corresponding to a large number of cycles is used) , K_T is the temperature factor (a value of 0.80 is used) and K_R is the reliability factor (a value of 0.70 corresponding to 99.99% success is used). The maximum value of the allowable bending stress for grade 1 steel with a Brinell hardness number of 170 is 206MPa [76].

Therefore, the constraint for bending stress can be expressed as Eq. (6.16), which checks the stress number for all the gears generated in the optimization process against a reference value, thus ensuring the non-failure of the generated gears due to bending.

Pitting Resistance

Pitting of the gear flanks are caused by alternating normal pressure on the contact surfaces of the teeth. It is found to occur most frequently at the pitch circle-where relative sliding of the teeth is zero, thereby causing high surface failure due to the removal of the material from the tooth surface due to the high contact stresses between the mating gears.

The expression for evaluating pitting resistance or surface durability of a gear tooth can be written as,

$$S_c = C_p \sqrt{\frac{W_t \cdot C_a}{C_v} \cdot \frac{C_s}{d \cdot b} \cdot \frac{C_m C_f}{I}}, \tag{6.17}$$

Where, S_c is the contact stress number (MPa), C_P is the elastic coefficient$(MPa)^{1/2}$, W_t is the maximum transmitted load (N), C_a is the application factor (a value of 1.15 for uniform application of load is used), C_s is the size factor (a value of 1.0 is used), C_m is the load distribution factor (a value of 1.1 corresponding to 95% facewidth contact at full

torque is used), C_f is the surface condition factor (a value of 1.0 is used), C_v is the dynamic factor (a value of 1.0 is used), d is operating pitch diameter (mm), b is the facewidth of the gears, and I is the geometry factor (a value of 0.30 is used). The values for the different factors correspond to those for contact stress number evaluation as described in [76]

The contact stress number, S_c is related to the allowable contact stress number, S_{sc} by,

$$S_c \leq S_{ac} \cdot \frac{C_L \cdot C_H}{C_T \cdot C_R}, \tag{6.18}$$

where, C_L is the life factor (a value of 0.90 corresponding to a large number of cycles is used), C_H is the hardness ratio (a value of 1 is used since both the gears are made of the same material with similar hardness number) factor , C_T is the temperature factor (a value of 0.80 is used) and C_R is the reliability factor (a value of 0.70 corresponding to 99.99% success is used). The maximum value of the allowable bending stress, S_{at} , for grade 1 steel with a Brinell hardness number of 170 is 206MPa [76].

Therefore, the constraint for pitting resistance or contact stress can be expressed as Eq. (6.18), which checks the stress number for all the gears generated in the optimization process against a reference value, thus ensuring the non-failure of the generated gears due pitting resistance.

6.2.3. Geometrical Constraints

The geometrical constraints ensure that the different calculated values based on the design variables are physically feasible.

The *Facewidth (b)* of the gears is calculated based on the displacement (V_d) of the machine which is assumed at the beginning of the optimization process. Since the gears considered are asymmetric, the displacement of the machine can be expressed as,

$$V_d = 2 \cdot \pi \cdot b \cdot \left(r_a^2 - r_0^2 \cdot \left(1 + \frac{\pi^2}{24 \cdot z^2} \cdot (\cos {\alpha_{0c}}^2 + \cos {\alpha_{0d}}^2) \right) \right). \tag{6.19}$$

The facewidth of the gears needs to be constrained in such a way that the gears generated are not severely disproportionate in terms of its aspect ratio. A restriction on the aspect ratio of the gears by limiting it between a minimum and maximum value as given by,

$$\left(\frac{b}{r}\right)_{MIN} \leq \left(\frac{b}{r}\right) \leq \left(\frac{b}{r}\right)_{MAX}, \tag{6.20}$$

will ensure that the gears are of the desired shape and size.

6.2.4. Constraints on Groove Design

The constraints for the grooves specifically ensure that both the grooves do not intersect with each other by ensuring the distance between the corresponding left and right wings of the delivery and suction grooves are above a certain minimum value.

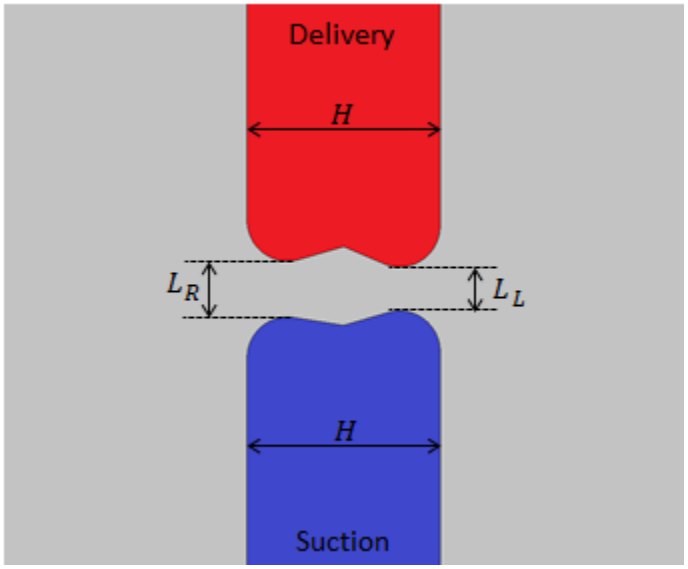

Figure 57: Zoomed in view of the grooves, detailing the minimum distance between the left and the right wings of the grooves.

The constraints of the minimum distances, L_R and L_L, ensure that the grooves are far enough, thereby preventing bypass flow of pressurized fluid from the high pressure region to the low pressure region.

The constraint for the grooves can be written as,

$$L_L : \frac{\pi \cdot m}{2}(\cos\alpha_{0d} + \cos\alpha_{0c}) - \left(\frac{r_a - r_r}{2}\right) \cdot (\tan\alpha_{DL} + \tan\alpha_{SL}) + \mathrm{S} + \mathrm{D} + \mathrm{R} > 0.60, \tag{6.21}$$

$$L_R: \frac{\pi \cdot m}{2}(\cos \alpha_{0d} + \cos \alpha_{0c}) - \left(\frac{r_a - r_r}{2}\right) \cdot (\tan \alpha_{DR} + \tan \alpha_{SR}) + \mathrm{S} + \mathrm{D} + \mathrm{R} > 0.60. \quad (6.22)$$

In order to reduce the number of design variables for the level 2 of optimization and hence improving the speed of the optimization, the horizontal length of the grooves is maintained to be constant as shown by,

$$H = r_a - r_r. \quad (6.23)$$

6.3. Optimization Strategies

One of the main features of this research is represented by the usage of a multi-level-multi-objective optimization algorithm. For the case of optimizing the design of the entire gear machine, the complexity in computation and computational time is large. Therefore, multi-objective optimization algorithms are required to face this demanding issue: to determine a satisfactory set of optimal design with relatively reduced number of evaluations. Response Surface Models (RSM) also known as metamodels help in tackling this situation by speeding up the optimization process. Previously evaluated designs can be used as a training set for building surrogate models: subsequently an inexpensive virtual optimization can be performed over these metamodels of the original problem. The candidate solutions determined at the end of the virtual optimization step are evaluated again by means of the real solver. This process can be iterated automatically, hence after every iteration, the newly evaluated designs enrich the training database, permitting more and more accurate models built adaptively. This entire procedure of using RSMs with a multi-objective algorithm is called fast optimizer. In this work, the optimization workflow has been implemented in modeFRONTIER® [77], a multi-objective optimization environment which allows the flexibility of integrating different softwares like HYGESim, MATLAB® etc. A detailed description of the fast optimizer used in this work is provided in this section.

6.3.1. Fast Optimizer

Fast optimizer uses metamodels to speed up the optimization process [77]. RSMs are implemented within the algorithm, in terms of performance on some validation points, for

virtual optimization. The so obtained virtual Pareto front is then validated (evaluated using HYGESim), obtaining some designs that iteration by iteration progress towards the real Pareto front. At each iteration the newly evaluated designs enrich the training database, permitting a more and more accurate RSM to be built in an adaptive and iterative way. The algorithm works on the analogy of a population of independent designs evolving through successive iterations (generations), like a genetic algorithm. Therefore, the total number of designs generated will be equal to the population size multiplied by the number of iterations.

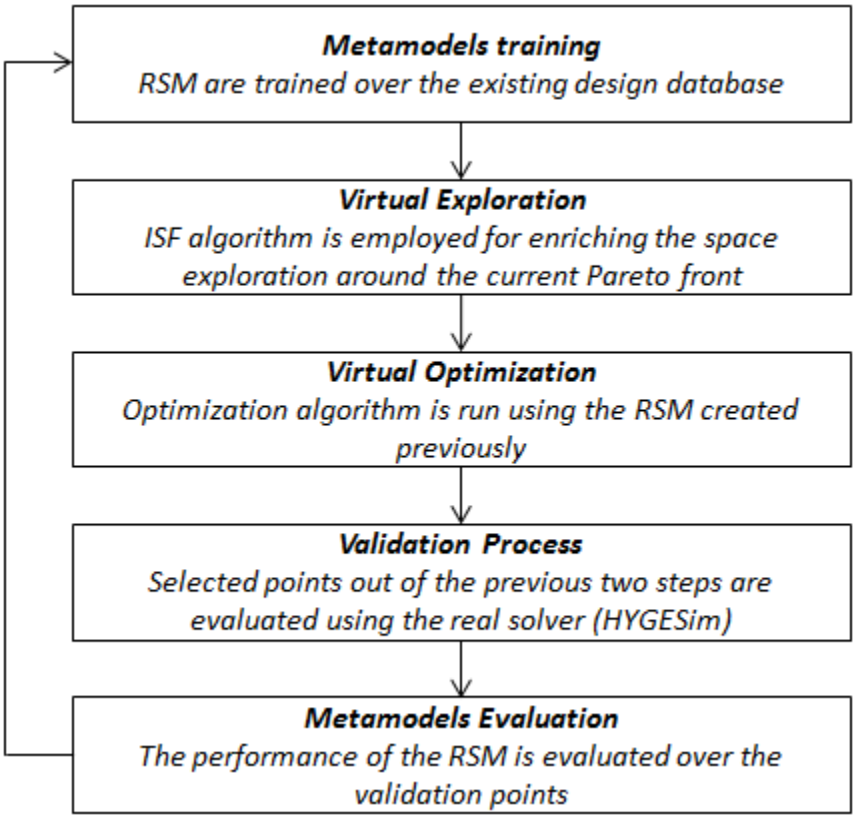

Figure 58: Steps followed in the Fast optimizer.

The virtual optimization is accompanied by a virtual run of the Incremental Space Filler (ISF) algorithm, for exploration purposes, thereby increasing the robustness of the optimizer. Hence for the validation process, the designs generated by the virtual optimization and virtual exploration steps become candidate points. For each objective function and for each design constraints a different RSM is trained for the virtual

optimization. In a nut shell, the different steps of the Fast Optimizer [77] have been depicted in Figure 58. A brief description of these steps is also provided.

6.3.1.1. Initialization

To train the metamodels, a set of designs which span the entire range of the design variables needs to be identified. Since the problem of optimizing the design of the gear machine involves a lot of constraints, specific designs needs to be selected which satisfy the constraints but still span the design space uniformly as much as possible. Therefore a uniform sampling of the design space is performed and particular care is taken to avoid clustering effects in the design chosen. In this way the initial set of designs are evaluated using, HYGESim (real solver) and post processing of the HYGESim simulation provides the actual value of the objective functions. With the help of this data, metamodels trained over the initial set of designs and hence would capture the behavior of the actual objective functions over the entire design space with a reasonable amount of accuracy.

6.3.1.2. Metamodels Training

The designs from the existing design table are used to create a new RSM at the end of every iteration. The particular RSM used in this research is Radial Basis Functions (RBF) [78], since they prove to be a powerful tool for multivariate scattered data interpolation. The design data in the designs table are not sampled at a regular gird; hence, the interpolating function should be able to be applicable for scattered data.

Radial Basis Functions

Given a training set of n points sampled from a functions, $f(x)$: $\mathbb{R}^d \rightarrow \mathbb{R}$,

$$f(X_i) = f_i\,, \quad i = 1, \dots, n. \tag{6.24}$$

A RBF interpolating function has the form,

$$s(X) = \sum_{j=1}^{n} c_j \cdot \phi\left(\frac{\|X - X_j\|}{\delta}\right). \tag{6.25}$$

Where, $\|.\|$ is the Euclidean norm in the d-dimensional space and δ a fixed scaling parameter. The radial function (or kernel) $\emptyset(r) : (0, +\infty) \rightarrow \mathbb{R}$ is assumed to be a multi-quadric function [39], which can be given by,

$$\emptyset(r) = \sqrt{1 + r^2}. \tag{6.26}$$

So the RBF interpolating function, *s*, is a linear combination of identical spherical symmetric functions, centered at the n different training/candidate points.

The coefficients, c_j represents the free parameters of the RBF model. Their values are obtained by imposing the interpolation equation,

$$s(X_i) = f(X_i) = f_i, \qquad \forall i = 1, \ldots, n. \tag{6.27}$$

By defining the symmetrical matrix *A*, the collocation matrix of the RBF as,

$$A_{ij} = \phi\left(\frac{\|X - X_j\|}{\delta}\right), \qquad i, j = 1, \ldots, n. \tag{6.28}$$

The interpolation equations can be represented as,

$$s(X_i) = \sum_{j=1}^{n} A_{ij} c_j = f_i, \qquad i, j = 1, \ldots, n. \tag{6.29}$$

In matrix form, the interpolating equations can be expressed as,

$$A \cdot c = f. \tag{6.30}$$

If the matrix, *A* is nonsingular, the unknown coefficients vector is obtained by inverting the linear system of equations, which can be represented as,

$$c = A^{-1} \cdot f. \tag{6.31}$$

However, a key point for obtaining a unique solution is the non-singularity of the matrix A, and it totally depends on the radial function chosen. For the multi quadric radial function, which is only conditionally positive definite, the RBF shown in Eq. (6.25) needs to be changed by the addition of polynomial terms to evaluate the corresponding interpolating functions.

A method for checking the goodness of an interpolating function is the leave-one-out methodology. In turn, each point belonging to the training set is excluded from the

training procedure. The value predicted in the excluded point by the so created surface is then compared to the known value. The leading idea is that the smaller this value on average, the better surface trained on the whole data set. On the other hand, this technique is computationally expensive, since n, different surfaces have to be created by using n-1 points, where n is the number of candidate points. However, this method needs to be used to get a good fit of the RSM. The minimization of the leave-one-out error criterion calculates the root mean square error at the point left out in turns and finds the particular fit which minimizes this error. This method is specifically used for determining the optimal value of the scaling parameter, δ. This value determines the shape of the radial function and it is strictly related to both approximation quality and numerical stability of RBF [77].

For the virtual optimization and exploration steps, the metamodel trained using RBF is used and the training is performed after every iteration in which more designs are added to the design table.

6.3.1.3. Virtual Exploration

An Incremental Space Filler (ISF) algorithm is used for enriching the database with designs lying in the region of interest, particularly around the current Pareto front. The purpose of the virtual exploration is to increase the robustness of the fast optimizer.

ISF is used for generating a uniform distribution of points in the design space. Particularly, this is an augmenting algorithm since it takes into consideration all the existing points in the design table previously generated and it adds new points in order to fill the space in a uniform way. A maxi-min criterion is used to add these points sequentially by maximizing the minimum distance of the existing points from these newly added points. The virtual exploration step can be imagined as adding new points within balls centered at the points belonging to the current Pareto front, with a specified radius. This zone radius is suitably related to a characteristic distance computed over the current Pareto designs. ISF is run in order to generate a sufficiently large number of possible candidate points. These designs are evaluated using the RSM created previously.

From the set of the virtual designs, the best fraction of, *m*, points are selected based on the function evaluations. These *m* points are used for the validation process [77].

6.3.1.4. Virtual Optimization

The exploitation stage is performed by means of the optimization algorithm run over the RSM previously created. Since the problem considers four objective functions simultaneously, the algorithm used in this research is Multi-Objective Genetic Algorithm (MOGA) [79],[80],[81],[82],[83]. Combining all the OFs in a suitable manner would optimize all of them simultaneously and it makes the process faster. The four objective functions are combined into a fitness function for the virtual optimization step as,

$$\begin{aligned} &minimize\ fitness \\ &= w_1 \cdot \left(\frac{OF_{1,max} - OF_1}{OF_{1,max}}\right) + w_2 \cdot \left(\frac{OF_2 - OF_{2,min}}{OF_{2min}}\right) + w_3 \\ &\cdot \left(\frac{OF_3 - OF_{3,min}}{OF_{3,min}}\right) + w_4 \cdot \left(\frac{OF_4 - OF_{4,min}}{OF_{4,min}}\right) + w_5 \\ &\cdot \left(\frac{OF_{5,max} - OF_5}{OF_{5,max}}\right), \end{aligned} \tag{6.32}$$

where, w_1, w_2, w_3, w_4 and w_5 are the weights corresponding to each objective functions. The sum of all weights should be equal to 1. In this research, the performance of the machine is assumed to be optimal when all the objective functions have been equally optimized, therefore all the weights equal to 0.20. $OF_{2,min}$, $OF_{3,min}$ and $OF_{4,min}$ are the minimum values which the corresponding objective functions can reach. These values were assumed to be a small number which would mean that, an objective function value close to the minimum value would represent an optimal performance. Similarly, a maximum value for OF_1 , $OF_{1,max}$ and for OF_4, $OF_{4,max}$ are chosen because, on contrary to the other OFs, OF_1 and OF_4 is supposed to be maximized and hence the maximum values in these cases are set to 1. In this way, all the OFs can be optimized simultaneously.

Since the performance of the machine with respect to the objective functions cannot be expressed in terms of the design variables, simple algorithms like, linear programming,

simples, sequential linear programming etc. cannot be applied for this research. Hence a more general and non-calculus based algorithm such as Genetic Algorithms need to be used.

Genetic Algorithm

Genetic algorithm (GA) is a programming technique that mimics biological evolution as a problem-solving strategy. Given a specific problem to solve, the input to the GA is a set of potential solutions to that problem, encoded in some fashion, and a metric called a fitness function that allows each candidate to be quantitatively evaluated. These candidates may be solutions already known to work, with the aim of the GA being to improve them, but more often they are generated at random [79],[80],[82].

The GA then evaluates each candidate according to the fitness function in a pool of randomly generated candidates. These promising candidates are kept and allowed to reproduce. Multiple copies are made of them, but the copies may not be perfect; random changes are introduced during the copying process. These digital offspring then go on to the next generation, forming a new pool of candidate solutions, and are subjected to a second round of fitness evaluation. Those candidate solutions which were worsened, or made no better, by the changes to their code are again deleted; but again, purely by chance, the random variations introduced into the population may have improved some individuals, making them into better, more complete or more efficient solutions to the problem at hand. Again these winning individuals are selected and copied over into the next generation with random changes, and the process repeats. The expectation is that the average fitness of the population will increase each round, and so by repeating this process for hundreds or thousands of rounds, very good solutions to the problem can be discovered [79],[80],[82].

Before a genetic algorithm is put to work on any optimization problem, a method is needed to encode the different design variables of the problem. The most common approach is to encode solutions as binary strings: sequences of 1’s and 0’s where the digit at each position represents the value of some aspect of the design variable. Binary coding is the most common procedure for encoding. Each variable is represented as a binary

string where the length of the string depends on the base (the number of allowed values for the variable). For example, if only integer values in the interval [0, 10] are to be allowed, there are 11 possible values; hence the base is set to 11. Thus the length of the string is equal to 4 and the variable can take values from [0000] to [1011]. Similarly, the coding is done for all the other design variables and they are attached end to end to form a huge chromosome. Therefore one design with a combination of different design variables is expressed as a single chromosome.

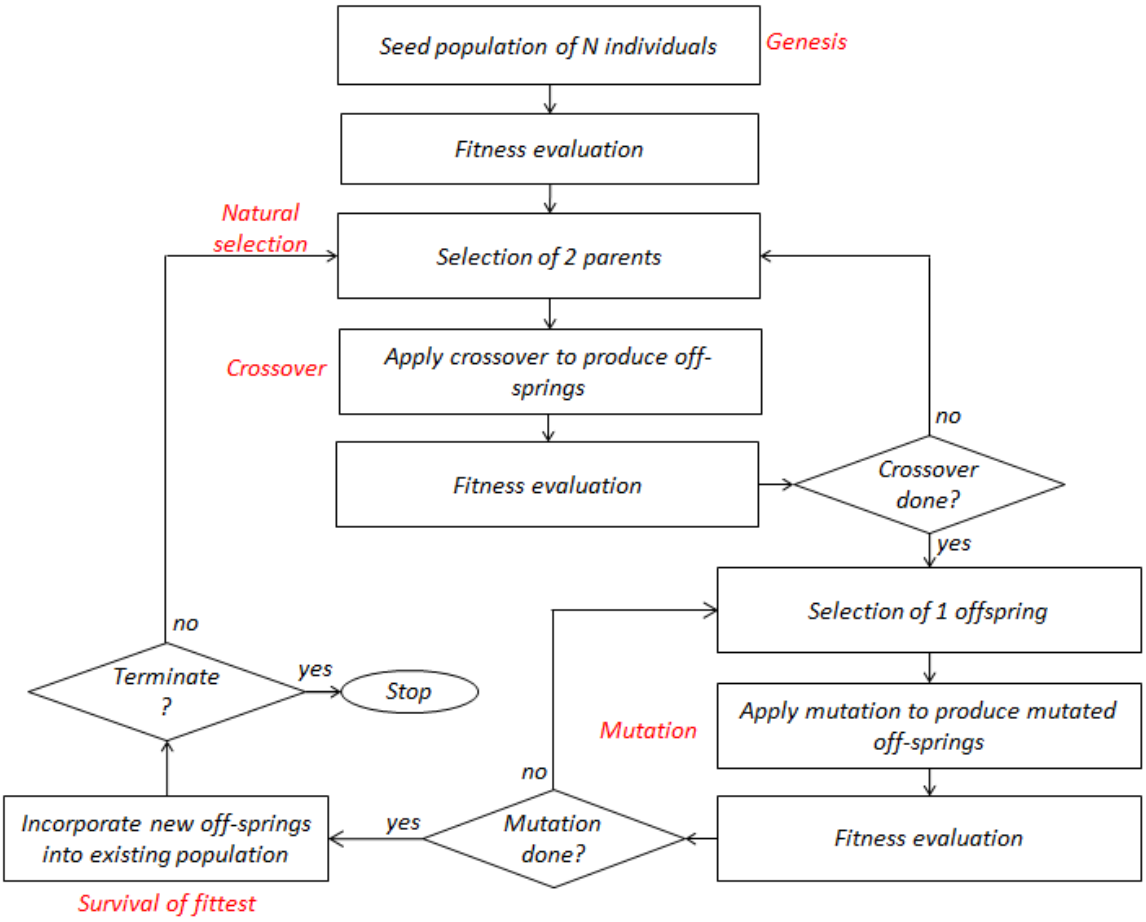

Figure 59: Flow chart for genetic algorithm.

Figure 59 represents the flowchart for genetic algorithms. There are three basic operators in genetic algorithms namely, *Selection*, *Crossover* and *Mutation* [79],[80],[82] as described as follows.

Starting from the random population of designs, the fitness of all the designs is evaluated. Based on the fitness, a new population is created using the three operators. Firstly, two parent chromosomes are *Selected*, from the parent population (better the fitness bigger the chance of being selected). It follows the "survival of the fittest" criterion to select the best parents to create a new off-spring. The fitness function quantifies the optimality of a chromosome so that a particular solution may be ranked against all the other solution [79],[80],[82].

Once two parents are successfully selected, they are mated by the *Crossover* operator. This operator combines two parent chromosomes to produce a new off-spring chromosome. The idea behind crossover is that the new chromosome may be better than both of the parents if it takes the best characteristics from each of the parents. Uniform crossover is used in this research, which based on a probability (usually 50%) decides which parent will contribute the gene values in the offspring chromosomes. Thus the chromosome operator allows the parent chromosomes to be mixed at the gene level rather than the segment level. Since the probability is 50%, half of the genes in the off-spring will be contributed by one parent and the other half by the other parent [79],[80],[82].

After a crossover is performed, mutation takes place. *Mutation* is a genetic operator used to maintain the genetic diversity from one generation of a population of chromosomes to the next. Usually, the mutation probability is set to a fairly low value of 1%. This operator alters one or more gene values in a chromosome from its initial state. This can result in entirely new gene values being added to the gene pool. With the new gene values, the GA may be able to arrive at better solutions than was previously possible. The mutation operator is an important part of the genetic search since, it helps preventing the population from stagnating at any local minima. Mutation is intended to prevent the search from falling into a local optimum of the design space.

The process of selection, crossover and mutation continues until an off-spring population with the same number of designs as the parent population is created. Based on the fitness values, duplicated designs are removed. At the end of the virtual optimization process, the best, m, designs are selected based on their fitness values for the next step.

6.3.1.5. Validation Process

In this step, *m*, candidate designs are selected out of the total of *2m* designs generated during both the virtual exploration and the virtual optimization stages. These designs represent the new population of the current iteration; therefore, they are evaluated using HYGESim and validated. These newly evaluated designs enrich the training database for the next iteration. They also form the validation set for evaluating the performance of the RSM [81],[82],[83].

6.3.1.6. Metamodels Evaluation

The designs which are validated in the validation process are used to evaluate the performance of the metamodel in the current iteration. The performance of the metamodel is expressed in terms of mean normalized error. The objective functions are normalized to their range of variation in order to avoid scale effects. The error is calculated as the difference between the value predicted by the metamodel and the actual value calculated by HYGESim. If the error appears to be an unreasonable value, the RSM model is adapted to accommodate more polynomial terms to account for the loss of accuracy. On the contrary if the metamodel is able to predict the values of the objective functions accurately, the training step of the algorithm is stopped to further speed up the optimization. However, if the performance of the RSM deteriorates, the training is performed again to obtain better metamodels which would predict the objective functions accurately [81],[82],[83].

7. SIMULATION RESULTS

In this chapter the results of the optimization process has been summarized. Particularly, the results have been categorized in two different sections. In the first section, the results are focused on the performance of an optimal design of a particular gear machine, particularly in terms of variable displacement. In this section, an effort is also made to numerically prove the reduction in torque considering a single TSV. In the second section, a separate optimization was performed to understand the potentials of EGMs with asymmetric gears particularly in terms of flow pulsations at the delivery. The design variables which were used for the optimization inclusive of their ranges and step sizes have already been discussed in Table 2 and Table 3 of Chapter 5.

7.1. Optimal Design for Variable Displacement

In this section the optimal design obtained at the end of the optimization process is presented. The optimal design was identified at the end of over 500 hours of computation (on a Dell® Precision T1600 workstation, with Intel® Xeon® processor). Several design configurations of gears and grooves were simulated in the autonomous design optimization process.

Around 900 gear designs were simulated with 60 grooves design each to determine the optimal design configuration. In order to ensure the possibility of testing the optimal design, the optimization was constrained in such a way that the gears generated will be able to fit inside the casing of commercial gear machine. Therefore, the facewidth, inter-axis distance (and hence the pitch diameter), and outer radius of the gears were constrained to that of the commercial gear pump with specification mentioned in Table 4.

Table 4: Specifications of the reference EGM, working fluid and materials for variable displacement.

Displacement of EGM	11.2 cc/rev
Number of teeth per gear	12
Maximum operating speed	3000 rpm
Maximum operating pressure	250 bar
Facewidth	17 mm
Pitch diameter	32.15 mm
Working Fluid	ISO VG 46 Hydraulic Oil
Density @ 50˚C, atmospheric pressure	851 kg/m^3
Viscosity @ 50˚C, atmospheric pressure	0.026 Pa-s
Lateral Bushings	Aluminum alloy
Gears	Steel

The optimal design of the gears which provided maximum reduction in displacement, while maintaining all the other performance parameters at an optimum is shown in the Table 5. It is observed that the optimal design chosen is capable of offering a remarkable range of variation of displacement for 100% (max) to 68% (min) [84].

Table 5: Design parameters for the optimal design of the gears.

Number of teeth	16
Module	2.01mm
Facewidth	17.0mm
Drive pressure angle	9.50˚
Coast pressure angle	5.00˚
Pitch diameter	32.15mm
Addendum diameter	38.34mm
Minor/root diameter	25.12mm
Drive base circle diameter	31.71mm
Coast base circle diameter	32.03mm
Maximum displacement	*11.90 cc/rev*
Minimum displacement	*8.09 cc/rev*
Minimum displacement (%)	*68*

The optimal design of the gears and the optimal grooves designs and the position of the slider in the lateral bushings for achieving maximum and minimum displacement are shown in Figure 60 [84].

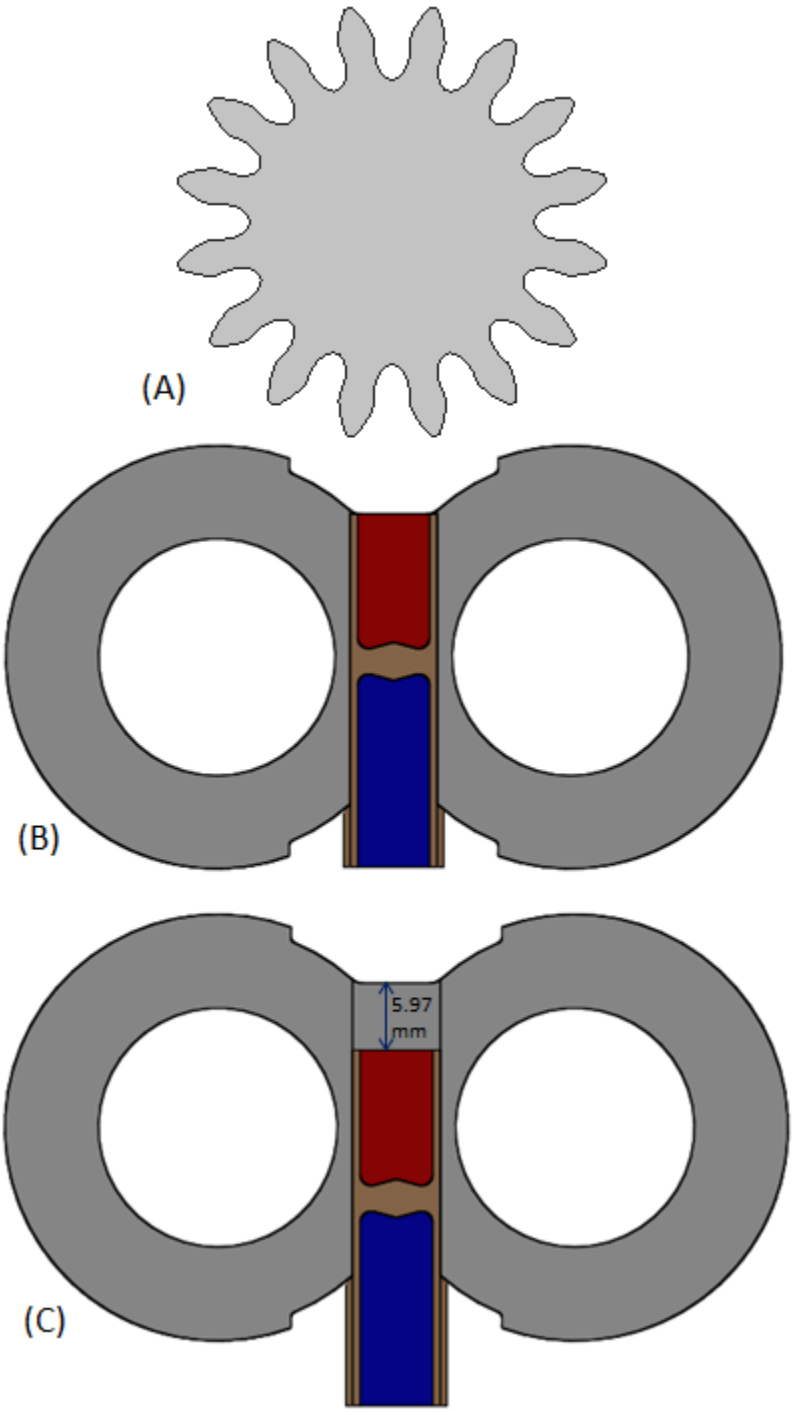

Figure 60: (A) Optimal design of the gears for variable displacement; (B) Optimal design of the grooves in the slider, with the slider positioned for achieving maximum displacement; (C) Optimal design of the grooves in the slider, with the slider positioned for achieving minimum displacement.

The values of the displacements were calculated using numerically using the geometrical model as explained in section 5.3.5. In order to have a validation of the evaluations made by the analytical expressions derived in section 3.2, Eqs. (3.67) and (3.73) need to be recalled. By substituting the geometric parameters pertaining to the gears (shown in Table 5) into Eq. (3.67) and Eq. (3.73), yields the following values,

$$V^{max} = 11.69\, {}^{cc}/_{rev}, \tag{7.1}$$

$$V^{min} = 8.01\, {}^{cc}/_{rev}. \tag{7.2}$$

Moreover, the minimum displacement can be expressed in a percentage format as,

$$\beta = \frac{V^{max}}{V^{min}} = 68.55\% \tag{7.3}$$

Comparing the values from Eqs. (7.1) – (7.3) with the values of maximum and minimum displacement from Table 5, it can be seen that the values predicted by the geometrical model is very similar to the ones predicted by the analytical equation and hence proving the validity of the equations and the model.

The design parameters governing the shape of the grooves in the lateral bushings are depicted in Table 6.

Table 6: Design parameters for the optimal design of grooves.

D	1.89mm
S	1.59mm
H	6.55mm
α_{DL}	15.0˚
α_{DR}	15.0˚
α_{SL}	15.0˚
α_{SR}	15.0˚

Detailed analyses of the optimal design were performed using HYGESim after the selection of the optimal design. Particularly, the different performance features such as the flow ripple, forces acting on the gears, input shaft torque required etc. were analyzed for several operating conditions as described below.

7.1.1. Delivery Flow

The simulated flow rates at the delivery for different operating conditions are represented in Figure 61 and Figure 62. It can be seen that the flow rate at reduced displacement has reduced proportionally (68%) to that at full displacement. This proves the concept that the VD-EGM is capable of providing lower flow rates at reduced displacement.

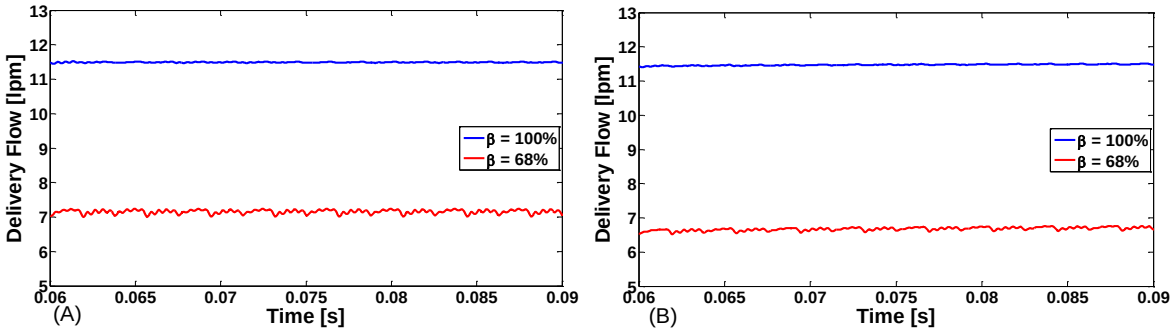

Figure 61: Delivery flow at maximum ($\beta = 100\%$) and minimum ($\beta = 68\%$) displacement for (A) 1000rpm, 100bar; (B) 1000rpm, 200bar.

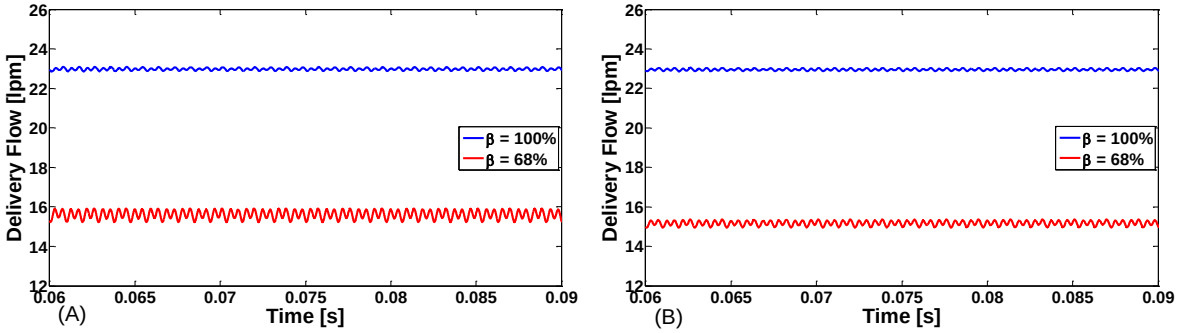

Figure 62: Delivery flow at maximum ($\beta = 100\%$) and minimum ($\beta = 68\%$) displacement for (A) 2000rpm, 100bar; (B) 2000rpm, 200bar.

Even though the design optimization process considered the performance at both max and min displacement, the flow oscillations at min displacement, ($\beta = 68\%$) is seen to be higher than that at max displacement for all the operating conditions. This difference in behavior was expected based on the analytical derivations which were made in Section 3.3, wherein a higher non-uniformity of flow rate was predicted analytically at min displacement.

7.1.2. Delivery Pressure Ripple

The simulated pressure ripple at the delivery for different operating conditions is represented in Figure 63 and Figure 64. The delivery pressure ripple greatly depends on the hydraulic circuit to which the pump is connected to. For the purpose of this study, it was assumed that the pump is connected to a steel pipe on one end and the other end of the pipe is connected to a variable orifice which controls the opening to regulate the pressure.

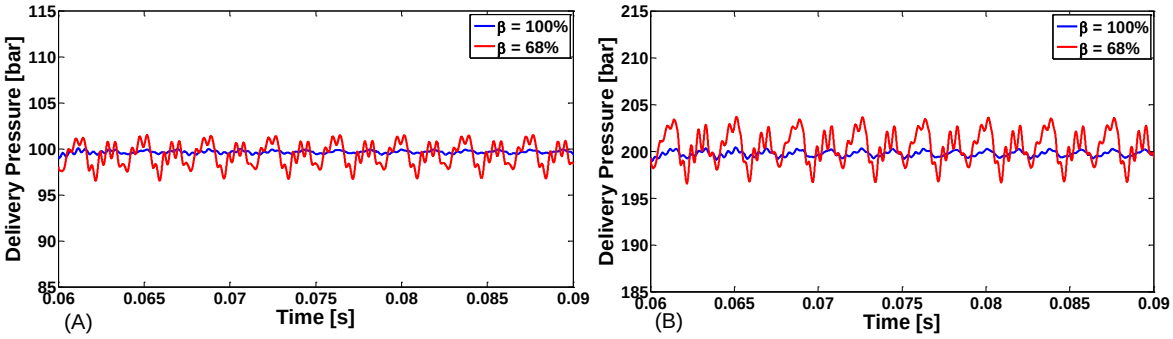

Figure 63: Delivery Pressure at maximum ($\beta = 100\%$) and minimum ($\beta = 68\%$) displacement for (A) 1000rpm, 100bar; (B) 1000rpm, 200bar.

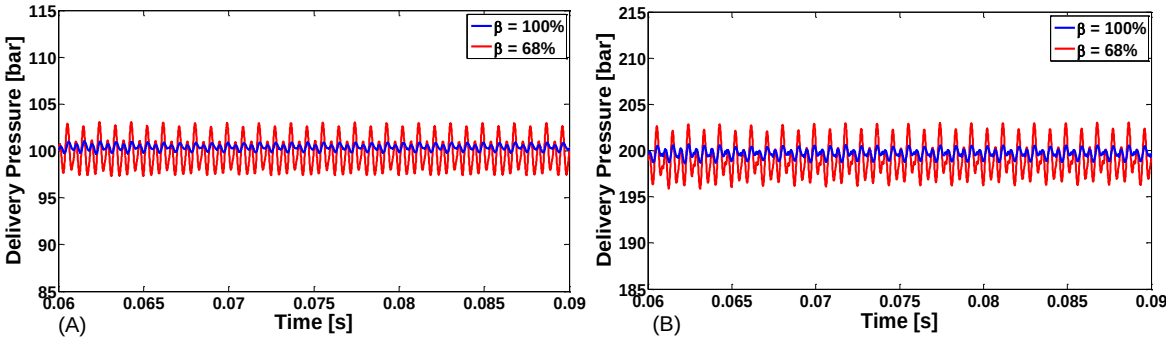

Figure 64: Delivery pressure at maximum ($\beta = 100\%$) and minimum ($\beta = 68\%$) displacement for (A) 2000rpm, 100bar; (B) 2000rpm, 200bar.

In general, the pressure ripple for min displacement is higher than that for full displacement, for similar reasons as explained for the case of delivery flow. It can be seen that the pressure ripple is higher for 1000 rpm than that for 2000rpm operating conditions, specifically because the optimization was performed considering only one operating condition – 2000rpm, 200bar (a representative condition to save on computational time).

7.1.3. Tooth Space Pressure

The drive tooth space pressures for different operating conditions are depicted in Figure 65 and Figure 66. The slave tooth space pressures for different operating conditions are depicted in Figure 67 and Figure 68.

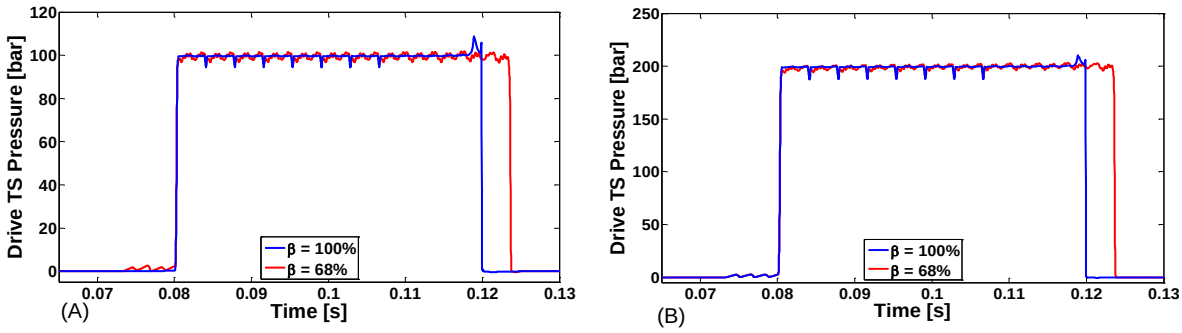

Figure 65: Drive tooth space pressure at maximum ($\beta = 100\%$) and minimum ($\beta = 68\%$) displacement for (A) 1000rpm, 100bar; (B) 1000rpm, 200bar.

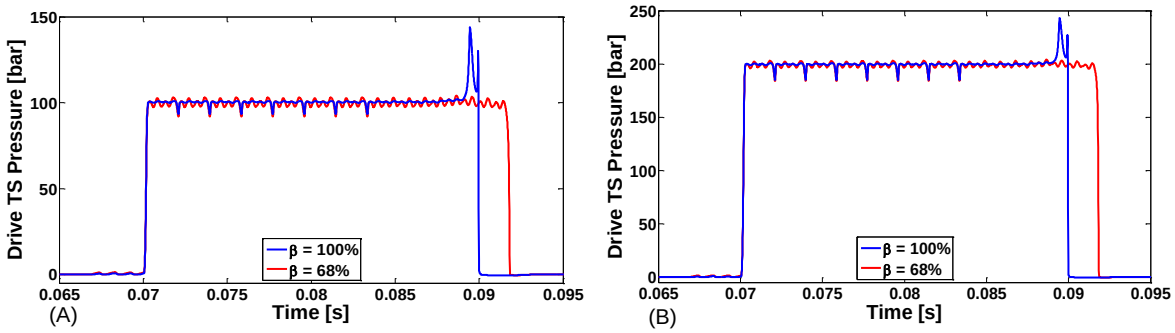

Figure 66: Drive tooth space pressure at maximum ($\beta = 100\%$) and minimum ($\beta = 68\%$) displacement for (A) 2000rpm, 100bar; (B) 2000rpm, 200bar.

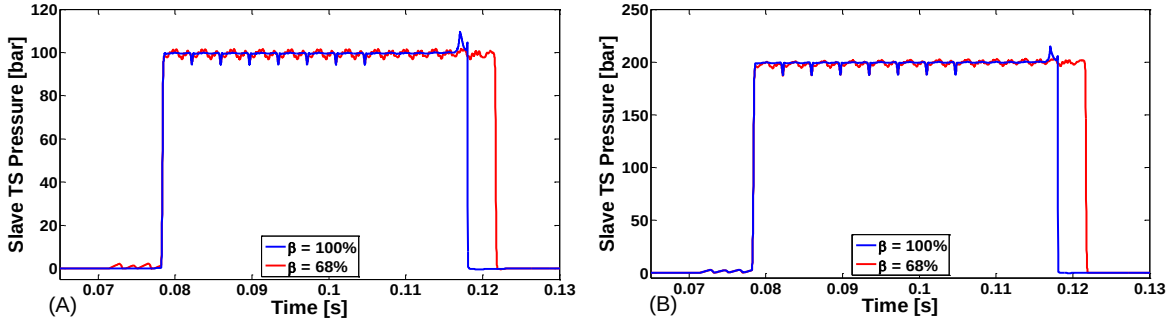

Figure 67: Slave tooth space pressure at maximum ($\beta = 100\%$) and minimum ($\beta = 68\%$) displacement for (A) 1000rpm, 100bar; (B) 1000rpm, 200bar.

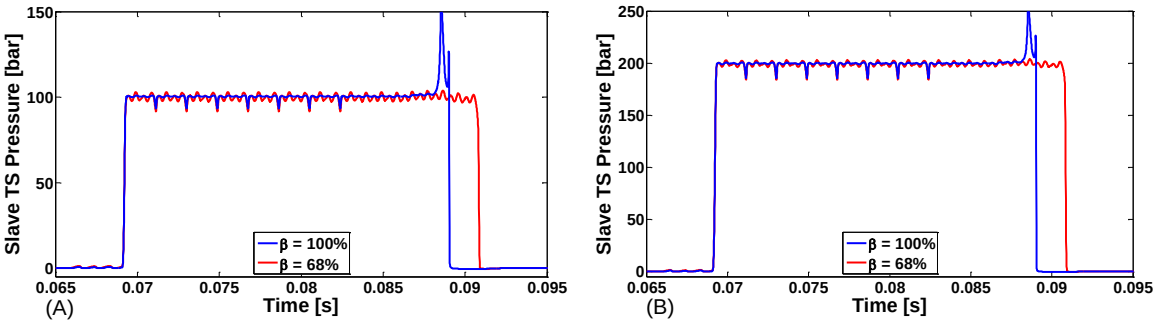

Figure 68: Slave tooth space pressure at maximum ($\beta = 100\%$) and minimum ($\beta = 68\%$) displacement for (A) 2000rpm, 100bar; (B) 2000rpm, 200bar.

It can be seen that for almost all the operating conditions considered, the pressure peak is very close to being negligible which proves that the design of the grooves is at an optimum. At 2000 rpm operating condition it is seen that there is higher pressure peak of about 50bars, but this value is still within acceptable values similar to those commercially available. As evidently visible from these figures, the tooth space pressure for min displacement ($\beta = 68\%$) extends for a larger time period as depicted by the red curves, because the TSVs are connected to the delivery/outlet groove for a larger time period to bring about a reduction in displacement

7.1.4. Detailed Analysis of Force and Torque Generation in the Proposed Concept for VD-EGM

In this section, an analysis of the resultant forces and hence the torque acting on the acting on the gears based on the pressure distribution on the gears is described. Particularly, it will be shown that the prolonged pressurization of the gears for min displacement conditions lead to reduction in input torque required.

In order to numerically understand the performance in terms of forces acting on the gears and input shaft torque required, a generic tooth space surface as represented in Figure 69 is considered. The instantaneous pressure force acting on a particular tooth space surface can be evaluated based on the previously calculated tooth space pressures. The tooth space surface is defined as the surface enveloped by adjacent teeth of a gear and bounded by the addendum circle of the gear as shown in Figure 69. Each tooth space surface is however, subdivided into three different sub-surfaces (as shown in Figure 69)

corresponding to the control volumes in the meshing zones defined by the fluid dynamic model of HYGESim [59]. Outside the meshing zone, the tooth space surface is acted upon by a single fluid control volume.

Assuming that pressures, p_1, p_2 and p_3 act on the sub-surfaces A_1, A_2 and A_3as shown in Figure 69, the pressure forces acting on the considered generic tooth space surface can be decomposed into its horizontal (x) and vertical (y) components. The projected areas required for the calculation of pressure forces in the x direction are represented as $A_{y,1}$, $A_{y,2}$ and $A_{y,3}$. Similarly, the projected areas required for the calculation of pressure forces in the y direction are represented as $A_{x,1}$, $A_{x,2}$ and $A_{x,3}$. For the calculation of the moment due to the pressure forces acting in the x and y direction, the distances from the center of the gear to the center of the projected areas are also necessary. The distances, y_1, y_2 and y_3 represent the distance of the forces acting in the x direction and the distances, x_1, x_2 and x_3 represent the distance of the forces acting in the y direction respectively. The plots of the different projected areas as well as the distance of the forces are shown in Figure 70 and Figure 71.

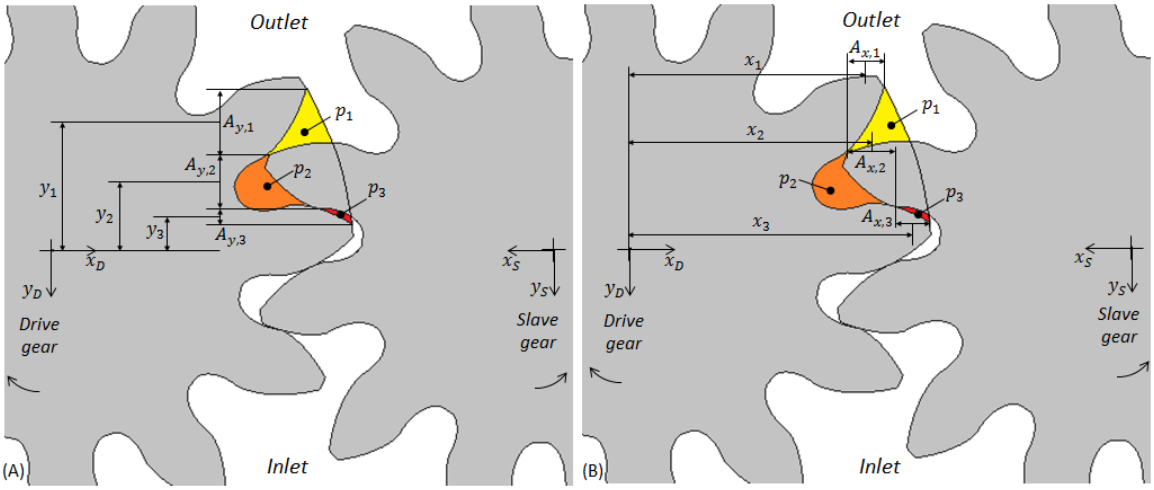

Figure 69: Subdivision of the tooth space surface between adjacent teeth on a gear. (A) Projected areas for calculation of forces along x direction; (B) Projected areas for calculation of forces along y direction.

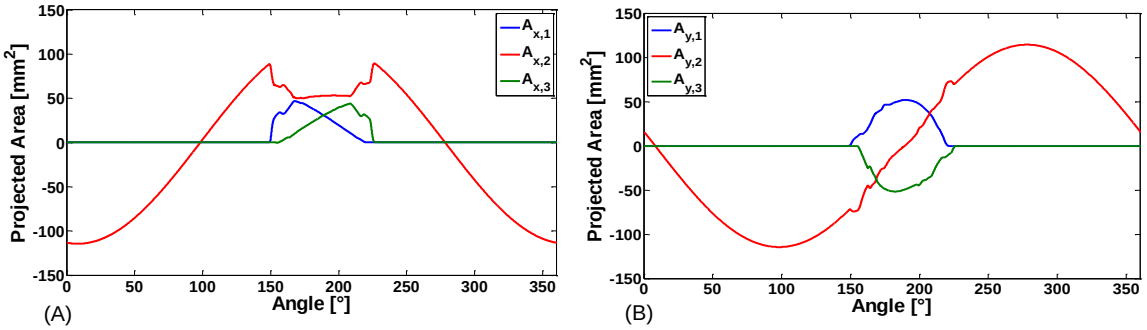

Figure 70: Plot of projected areas (considering a single TSV) for calculation of forces in (A) x-direction; (B) y-direction.

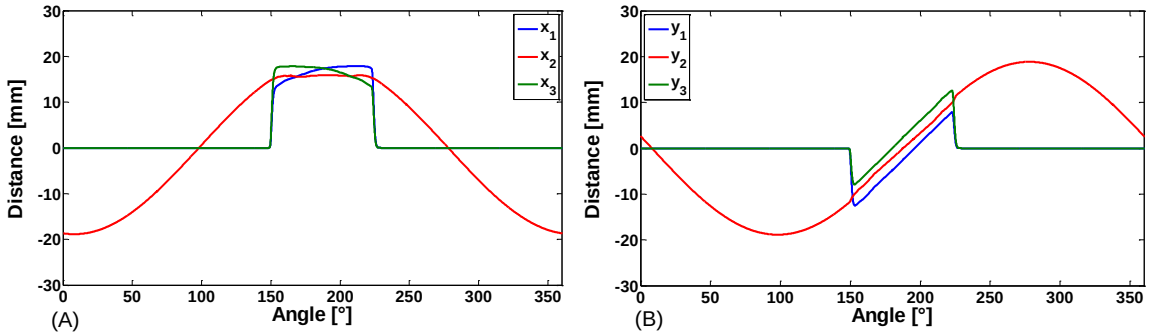

Figure 71: Plot of distances for calculation of moments due to forces in (A) x-direction; (B) y-direction.

The pressures acting in the sub-surfaces of the considered tooth space surface have been depicted in Figure 72, Figure 73 and Figure 74. It can be seen from these figures that the trends of the pressure remain the same, however the angular position at which the TSV transitions from high pressure to low pressure is different for p_1, p_2 and $p_3$both at max and min displacement.

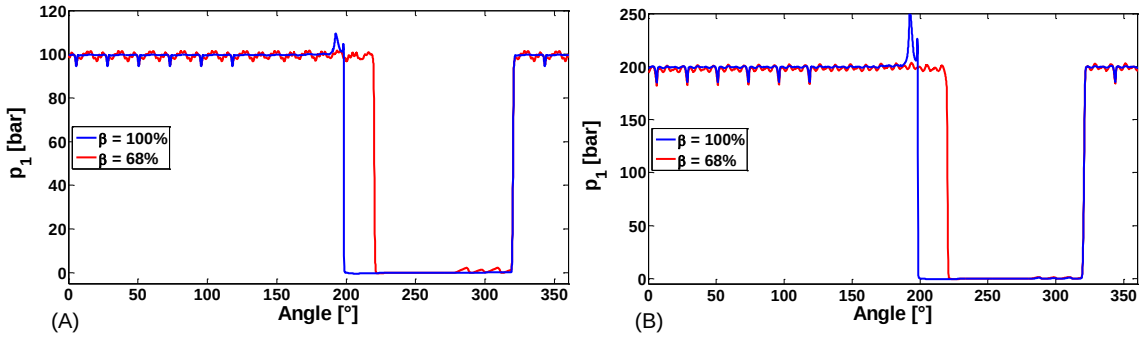

Figure 72: Pressure $p_1$for (A) 1000rpm 100bar; (B) 2000rpm 200bar.

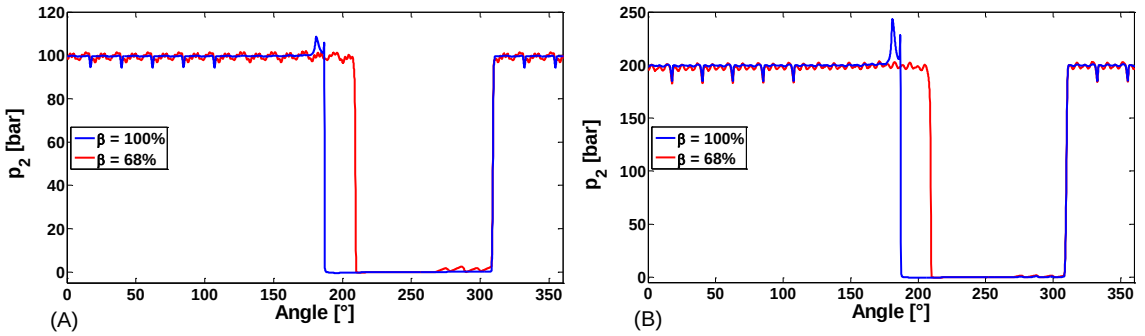

Figure 73: Pressure p_2 for (A) 1000rpm 100bar; (B) 2000rpm 200bar.

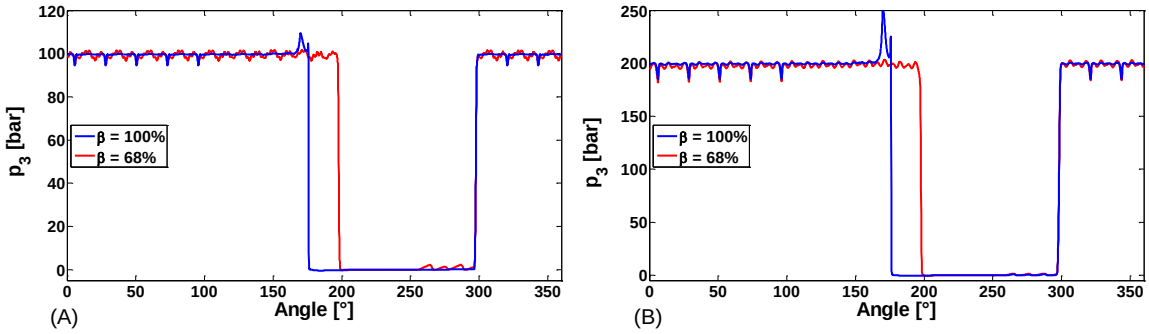

Figure 74: Pressure p_3 for (A) 1000rpm 100bar; (B) 2000rpm 200bar.

The tooth space force in the x and y direction can be written as,

$$F_x = p_1 \cdot A_{y,1} + p_2 \cdot A_{y,2} + p_3 \cdot A_{y,3}, \tag{7.4}$$

$$F_y = p_1 \cdot A_{x,1} + p_2 \cdot A_{x,2} + p_3 \cdot A_{x,3}. \tag{7.5}$$

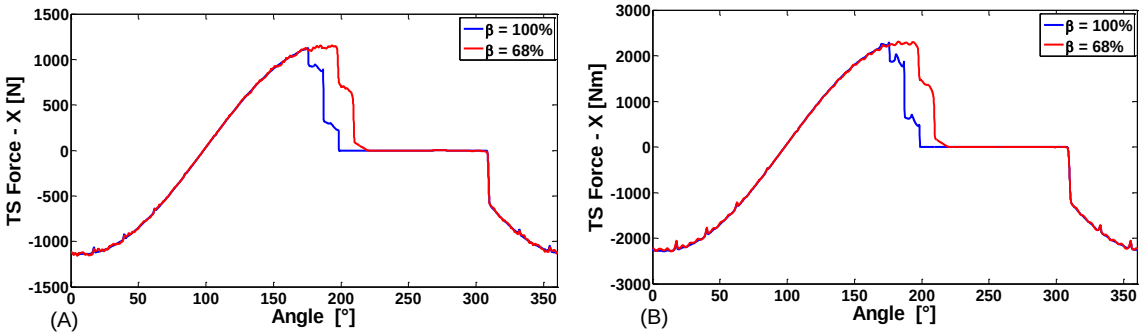

Figure 75: Tooth space force in the x direction for (A) 1000 rpm 100bar; (B) 2000rpm 200bar.

Therefore, for an entire 360° rotation of a tooth space surface F_x and F_y are calculated as shown in Figure 75 and Figure 76 for two different operating conditions. It can be clearly

seen from these figures, that there is difference between the forces at max and min displacement, due to the change in the pressure distribution obtained by the different positon of the slider.

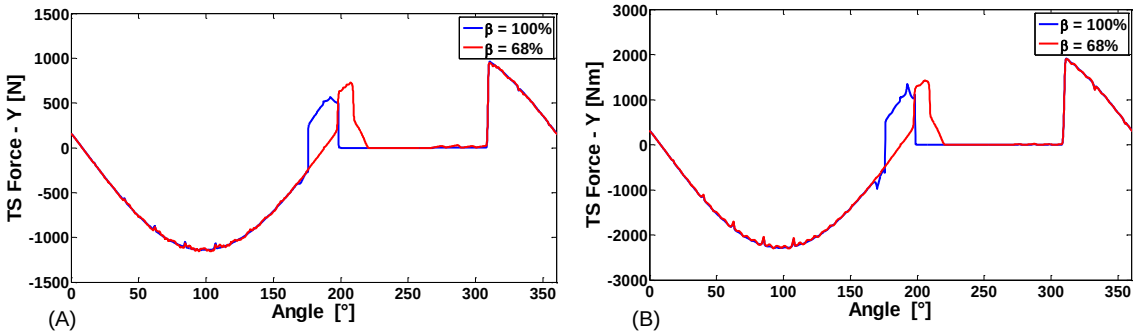

Figure 76: Tooth space force in the y direction for (A) 1000 rpm 100bar; (B) 2000rpm 200bar.

Neglecting the effect of forces acting on the tooth tip of the gears, the calculation of the moments due to the forces in x and y direction can be calculated using the expressions,

$$M_x = p_1 \cdot A_{y,1} \cdot x_1 + p_2 \cdot A_{y,2} \cdot x_1 + p_3 \cdot A_{y,3} \cdot x_1, \tag{7.6}$$

$$M_y = p_1 \cdot A_{x,1} \cdot y_1 + p_2 \cdot A_{x,2} \cdot y_2 + p_3 \cdot A_{x,3} \cdot y_3. \tag{7.7}$$

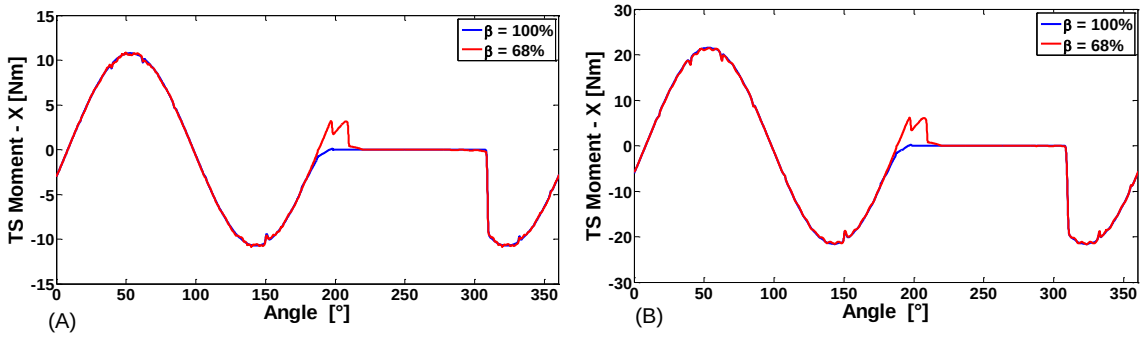

Figure 77: Tooth space moment due to force in the x direction for (A) 1000 rpm 100bar; (B) 2000rpm 200bar.

The calculations of the moments due to the forces in the x and y direction, acting on the considered tooth space surface are shown in Figure 77 and Figure 78 for two different operating conditions. Again, due to the change in the position of the slider from max to min displacement, there exists a difference in the moments.

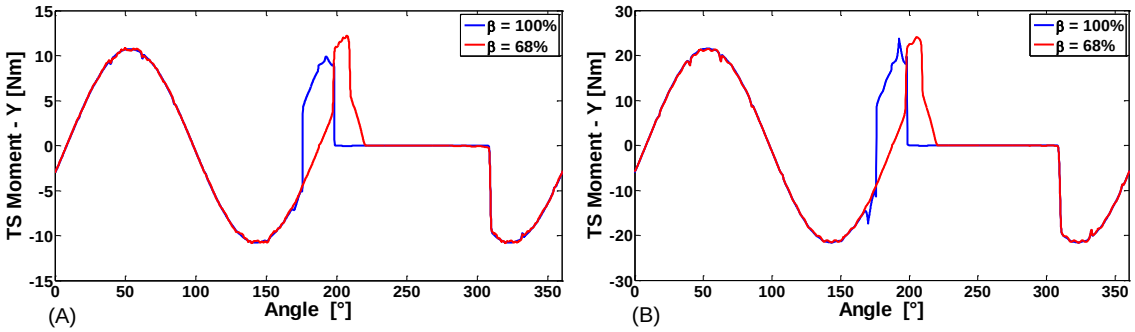

Figure 78: Tooth space moment due to force in the y direction for (A) 1000 rpm 100bar; (B) 2000rpm 200bar.

Since the moments, M_x and M_y act in opposite directions about the center of the considered gear, the moment/torque required to transfer the fluid in the considered TSV for a complete revolution of the gear can be written as,

$$M_{net} = M_y - M_x. \tag{7.8}$$

The net torque required for max and min displacement are shown in Figure 79 for two different operating conditions. It is evident from the figures that the area under the curve for min displacement is smaller than that at max displacement.

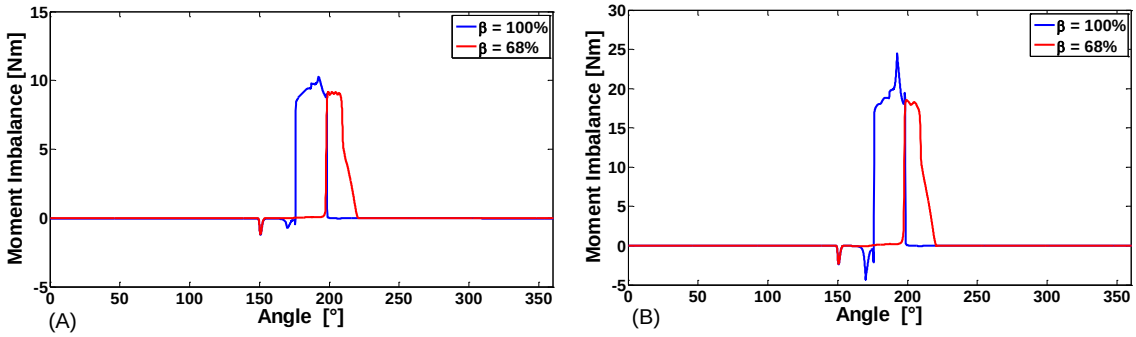

Figure 79: Moment imbalance for (A) 1000 rpm 100 bar; (B) 2000rpm 200bar.

In order to better understand the difference in torque, an estimate of the energy consumption can be made by calculating the area under the net torque curve.

The area under the net torque curve can be expressed as,

$$E = \int_0^{2\cdot\pi} M_{net} \cdot d\theta. \tag{7.9}$$

Table 7 shows the summary of the calculated estimates of energy using Eq. (7.9). As can be seen from the ratio of the estimates, for 1000rpm 100bar case, the model predicts that at min displacement it consumes only 68% of the energy at max displacement. However, for 2000rpm 200bar case, there is an every further reduction in the energy consumption; this is due to the fact that there is a higher pressure peak (as compared to a negligible peak for 1000rpm 100bar case) in the tooth spaces during the meshing zone as can be seen from Figure 72 through Figure 74. Hence, numerically it has been proved that at min displacement there is reduction of torque and hence energy while considering a single tooth space surface.

Table 7: Summary of the estimate of energy consumption for max and min displacement.

Operating Condition	E_{max}	E_{min}	$\frac{E_{min}}{E_{max}}$
1000 rpm 100bar	193.25	132.66	0.68
2000 rpm 200bar	410.02	266.70	0.65

By symmetry the analysis can be extended to consider all the tooth spaces in both the gears and hence a holistic picture of the forces and the torque acting on a gear can be studied. The information has been directly captured from HYGESim simulations performed at multiple operating conditions.

The horizontal component of the total pressure force acting on the drive gear is depicted in Figure 80 and Figure 81. Similarly, horizontal component of the total pressure force acting on the slave gear is depicted in Figure 82 and Figure 83. It can be seen that at all the operating conditions, the horizontal component of force has a negative value reflecting the direction of action of forces (in the direction opposite to x_D as shown in Figure 69). It can also be observed that at min displacement the magnitude of force (x-component) is less compared to that at max displacement, since the gears are exposed to a larger time period in the high pressure zone, at min displacement.

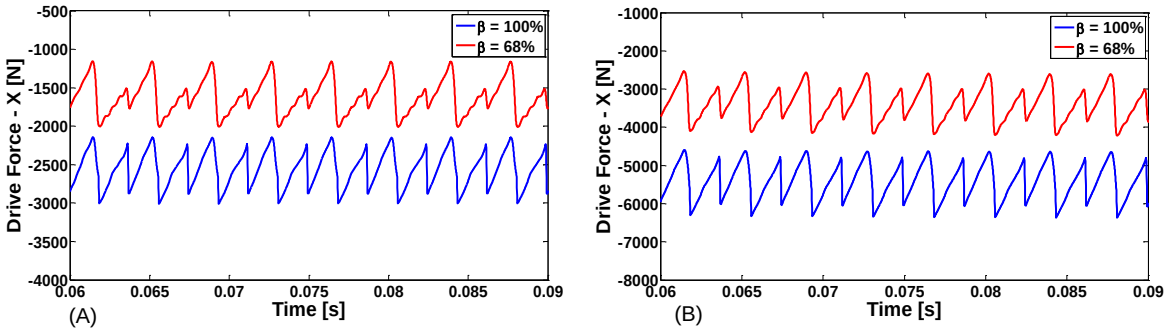

Figure 80: Horizontal component of force acting on the drive gear at maximum ($\beta = 100\%$) and minimum ($\beta = 68\%$) displacement for (A) 1000rpm, 100bar; (B) 1000rpm, 200bar.

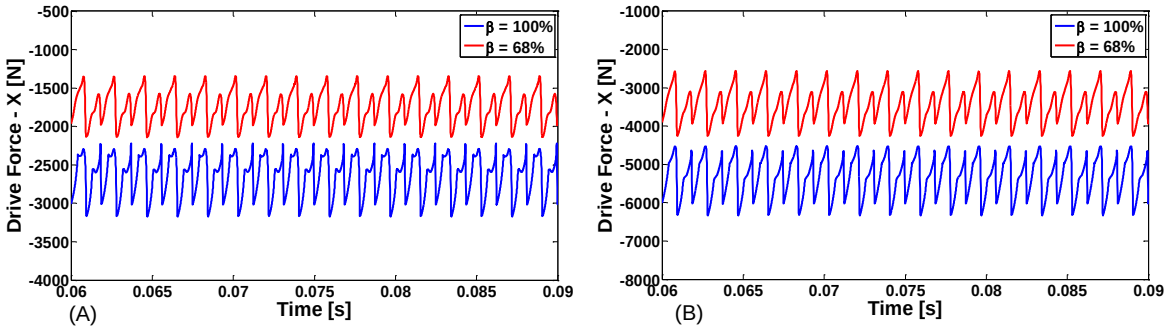

Figure 81: Horizontal component of force acting on the drive gear at maximum ($\beta = 100\%$) and minimum ($\beta = 68\%$) displacement for (A) 2000rpm, 100bar; (B) 2000rpm, 200bar.

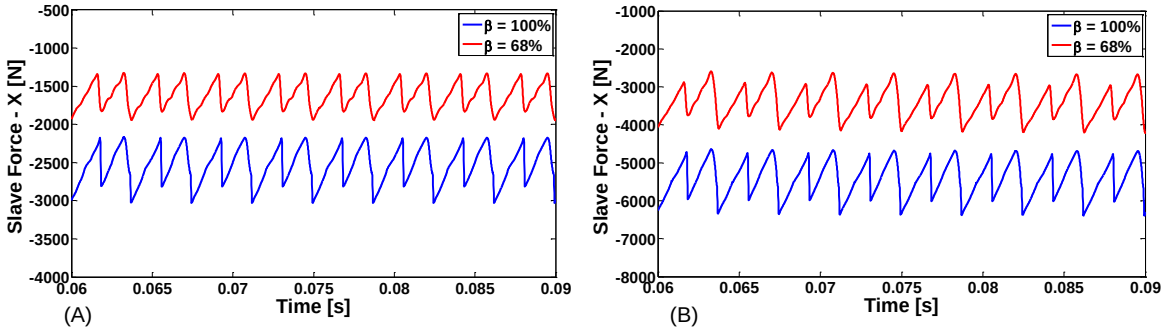

Figure 82: Horizontal component of force acting on the slave gear at maximum ($\beta = 100\%$) and minimum ($\beta = 68\%$) displacement for (A) 1000rpm, 100bar; (B) 1000rpm, 200bar.

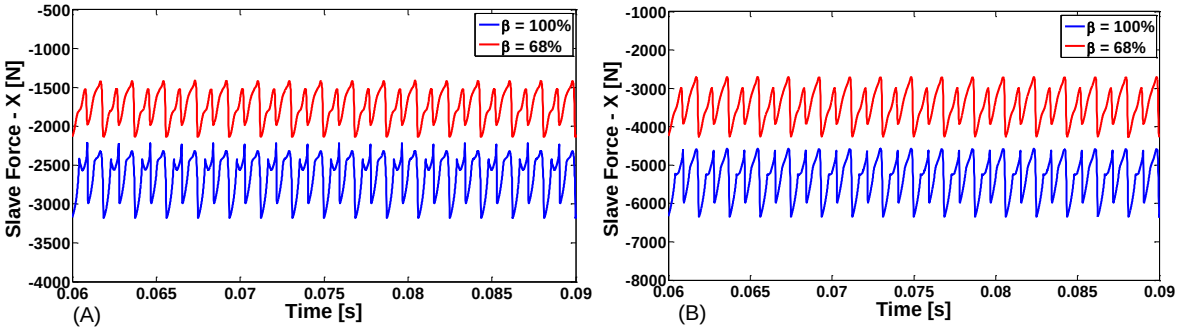

Figure 83: Horizontal component of force acting on the slave gear at maximum ($\beta = 100\%$) and minimum ($\beta = 68\%$) displacement for (A) 2000rpm, 100bar; (B) 2000rpm, 200bar.

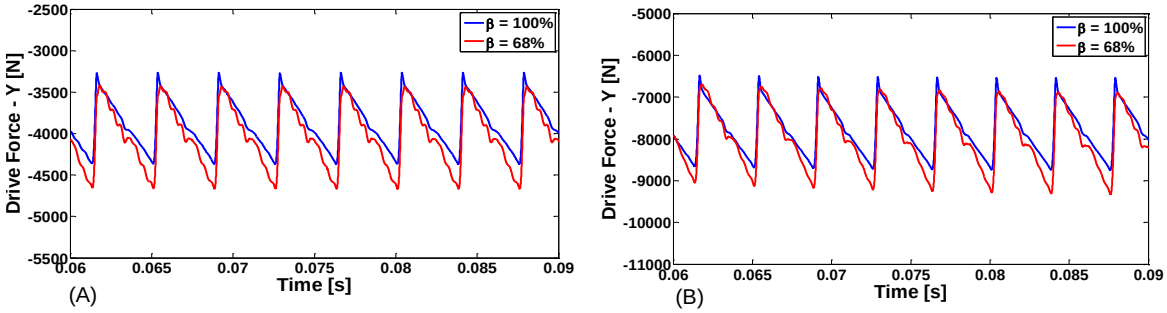

Figure 84: Vertical component of force acting on the drive gear at maximum ($\beta = 100\%$) and minimum ($\beta = 68\%$) displacement for (A) 1000rpm, 100bar; (B) 1000rpm, 200bar.

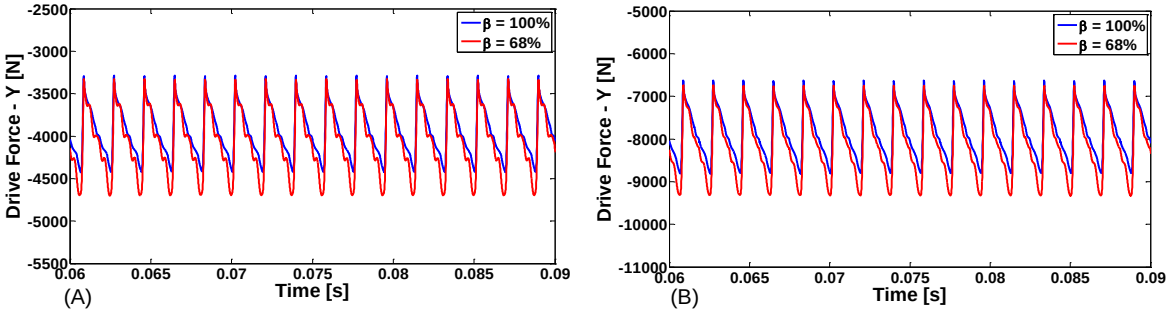

Figure 85: Vertical component of force acting on the drive gear at maximum ($\beta = 100\%$) and minimum ($\beta = 68\%$) displacement for (A) 2000rpm, 100bar; (B) 2000rpm, 200bar.

The vertical component of the total force acting on the drive gear is depicted in Figure 84 and Figure 85. Similarly, vertical component of the total force acting on the slave gear is depicted in Figure 86 and Figure 87. It can be seen that the force (in y direction) is of

almost of similar magnitude at both max and min displacement for all the operating conditions. The change in the position of the grooves does not influence the vertical component of forces.

Since for all the operating conditions considered the horizontal component of the pressure force has a reduced average magnitude for min displacement as compared to that at max displacement, it can be concluded that the resultant pressure force on the gears is of a lower magnitude at min displacement (since the vertical component of the forces remain the same regardless of the displacement). These reduced pressure forces are reflected on the lower input torque necessary to operate the pump at min displacement.

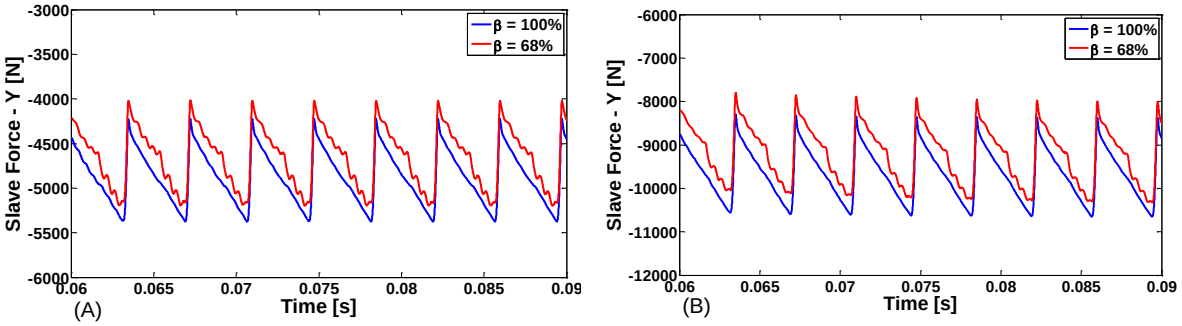

Figure 86: Vertical component of force acting on the slave gear at maximum ($\beta = 100\%$) and minimum ($\beta = 68\%$) displacement for (A) 1000rpm, 100bar; (B) 1000rpm, 200bar.

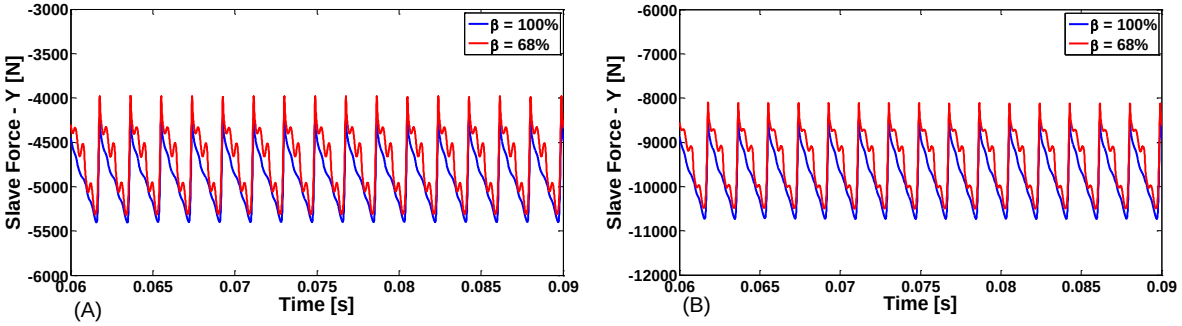

Figure 87: Vertical component of force acting on the slave gear at maximum ($\beta = 100\%$) and minimum ($\beta = 68\%$) displacement for (A) 2000rpm, 100bar; (B) 2000rpm, 200bar.

The total input torque predictions considering the entire gear for max and min displacement at four different operating conditions are shown in Figure 88 and Figure 89. It can be seen that the required torque at min displacement is 68% of that provided at 100%

displacement, due to the lower total force acting on the gear as explained previously. The lower input shaft torque required reflects on the lower energy consumption at min displacement, thus supporting the viability of a VD-EGM.

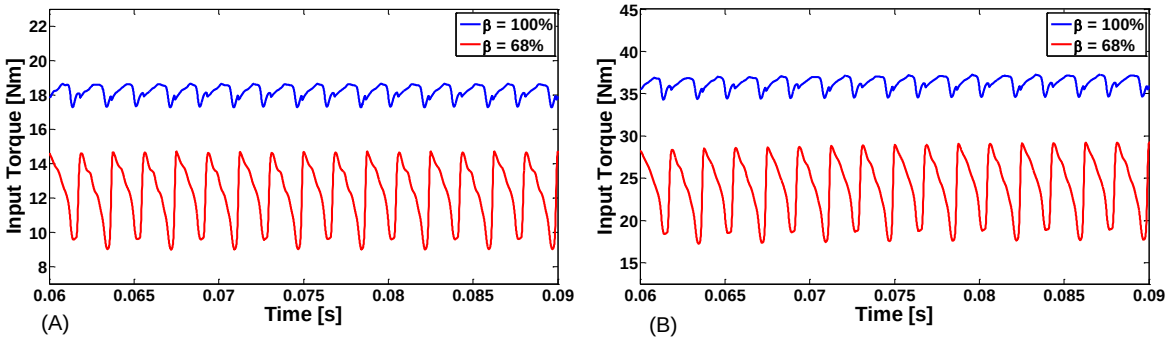

Figure 88: Total torque required at maximum ($\beta = 100\%$) and minimum ($\beta = 68\%$) displacement for (A) 1000rpm, 100bar; (B) 1000rpm, 200bar.

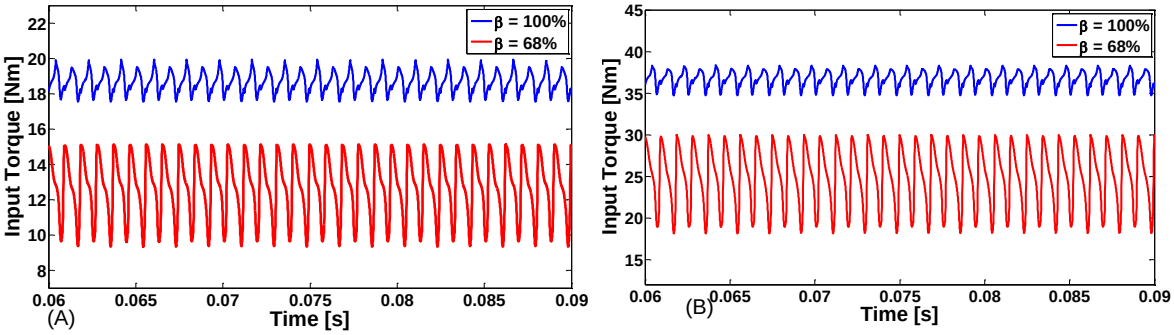

Figure 89: Total torque required at maximum ($\beta = 100\%$) and minimum ($\beta = 68\%$) displacement for (A) 2000rpm, 100bar; (B) 2000rpm, 200bar.

It can be seen from these figures, that the oscillations of the shaft torque are higher at min displacement as compared to that at max displacement. The higher torque pulsations at min displacement were expected from the analytical expressions previously derived in Section 3.3. However, the amplitudes of the oscillations are in line and similar with that of commercial pumps, hence these oscillations are not expected to be adversely affecting the performance of the machine in a negative manner.

7.1.5. Inter-axis Distance

Another interesting and important performance feature that needs to be considered is the variation of the inter-axis distance between the gears and hence the radial balance of the

gears. The predicted inter-axis distances for different operating conditions are depicted in Figure 90 and Figure 91.

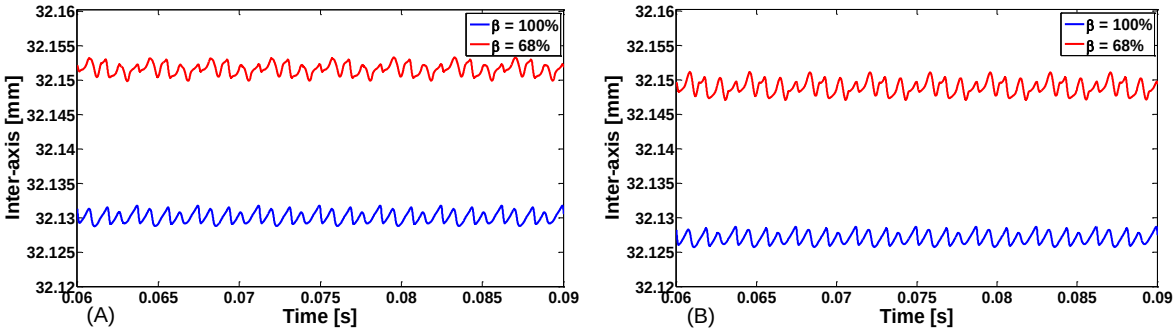

Figure 90: Inter-axis distance at maximum ($\beta = 100\%$) and minimum ($\beta = 68\%$) displacement for (A) 1000rpm, 100bar; (B) 1000rpm, 200bar.

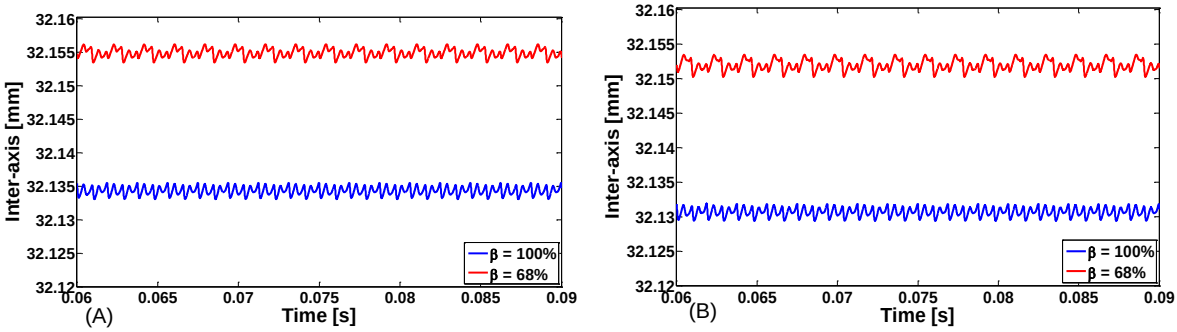

Figure 91: Inter-axis distance at maximum ($\beta = 100\%$) and minimum ($\beta = 68\%$) displacement for (A) 2000rpm, 100bar; (B) 2000rpm, 200bar.

The nominal inter-axis distance is 32.15mm. From the figures, it can be observed that the optimal design operates at a lower inter-axis distance (lesser by around 20 microns) for max displacement compared to that at min displacement. The difference in the operating inter-axis distance values can also be attributed to the difference in total resultant force acting on the gears.

7.2. Optimal Design for Variable Displacement - Unconstrained

In this section, an optimization similar to the one presented in Section 7.2 is implemented without the constraints on the inter-axis distance, facewidth and outer radius. It should be noted that the Level 2 of the optimization described in Chapter 6 was turned off identify the maximum possible reduction in displacement based on the input parameters in Table 2. The optimization process analyzed over 200 gear designs and a particular trend-line for min displacement as a percentage of max displacement as a function of number of teeth per gear was identified as shown in Figure 92.

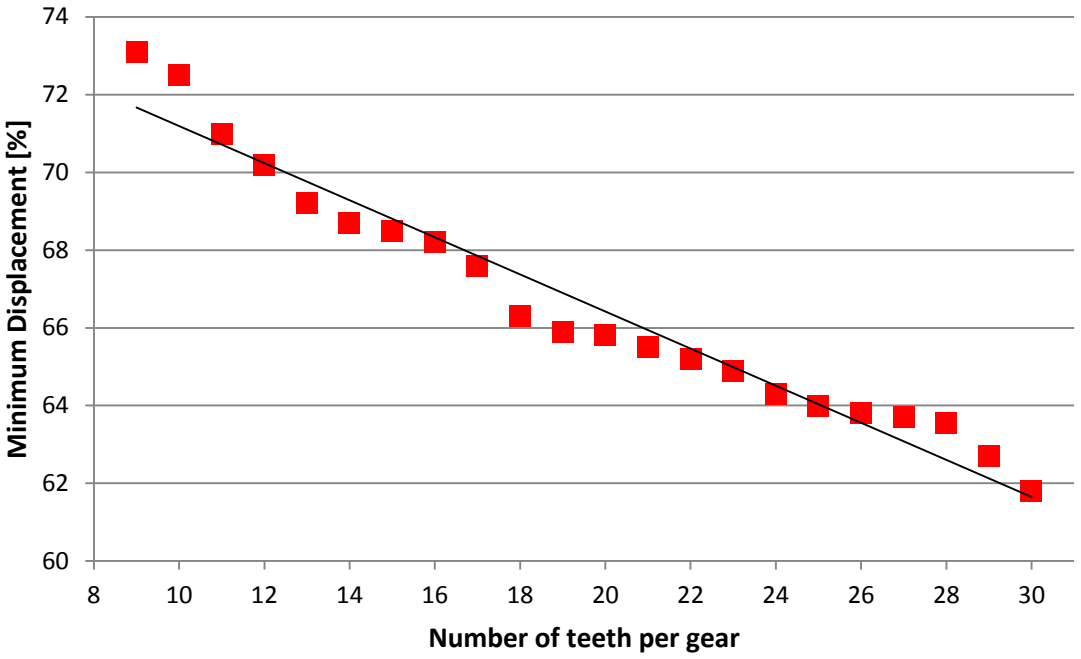

Figure 92: Trend of min displacement as a function of number of teeth per gear.

The red squares displayed in Figure 92, represents the min displacement for the particular number of teeth considering all of its different combinations with the other design variables. It can be seen that there is a clear linear trend for the min displacement as the number of teeth increases. The maximum number of teeth was restricted to 30, above this value very few designs can achieve considerable tooth thickness able to guarantee proper structural resistance.

The design of the gear which is predicted to obtain the maximum possible reduction in displacement of 38% (from 100% to 62%) is shown in Figure 93 and the design parameters for the same are shown in Table 8.

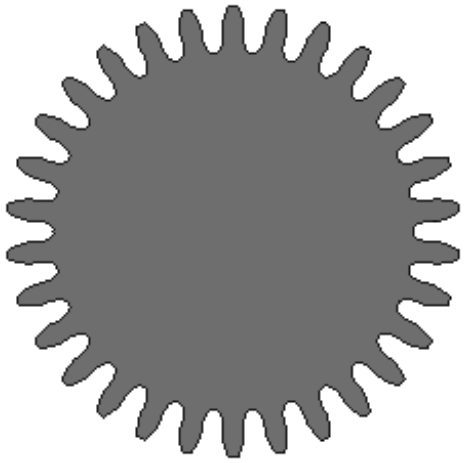

Figure 93: Design of gears which maximized the reduction in displacement in an unconstrained optimization.

Table 8: Design parameters of the gears which maximized the reduction in displacement for unconstrained optimization.

Number of teeth	30
Module	1.085mm
Facewidth	27.0mm
Drive pressure angle	6.50˚
Coast pressure angle	5.00˚
Pitch diameter	32.55mm
Addendum diameter	36.04mm
Minor/root diameter	28.60mm
Drive base circle diameter	32.34mm
Coast base circle diameter	32.43mm
Maximum displacement	*11.50 cc/rev*
Minimum displacement	*7.10 cc/rev*
Minimum displacement (%)	*62*

Comparing the design parameters in Table 5 and Table 8, it can be seen that the design of the gear predicted by the unconstrained optimization is much more aggressive than that

obtained using constrained optimization. It should be also noted that the gear in Figure 93 is much shorter and thinner than the one in Figure 60(A), nevertheless, the gear design show the maximum potentials or the extent to which reduction in displacement is possible using asymmetric gears.

7.3. Optimal Design for Low Pressure Ripple

The optimization process described in Chapter 6 can also be used for determining the optimal design of an EGM. Particularly, maximization of reduction in displacement objective function can be switched off, thereby, easily capable of changing the optimization process to be focused on the performance of the EGM at the max displacement. The reference design considered in this section is different from the one described earlier in the previous section. The specification of this new reference EGM is shown in Table 9.

Table 9: Specifications of the reference EGM, working fluid and materials for low pressure ripple.

Displacement of EGM	38 cc/rev
Number of teeth per gear	14
Maximum operating speed	3000 rpm
Maximum operating pressure	250 bar
Facewidth	39.50 mm
Pitch diameter	40.63 mm
Working Fluid	ISO VG 46 Hydraulic Oil
Density @ 50˚C, atmospheric pressure	851 kg/m^3
Viscosity @ 50˚C, atmospheric pressure	0.026 Pa-s
Lateral Bushings	Bronze Alloy
Gears	Steel

The optimal design of the gears and the lateral bushing at the end of the optimization process are depicted in Figure 94 .

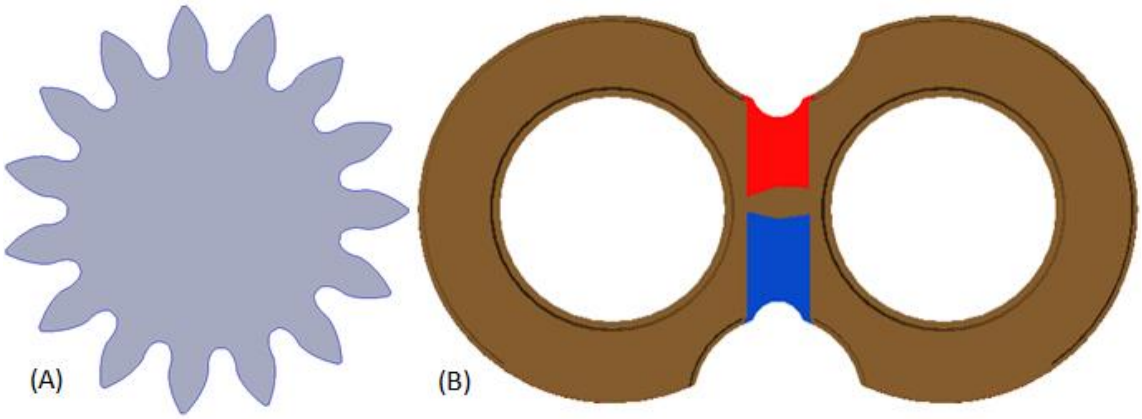

Figure 94: (A) Optimal design of gears for low pressure ripple; (B) Optimal design of grooves in the lateral bushings for low pressure ripple.

The specifications of the optimal design of the gears for low pressure ripple are presented in Table 10.

Table 10: Design parameters for the optimal design of gears and grooves in the lateral bushings for low pressure ripple.

Number of teeth	15
Module	2.71mm
Facewidth	39.5mm
Drive pressure angle	22.0˚
Coast pressure angle	19.0˚
Pitch diameter	40.63mm
Addendum diameter	47.77mm
Minor/root diameter	32.45mm
Drive base circle diameter	37.67mm
Coast base circle diameter	38.42mm
D	1.2 mm
S	1.2 mm
α_{DL}	8°
α_{DR}	13°
α_{SL}	-3°
α_{SR}	19°

It can be noticed from Table 10, that the pressure angles for both the drive and coast sides are different by three degrees, causing only a slight asymmetricity in the gears. Also, it was assumed that the grooves in the lateral bushing will be manufactured using sintering process, therefore the assumption of using a milling tool to cut the grooves as applied in the previous section was removed. This would further help in understanding the benefits of using novel designs of grooves which significantly unconventional designs.

The performance of the optimal design was compared in terms of pressure ripple at the delivery and tooth space pressure with those of the commercial pumps available both in single flank and dual flank contact configuration. Comparisons of this sort will clearly bring about the potentials of introducing the asymmetricity in the gears thereby providing new ventures in the design of EGMs.

7.3.1. Delivery Pressure Ripple

The pressure ripple comparisons in simulation for the optimized design with respect to the single flank reference design is shown in Figure 95. It can be seen that the optimal design performs much better than the reference design

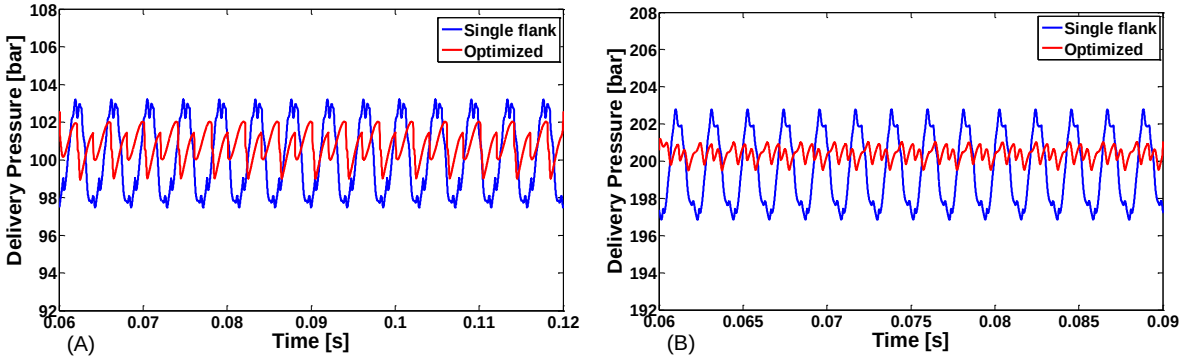

Figure 95: Delivery pressure ripple for reference single flank design and optimal design for (A) 1000rpm, 100bar; (B) 2000rpm, 200bar.

Similarly, comparisons of the pressure ripple of the optimized design with the dual flank reference design (as shown in Figure 96) show that the optimized design performs better compared to the reference design. In a nutshell, the optimized design has a lower pressure ripple and hence predicted to have lower noise emissions compared to the reference single flank and dual flank designs.

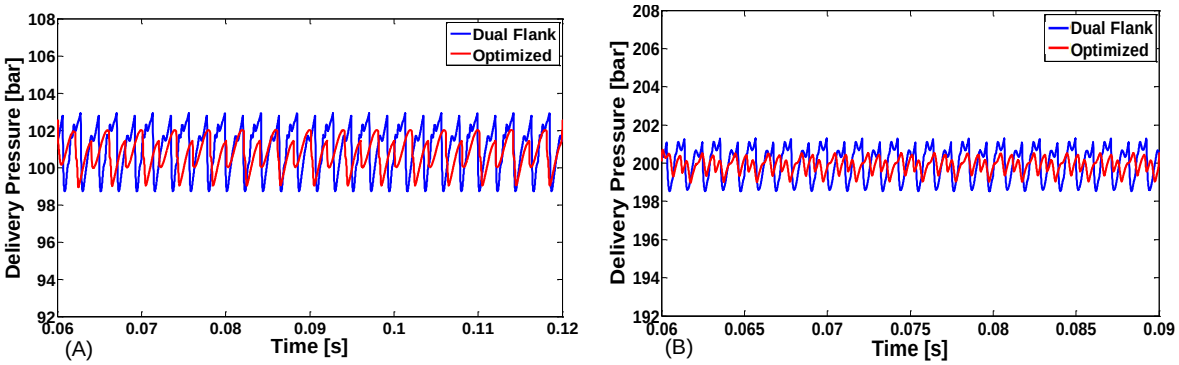

Figure 96: Delivery pressure ripple for reference dual flank design and optimal design for (A) 1000rpm, 100bar; (B) 2000rpm, 200bar.

7.3.2. Tooth Space Pressure

Figure 97 shows the plots of the tooth space pressure for the single flank and optimized design. It can be seen that optimized design has significantly cut down the pressure overshoots which were present in the reference design. Similar performance is achieved by the optimized design in comparison with the dual flank reference design. The tooth space pressure plots assert that the grooves in the lateral bushings perform well at all the operating conditions.

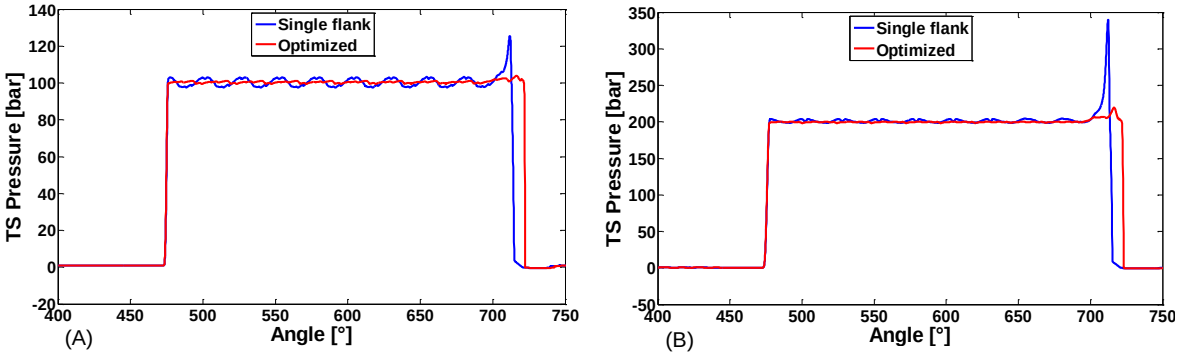

Figure 97: Tooth Space Pressure for reference single flank design and optimal design for (A) 1000rpm, 100bar; (B) 1000rpm, 200bar.

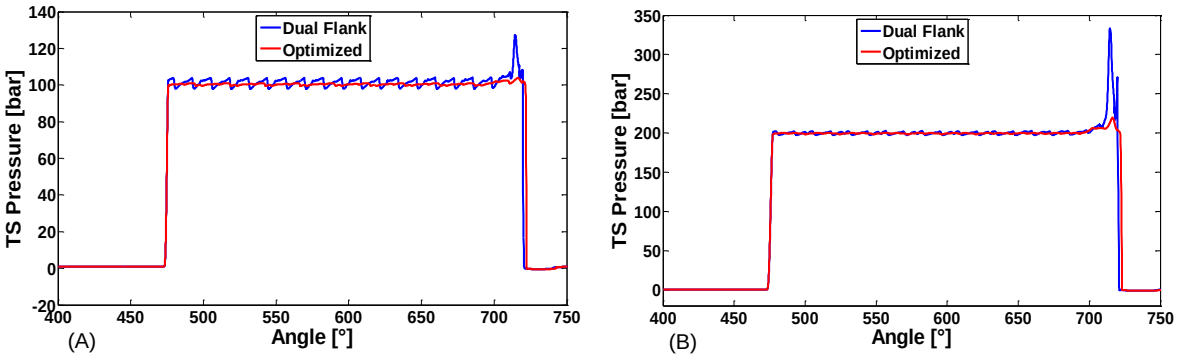

Figure 98: Tooth Space Pressure for reference dual flank design and optimal design for (A) 2000rpm, 100bar; (B) 2000rpm, 200bar.

7.3.3. Summary of the Objective Functions

In order to better understand the performance of the optimal design the objective functions concerning pressure ripple (as the energy of the signal derived from the FFT of the signal) , cavitation (expressed as the area of the TS pressure curve under the saturation pressure of the fluid) are compared with those of the reference designs. As can be seen from Figure 99, the optimal design shows a significant reduction in pressure ripple for a wide range of operating conditions. As far as the features of the meshing process such as the internal pressure peaks are concerned, the novel design shows good improvement as can be inferred from Figure 97**,** and Figure 98.

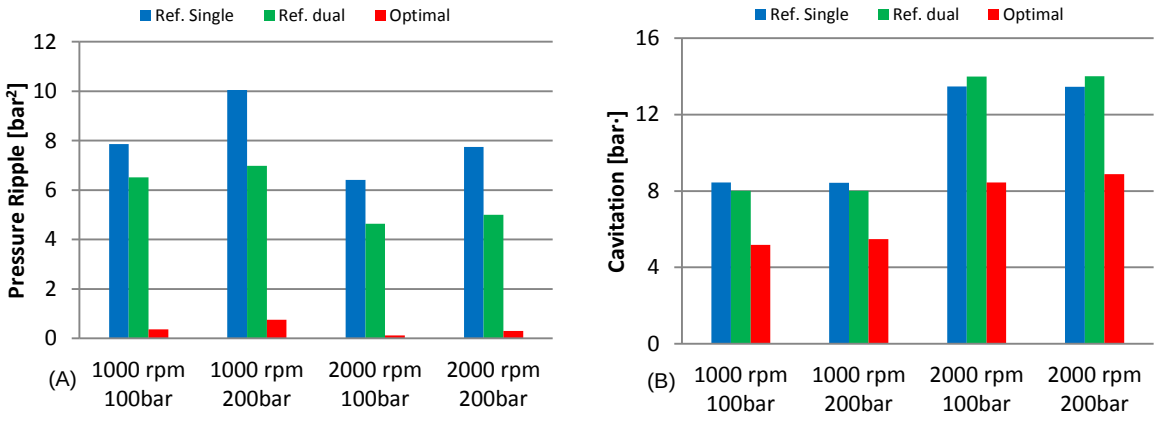

Figure 99: (A) Pressure ripple; (B) Cavitation for the optimal design, reference single flank and dual flank designs.

The improvement in the volumetric performance of the optimal design compared with the reference can be deduced from Table 11. It can be seen clearly that the volumetric efficiency of the pump has been improved by over 2% with respect to both the reference designs for all the operating conditions considered.

Table 11: Improvement in volumetric efficiency of the optimal design.

Operating Condition	*% improvement in Vol. Efficiency*
1000 rpm 100bar	2.50
1000 rpm 200bar	2.20
2000 rpm 100bar	2.80
2000 rpm 200bar	2.60

The maximum pressure considered for simulations as shown in previous parts of the chapter is 200bar, however, the principle and the concept applies for higher pressure applications with higher leakages.

8. PROOF OF CONCEPT TESTS AND VALIDATION

The encouraging performance potentials obtained in simulations as explained in 7 for a wide range of operating conditions, provided motivation for designing a proof of concept test, whose primary goal is to prove the working concept of VD-EGM. The description of the proof of concept tests is described in this chapter.

8.1. Prototype Design

The optimal design of the gears with asymmetric teeth (as shown in Figure 100(A)) was manufactured using a wire electric discharge machining process (Wire EDM) for prototyping process. It should be noted that the prototypes generated correspond to the optimal design considered for variable displacement for a reference case of 11.2 cc/rev (as previously described in section 7.1).

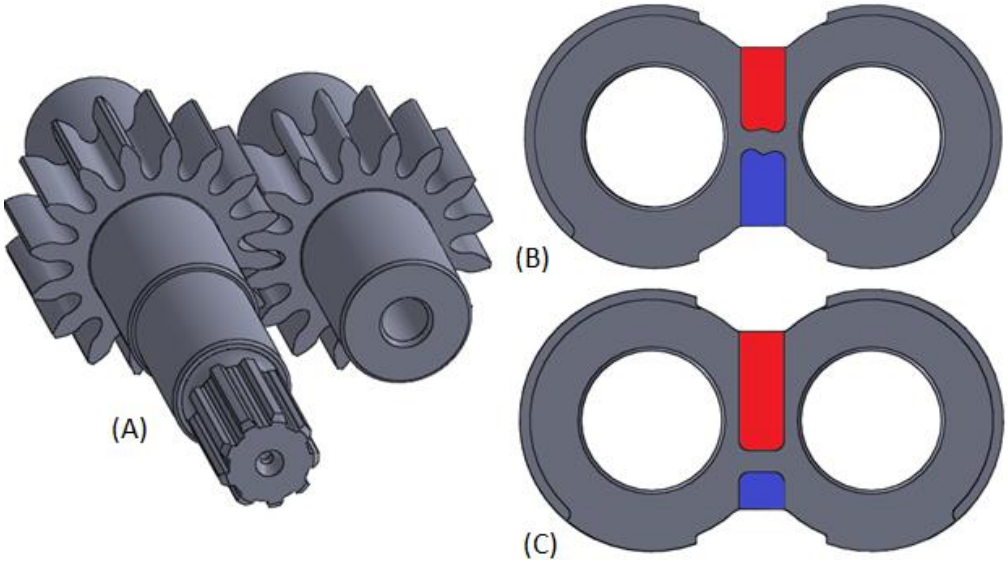

Figure 100: CAD model of (A) the optimal asymmetric gears; (B) Grooves for max displacement (C) Grooves for min displacement.

As can be seen from Figure 100(B) and (C), the grooves for min displacement are significantly different from that for max displacement. The grooves for min displacement were designed at the limit of achieving the min displacement considering only the volumetric performance. However, these grooves were not optimized considering flow pulsations and other performance parameters, since the purpose of the tests was to understand the maximum potential of operation of a VD-EGM and to validate the working concept in terms of displacement reduction alone.

Conventionally, before assembling the gears inside an EGM, the gears undergo grinding process to increase the surface finish thereby smoothing the meshing process of the gears and hence reducing structural vibrations and noise. The gears also undergo heat treatment process to increase their hardness and reliability. Since the sole purpose of the prototype and the experiments were to prove the concept of VD-EGM and to validate the performance of the machine, the gears were neither subject to additional heat treatment processes nor any grinding/finishing operations in this research.

In order to validate the working of VD-EGM, it is however not necessary to consider the design of the slider in the lateral bushings. Instead, two different lateral bushings with different groove designs corresponding to maximum and minimum displacement (as shown in Figure 100 (B) and (C)) can be used to determine the performance at the respective desired levels of displacement. The grooves for min displacement were machined in such a way that the TSV switched its connection from the outlet to the inlet at the point at which the TSV seizes to be trapped between the contact points of the gears. All the other parts of the commercial design such as the casing, the balance side of the lateral bushings, seals, flanges etc. were maintained the same during the testing phase. The final machined gears and lateral bushings are shown in Figure 101.

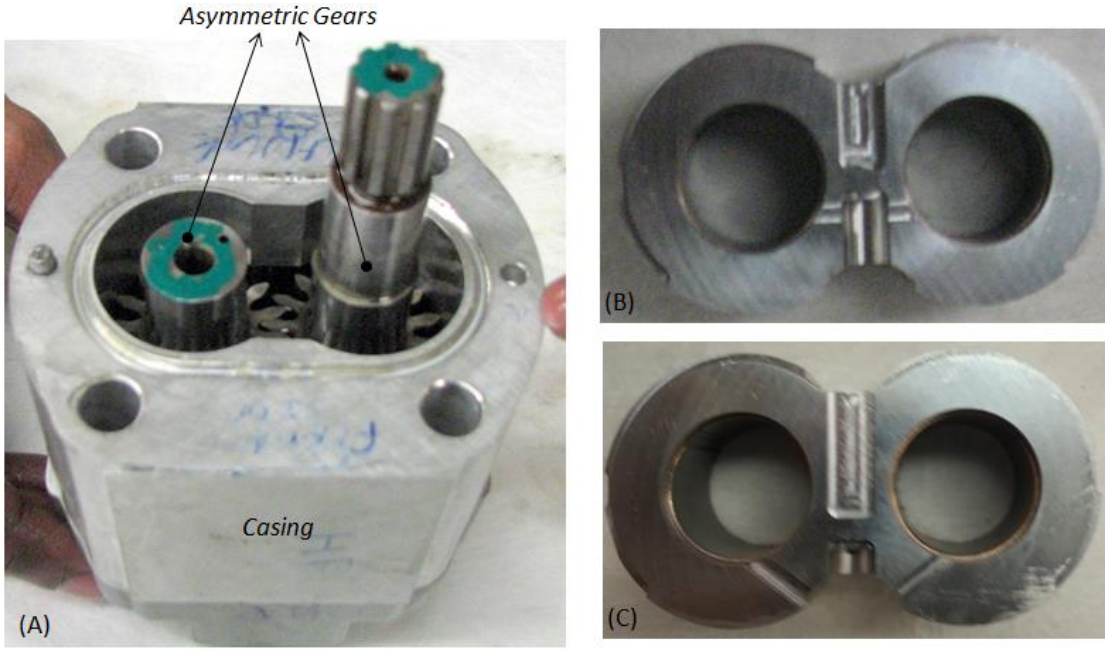

Figure 101: Prototype optimal gears assembled within the commercial casing; (B) Lateral bushings with grooves for max (100%) displacement; (C) Lateral bushings with grooves for min (68%) displacement.

8.2. Experimental Setup

Experimental measurements were performed using the multi-purpose test rig available at the Maha Fluid Power Research Center of Purdue University. The objective of the experiments was to measure the steady state performance parameters of the EGM with lateral bushings for max and min displacement. Dynamic pressure ripple measurements were also performed to understand the performance of the machine in terms of delivery flow pulsations. A view of the test rig with the prototype installed is shown in Figure 102, and the corresponding ISO hydraulic circuit is shown in Figure 103. The prototype EGM was driven using a 93.2 kW electric motor at the main shaft line (driving axle, a 4-quadrant electric motor drive produced by ABB, (EM in Figure 103). The driveline was also equipped with an optical speed measurement system and a torquemeter. The outlet pressure for the EGM was set using a variable orifice at the desired value, and the suction and the delivery lines were equipped with thermocouples, pressure sensor and flowmeter. A system of coolers and heaters integrated in the test-rig permits a closed loop control of

fluid temperature at EGM inlet (T1). The specifications of the instrumentation used in the test rig are represented in table 4.

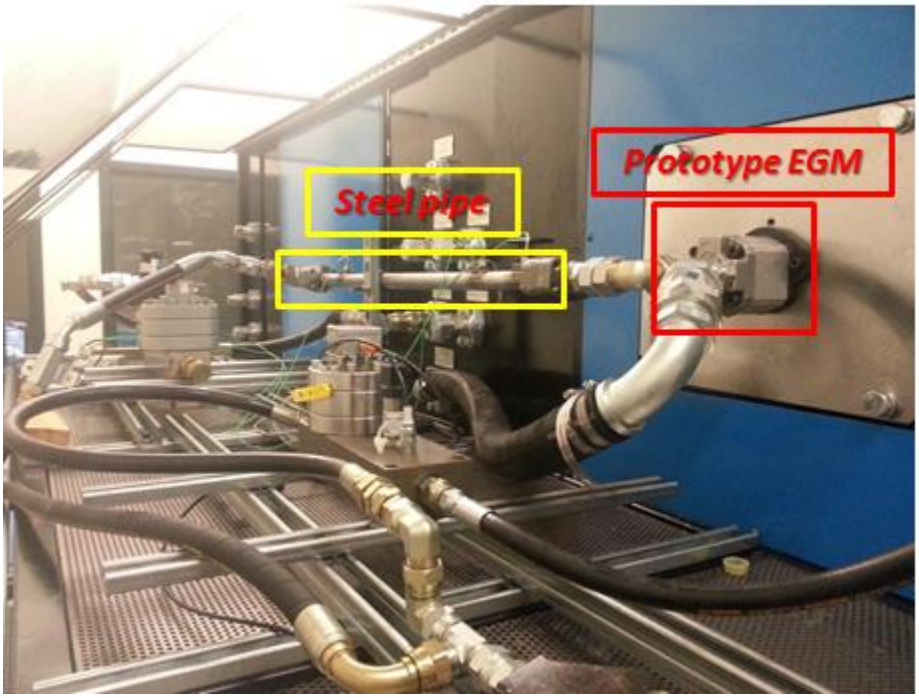

Figure 102: A view of the test rig with prototype EGM and rigid steel pipe installed.

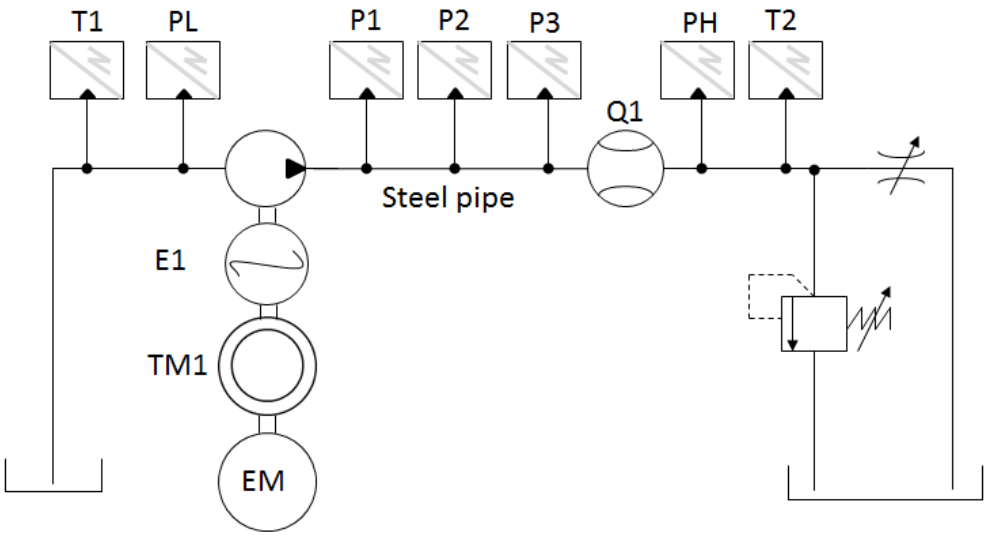

Figure 103: Hydraulic schematic of the test circuit.

Table 12: Specifications of the sensors and equipment used in the test rig.

Symbol	Type	Specifications
EM	Electric Motor	ABB®, 4-quadrant electric motor, 93.2 kW
T1, T2	Resistive thermocouple	Omega® K-Type, Scale: -50°..+200°C
PL, PH	Piezo-resistive pressure sensors	WIKA®, Scale: 0..250 bar
P1, P2, P3	Piezo-electric pressure sensors	KISTLER® 03B1, Scale: 0..1000bar
Q1	Flow Meter	VSE®, Scale 0.05..150 l/min
TM1	Torquemeter	HBM® T10FS, Scale: 0..500 Nm
E1	Optical speed measurement system	HBM® T10FS, Scale: 0..15000RPM

All testing conditions were performed with an inlet temperature of 50°C within a range of $\pm 1^{\circ}$C using an ISO VG46 oil (Density: 846.9 kg/m^3, Bulk Modulus: 13703bar at 50°C and atmospheric pressure). Before conducting any measurements on the prototype, the casing of the commercial reference pump was broken-in by using the standard gears (available commercially) which were heat treated. During this process, the pressure at the delivery of the pump was varied from 0 to 125 bar over a long period of operation of the machine at a constant speed. This method was repeated for 3 different speed conditions (1000, 1500 and 2000rpm). During the breaking in process, the volumetric efficiency of the pump was monitored and the pressure was increased only when a steady state value of the flow rate was obtained. Once the casing was broken in, the traditional gears and the lateral bushings were removed and substituted with the prototype gears and the lateral bushings for max displacement and measurements were conducted. Following this step, the pump was disassembled again and only (prototype gears remain the same) the lateral bushings for min displacement were replaced with those for max displacement, and measurements were performed.

8.3. Experimental Results and Validation

In this section the results of the proof of concept tests particularly concerning delivery flow rate, input shaft torque are presented. The results of the experiments are compared with those of the simulations provided by HYGESim for a wide range of operating conditions.

It can be seen from Figure 104(A), Figure 105(A) and Figure 106(A) that the flow rate proportionally (68%) reduces at min displacement as compared to those at full or max displacement. The simulated data matches very closely with that of the measurements. Having a closer look at these plots, it can be seen that there is an offset between the measured and simulated flow rates at both the displacements. This offset can be explained due to the fact that in simulations, a perfect profile of the asymmetric gears with dual flank contact configuration is considered, however due to the manufacturing tolerance introduced by the wire EDM process, the gears in reality will not operate in dual flank configuration. Due to this imperfection in achieving zero backlash between the gears, a certain amount of bypass leakage is introduced from the high pressure to the low pressure side through the TSVs hence causing an offset in the flow rates. Additionally there are also simplifications in the model for the calculation of leakages.

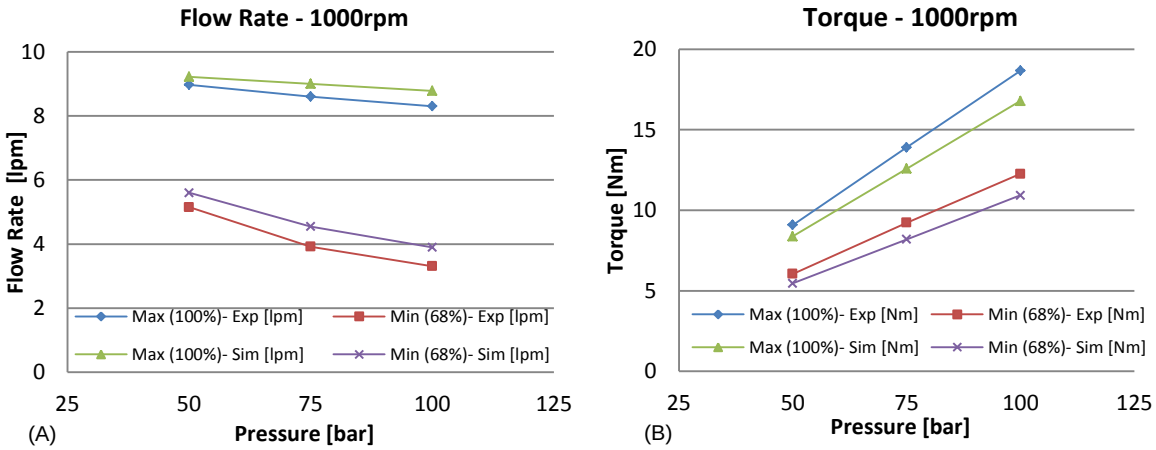

Figure 104: Validation for (A) Flow rate and (B) Input torque for 1000 rpm.

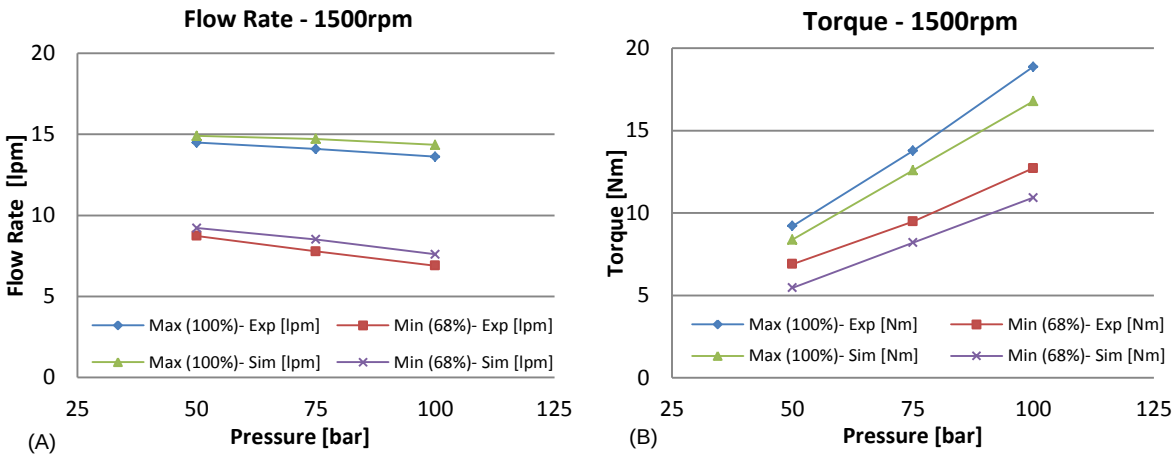

Figure 105: Validation for (A) Flow rate and (B) Input torque for 1500 rpm.

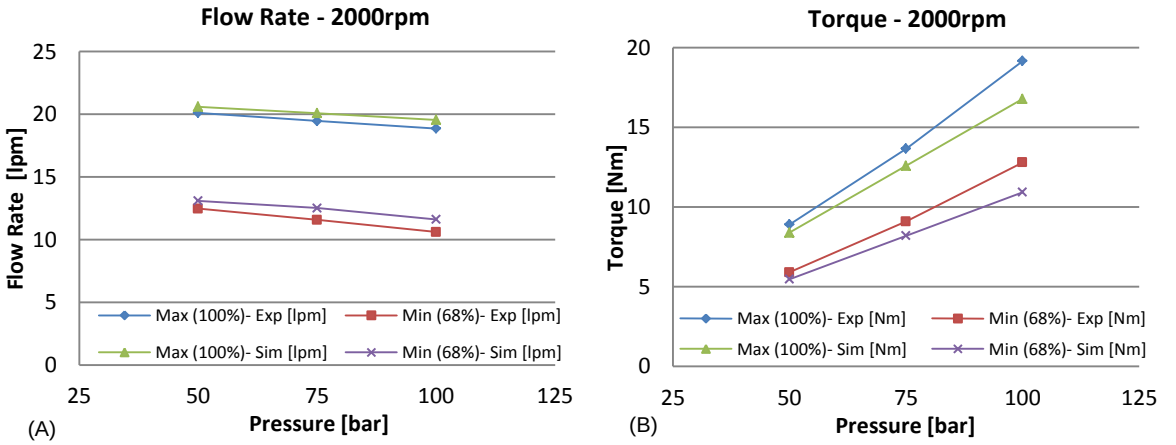

Figure 106: Validation for (A) Flow rate and (B) Input torque for 2000 rpm.

Figure 104(B), Figure 105(B) and Figure 106(B) represent the input shaft torque validation. It can be seen that the input shaft reduces proportionally at min displacement. Approximately 32% reduction in torque is obtained at all the operating conditions tested for min displacement. The simulations under predict the input shaft torque because the shear losses in the lateral gaps and also the effect of friction due to the sliding of the gear teeth with each other have been neglected hence there is an offset between the experimental and simulated torque curves.

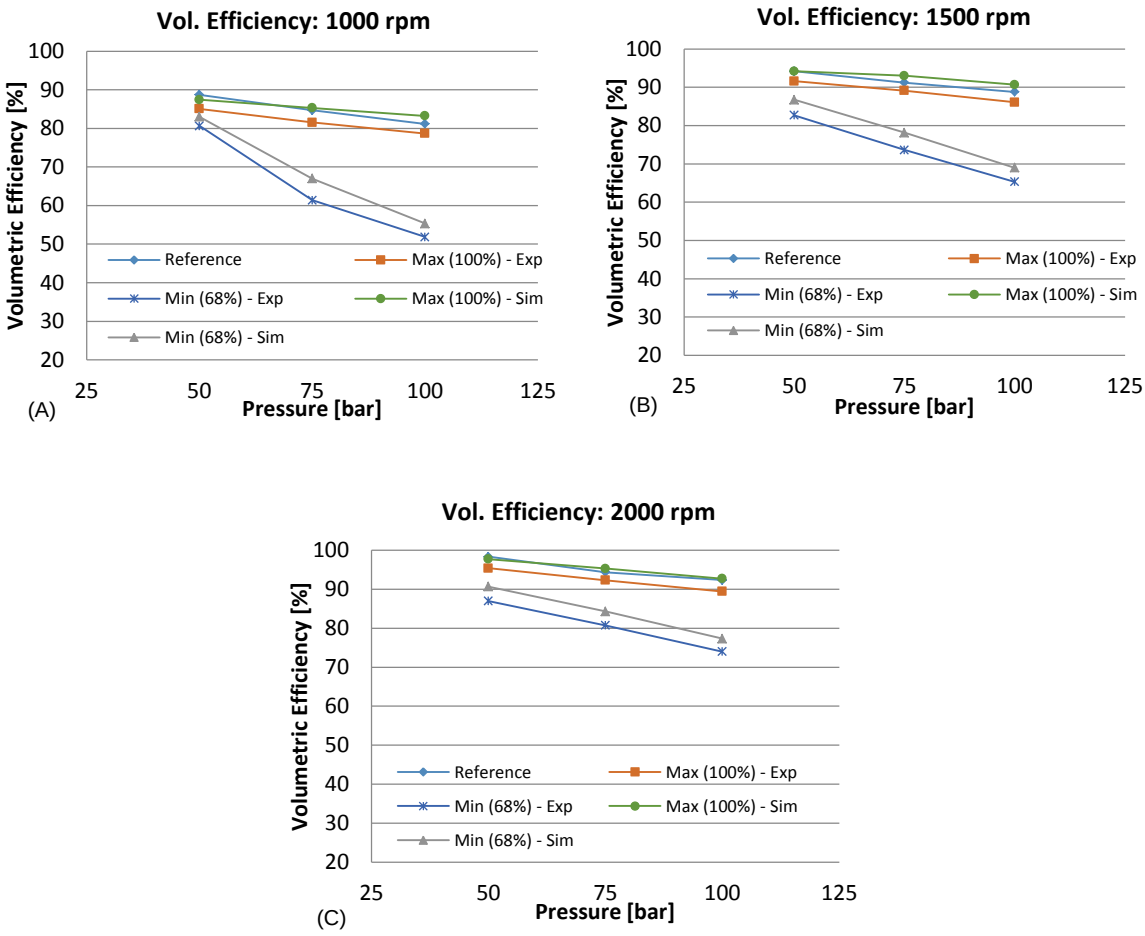

Figure 107: Volumetric efficiency for (A) 1000rpm; (B) 1500rpm; (C) 2000rpm.

Experimental comparisons of volumetric efficiency are reported in Figure 107. Firstly, the blue curve (with diamond dots) represents the performance of the reference commercial EGM (of the same max displacement). It can be noticed that the volumetric performance at max displacement as shown by the orange curve (square dots) matches very closely to that of the reference design. The minor discrepancies between the red and the blue curve can be attributed to the fact that, the radial leakages using optimal gears at max displacement is slightly higher than that of the reference design. As already mentioned, the casing of the EGM was broken in using the standard commercial gears of the reference design, therefore it achieves better radial sealing (as explained in Figure 8) hence a better volumetric performance compared to that at max displacement (gears are different). However, if the casing was broken in using the optimal gears, the volumetric

performance will be very close to that of the reference design. It should also be noted that the volumetric efficiency at both max and min displacement increases as the speed increases, this is because the maximum speed at which the casing was broken in was 2000 rpm and hence the gears are capable of achieving better radial sealing and hence better performance at higher speeds. The volumetric efficiency at min displacement is lower than those at max displacement, due to the fact that the leakages: both radial and lateral leakages are most prominently dependent on the pressure and hence have a larger influence at lower displacement. It can also be seen that the trends of the simulated volumetric efficiency are in close agreement with those of the experiments for both max and min displacement, hence, purporting the capabilities of HYGESim to predict the performance of the VD-EGM at varying levels of displacement.

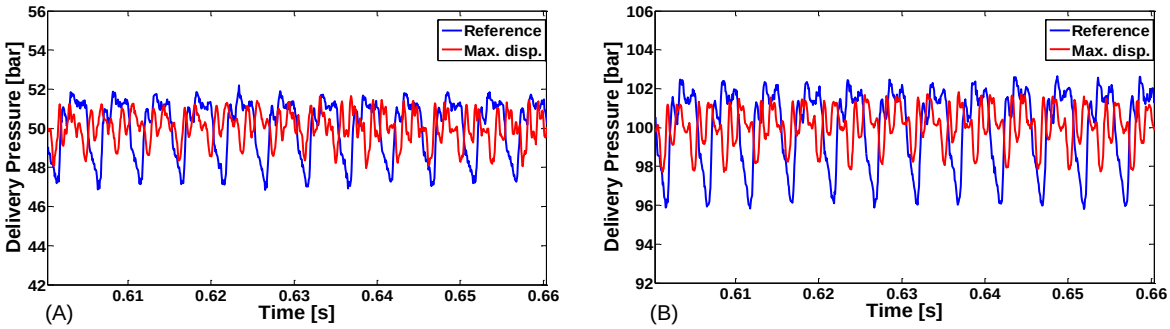

Figure 108: Delivery pressure ripple for the reference and max displacement for (A) 1000rpm, 50bar; (B) 1000rpm, 100bar.

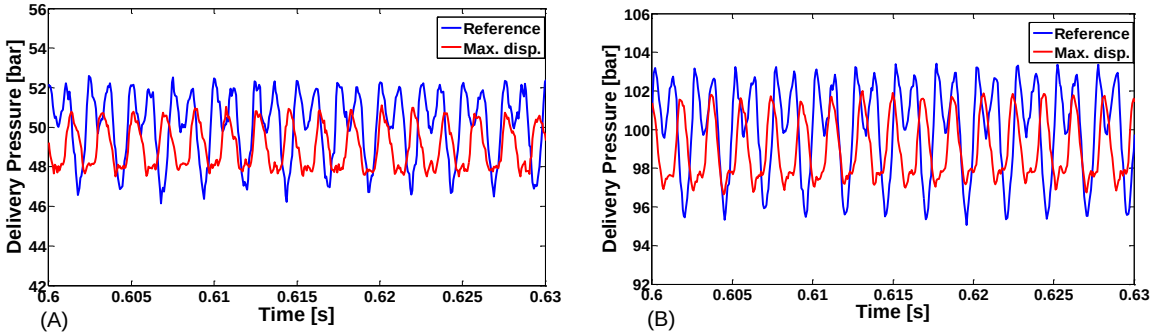

Figure 109: Delivery pressure ripple for the reference and max displacement for (A) 2000rpm, 50bar; (B) 2000rpm, 100bar.

The pressure ripple at the delivery of the pump was also measured for a wide range of operating conditions. It can be seen from Figure 108, Figure 109 that the optimal design

of the EGM for max displacement provides a very low pressure ripple compared to the reference design in time domain and hence leading to lower fluid borne noise emissions.

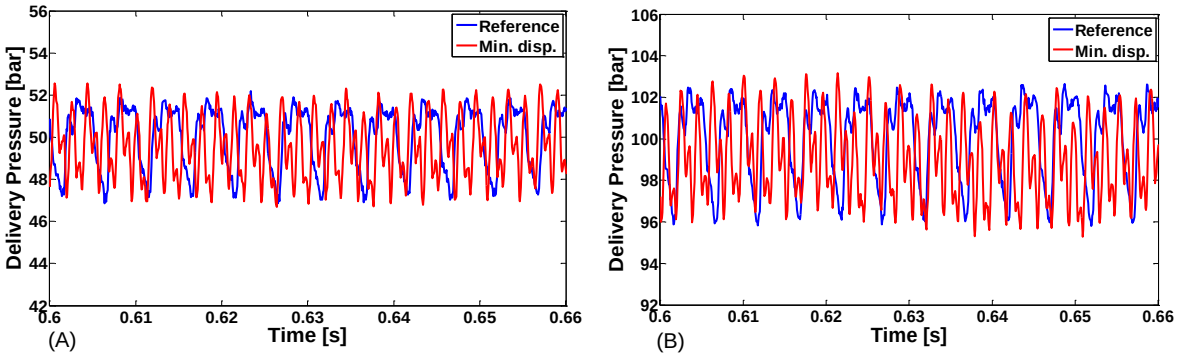

Figure 110: Delivery pressure ripple for the reference and min displacement for (A) 1000rpm, 50bar; (B) 1000rpm, 100bar.

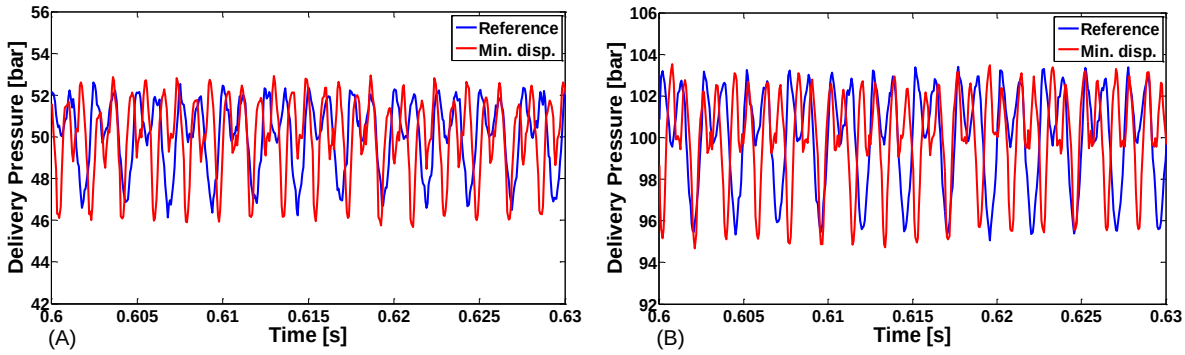

Figure 111: Delivery pressure ripple for the reference and min displacement for (A) 2000rpm, 50bar; (B) 2000rpm, 100bar.

The performance of the gear machine at min displacement was also measured. However, it was observed that the pressure pulsations at the delivery for min displacement was higher than that at max displacement, but of similar amplitude as of the pressure ripple of the reference design (as can be seen from Figure 110 and Figure 111). The better performance at max displacement is due to the correct functioning of the optimal design of the gears and the grooves, thus verifying the efficiency of the implemented optimization process. However, the design of the grooves was not optimized for operation at a min displacement position therefore the pressure ripple is different (higher) than that at max displacement.

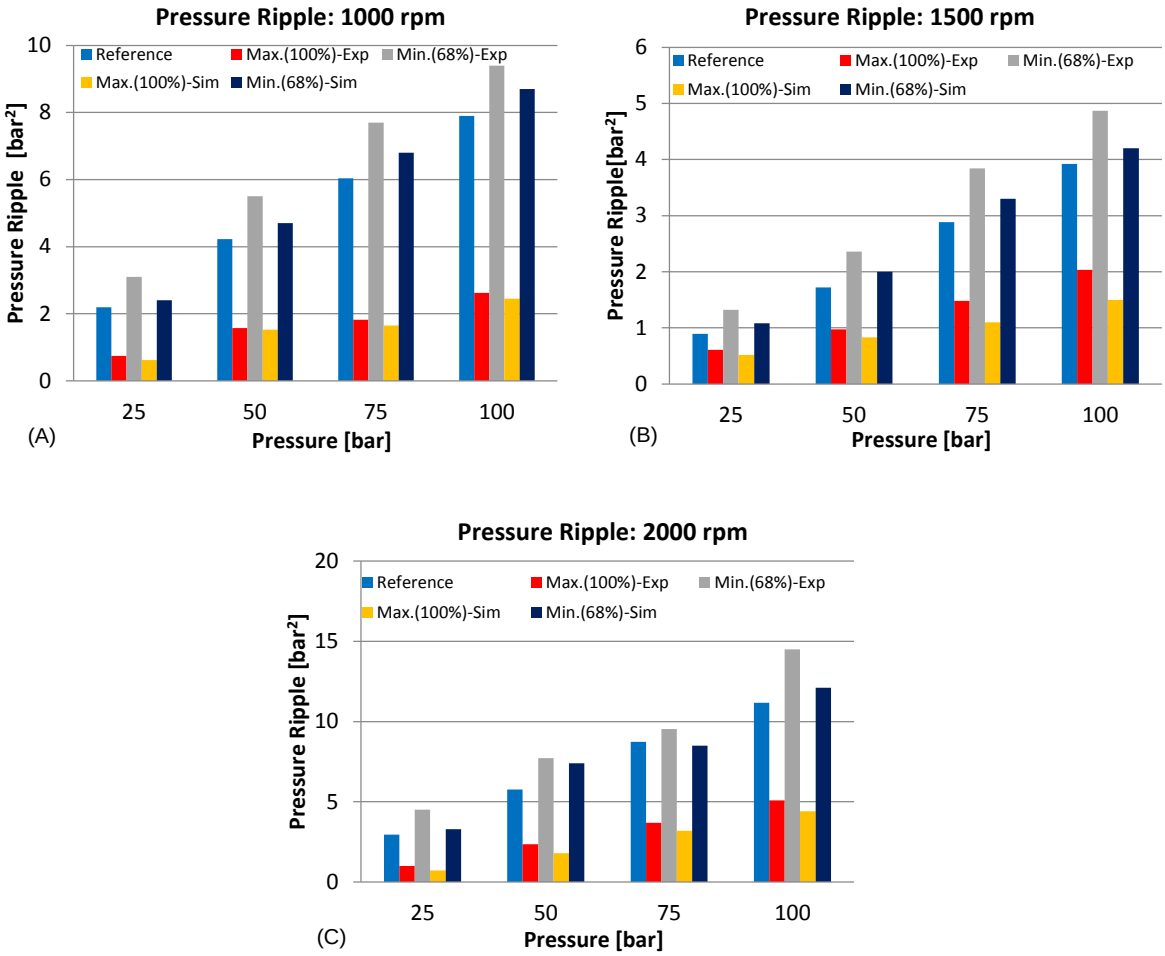

Figure 112: Pressure ripple comparisons at (A) 1000 rpm; (B) 1500 rpm; (C) 2000 rpm.

In order to gain a better understanding of the performance of the different designs, the energy of the pressure ripple (as explained previously in section 6.1.1) is compared (both in simulation and in experiments for different operating conditions and displacements) as depicted in Figure 112. The experimental pressure ripple for max and min displacement are shown as the red and grey bars respectively. The simulated pressure ripple for max and min displacement are shown as the yellow and dark blue bars respectively. As can be seen from the trends of the red and yellow bars as wells as those of the grey and dark blue bars, the pressure ripple predicted by the simulations match pretty closely with those of the measured values.

It is also worth noting that, even though the pressure ripple at min displacement is higher than that at max displacement, it is not very high compared to that of the reference design.

(comparison between light blue and dark blue bars in Figure 112). Therefore, the pump will be capable of performing with comparable fluid-borne-noise emissions similar to the reference pump which is representative of the commercially available pump.

9. DESIGN OF A CONTROL MECHANISM FOR VARYING THE DISPLACEMENT OF A VD-EGM

In this chapter, a simple and novel concept for achieving an automatic control of flow rate in a VD-EGM is described. The basic aim of this design is to automatically control the flow rate of the pump based on the pressure at the delivery of the pump, by ensuring a compact shape of the machine with the introduction of only a few additional components. Basically the displacement of the pump is reduced proportionally according to the pressure at the delivery of the pump. The chapter focuses on design of the different parts of the VD-EGM, and experimental results detailing the performance of the prototype VD-EGM at various operating conditions.

9.1. Working Idea

The working idea for the pressure compensated design for VD-EGM can be explained using Figure 113. As can be seen from Figure 113, the asymmetric gears are placed inside the casing which has inlet and the outlet ports on the rear flange of the pump. The particular kind of design with ports on the flange allows more room for the placement of additional parts of the actuation system. The high pressure and low pressure regions are represented by HP and LP. The grooves are machined on a movable slider as shown and it is connected with the help of a connecting rod to the connecting piston. The connecting piston is acted upon by the spring force on the right.

During the operation of the EGM, the fluid at HP acts on the left of the slider and on the right the spring force corresponding to its compressed length on the right. Since the slider is movable a balance of forces is achieved on the slider and an equilibrium position of the slider is obtained according to the pressure at the HP and the pre-set spring force. In this way an automatic variation of the displacement can be achieved. As already explained in

Chapter 2, there is a minimum limit to which the displacement can be changed beyond which the volumetric efficiency of the pump is compromised significantly due to the abrupt bypass flow of fluid from the HP to the LP region.

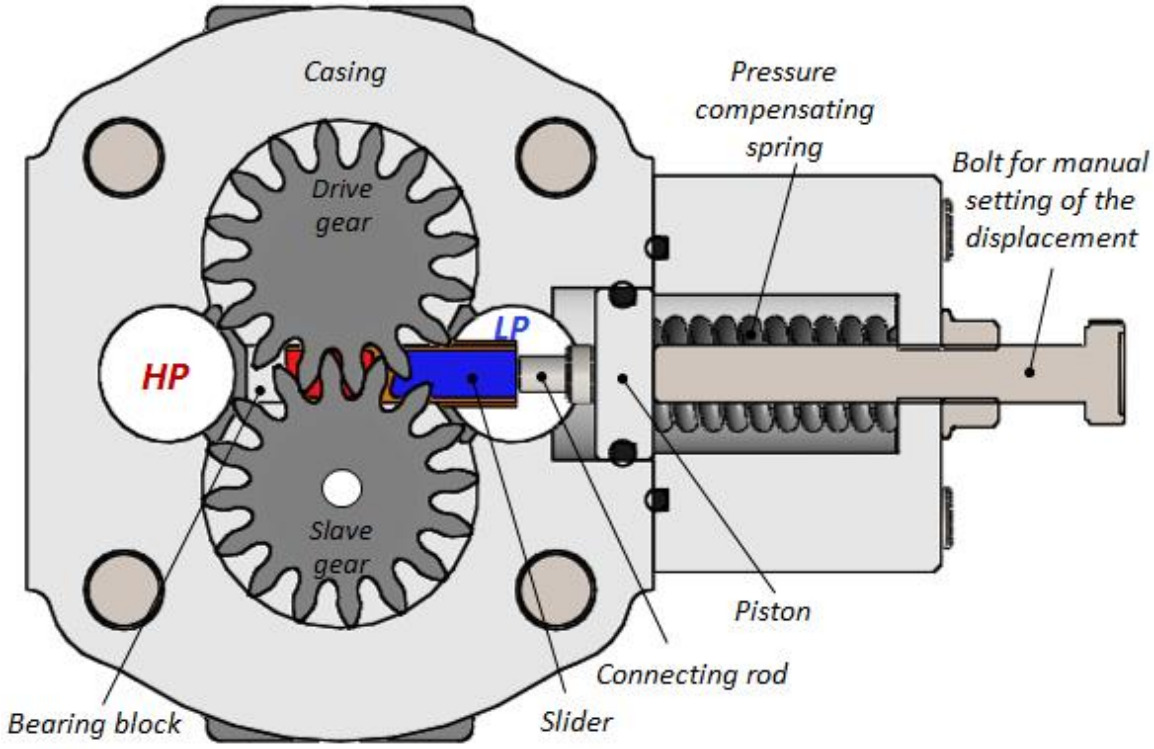

Figure 113: Working concept for pressure compensated design.

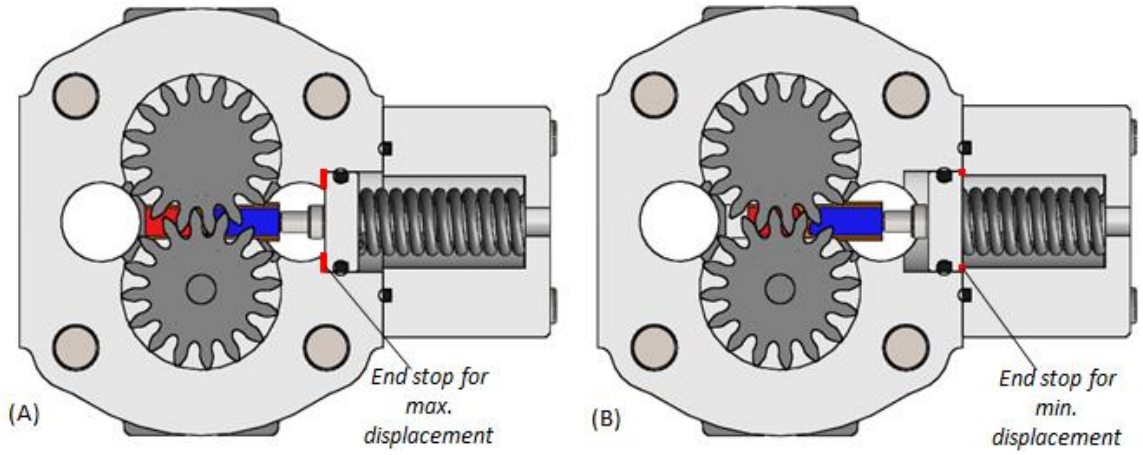

Figure 114: Detail of the pressure compensated design depicting the end stop for (A) max displacement; (B) min displacement.

In order to avoid conditions of bypass flow, the linear motion of the slider is limited by the end stops machined on the casing as shown in Figure 114. The stroke of the slider is therefore restricted to 5.97mm.

With the considered design, it is also easily possible to set the displacement of the VD-EGM manually with the help of the bolt (for manual setting) as shown in Figure 113. For this case however, the pressure compensator springs are not necessary for performing their designated function and hence can be removed from the assembly.

If the end stop for min displacement is removed, the slider would move towards the suction and cause a bypass flow from the outlet to the inlet thereby functioning as a relief valve, thus maintaining the outlet. However, in this study the working of the machine as a relief valve is not considered.

Although the working idea has been described based on the assumption of a VD-EGM for high pressure applications, the idea can be extended to low pressure applications as well as to other actuation systems for controlling the flow.

The details of the design of the different parts of the VD EGM are described in the further parts of this chapter.

9.2. Bearing Block

The bearing block for the pressure compensated design is slightly different from that of the traditional design as described in the previous chapters. In this new design, material is removed from the center of the bearing block to allow for a room for the slider as shown in Figure 115(A). The cross section of the slider seat (shown in Figure 115(B)) is designed in such a way that the slider is capable of movement only in the direction shown in Figure 115(A).

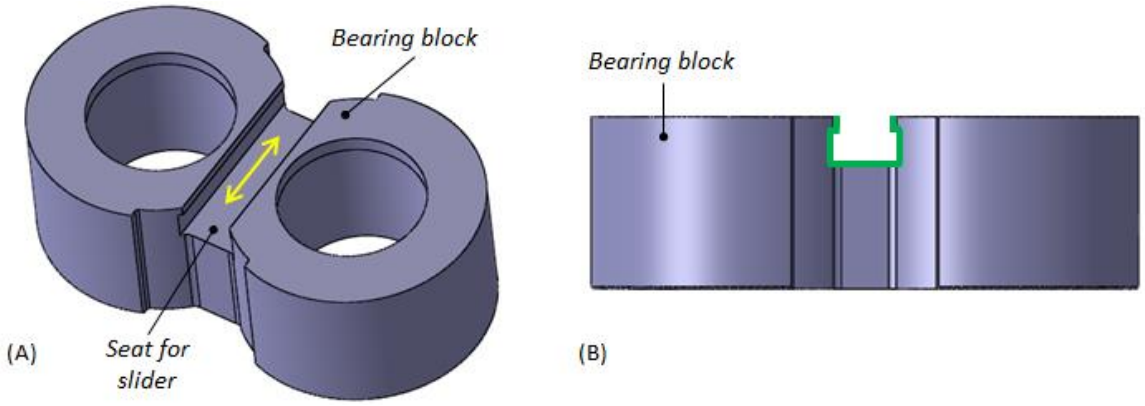

Figure 115: (A) Bearing block for the pressure compensated design; (B) Front view of the bearing block showing the cross-section of the slider seat.

Since the slider-bearing block interface forms an additional leakage connection directly from the high pressure outlet to the low pressure inlet. The machining of the seat for the slider needs to be performed with utmost precision and high surface finish, in order to ensure very small gap in the interface and hence minimizing leakages. In contrast to the traditional design of bearing blocks the grooves which are directly machined on the bearing blocks, the grooves are machined on the slider as described in the next section.

9.3. Slider

The function of the slider is to enable the variation of the timing of the connection of the TSV (displacement chamber) to the suction (inlet) or delivery (outlet). The design of the slider is shown in Figure 116. The cross-section of the slider as shown in Figure 116(B) corresponds to the seat for the slider on the bearing block.

A slot for the connecting rod is situated on the bottom part of the slider as shown in Figure 116(C). The position of the slider for max and min displacement has been depicted in Figure 117. The machining of the slider surfaces need to be also performed at high precision: firstly to ensure that the grooves are located properly to achieve their functions and secondly to ensure that the gap between the slider and the bearing block is minimized, thus reducing the leakages.

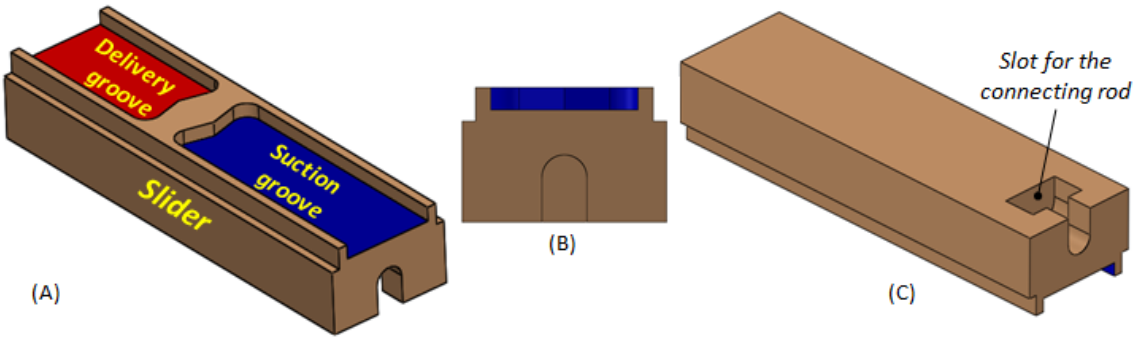

Figure 116: (A) Design of the slider showing the grooves; (B) Side view of the slider showing its cross-section; (C) Bottom view of the slider.

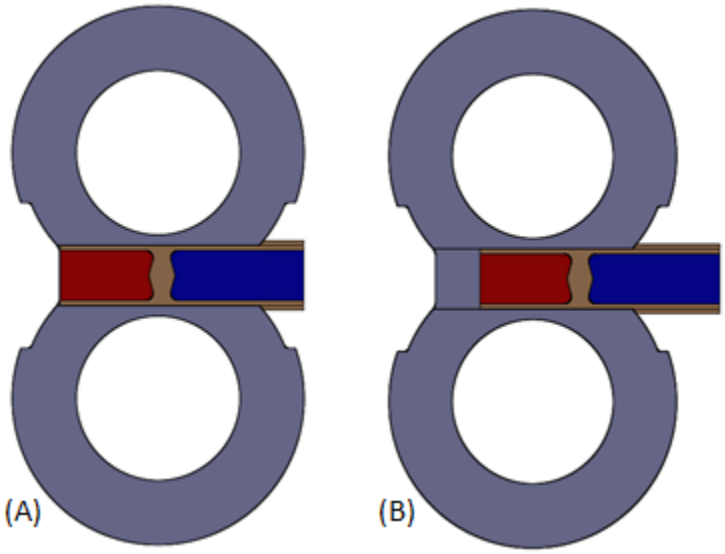

Figure 117: Position of the slider for (A) max displacement; (B) min displacement.

9.4. Connecting Rod and Piston

The purpose of the connecting rod is to connect the slider to the piston as shown in Figure 118. Also, it provides for a better access to the slider while assembling the parts of the VD EGM. The connecting rod has the insert for connecting it to the slider and an e-ring groove for securing the piston as shown in Figure 118.

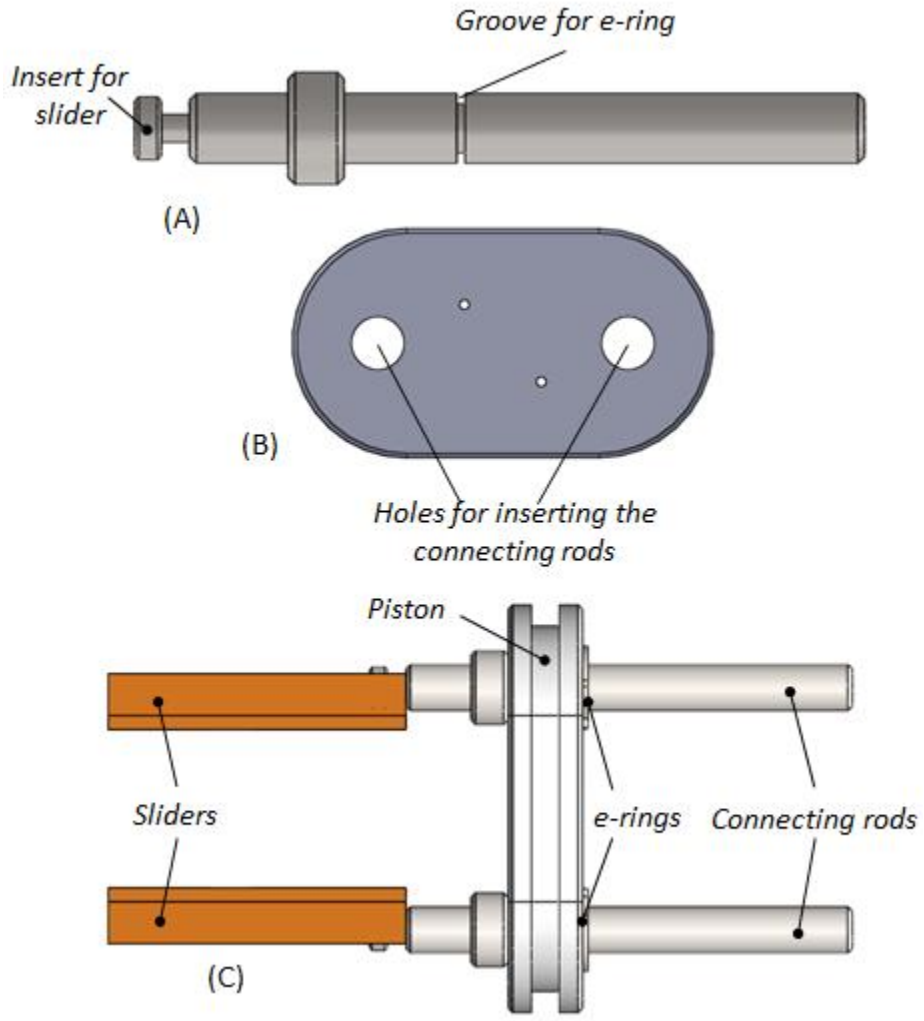

Figure 118: (A) Design of the connecting rod; (B) Design of the piston; (C) Sliders, connecting rods and the piston assembled together.

The piston acts as the element which controls the position of the slider. The right side of the piston shown in Figure 118: (A) Design of the connecting rod; (B) Design of the piston; (C) Sliders, connecting rods and the piston assembled together acts as a resting spot for the springs.

9.5. Casing

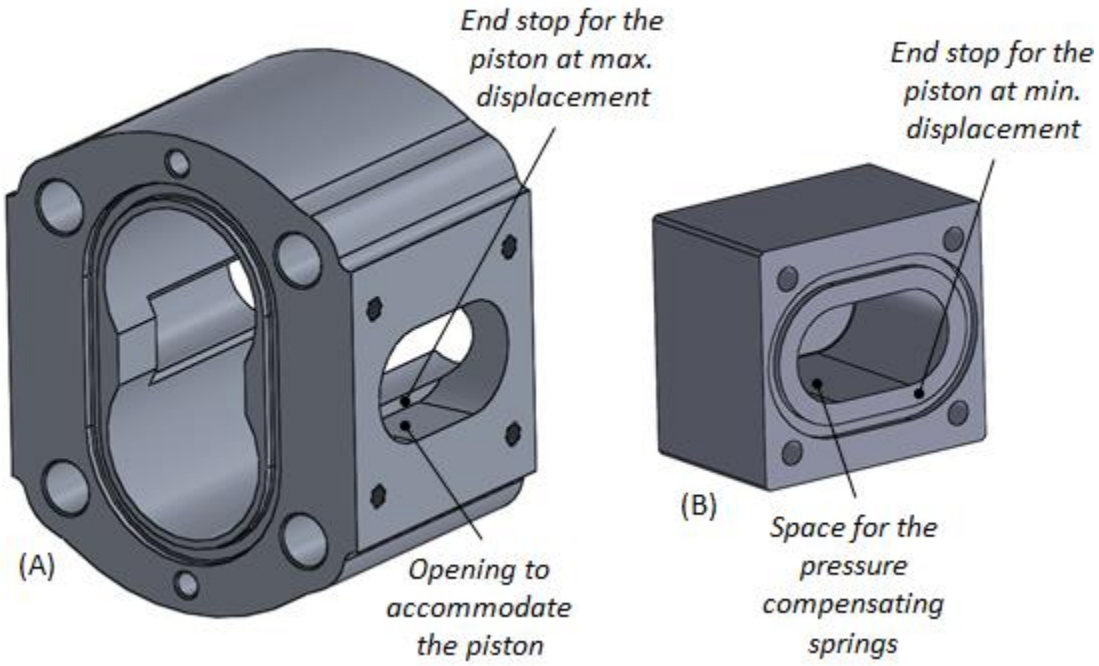

Figure 119: (A) Design of the casing, showing the opening to accommodate the piston and the end stop for max displacement; (B) View of the pressure compensator casing showing the space for the pressure compensating springs and the end stop for min displacement.

The casing (for housing the gears and the bearing blocks) was designed by modifying an already existing commercial casing as shown in Figure 119(A). Particularly, material has been removed from the low pressure side of the casing, to accommodate the piston. In addition to the casing there is also a pressure compensator casing (as shown in Figure 119(B)) for accommodating the pressure compensating springs. This pressure compensator casing will be assembled with the casing using the bolts. In order to restrict the movement of the piston and hence the position of the slider between max and min displacement, end stops are designed on the casing and the pressure compensator casing. The end-stop for max displacement, is on the casing, while the end stop for min displacement is achieved by having an opening of smaller dimensions (compared to the size of the piston) into the pressure compensator casing.

9.6. Pressure Compensator Spring

The pressure compensator spring forms one of the most crucial components in the VD-EGM, as it controls the movement of the slider and hence the displacement change. Assuming a preset pressure of $p^* = 100bar$ for the springs, this means that the VD-EGM operates at max displacement until the pressure at the delivery/outlet reaches 100bar. If the pressure exceeds more than 100bar, the springs would deflect and reach force equilibrium and hence reduce the displacement.

Based on the dimensions of the casing, pressure compensator casing and the piston, the length available to accommodate the spring is $x_0 = 39.70mm$. The area of cross-section of the slider where the pressure forces act is $46.25mm^2$. However, there are two such sliders and hence the total area where the pressure forces act is $A = 92.50mm^2$. The diameter of the opening in the pressure compensator further restricts the diameter of the springs. Therefore, it is assumed that two springs of the same spring constant, k will be implemented in parallel, therefore, the resultant spring constant will be $2 \cdot k$. Several selections of the springs were considered, but the one chosen for the design is a closed ground compression spring with $k = 22.90\ N/mm$ and having a free length of $x_L = 60.325mm$ with 11.5 coils. The pre-set pressure can be calculated (based on the force equilibrium shown in Figure 120(A)) as,

$$p^* = \frac{F^*}{A} = \frac{2 \cdot k \cdot (x_L - x_0)}{A} = 102.3\ bar \approx 100bar. \tag{9.1}$$

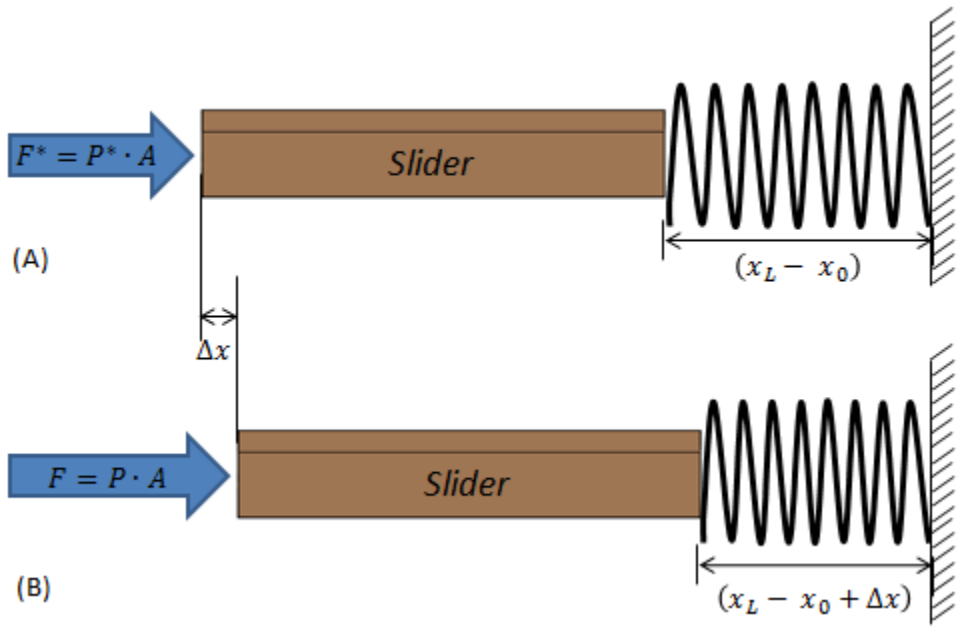

Figure 120: Simplified representation of pressure force and spring force acting on the slider (A) When outlet pressure is preset pressure of the spring; (B) When outlet pressure is greater than the preset pressure of the spring.

When the outlet pressure, $p > p^*$, the spring gets compressed further by Δx, thereby moving the slider to the right (shown in Figure 120(B)) to compensate for the higher pressure. Therefore, the force balance can be written as,

$$p = \frac{F}{A} = \frac{2 \cdot k \cdot (x_L - x_0)}{A} + \frac{2 \cdot k \cdot \Delta x}{A}. \tag{9.2}$$

Substituting Eq. (9.1) into Eq. (9.2) yields,

$$p = p^* + \frac{2 \cdot k \cdot \Delta x}{A}. \tag{9.3}$$

The displacement of the slider, can be expressed as,

$$\Delta x = \frac{(p - p^*) \cdot A}{2 \cdot k} \tag{9.4}$$

For $(p - p^*) = 10 bar$, the displacement of the slider can be calculated as,

$$\Delta x = 2.00\ mm \tag{9.5}$$

The stroke of the slider however is 5.97 mm, which corresponds to a 32% variation from max (100%) to min (68%) displacement. Therefore, for every 2.00 mm displacement of the slider, there will be a 10.70% reduction in displacement of the pump.

Hence, for every 10 bar increase in the delivery pressure, the slider moves towards the suction side by 2.00 mm and reduces the displacement by 10.70%.

9.7. Assembly Design

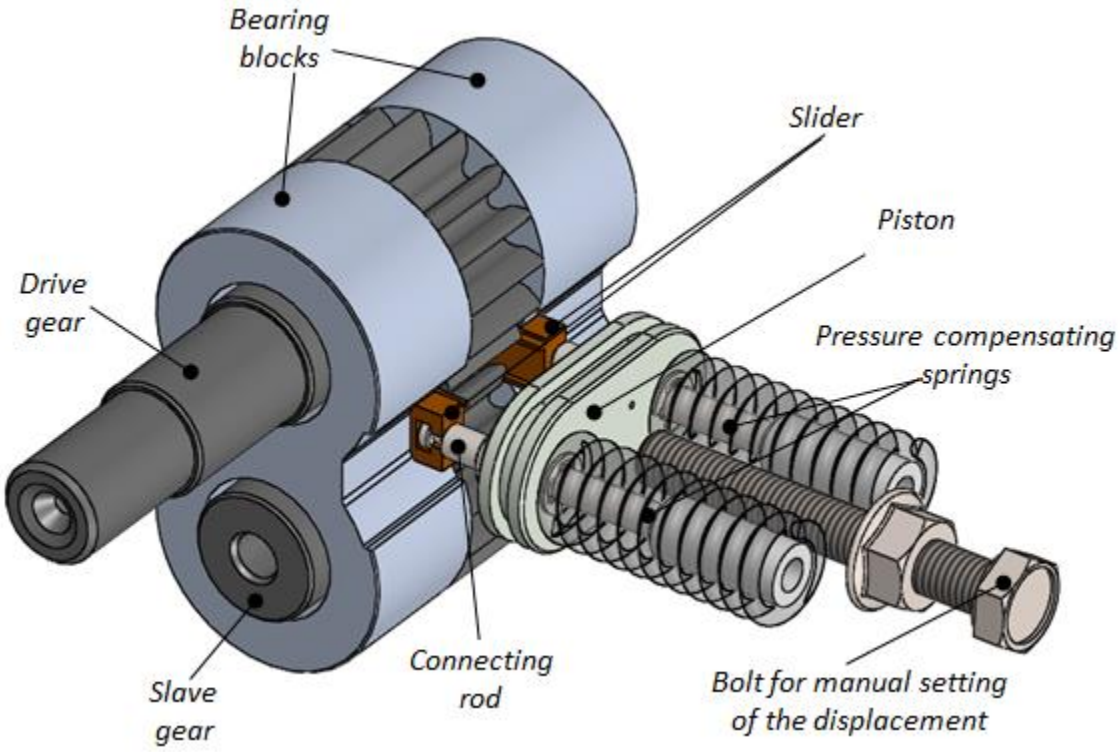

Figure 121: Details of the internal parts of the VD EGM assembly.

The assembly design shown in Figure 121, has all the parts except the casing, flange and the cover. The sliders are placed inside the bearing blocks. The sliders are connected by their respective connecting rods which in turn are connected to the piston as shown in Figure 121. The piston is acted on by the spring assembly which is capable of setting the pressure above which the slider should move to a position of reduced displacement. When the delivery pressure is higher than the preset pressure of the spring, the slider

moves to the suction there by discharging lesser output flow at the expense of a reduced amount of input torque. It can also be seen from Figure 121 that there are only a few more components which are added to the assembly thus making it a simple and cheap design. It can be also seen from Figure 121 that there is an additional bolt which can be used to manually set the position of the slider and hence the displacement of the machine. In this case for manual setting of the displacement, however, the springs are not necessary for performing any particular function. The external view of the VD-EGM is shown in Figure 123.

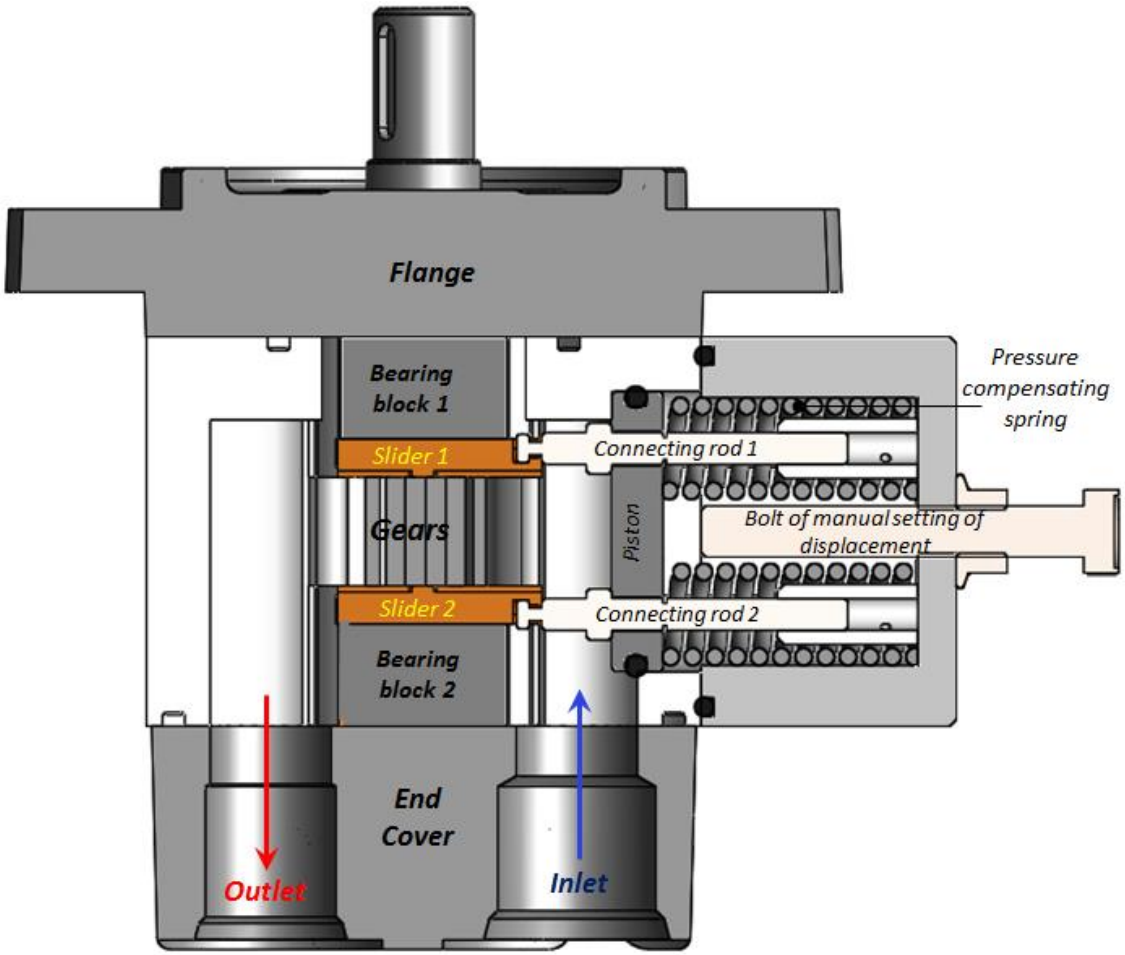

Figure 122: Cut section view of the prototype VD-EGM.

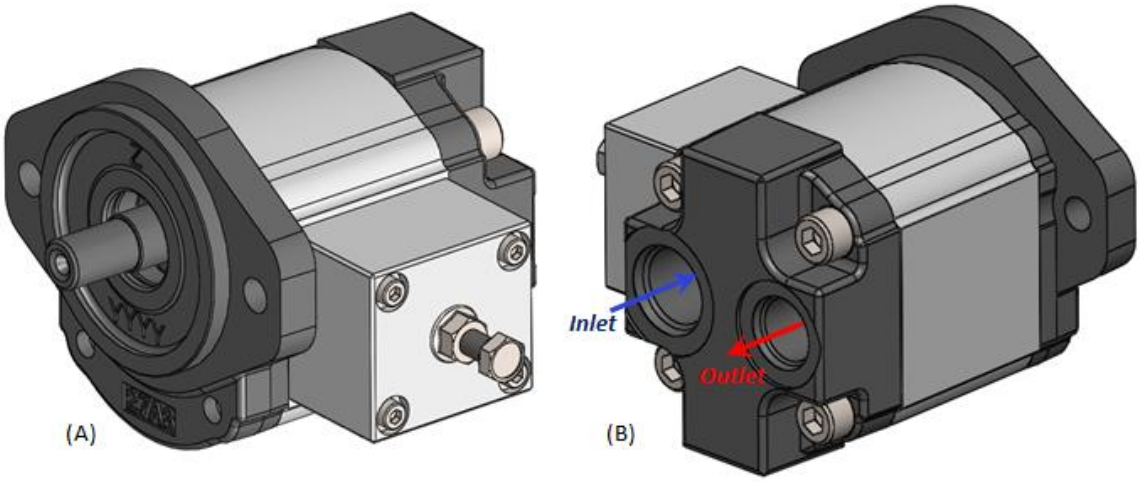

Figure 123: Final complete assembly with (A) flanges and end cover; (B) Inlet and outlet ports.

9.8. Prototype VD-EGM

The designs of the various parts of the VD-EGM previously described previously in this chapter were machined using local machinists available in Lafayette, IN.

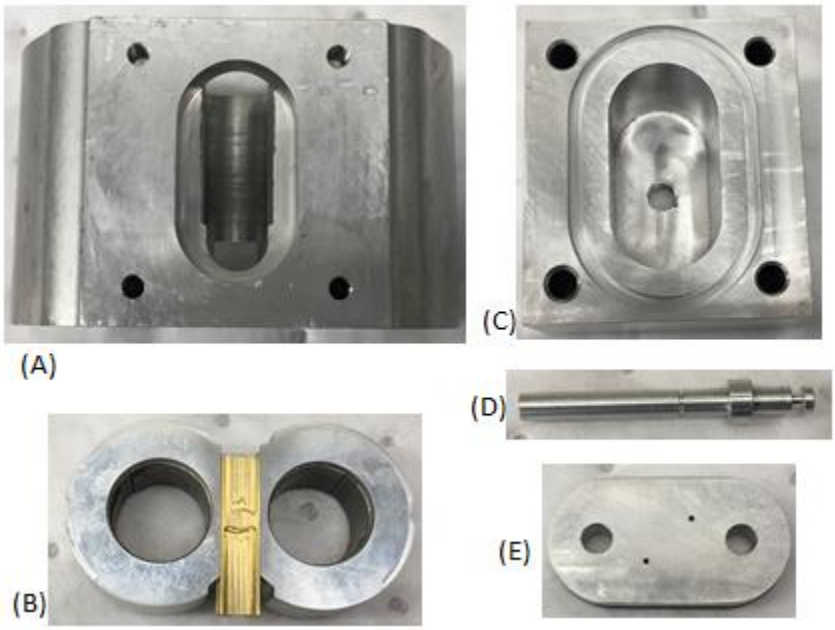

Figure 124: (A) Casing; (B) Bearing block with slider assembled; (C) Pressure compensator casing; (D) Connecting rod; (E) Piston.

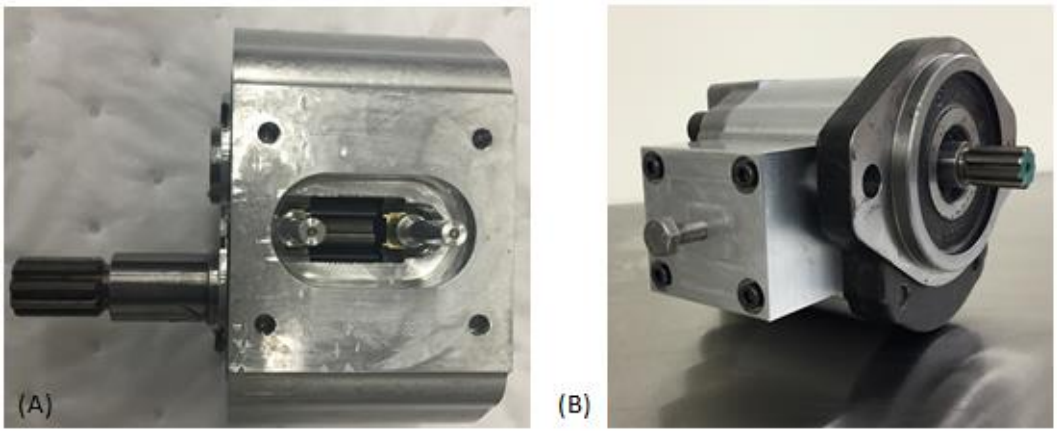

Figure 125: (A) VD-EGM with most of the internal components assembled; (B) Exterior view of the VD-EGM.

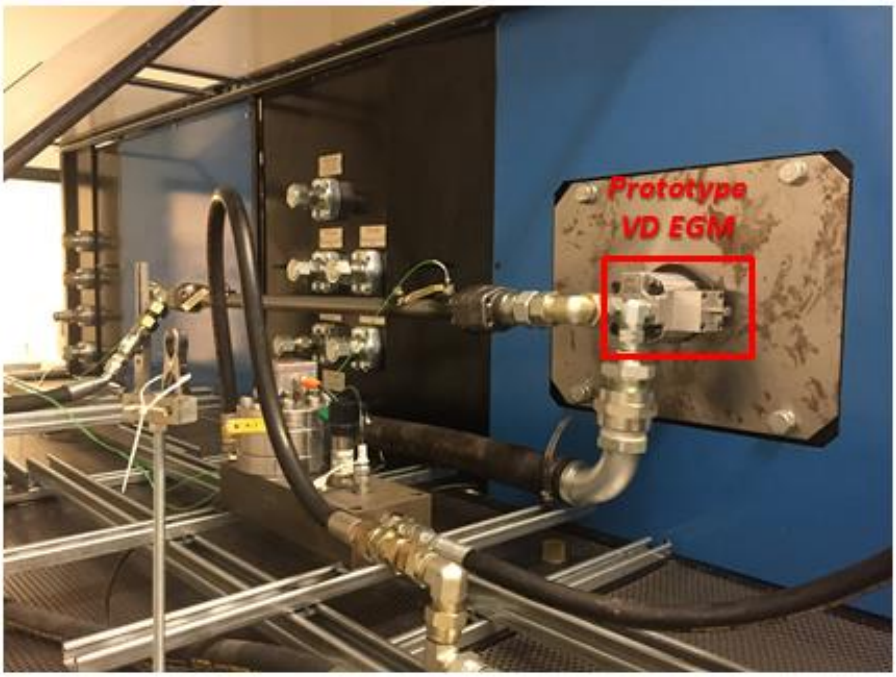

Figure 126: Prototype VD-EGM installed in the multi-purpose test rig during testing.

Figure 124 shows the different parts which were manufactured for the VD-EGM prototype. The optimal asymmetric gears which were previously manufactured for the proof of concept tests were directly used in the prototype. It should be noticed that the slider was machined out of brass material so that close tolerances could be achieved during machining and hence the clearance between the slider and the bearing block can be maintained as low as possible. Figure 125(A) shows the prototype at an intermediate

step in the assembly showing all the internal components of the casing, and Figure 125(B) shows the exterior view of the prototype. The prototype was tested in the steady state test rig (as shown in Figure 126) as already described in Chapter 8.

10. EXPERIMENTAL RESULTS

In this chapter the experimental results pertaining to the performance of the prototype VD-EGM are presented. Firstly, the performance of the VD-EGM in experiments with manual displacement setting is described. Finally, the performance of the VD-EGM with pressure compensation as the actuation system is described.

10.1. Performance of VD-EGM with Manual Setting of Displacement

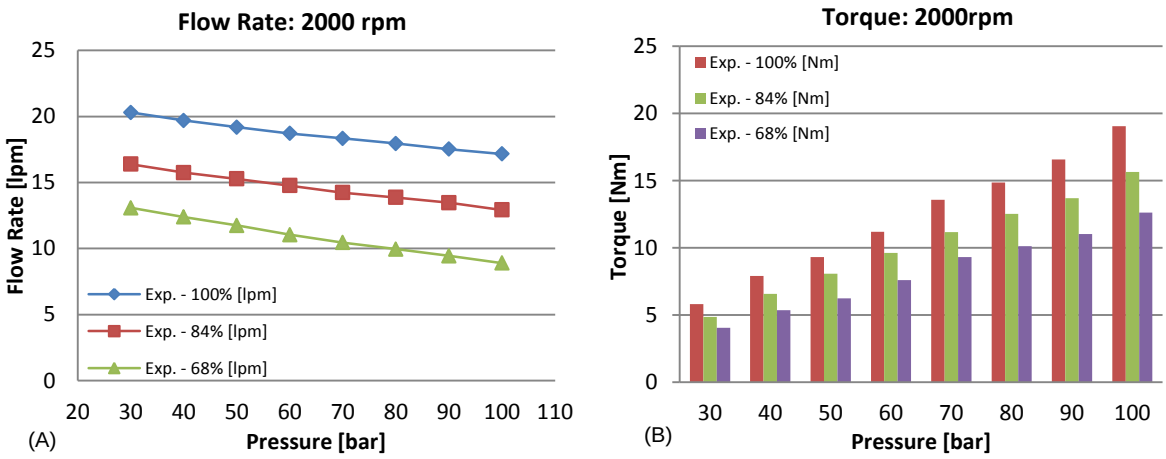

Figure 127: (A) Measured flow rate; (B) Measured torque for 2000 rpm at three levels of displacement.

The VD-EGM can be configured at several displacement settings, by careful positioning of the slider with the help of the bolt for the manual setting of the displacement. Since the stroke of the slider is 5.97mm, max displacement (100%) will be achieved at 0 mm, min displacement (68%) at 5.97mm and an intermediate displacement setting can be chosen at 2.99 mm which corresponds to 84%. The performance in terms of flow rate and input shaft torque was measured for five different speeds of the shaft and eight different

pressure settings at the delivery of the pump (as depicted in Figure 127, Figure 128, Figure 129, Figure 130 and Figure 131).

As can be seen from Figure 127(A) through Figure 131(A), the flow rate reduces proportionally with displacement. There is approximately a 16% reduction in flow rate for the intermediate displacement and a 32% reduction in flow rate at min displacement compared to that at max displacement. Similarly, the input shaft torque required for the operation of the pump has reduced approximately by 16% for intermediate displacement and approximately by 32% at min displacement.

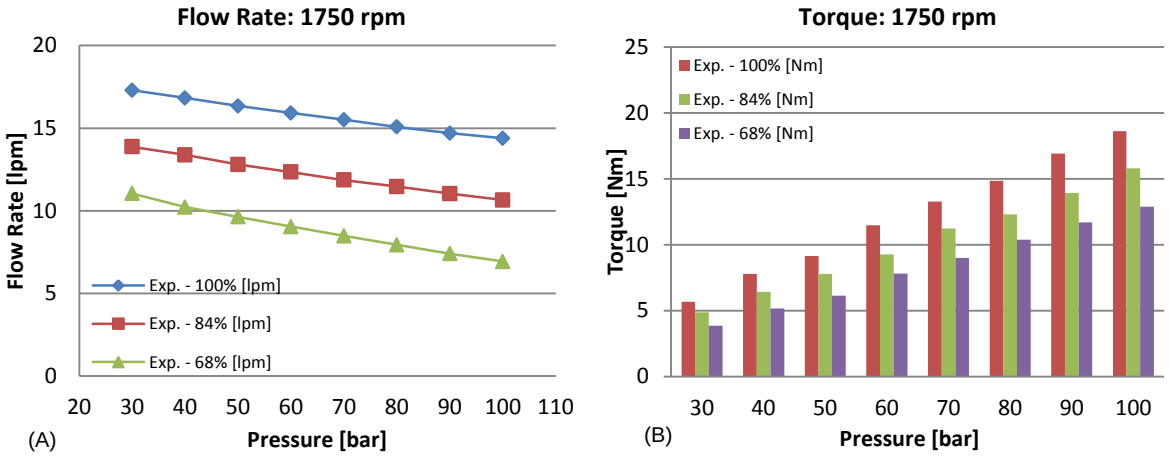

Figure 128: (A) Measured flow rate; (B) Measured torque for 1750 rpm at three levels of displacement.

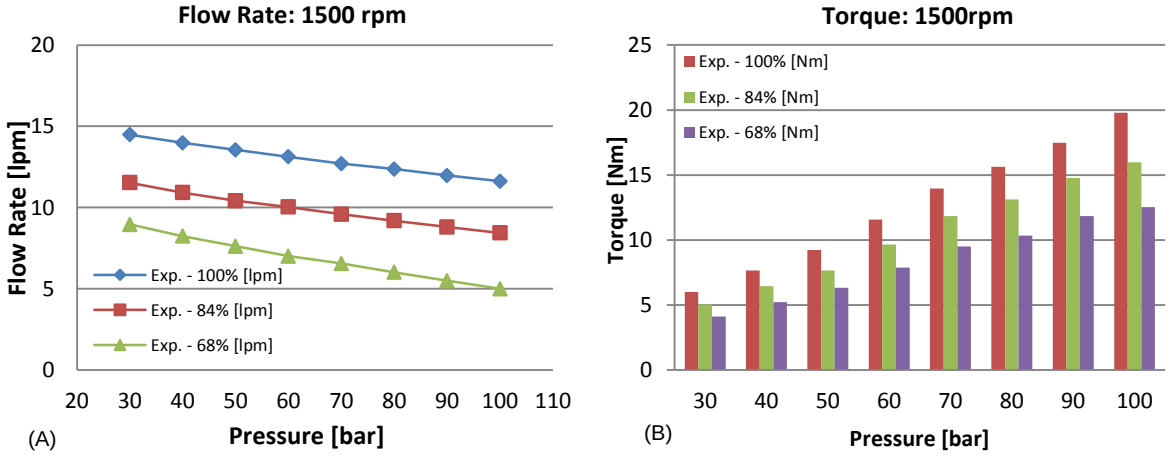

Figure 129: (A) Measured flow rate; (B) Measured torque for 1500 rpm at three levels of displacement.

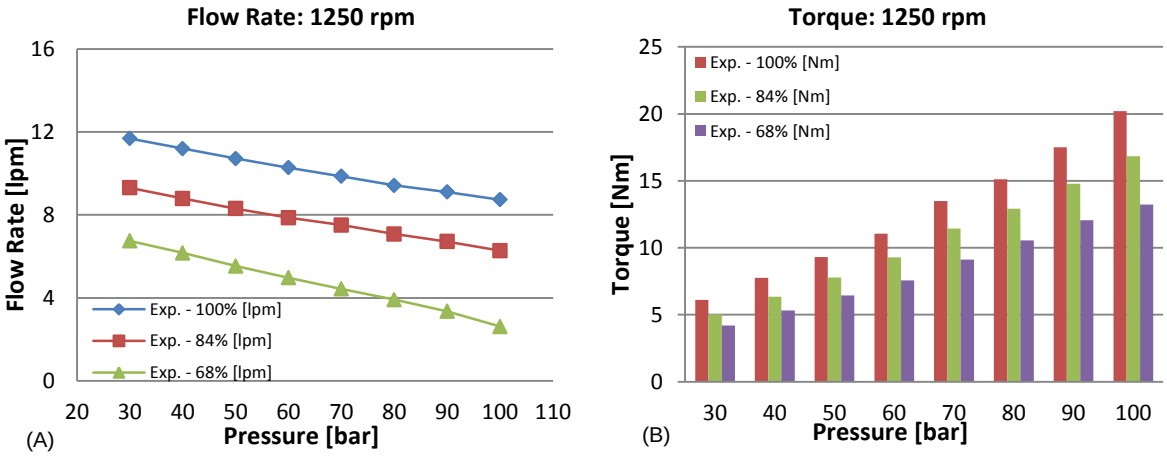

Figure 130: (A) Measured flow rate; (B) Measured torque for 1550 rpm at three levels of displacement.

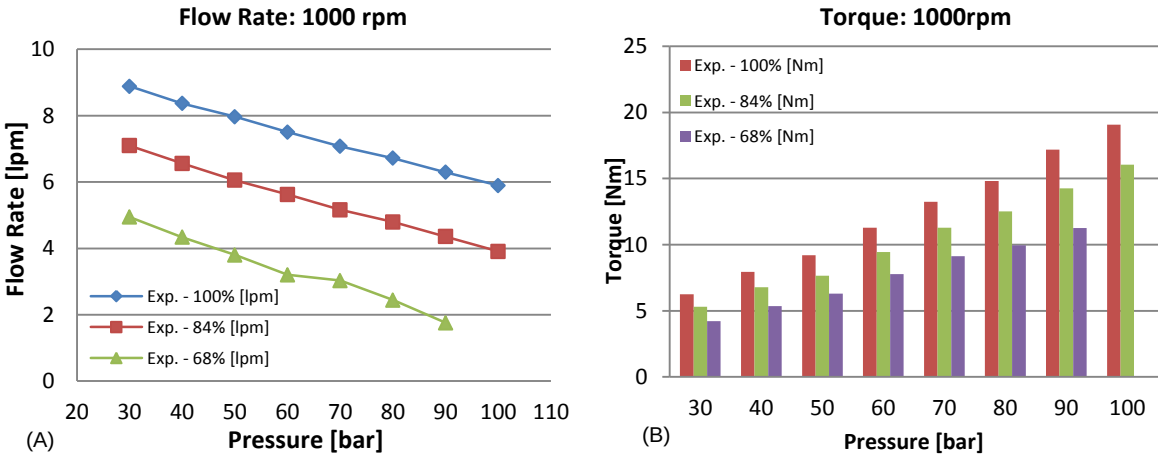

Figure 131: (A) Measured flow rate; (B) Measured torque for 1000 rpm at three levels of displacement.

As expected there is a leakage interface created between the slider and the bearing block which entirely depends on the milling process which was used to machine these parts. According to the measurements, there is a $10\mu m$ of tolerance in machining these parts, therefore in the worst case scenario there will be a gap of $20\mu m$ in the interface. Using the well-known Poiseuille's equation Eq. (10.1), the leakage flow through the gap can be written as,

$$Q_{leak} = \frac{h^3}{12 \cdot \mu} \cdot \frac{\Delta p}{L} \cdot b, \tag{10.1}$$

Where, h is the gap height, L is the gap length, b is the gap width and Δp is the difference in pressure across the gap. Due to the presence of two slider/bearing block interfaces, the total leakage through the interface will be equal to twice the value predicted by Eq. (10.1). Since the slider position changes for different displacement positions, the gap length changes (decreases as the slider moves towards lower displacement positions) and hence the leakage value changes (increases for lower displacement positions, since L appears in the denominator of the Poiseuille's equation) as shown in Figure 132(A). Experimentally, the leakage flow through the gap between the slider and the bearing block can be quantified by calculating the difference between the outlet flow from proof of concept tests (described in Section 8.3) and the flow rates from the tests on the VD-EGM. As described previously in Chapter 8, the proof of concept tests were performed with no slider implemented in the bearing block but with the help of grooves which were directly machined on the bearing blocks.

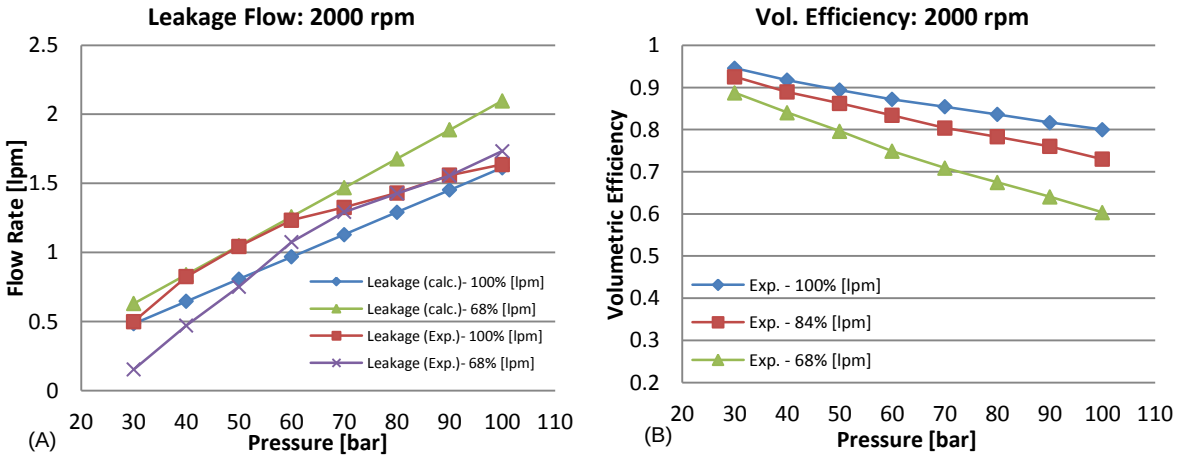

Figure 132: (A) Leakage flow calculation for VD-EGM; (B) Volumetric efficiency of VD-EGM for 2000rpm.

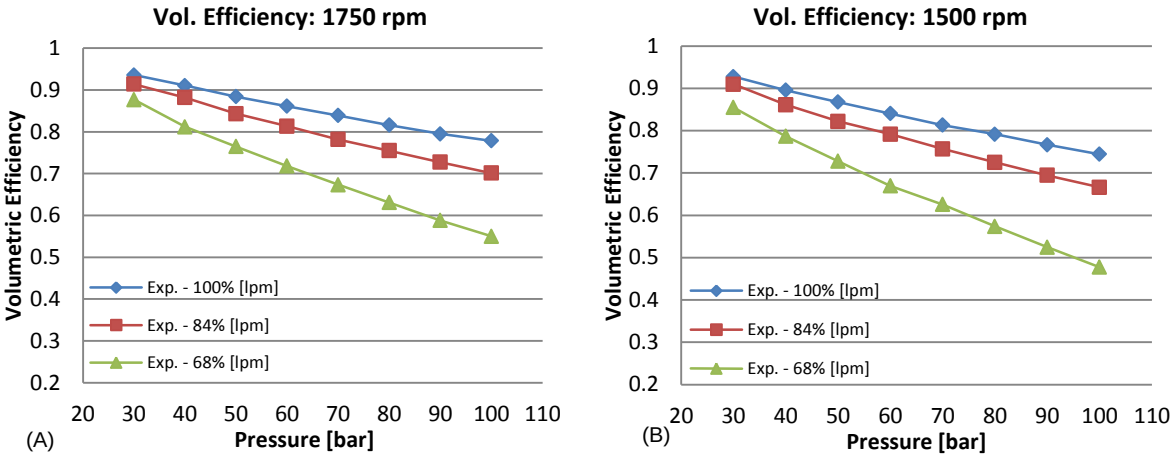

Figure 133: Volumetric efficiency of VD-EGM for (A) 1750rpm; (B) 1500rpm.

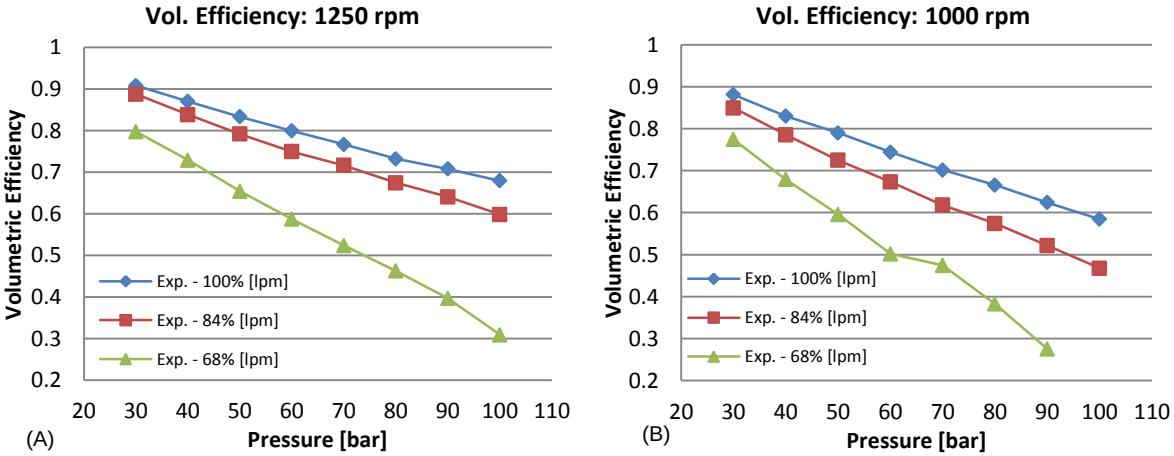

Figure 134: Volumetric efficiency of VD-EGM for (A) 1250rpm; (B) 1000rpm.

It is somewhat safe to assume that the radial leakages (through the gap between the gear tooth tip and the casing) and the lateral leakages (through the gap between the gears and the bearing blocks) remain the same for the proof of concept test and the tests on the VD-EGM. From Figure 132(A), it can be seen that the leakage flow calculated follows a similar trend as compared to that of the experiments, which proves that the additional leakage is introduced due to the gap in the slider/bearing block interface. It should also be noticed that the leakages were calculated based on a linear interpolation of the flow rates from the proof of concept tests since measurements were available for only three different pressure points. Although, a minor discrepancy between the calculated and the experimental leakages, are seen, these can be attributed due to the combined effect of the

tilt in the bearing blocks which may occur during the operation of the machine, the slider position and manufacturing tolerances within the gap. It is also probable that with the introduction of the slider, the bearing blocks will achieve a different axial balance and hence may additionally contribute to the leakages.

Figure 132 though Figure 134, also show the plots of volumetric efficiency for several operating conditions. It can be seen that the volumetric efficiency decreases with displacement, due to the fact that the internal leakages: radial and lateral remain dependent on pressure and hence have a larger influence as the displacement reduces. From these figures it can be noticed that the volumetric efficiency at all displacement settings, increase with speed. This can be explained due to the fact that the casing was broken in during the proof of concept tests at a maximum speed of 2000 rpm, hence the gears achieve better radial sealing and hence better volumetric performance progressively as the speed increases. Overall, a better volumetric performance at all displacement settings can be achieved by maintaining very low clearance values in the slider/bearing block interface.

10.2. Performance of VD-EGM with Pressure Compensation

After characterizing the performance of the VD-EGM at several different displacements using manual actuation system, the VD-EGM was re-assembled with the pressure compensator springs in place. The volumetric performance of the pressure compensated VD-EGM is shown in Figure 135.

From Figure 135, it can be seen that the pressure compensator is working after the preset pressure of $p^* = 100bar$, evidently the flow rate reduces automatically above 100bar. Figure 135 also shows the values of the flow rates at reduced displacements at 84% and 68%, these values were calculated using linear interpolation from the data available from section 10.1. As already described in section 9.6, the pressure compensator has been designed in such a way that above the pre-set pressure of $p^* = 100bar$, the displacement changes automatically by 10.70% per 100 bar increase in the outlet pressure. Hence at 120 bar, the displacement would be equal to 78%. As can be seen from the figure, the

flow rate at 120 bar is lower than that at 84%, which proves the working of the pressure compensator. However, pressures higher than 120 bar were not tested since the gears were not heat treated or hardened.

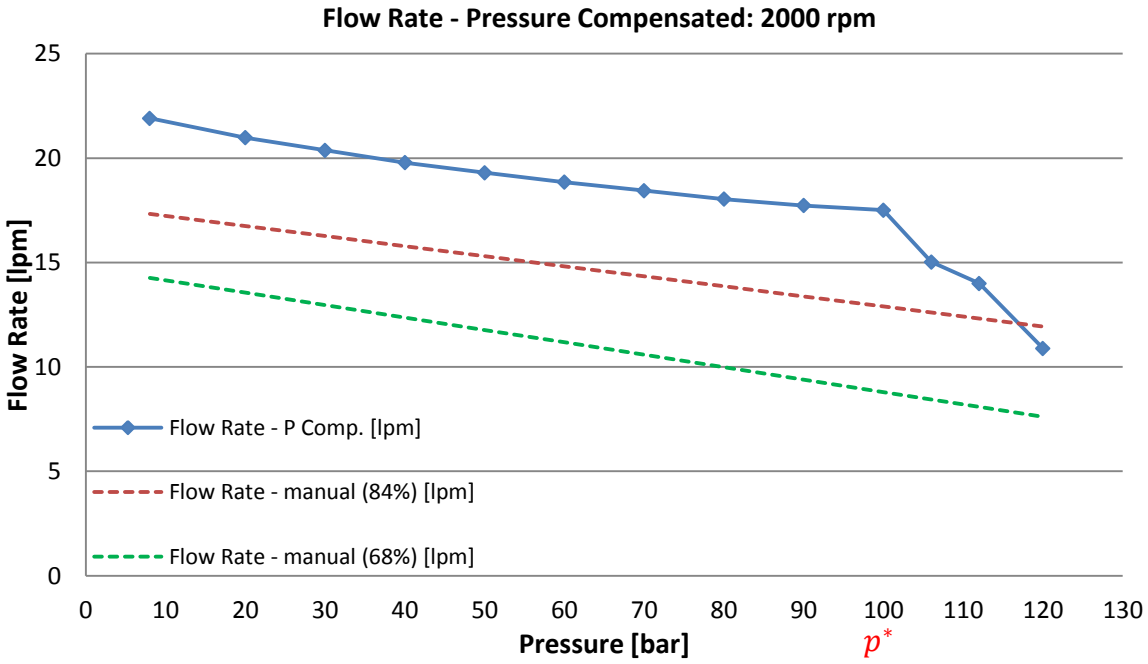

Figure 135: Flow rate of pressure compensated VD EGM at 2000 rpm.

Even though Figure 135 shows the successful working of the pressure compensated system, a steeper slope of the graph above the preset pressure, p^* is desired to change the displacement in a much more rapid manner with pressure. This can be achieved by changing the sizing of the pressure compensator spring, in order to have a faster response to pressure.

The input shaft torque measured from the experiments is shown in Figure 136. It can be seen that due to the pressure compensating mechanism, after $p^* = 100bar$, the displacement is automatically reduced and hence the torque values do not increase further with pressure, but instead it corresponds to the particular displacement setting at which the machine is operating. Therefore at 120 bar, the input shaft torque at full displacement should be 22.43Nm, but due to pressure compensation, the displacement is lowered to 78% and hence the torque reduces top 17.55Nm, thus leading to lower energy consumption.

Figure 136 also shows the torque at 84% and 68% to give a good understanding of the performance of the pressure compensator in terms of torque.

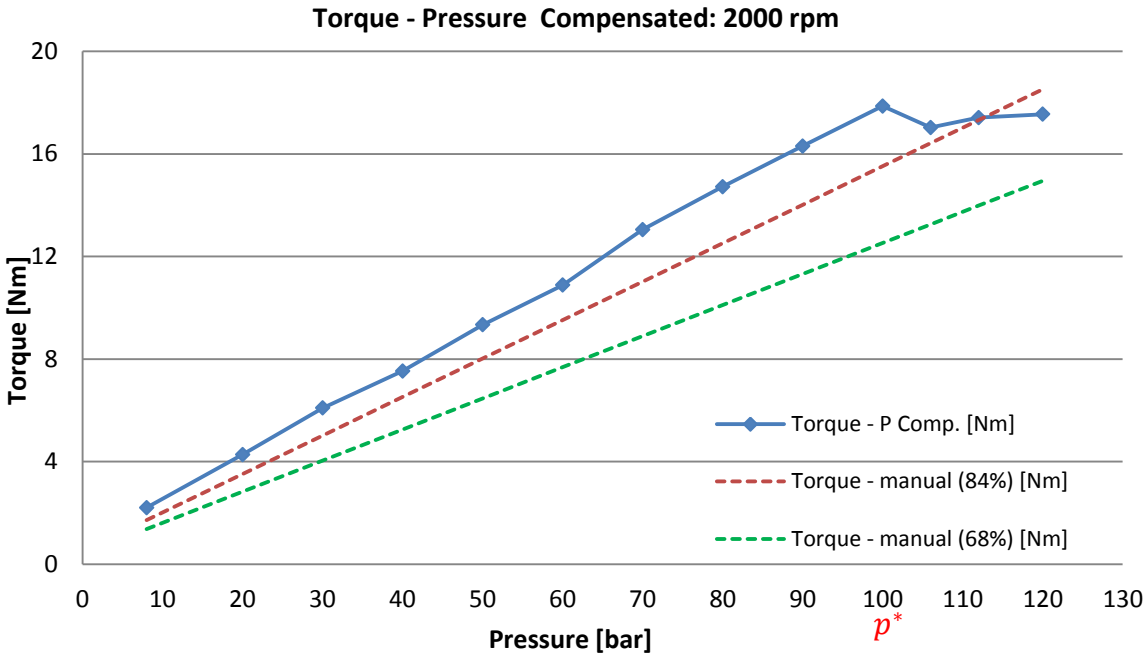

Figure 136: Input shaft torque of pressure compensated VD EGM at 2000 rpm.

Figure 135 and Figure 136 positively shows the working of the pressure compensated VD-EGM and its potentials for reducing energy consumption.

11. SUMMARY AND CONCLUSIONS

The current study presents an innovative approach for a working concept for variable delivery flow type EGM. The main idea behind the working concept for VD-EGM is based on the optimal timing of the connections of the TSVs with the delivery or the suction grooves in the lateral bushings. Particular effort was made to analytically study the concept in terms of displaced volume, delivered flow and input shaft torque. The concept was proved analytically that there is a possible reduction in torque by changing the displacement.

In order to achieve larger range of variation of displacement, novel design of the gears were analyzed. Particularly, gears with asymmetric teeth were proven to be beneficial by offering a larger range of extent of the trapped TSV thereby increasing the range of variation of the displacement. A gear generator was developed, which is capable of designing asymmetric gear based on the different input parameters controlling the shape of the teeth. A lateral bushing designer was also developed, which is capable of designing complicated shapes of the suction and delivery grooves. The gear generator and the lateral bushing designer were integrated inside the geometrical model of HYGESim.

A generalized multi-level-multi-object optimization workflow was created to determine the optimal design of the gears and the grooves simultaneously. The design of the gears and grooves were based on five different objective functions such as: displacement reduction, flow oscillations at the delivery of the pump, features of the meshing process such as internal pressure peaks, local cavitation effects and volumetric efficiency. The optimization process is flexible of switching on and off different objective functions, hence it can be used for designing VD-EGMs as well conventional EGMs. Two different reference cases were considered, one specifically for obtaining VD and the other one to

understand the performance benefits in terms of pressure pulsations at the delivery of the pump.

The optimal design determined by the optimization process, offered a remarkable 32% reduction in displacement while maintaining all the other performance features an optimum. The parameters of the design of the gears were substituted in the analytical expressions for displacement, flow rate and torque. The displacements calculated by the analytical expression matches very closely with that predicted numerically by the optimization tool. However, the optimization was constrained in such a way that the end results can be used for testing in a commercially available casing of an EGM. Therefore, more aggressive designs with reduction in displacements of up to 40% were rejected in the design selection process. Extensive numerical analysis of the forces and torque acting on a particular tooth space surface was performed and the reduction in torque was verified. The performance of the optimal design at max (100%) and min (68%) displacement were analyzed using HYGESim for a multitude of operating conditions. The simulation results showed that the delivery flow rate as well as the input shaft torque reduced proportionally based on the reduction in displacement predicted.

The promising results obtained in simulations motivated for a proof of concept test on a test rig. The gears and the lateral bushings were prototyped and steady state measurements were performed. Experimental results proving the concept of a feasible VD-EGM concept was obtained particularly in terms of delivery flow rate as well as input shaft torque. The reduction in input shaft torque provides a reflection of the reduction in energy consumption thereby promoting the research on VD-EGM. A very good agreement between the predictions of the simulations using HYGESim and those recorded during experiments was obtained.

Following the successful proof of concept tests, a pressure compensated design for VD-EGM was conceptualized (among all the different implementations for the flow control system). The advantages of traditional EGMs such as compact size, shape and inexpensive units were respected in the design process. All the parts were machined and prototyped. Two particular test regimes were designed to completely understand the

performance of the VD-EGM. The first test was based on manual displacement setting. The second test was based on pressure compensation principle. Firstly, the performance of the machine at three different levels of displacement was characterized. It was seen that the flow rate as well as torque reduced proportionally with displacement. The volumetric efficiency of the prototype was lower than that considered during the proof of concept tests, due to the additional leakage interface created by the implementation of the slider within the bearing block.

Secondly, the working of the pressure compensated design was studied. It was seen that the VD-EGM automatically changes its displacement above a certain preset pressure. However, it was understood that the sizing of the spring could be changed to have a faster response of the pressure compensator to change the displacement.

The working of the VD-EGM was successfully demonstrated in simulations and in experiments, proving the feasibility of the concept for achieving significant energy savings. The energy savings benefits of VD-EGMs will open new ventures in the design of EGMs. The new VD-EGM can has potentials to improve the energy efficiency and hence the fuel consumption of current systems based on fixed displacement EGMs by introducing a cost effective solution for realizing flow-on-demand capabilities. With the proposed design of VD-EGM capable of offering a flow variation of 40%, applications such as hydraulic fan drive and fuel injection systems, charge pumps for hydrostatic transmissions can benefit remarkable fuel savings.

Future Work

Since this study only dealt with the design of asymmetric gears, the amount of reduction in displacement was restricted, therefore novel designs of gears with unconventional profiles (such as multi-involute, or shark fin shaped profiles) could be studied to extend the range of displacement variation. An analysis of the sealing of the gap between the slider and the bearing block needs to be performed to design a seal for reducing the leakages through the interface. Other flow actuation systems such as the implementation of an electro-hydraulic mechanism to change the displacement could also be studied for particular applications and to test the machine in a real-life application.

LIST OF REFERENCES

LIST OF REFERENCES

[1]. H. Murrenhoff, S. Sgro, M. Vukovic, 2014, *An Overview of Energy Saving Architectures for Mobile Applications*, 9th International Fluid Power Conference, March 24-26 2014, Aachen, Germany

[2]. M. Ivantysynova, 1998, *Pump Controlled Actuator - a Realistic Alternative for Heavy Duty Manipulators and Robots*, International Scientific Forum in Fluid Power Control of Machinery and Manipulators, Cracow, Fluid Power Net Publication, 1998, chapter 5, pp. 101 – 123.

[3]. D. Yang, D. Zhong, 1987, *Radial-Movable Variable Displacement Gear Pump (Motor)*, CN85109203.

[4]. W. Reiners, G. Wiggermann, 1960, *Variable Delivery Gear Pumps*, The Patent Office London, GB968998.

[5]. L.F. Winmill, 2001, *Adjustable-Displacement Gear Pump*, Patent Application Publication, US2001024618.

[6]. E. Bussi, 1992, *Variable Delivery Gear Pump*, European Patent Application, EP0478514.

[7]. T. Hoji, S. Nagao, K. Shinozaki, 2008, *Gear Pump*, Patent Application Publication, US2008044308.

[8]. J.M. Clarke, 2002, *Hydraulic Transformer using a Pair of Variable Displacement Gear Pumps*, Patent Application Publication, US2002104313.

[9]. C. Bowden, 1989, *Variable Discharge Gear Pump With Energy Recovery*, Patent Application Publication, US4824331.

[10]. C. Bowden, 1990, *Variable Discharge Gear Pump With Energy Recovery*, Patent Application Publication, US4902202.

[11]. P. Zavadinka, R. Grepl, 2014, *Energy Saving Potential of a Hydrostatic Drivetrain with Variable Charge Pump*, Proceeding of the 8th FPNI PhD. Symposium on Fluid Power, FPNI 2014, Finland.

[12]. N. Nervegna, 2003, *Oleodinamica e pneumatica, Volume 1 – Sistemi*, Editore Politeko, maggio 2003.

[13]. M. Nieling, F.J. Fronczak, N.H. Beachley, 2005, *Design of a Virtually Variable Displacement Pump/Motor*, NCFP.

[14]. J. Mahrenholz, J.J. Lumkes, 2009, *Model Development and Experimental Analysis of a Virtually Variable Displacement Pump System*, International Journal of Fluid Power.

[15]. M.B. Rannow, H. Tu, 2006, *Software Enabled Variable Displacement Pumps - Experimental Studies*, ASM*E*-IMECE06 2006 ASME Int. Mechanical Engineering Congress and Exposition. Chicago, Illinois, USA.

[16]. M.B. Rannow, P.Y. Li, 2009, *Soft Switching Approach to Reducing Transition Losses in an ON/OFF Hydraulic Valve*, ASME 2009 Dynamic Systems and Control Conference, Hollywood, California, USA

[17]. S.P. Tomlinson, C.R. Burrows, 1990, *Achieving a Variable Flow Supply by Controlled Unloading of a Fixed- Displacement Pump*, ASME Journal of Dynamic Systems Measurement and Control, vol. 114, no. 1, pp. 166-171.

[18]. J. Ikeda,2002, *Variable Displacement Gear Pump*, JP2002106479.

[19]. E.J. Svenson,1930, *Adjustable Displacement Gear Pump*, United States Patent Office, US1912737.

[20]. J. Grabbel, M. Ivantysynova, 2005. *An investigation of swash plate control concepts for displacement controlled actuators*, International Journal of Fluid Power, Vol. 6, No. 2, pp.19- 36.

[21]. C. Williamson, J. Zimmerman, M. Ivantysynova, 2008. *Efficiency Study of an Excavator Hydraulic System Based on Displacement-Controlled Actuators*. Bath ASME Symposium on Fluid Power and Motion Control (FPMC2008), pp.291-307.

[22]. T.E. Beacham, 1946, *High Pressure Gear Pumps*, Proc. I. Mech. E., 154.

[23]. C. Bonacini, 1961, *Sulla Portata delle Pompe ad Ingranaggi*, L'Ingegnere, Anno, Milan, Italy (in Italian).

[24]. J. Ivantysyn, M. Ivantysynova, 2003, *Hydrostatic Pumps and Motors*, Tech Books Int., New Delhi, India.

[25]. N.H. Manring, S.B. Kasaragadda, 2005, *The theoretical flow ripple of an external gear pump*, ASME Journal of Dynamic Systems, Measurement and Control, 125.

[26]. D. Fielding, C.J. Hooke, K. Foster, M.J. Martin, 1977, *Sources of Pressure Pulsation from a Gear Pump*, Quiet Oil Hydraulic Systems, London, U.K.

[27]. G. Castellani, 1967, *Pompe ad Ingranaggi a Denti Dritti*, Progetto delle Dentature, Giornata Mondiale Della Fluidodinamica, FLUID'67, Milan, Italy. (in Italian).

[28]. M. Eaton, K. Edge, 2001, *Modelling and Simulation of Pressures within the Meshing Teeth of Gear Pumps*, Proceedings of Conference on Recent Advances in Aerospace Actuation Systems and Components, pp. 21-26, Toulouse, France, June, 2001.

[29]. M. Borghi, M. Milani, B. Zardin, F. Patrinieri, 2006, *The influence of cavitation and aeration on gear pump and motors meshing volume pressures*, Proceedings of ASME- International Mechanical Engineering Congress & Exposition, pp. 47-56, Chicago, IL, USA.

[30]. S. Manco, N. Nervegna, 1993, *Pressure Transient in an External Gear Hydraulic Pump*, Proceedings of 2nd JFPS, International Symposium on Fluid Power, pp. 221-228, Tokyo.

[31]. P. Casoli, A. Vacca, G. Franzoni, M. Guidetti, 2008, *Effects of some relevant design parameters on external gear pumps operating: numerical predictions and experimental investigations*, 6th IFK International Fluid Power Conference , Dresden, Germany

[32]. P. Casoli, A. Vacca, G.L. Berta, 2008, *Optimization of Relevant design parameters of external gear pumps*, 7th JFPS International Symposium on Fluid Power, Toyama, Japan,

[33]. B. Zardin, M. Borghi, F. Paltrinieri, M. Milani, 2004, *About the prediction of pressure variation in the inter-teeth volumes of external gear pumps*, 3rd FPNI – PhD Symposium on Fluid Power, Terrassa, Spain.

[34]. K. Nagamura, K. Ikejo, F.G. Tutulan, 2004, *Design and performance of gear pumps with a non-involute tooth profile*, Proc. I. Mech. E., vol. 218. Part B: Journal of Engineering Manufacture.

[35]. W. Kollek, P. Osinski, 2009, *Modeling and Design of Gear Pumps*, Oficyna Wyudawnicza Politechniki Wroclawskiej, Wroclaw, Poland.

[36]. S. Falfari, P. Pelloni, 2007, *Setup of a 1D model for simulating dynamic behaviour of external gear pumps*, Commercial Vehicle Engineering Congress and Exhibition, Rosemont, IL, USA.

[37]. B. Zardin, M. Borghi, 2008, *Modelling and simulation of external gear pumps and motors*, 5th FPNI PhD Symposyum, Kracow, Poland.

[38]. E. Koç, O. Kurban, C.J. Hooke, 1997, *An analysis of the lubrication mechanisms of the bush-type bearing in high pressure pumps*, Tribol. Int., 30 (8).

[39]. E. Koc, C.J. Hooke, 1997, *An experimental investigation into the design and performance of hydrostatically loaded floating wear plates in gear pumps*, Wear, 209.

[40]. M. Borghi, M. Milani, F. Paltrinieri, B. Zardin, 2005, *Studying the axial balance of external gear pump*, SAE 2005 Commercial Vehicle Engineering Congress and Exhibition, Chicago, USA.

[41]. P. Casoli, A. Vacca, G.L. Berta, M. Zecchi, 2009, *A CFD analysis of the flow field in the lateral clearance of external gear pumps*. 11th Scandinavian Int. Conference on Fluid Power, SICFP'09 , Linköping, Sweden.

[42]. M. Zecchi, A. Vacca, P. Casoli, 2010, *Numerical analysis of the lubricating gap between bushings and gears in external spur gear machines*, FPMC 2010 Bath/ASME Symposium on Fluid Power and Motion Control, Bath, UK.

[43]. G. Seeniraj, M. Ivantysynova, 2008, *Multi-objective Optimization Tool for Noise Reduction in Axial Piston Machines*. SAE International Journal of Commercial Vehicles.1(1).

[44]. G. Seeniraj, M. Ivantysynova, 2011, *A Multi-Parameter Multi-Objective Approach to Reduce Pump Noise Generation*. International Journal of Fluid Power, Vol. 12,2011.

[45]. D. Kim, M. Ivantysynova, 2012, *Valve plate optimization focusing on noise reduction in the axial piston machine with high volumetric efficiency*. Proc. of the 7th FPNI PhD Symposium, Reggio Emilia, Italy.

[46]. K. Huang, W. Chang, W. Lian, 2008, *An Optimization approach to the displacement volumes for external spur gear pumps*, Material Science Forum (594).

[47]. K. Huang, C. Chen, 2008, *Kinematic Displacement Optimization of External Helical Gear Pumps*, Chung Hua Journal of Science and Engineering, (6).

[48]. S. Wang, H. Sakurai, A. Kasarekar, 2011, *The Optimal Design in External Gear Pumps and Motors*, IEEE/ASME Transactions on Mechatronics, (16).

[49]. A. Vassena., A. Vacca, 2010, *Design Optimization of the Sliding Elements of External Gear Machines*, 6th FPNI-PhD Symposium, 2010, West Lafayette, USA.

[50]. D. Schwuchow, 2002, *Design tools for Modern External Gear Pumps*, Proceedings of the 3rd International Fluid Power Conference, Aachen, Germany, Vol. 3, pp. 141-152.

[51]. S. Negrini, 1996, *A gear pump designed for noise abatement and flow ripple reduction*, Proceedings of the International Fluid Power Expositions and Technical Conference.

[52]. M. Lätzel, D. Schwuchow, 2012, *An innovative external gear pump for low noise applications*, Proceedings of 8th International Fluid Power Conference, Dresden, Germany.

[53]. K. Nagamura, K. Ikejo, F.G. Tutulan, 2004, *Design and performance of gear pumps with a non-involute tooth profile*, Proceedings of the Institution of Mechanical Engineers, Part B: Journal of Engineering Manufacture, Vol. 218, pp. 699 – 711.

[54]. V.S. Kumar, D.V. Muni., G. Muthuveerappan., 2008, *Optimization of asymmetric spur gear drives to improve the bending load capacity*, Mechanism and Machine Theory, Vol. 43, pp. 829-838

[55]. A. Kapelevich, 2000, *Geometry and design of involute spur gears with asymmetric teeth*, Mechanism and Machine Theory, Vol. 35, pp. 117 – 130.

[56]. G. Campanella, 2009, *Analisi Della Variazione Di Cilindrata Di Macchine ad Ingranaggi Esterni Agendo Sulla Distribuzione*, MS Thesis, University of Parma.

[57]. P. Casoli, A. Vacca, G. Berta, 2007, *A Numerical Model for the Simulation of Flow in Hydraulic External Gear Machines*, *Power Transmission and Motion Control*, Bath, UK.

[58]. A. Vacca, G. Franzoni, P. Casoli, 2007, *On the Analysis of Experimental Data for External Gear Machines and their Comparison with Simulation Results*, ASME International Mechanical Engineering Congress and Exposition, Seattle, (WA), USA.

[59]. A. Vacca, M. Guidetti, 2011, *Modelling and experimental validation of external spur gear machines for fluid power applications*, Elsevier Simulation and Modelling Practice and Theory, vol. 19, pp. 2007-2031.

[60]. A. Vacca, S. Dhar, T. Opperwall, 2011, *A Coupled Lumped Parameter and CFD Approach for Modeling External Gear Machines*, SICFP 2011 The Twelfth Scandinavian International Conference on Fluid Power, Tampere, Finland

[61]. S. Dhar, A. Vacca, A. Lettini, 2012, *A Fluid – Structure Interaction model to analyze Axial Balance in External Gear Machines*, International Conference on Fluid Power (IFK).

[62]. S. Dhar, A. Vacca, A. Lettini, 2012, *A Novel Elastohydrodynamic Model for the Lubricating Gaps in External Gear Machines: Evaluation of Axial Balance*, FPNI PhD. Symposium on Fluid Power.

[63]. S. Dhar, A. Vacca, 2012, *A Novel CFD-Axial motion coupled model for the axial balance of lateral bushes in external gear machines*. Elsevier Simulation Modelling Practice and Theory, (26).

[64]. S. Dhar, A. Vacca, 2013, *A Fluid Structure Interaction-EHD Model of the Lubricating Gaps in External Gear Machines: Formulation and Validation*. Tribology International.

[65]. P. Casoli, A. Vacca, G. Franzoni, G.L. Berta, 2006, *Modelling of fluid properties in hydraulic positive displacement machines*, Elsevier. Simulation. Modelling. Practice and Theory Vol. 14, Issue 8, pp. 1059-1072, November.

[66]. LMS.Imagine SA, 2008, *HYD Advanced Fluid Properties*, Technical Bulletin no. 117, rev 8B.

[67]. J. Zhou, A. Vacca, P. Casoli, A. Lettini, 2014, *Investigation of the impact of Oil Aeration on Outlet Flow Oscillations in External Gear Pumps*, IFPE 2014, Int. Fluid Power Expo, March 4-8, Las Vegas, USA.

[68]. R.S. Devendran, A. Vacca, 2013, *Optimal design of gear pumps for exhaust gas aftertreatment applications*, Simulation Modelling Practice and Theory (Elsevier), 38, pp. 1-19.

[69]. R.S. Devendran, A. Vacca, 2012, *Optimal design of gears and lateral bushes of external gear machines*, Proceedings of Bath/ASME Symposium on Fluid Power and Motion Control, FPMC 2012, September 12-14, 2012, Bath, UK.

[70]. V. Marinov, 2011, *Manufacturing Process Design*. Kendall/Hunt Publishing, Dubuque, IA.

[71]. F.L. Litvin, A. Fuentes, 2004, *Gear Geometry and Applied Theory*, 2nd edition, Cambridge University Press.

[72]. Geometric Polygon Clipper Library:- http://www.cs.man.ac.uk/~toby/gpc/

[73]. R. Klop, A. Vacca, M. Ivantysynova, 2009, *A Method of Characteristics Based Coupled Pump/Line Model to Predict Noise Sources of Hydrostatic Transmission*, Proceedings of Bath/ASME Symposium on Fluid Power & Motion Control, Hollywood, California, pp. 291-298.

[74]. T. Opperwall, A. Vacca, 2013, *A combined FEM/BEM model and experimental investigation into the effects of fluid-borne noise sources on the air-borne noise generated by hydraulic pumps and motors*, Proceedings of IMechE Part C: Journal of Mechanical Engineering Science.

[75]. R. Trautschold, 1955, *Gear Design and Production Rules and Working Formulas*, Columbia Graphs

[76]. J.E. Shigley, C.R. Mischke, 1996, *Standard Handbook of Machine Design*, 2nd Edition, Mc Graw Hills

[77]. http://www.esteco.com/home/mode_frontier/mode_frontier.html

[78]. M.D. Buhmann., *Radial Basis Functions*, 2003, Theory and Implementations, ., 2003, Cambridge University Press

[79]. K. Deb, A.Pratap, S.Agarwal, T. Meyarivan, 2000. *A fast and elitist multi-objective genetic algorithm-NSGA-II*, KanGAL

[80]. D.E. Goldberg, 1989, *Genetic Algorithms in Search, Optimization and Machine Learning*. Addison-Wesly Longman Publishing Co.,Inc, Boston, MA, USA

[81]. G. Box, N.R. Draper, 1987, *Empirical model building and Response Surfaces Methodology*, J.Wiley & Sons.

[82]. C. Poloni, V. Pediroda, 1997, *GA Coupled with Computationally Expensive Simulations: Tools to Improve Efficiency, Genetic Algorithms and Evolution Strategies in Engineering and Computer Science*, J.Wiley and Sons.

[83]. C. Poloni, A. Giurgevicch, L. Onesti, V. Pediroda, 2000, *Hybridization of a Muti-Objective Genetic Algorithm, a Neural Network and a Classical Optimizer for a Complex Design Problem in Fluid Dynamics*, Computer Methods in Applied Mechanics and Engineering, Vol. 186, pp. 403-420.

[84]. R.S. Devendran, A. Vacca, 2014, *A novel design concept for variable delivery flow external gear machines*, International Journal for Fluid Power, 15:3, pp. 127-137

VITA

VITA

Ram was born on September 26th, 1987 in Kollam, India. He received his Bachelor of Engineering (Hons.) in Mechanical Engineering and Master of Science (Hons.) in Economics from the Birla Institute of Technology and Science (BITS) Pilani, India. After one year of internship at the General Electric – Global Research Center, in Bangalore, India, Ram moved to the Lafayette, IN for pursuing graduate studies at Purdue University. He joined the Maha Fluid Power Research Center in September 2010 to pursue Master of Science in Mechanical Engineering under the guidance of Prof. Andrea Vacca. His Masters' thesis focused on the development of a novel optimization methodology for designing external gear machines. After completing his Masters' degree, Ram continued to pursue a PhD degree in the same lab, under the supervision of Prof. Andrea Vacca. His PhD research focused on the design and development of a new energy efficient external gear machine which brings about significant reduction in fuel consumption of the particular system in which it is used.